Universidade de Aveiro Departamento de Física

2020

Pedro Rafael dos Santos Prezas

Polarização elétrica de biomateriais baseados em hidroxiapatite, como filmes em substratos metálicos, para aumento da bioatividade

Universidade de Aveiro

Departamento de Física

2020

Pedro Rafael dos Santos Prezas

Polarização elétrica de biomateriais baseados em hidroxiapatite, como filmes em substratos metálicos, para aumento da bioatividade

Tese apresentada à Universidade de Aveiro para cumprimento dos requisitos necessários à obtenção do grau de Doutor em Física, realizada sob a orientação científica do Doutor Manuel Pedro Fernandes Graça, Investigador Principal do Departamento de Física da Universidade de Aveiro e co-orientação do Doutor Manuel Jorge de Araújo Pereira Soares, Professor Auxiliar do Departamento de Física da Universidade de Aveiro.

O autor agradece o apoio financeiro da FCT através da bolsa de doutoramento PD/BD/114457/2016

.

Dedico este trabalho aos meus pais, por sempre me terem incentivado a aprender.

o júri

presidente

Prof. Doutor João Carlos de Oliveira Matias

Professor Catedrático da Universidade de Aveiro

Prof. Doutor Mauro Miguel Costa

Professor Titular, Universidade Federal de Mato Grosso

Prof. Doutor João Filipe Calapez de Albuquerque Veloso

Professor com Agregação, Universidade de Aveiro

Prof. Doutor João Paulo Miranda Ribeiro Borges

Professor Associado com Agregação, Faculdade de Ciências e Tecnologia – Universidade Nova de Lisboa

Prof. Doutora Sandra Maria Fernandes Carvalho

Professora Auxiliar, Universidade do Minho

Prof. Doutor Manuel Pedro Fernandes Graça

Professor Auxiliar em Regime Laboral, Universidade de Aveiro (Orientador)

agradecimentos

Começo por agradecer especialmente aos meus orientadores, Prof. Dr. Manuel Graça e Prof. Dr. Jorge Soares, pela orientação, acompanhamento e motivação prestados no decorrer deste trabalho, bem como pelo companheirismo de longa data.

Um agradecimento especial a todos os meus colegas e amigos do "Laboratório de Medidas Eléctricas", pelo apoio, disponibilidade e principalmente pela amizade. Agradeço também especialmente aos meus amigos mais próximos, com uma menção especial aos ilustres membros do grupo "Conferência de Solvay".

Aos técnicos do Departamento de Física da UA, Ivo Mateus, Miguel Rocha e Júlio Gonçalves, pelo apoio fundamental prestado no desenvolvimento do tríodo de corona. Agradeço ao Dr. Filipe Oliveira e ao Dr. Miguel Neto, do Departamento de Engenharia de Materiais e Cerâmica da UA, pela disponibilidade e auxílio prestado nas medidas de perfilometria óptica e ensaios mecânicos. Á Dra. Rosário Soares, do Laboratório Central de Análises da UA, pela realização dos difractogramas de DRX.

Agradeço à Ceramed pela disponibilização do equipamento CoBlast bem como o auxílio prestado à realização deste trabalho através da facultação de matérias primas e revestimentos depositados por spray de plasma.

Agradeço ao Prof. Dr. João Paulo Borges e ao Prof. Dr. Jorge Silva, do Departamento de Ciências dos Materiais da FCT/UNL, pela disponibilidade e colaboração na realização dos testes biológicos *in vitro*.

E finalmente um agradecimento muito especial aos meus pais, José e Alcina, por sempre me terem incentivado a alcançar esta meta.

palavras-chave

Hidroxiapatite, Tríodo de corona, Plasma spray, CoBlast, Revestimentos bioactivos, Carregamento eléctrico, Testes biológicos

resumo

Foi desenvolvido de raiz um sistema experimental que permite carregar amostras através de uma descarga controlável num tríodo de corona. O sistema desenvolvido permite produzir uma descarga de polaridade positiva ou negativa, aplicar o método de carregamento com corrente de carga constante, seguir em tempo real o aumento do potencial de superfície da amostra, controlar a temperatura de descarga até 200 ºC e possui uma atmosfera reprodutível de baixa humidade.

O sistema foi desenvolvido com o intuito de carregar com uma descarga de corona negativa revestimentos bioactivos de hidroxiapatite depositados por dois processos: spray de plasma e CoBlast, este último um processo relativamente recente.

Foram estudados os seguintes parâmetros de processo do CoBlast: razão mássica entre abrasivo e dopante, distância de ejeção e pressão de ejeção. Mostrou-se que razões mássicas de 50/50 e distâncias inferiores a 30 mm são vantajosas.

O método de carregamento com corrente de carga constante não é possível ser aplicado nos revestimentos produzidos por CoBlast, pois estes são caracterizados como tendo regiões onde substrato metálico está directamente exposto à descarga. Os revestimentos produzidos por spray de plasma, com uma espessura média de 70 μm, foram carregados negativamente a 200 ºC com sucesso, atingindo potenciais de superfície na gama dos - 1400-1800 V, traduzindo-se em campos eléctricos nas amostras praticamente impossíveis de serem atingidos por polarização convencional de contacto. O controlo de corrente de carga é melhor para mais baixas correntes de carga. Ensaios e medidas complementares feitas em pastilhas de hidroxiapatite revelaram densidades de carga armazenada na gama dos 10^{-5} - 10^{-4} C/cm^2, bem como uma estabilidade temporal da carga armazenada muito promissora.

Os testes biológicos *in vitro* revelaram uma maior proliferação osteoblástica nos revestimentos carregados comparativamente com os revestimentos de controlo não carregados, indicando também um estágio mais avançado de formação de nova hidroxiapatite em solução simuladora de fluido corporal.

keywords Hydroxyapatite, Corona triode, Plasma Spray, CoBlast, Bioactive coatings, Electrical charging, Biological tests.

abstract

A corona triode experimental system was developed “from scratch”. The developed system is able to produce a negative or positive discharge, to apply the constant charging current method, to follow in real-time the surface potential buildup of the sample, to control the discharge temperature up to 200 ºC and a low humidity, reproducible atmosphere is maintained in all the charging experiments.

The system was developed in order to charge with a negative corona discharge hydroxyapatite bioactive coatings produced by two processes: plasma spray and CoBlast, the former being a relatively recent process.

The following CoBlast process parameters were studied: the weight ratio between the abrasive and dopant, the blasting distance and the blasting process. It was shown that a weight ratio of 50/50 and distances lower than 30 mm are preferable.

The constant charging current method cannot be applied in the coatings produced through the CoBlast process, because they are characterized by having regions where the metallic substrate is directly exposed to the discharge. The coatings produced through the plasma spray process, with an average thickness of 70 μm, were successively charged at 200 ºC, reaching surface potentials in the - 1400-1800 V range, translating in electric fields across the samples which are practically impossible of being reached through conventional contact polarization. The charging current controllability is better for lower charging current values. Complementary experiments performed in hydroxyapatite coatings revealed stored charge densities in the 10^{-5} – 10^{-4} C/cm^2 range, as well as a very promising temporal stability of the stored charge.

The *in vitro* biological tests revealed an increased osteoblastic proliferation in the charged coatings compared to non-charged control coatings, also indicating a more advanced stage of new hydroxyapatite development in a simulated body fluid solution.

List of Acronyms

ACP	amorphous calcium phosphate
Alu	alumina
ALP	alkaline phosphatase
APS	atmospheric plasma spray
α-TCP	alfa-tricalcium phosphate
β-TCP	beta-tricalcium phosphate
BCP	biphasic calcium orthophosphates
CDHap	calcium-deficient hydroxyapatite
CGDS	cold gas dynamic spraying
CHap	carbonated hydroxyapatite
CpTi	commercially pure titanium
ECD	electrochemical deposition
EDX	energy dispersive X-ray spectroscopy
FTIR	Fourier-transform infrared spectroscopy
Hap	hydroxyapatite
IS	impedance spectroscopy
ISO	International Organization for Standardization
LPPS	low-pressure plasma spraying
MCD	sintered hydroxyapatite
OHap	oxyhydroxyapatite

PS	plasma spray
R_a	arithmetic average roughness
RT	room temperature
S_a	arithmetic average surface roughness
SBF	simulated body fluid
SEM	scanning electron microscopy
TGA	thermogravimetric analysis
THR	total hip replacement
Ti	titanium
TMA	thermomechanical analysis
TSDC	thermally stimulated depolarization currents
TTCP	tetracalcium phosphate
XRD	X-ray diffraction

List of Figures

List of Tables

Chapter 1 Introduction

1.1 State of the Art

1.1.1 A growing market

The global market of orthopaedics reached US$49 billion in 2017, about 1/5 of the Portuguese gross domestic product in that year, and shows an increasing trend, being projected to reach US$60 billion by the year of 2022, fuelled by a global increasing demand and need of orthopaedic surgical interventions [1, 2]. The prevailing factors behind this increasing demand are related to unhealthy lifestyles and aging of the worldwide population. An unhealthy lifestyle, characterized by a lack of physical activity and poor dietary habits, causing overweight problems, is prejudicial to our hard tissues. Mechanical stimuli are a key factor to keep our bones in a healthy state because they are constantly being remodelled to cope with the mechanical loads they are subjected to [3]. Lack of exercise and mechanical stimuli will weaken the bones, decreasing their density and leading to diseases such as osteoporosis. This is the reason why astronauts, in a zero-gravity condition during a space mission, are required to do vigorous exercise every day, in order to maintain musculoskeletal health after the mission. Overweight issues are also promoting osteoarthritis conditions. The aging of the global population, together with the increase of the average lifespan, are also important factors leading to a progressively higher amount of orthopaedical surgeries. More surprisingly, the number of younger patients is growing, due, among other factors, to the practice of dangerous and physical-damaging sports activities [2, 4]. Younger people will have a much higher probability to need additional and revision surgeries compared with older people since the average lifespan of the majority of the biomedical implants is not "planned" for the younger. An example of a fact that corroborates this discussion is the increasing number of total hip replacement (THR) surgical interventions. Fig. 1.1 shows a THR, embodying the femoral stem, the femoral head and the acetabular cup [4]. The femoral stem is usually made from titanium (Ti) or the Ti6AL4V alloy and the femoral head is made from alumina (Al_2O_3 - Alu) or Ti. The acetabular cup is normally a Ti cup containing an Alu insert (or sometimes a polymer is

used, such as polyethylene), as fig. 1.1 depicts. However, Alu is being preferred due to a much lower wear rate than metal on polyethylene contact. Moreover, the release of small polymer particles can trigger inflammatory processes. Over the past years, a great number of orthopaedic implants are coated with a bioactive ceramic material known as hydroxyapatite. The rationale behind this bioactive coating will be explained in detail on the following topics, but basically it is able to promote a direct bonding between the metallic implant and the surrounding biologic bone. It should be noted that, for example, that when the surgeons place a THR inside the body, they will open a cavity in the femur where they introduce the implant (observe fig. 1.1). In consequence, the implant is surrounded by biologic bone, especially in the femoral stem region, and a small gap exists between them. As it will be shown, the non-coated Ti implant is not able to promote a direct and stable bonding with the biologic bone, because it is bioinert, while the bioactive hydroxyapatite coating is able to promote such bonding. In fig. 1.1, the hydroxyapatite [$Ca_{10}(PO_4)_6(OH)_2$, Hap] coating can be seen in both the femoral stem and acetabular cup components.

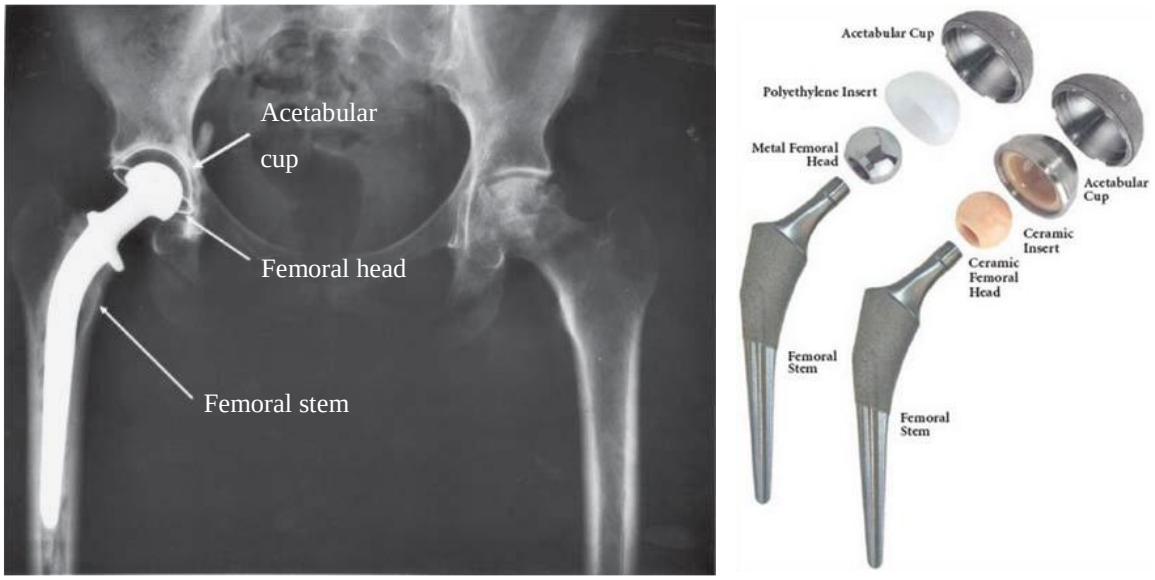

Figure 1.1 In the left: A total hip replacement (THR) [4]. In the right: The acetabular cup: a Ti or Ti alloy metallic cup with an Alu insert (ceramic insert) or with a polymer (polyethylene) insert.

In the United States, based on the U.S. National Center for Health Statistics, the number of THR interventions increased from 138.700 in 2000 up to 310.800 in 2010. While the replacements increased 92% among patients aged 75 or older, they increased by 205%

among patients aged 45 to 54 [5]. In Portugal, the number of THR performed in 2010 is estimated to be more than 6000, only supplanted by total knee replacements [6]. In fact, THR and total knee replacements are two of the most common orthopaedic implants that people receive every year. Here, we decided to focus on THR statistics. In Germany, between 2003 and 2009, 1.38 million THR were performed [4]. This large number is related to the fact that the German healthcare system is considered the most restriction-free and consumer-oriented in Europe, allowing patients to get an easy access to any type of treatment they wish, with short waiting times. On the flip side of the coin, medical professional organizations and the media have been criticizing cases where THR procedures are carried out while there is no medical evidence that such procedure would be required for that particular patient [4]. In England, the National Joint Registry recorded that more than 790.000 THR were performed between 2003 and 2015. In South Korea, the Health Insurance Review and Assessment Service informed that more than 60.000 THR were performed between 2010 and 2017.

The United States is currently the largest market in the world, however the Asia-Pacific region (India, China, Australia, Indonesia, Taiwan, etc.) represents the fastest growing market in the world, mainly led by the fast-developing countries, which are improving their healthcare systems and infrastructures, as well as the money spent per capita on the population health issues. Globally, the market growth is also benefiting from the advancements in the research and development of new bone substitutes and implants with improved properties, such as the level of bioactivity. Additionally, new advantageous and low-cost processing techniques, e.g. new techniques for deposition of a bioactive film in the surface of a metallic implant, are being researched and developed, opening new doors towards new paths of differentiation in a growing market [2].

Table 1.1 shows the total orthopaedic sales performance ($millions) of the "big players" in the market [1]. The data does not include the dental implants market. This industry reached $49 billion in 2017. The seven companies explicitly referred in table 1.1 held about 66% of the total market in 2017. The three largest product segments by revenue

are joint reconstruction (THR, knee replacement, etc.), spine interventions and trauma (fractures, broken bones). In 2017, they represented about 70% of the total revenue [1].

Table 1.1 Total orthopaedic sales performance ($millions) concerning the years 2016 and 2017 [1].

	2017	2016	$ Change	% Change
DePuy Synthes	$8,791.4	$8,756.5	$34.9	0.4%
Zimmer Biomet	$7,273.9	$7,100.9	$173.0	2.4%
Stryker	$6,670.0	$6,330.8	$339.2	5.4%
Smith & Nephew	$3,353.4	$3,250.5	$102.9	3.2%
Medtronic	$2,966.0	$2,930.0	$36.0	1.2%
Arthrex	$2,267.3	$2,048.1	$219.2	10.7%
NuVasive	$1,029.5	$962.0	$67.5	7.0%
5 companies with revenue between $400MM and $800MM	$3,000.3	$2,817.4	$182.9	6.5%
8 companies with revenue between $200MM and $399MM	$1,982.8	$1,843.3	$139.5	7.6%
19 companies with revenue between $100MM and $199MM	$2,629.2	$2,464.5	$164.7	6.7%
7 Orthobiologics companies with revenue between $100MM and $400MM	$1,884.9	$1,825.2	$59.7	3.3%
~1,000 companies with revenue below $99MM	$7,520.1	$7,256.7	$263.4	3.6%
Total	**$49,368.8**	**$47,585.9**	**$1,782.9**	**3.7%**

1.1.2 Human bone: an ingenious functional gradient composite

With the branching of physics into different interdisciplinary fields, physicists, depending on their subject of interest, are required to acquire knowledge about different fields such as medicine, geology, biology, etc. The biology and medicine concepts discussed in this thesis are presented in such a way that they should allow a relatively easy comprehension for those who are not experts on the subjects, as it is our case. We will not dive into unneeded complexity and details, because the dynamics and interactions between the human bone and the surrounding physiological medium are very complex, involving many players and complex biochemical, biophysical and mechanical processes. We expect that these concepts support and enrich the main physical core of this thesis.

Even the best materials research scientist will be a layman when compared to Nature. Human bones are complex natural functional gradient composites containing both an organic component, mainly type-I collagen, and a mineral inorganic component, comprised of Hap parallelepipedic nanocrystals with dimensions of about ~ 50x25x3 nm, as shown in fig. 1.2, at the nanostructural hierarchical level [7]. The Hap nanocrystals are

oriented with their c-axis parallelly aligned to the collagen fibrils, providing the strength and toughness of the bone while the collagen provides the flexibility and the medium for the precipitation of the Hap nanocrystals. These organic and inorganic components represent about 95 wt% of the dry bone [7].

On a macroscopic scale, there are basically two types of bone: cortical bone, which is denser and stronger and comprises about 80% of the skeleton and the trabecular (also known as cancellous or spongy) bone, less dense (porosity ranges between 50 and 90%) and having weaker mechanical properties, such as a considerable lower modulus of elasticity. Cortical bone is found in shafts of long bones (e.g. femur, tibia, etc.) and in the surfaces of the flat bones (e.g. skull, mandible, etc.) while trabecular bone can be found primarily in the extremities of long bones and in the inner part of flat bones, as it is also shown in fig. 1.2 [8]. Cortical bone has additionally an outer fibrous structure that allows the presence of nutrient supplying blood vessels, nerve endings and bone specialized cells known as osteoclasts and osteoblasts, the function of which be discussed on the following topic 1.1.3. At the microstructural level, the building block of cortical bone is the osteon, while for trabecular bone is a porous network of trabeculae, as illustrated in fig. 1.2 [7].

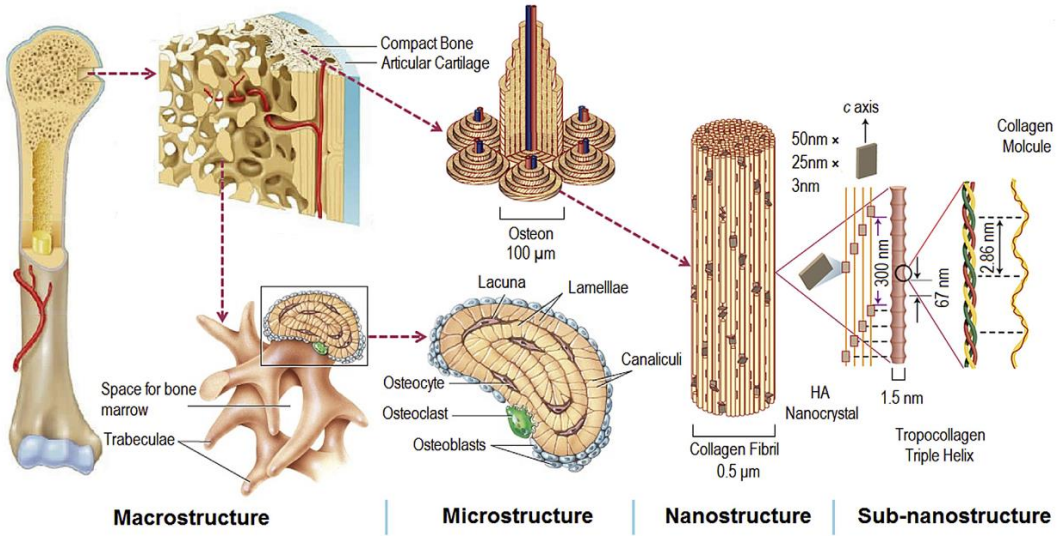

Figure 1.2 The hierarchical structure of the human bone across several characteristic length scales, ranging from the macrostructure down to the nanostructure [7].

Table 1.2 shows some important mechanical properties of human bones and also other skeletal-related tissues, known as soft connective tissues (articular cartilage and tendon, the former is a tissue that connects the muscle to the bone) [4]. The connection between all the different tissues, including bones and muscles, together with the "carefully planned" differences in the mechanical parameters of each component, namely the Young's modulus, is characterized by a smooth and balanced gradient of mechanical stresses distribution along all the connections. One of the mechanical problems that can occur at the bone/biomedical implant interface is the stress shielding of the natural biologic bone: considering that the implant constituent materials have typically larger modulus of elasticity compared to both cortical and cancellous bone, the implant will sustain almost all of the mechanical loads. However, since bone needs mechanical stimulation to remain healthy, the insufficient loading may result in bone weakening in the affected areas. Hence, work is under progress in order to develop implant materials with a modulus that approaches that of biologic bone. In an ideal situation, an "isoelastic" implant should be developed, which, so far, is an impossible task considering the materials typically used. Nonetheless, there are materials which have a very similar modulus compared to bone (cortical bone, more particularly), as it is the case of the 45S5 bioglass®.

Table 1.2 Some important mechanical physical properties of human bones and also other skeletal-related tissues [4].

Property	Cortical bone	Cancellous bone	Articular cartilage	Tendon
Compressive strength (MPa)	100–230	2–12	—	—
Flexural or tensile strength (MPa)	50–150	10–20	10–40	80–120
Strain to failure (%)	1–3	5–7	15–50	10
Young's (tensile) modulus (GPa)	7–30	0.5–0.05	0.001–0.0	1
Fracture toughness ($MPa\sqrt{m}$)	2–12	—	—	—
Compressive stiffness ($N\,mm^{-1}$)	—	—	20–60	—
Compressive creep modulus (MPa)	—	—	4–15	—
Tensile stiffness (MPa)	—	—	50–225	—

Overall, it is safe to claim that human bones comprise a natural ingenious functional gradient composite system.

1.1.3 Osteocytes, osteoclasts and osteoblasts: the bone remodelling agents

Osteoclasts and osteoblasts are bone specialized cells, fundamental in the bone remodelling dynamics, a continuous process within our body. In fact, our bones are not static, they are continuously being rebuilt and remodelled in order to adapt to the external stimuli requirements. This continuous adaptation can include processes such as density changes, replacement of old bone by new bone, resorption and removal of damaged bone and formation of new bone in the resorption area. The damaged areas being repaired are not necessarily related to large defects such as fractures, but actually, microdamaged areas are frequently being repaired.

Osteoblasts have a much higher abundance than osteoclasts and their functions include the production and mineralization of the bone matrix: they are able to synthesize both the organic (collagen) and inorganic (Hap) components. Additionally, and not least important, they are the cells that regulate both the amount of formed bone and the number of osteoclasts, i.e., the expression and differentiation of osteoclasts are controlled by the osteoblasts [9]. Osteoclasts, on its turn, are specialized in the degradation of the bone tissue, both the organic component, by the secretion of several proteolytic enzymes, and the inorganic component, by the secretion of H^+ ions which increase the acidity of the surrounding physiologic fluid, causing the Hap dissolution. Abnormal osteoclastic formation and activity is related to pathogenic mechanisms leading to bone loss in diseases such as osteoporosis, periodontitis and peri-implantitis, metastatic tumor diseas and loosening of implants [9]. There is still another type of cells, the osteocytes, that actually comprise more than 90% of all bone cells, and most of the times they are found enclosed within the bones. They are essentially osteoblasts that were incorporated into the bone matrix. Recent researches have shown that they are responsible for the regulation of both osteoblastic and osteoclastic activities, by expressing activators and inhibitors of both kinds of activities. In fig. 1.3, the left diagram shows the communication paths between the bone

cells: osteocytes express RANKL (receptor activator of nuclear factor kappa B ligand, a specific protein) to control the osteoclastic activity and sclerostin (another specific communication protein) to control the osteoblastic activity [10]. Bone remodelling and repair dynamics is, therefore, a balance between the osteoblastic and the osteoclastic activities, as depicted in fig. 1.3. Osteocytes also contribute to the systemic control of phosphate metabolism [9]. Phosphate is essential for various cellular metabolic processes and of course for Hap mineralization in our bones. It is the sixth most abundant ion in the human body, and of its total content, 80 up to 85% is located in the Hap of our bones [11].

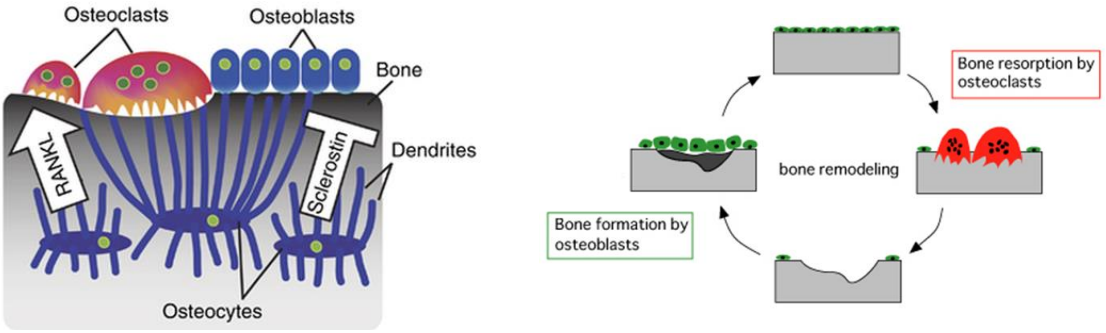

Figure 1.3 In the left: the bone specialized cells - osteocytes regulate the osteoclastic and osteoblastic activity through the expression of RANKL and sclerostin proteins, respectively [10]. In the right: bone remodelling and repair dynamics is a balance between osteoblastic and osteoclastic activities.

In conclusion, our bones are not static but instead, they are a complex system always adapting to the external stimuli they are subjected to. They are also frequently remodelled due to frequent formation of microcracks. For such duties, three bone specialized cells are in constant activity: osteocytes, osteoblasts and osteoclasts, the bone remodelling agents.

1.1.4 Biomaterials: from the prehistory to the present day

There are different definitions of what is a biomaterial, but one of the most accepted was established in 1982 during the conference "Clinical Applications of Biomaterials", held at the National Institutes of Health, in Maryland, USA. It states: "a biomaterial is defined as any substance (other than a drug) or combination of substances, synthetic or natural in

origin, which can be used for any period of time, as a whole or as a part of a system, which treats, augments, or replaces any tissue, organ, or function of the body" [12].

The use of foreign materials to be applied as implants within the human body for hard tissue substitution is already a very old practice. Some archaeological findings showed that efforts to replace missing teeth date back to the prehistoric period [13]. There are also reports that indicate that the replacement/substitution of harshly damaged hard tissues is a practice with over than 2000 years [14]. The materials applied back were typically based on metals such as copper and bronze, but also shells, corals and ivory, mainly from elephant tusks [13, 14]. Metals, in particular, became the most popular materials used for bone substitution for a long time period, and a "science" in which other materials than copper and bronze were regarded as potential good bone substitutes was not developed until the middle of the XIX century. One of the main problems of metals such as copper is that it corrodes in the physiological media of the human body, causing the release of Cu^{2+} ions (which in high concentrations may become biotoxic), which often led to severe infections which threaten the life of the patients [14]. In 1880, based on the resemblance between the composition of ivory and the bone, Gluck et al. applied an ivory prosthesis using anchoring cement based on colophony [15]. In 1902, Jones et al. implanted some gold capsules between the knee joints, with good long-term results [15]. This led to the general knowledge that chemically inert materials are more desirable and stable within the organism [15, 16]. Smith-Peterson et al., in 1923, conducted some studies in order to achieve a stable and practical arthroplasty [15]. Initially, they used some glass-based capsules, which were found to be too fragile. Afterward, they applied a kind of celluloid that no longer is available in the market, which produced some unwanted reactions. Lastly, they discovered the Vitallium alloy, an alloy of cobalt-chromium which presented better characteristics than all the materials applied until that time, namely good mechanical resistance/stability and chemical inertness, having become one of the most applied materials [15, 16]. The first hip prosthesis with the Vitallium alloy was made in 1938, by Bires and Wills, and in 1939 by Bursh, which used PMMA (polymethylmethacrylate) for its fixation [16]. The Vitallium alloy kept being applied frequently until 1960, when it was found that the metal-metal contact was harmful, due to corrosion processes and release of

biotoxic ions [16]. In the following years, plastic-based materials gained popularity, and by the end of the sixties the use of polyethylene had become widespread [17]. However, several studies conducted on these plastic-based materials shown that they have carcinogenic potential, which raised doubts about long-term applications. Therefore, in the seventies, the search for new non-toxic materials had begun. Compounds based on Alu and zirconia (ZrO_2) attracted the attention of Boutin et al. Around 1973, Nicolini started promising experiences in ceramic glasses, whose properties were found to be favourable compared to the majority of the materials applied until that time. Nonetheless, harmful reactions occurred in the bonding area between the prosthesis and the bone, mainly related to the heat released during the polymerization of the PMMA (the cement used for the prosthesis fixation), which can lead to temperatures in the order of 80-90 ºC. This is a serious problem because temperatures above 56 ºC can lead to the denaturation of the proteins, i.e., they may become unable to perform their function. Another drawback is the cytotoxicity of the monomer contained in the mixture (cement) [17].

So, the need of applying a prosthesis together with the need of fixing them without using any cement encouraged the research of a material which is not bioinert, but biologically active, which stimulates a natural and strong fixation between the implant and the bone, i.e., a bioactive material. This bioactivity requirement is fulfilled by biomaterials such as calcium orthophosphate-based bioceramics, a group to which Hap belongs, and some bioactive glasses [17]. These new materials have chemical, physical and mechanical properties very appealing to be applied as bone (or dental) substitutes because some of their properties are similar to the natural biologic hard tissues of the human body.

The ensuing topic explores the calcium orthophosphate ceramics group, with a strong emphasis on Hap. Additionally, some important concepts related to bioactive properties are introduced and defined.

1.1.5 Hydroxyapatite: the boss of the calcium orthophosphates

By definition, three major chemical elements integrate all calcium orthophosphate compounds: calcium with an oxidation state +2, phosphorous with an oxidation state +5 and oxygen with a reduction state -2. Plus, many compounds include hydrogen in their chemical composition, as a hydroxide (e.g., $Ca_{10}(PO_4)_6(OH)_2$), incorporated water (e.g. $CaHPO_4.2H_2O$) or as an acidic orthophosphate (e.g., HPO_4^{2-} and $H_2PO_4^-$). There are several possible combinations of CaO and P_2O_5 (we are dealing with the CaO-P_2O_5-H_2O ternary system), and different compounds are distinguished and labelled by the type of the phosphate anion: ortho- (PO_4^{3-}), meta- (PO_3^-), pyro- ($P_2O_7^{4-}$and poly- $[(PO_3)_n^{n-}]$ [18]. Table 1.3 shows the list of existing calcium orthophosphate and their stability in aqueous solution [19].

Table 1.3 List of existing calcium orthophosphate compounds and their stability on an aqueous solution. [a] Compounds that cannot be precipitated from aqueous solution (at least in one single step); [b] Accurate measurements not available; [c] Stable at temperatures above 100 ºC; [d] Always metastable; [e] Sometimes also designated as precipitated Hap; [f] In the case x = 1, CDHA has the following chemical formula $Ca_9(HPO_4)(PO_4)_5(OH)$, also known as apatitic tricalcium phosphate [19].

Ca/P molar ratio	Compound	Formula	Solubility at 25 °C, -log(K_s)	Solubility at 25 °C, g/L	pH stability range in aqueous solutions at 25 °C
0.5	Monocalcium phosphate monohydrate (MCPM)	$Ca(H_2PO_4)_2 \cdot H_2O$	1.14	~18	0.0–2.0
0.5	Monocalcium phosphate anhydrous (MCPA)	$Ca(H_2PO_4)_2$	1.14	~17	[c]
1.0	Dicalcium phosphate dihydrate (DCPD), mineral brushite	$CaHPO_4 \cdot 2H_2O$	6.59	~0.088	2.0–6.0
1.0	Dicalcium phosphate anhydrous (DCPA), mineral monetite	$CaHPO_4$	6.90	~0.048	[c]
1.33	Octacalcium phosphate (OCP)	$Ca_8(HPO_4)_2(PO_4)_4 \cdot 5H_2O$	96.6	~0.0081	5.5–7.0
1.5	α-Tricalcium phosphate (α-TCP)	α-$Ca_3(PO_4)_2$	25.5	~0.0025	[a]
1.5	β-Tricalcium phosphate (β-TCP)	β-$Ca_3(PO_4)_2$	28.9	~0.0005	[a]
1.2–2.2	Amorphous calcium phosphate (ACP)	$Ca_xH_y(PO_4)_z \cdot nH_2O$, $n = 3$–4.5; 15–20% H_2O	[b]	[b]	~5–12[d]
1.5–1.67	Calcium-deficient hydroxyapatite (CDHA)[e]	$Ca_{10-x}(HPO_4)_x(PO_4)_{6-x}(OH)_{2-x}$[f] $(0 < x < 1)$	~85.1	~0.0094	6.5–9.5
1.67	Hydroxyapatite (HA or OHAp)	$Ca_{10}(PO_4)_6(OH)_2$	116.8	~0.0003	9.5–12
1.67	Fluorapatite (FA or FAp)	$Ca_{10}(PO_4)_6F_2$	120.0	~0.0002	7–12
2.0	Tetracalcium phosphate (TTCP or TetCP), mineral hilgenstockite	$Ca_4(PO_4)_2O$	38–44	~0.0007	[a]

Although there are several calcium orthophosphate compounds, practically only Hap, β-TCP and α-TCP are used in orthopaedic applications, as bioactive coatings in metallic implants, in bulk form, or as self-setting cements. Biphasic ceramics of Hap/β-TCP or Hap/α-TCP are also used. The reason explaining why only these three compounds are applied is that most of the calcium orthophosphates are not stable in the physiological

media conditions, and most of them would dissolve very quickly. Considering α-TCP, β-TCP and Hap, the former is the most stable phase under the physiological conditions, with a lower solubility and thus lower resorption kinetics [19].

For an insightful discussion about these compounds, it is required to introduce and define important concepts related to bioactivity. When inside the body, any foreign material will cause an immediate response of the organism. The type of response will depend on the classification of the biomaterial. Bioactivity, within the orthopaedic field, is defined as the ability of the biomaterial to promote and form a strong bond with the newly forming biologic bone, a phenomenon which was first observed in the sixties by Hench et al., in his works with silica-based bioactive glasses [13, 19, 20]. This bioactivity process is directly related to the biodegradation process of the biomaterial, which occurs by a mixture of cellular activity and dissolution *in vivo*, in the physiological media conditions. On the other hand, a bioinert material, instead of promoting a direct bond with the newly forming bone, it will evoke a physiological response consisting in the formation of a fibrous capsule around it, isolating the material from the physiological media and thus from the body, i.e., unlike the bioactive material, the body will recognize the bioinert material as a foreign material. The thickness of such fibrous capsule is sometimes used to evaluate the level of bioinertness of the material [19].

There is a dichotomy between advantageous biological properties (bioactivity) and advantageous mechanical properties: bioactive materials like Hap tend to have poor mechanical properties and bioinert materials like Ti tend to have good mechanical properties [4]. The ideal material would be one that could combine a high bioactivity level with good mechanical properties, to confer them stability. In fig. 1.4 we can see this bioactivity versus mechanical properties dichotomy [4]. All the materials in the best biological properties column are bioactive (Hap, tricalcium phosphate, etc.), while all the others (Ti, Al, zirconia, etc.) with better mechanical properties are bioinert, and thus they do not evoke the desired physiological response. This is the reason why bulk Hap orthopaedic implants are rarely applied, especially in load-bearing applications, i.e., in parts of the human body that are regularly subjected to mechanical loads. Instead, the

favourite solution is to make bioactive coatings on metallic implants, in order to combine the advantageous mechanical properties of the metal with the bioactive properties of the coatings. In this way, the formation of the unwanted fibrous capsule is avoided, and the bonding between the implant and surrounding biologic bone is improved, therefore optimizing the implant stability and longevity.

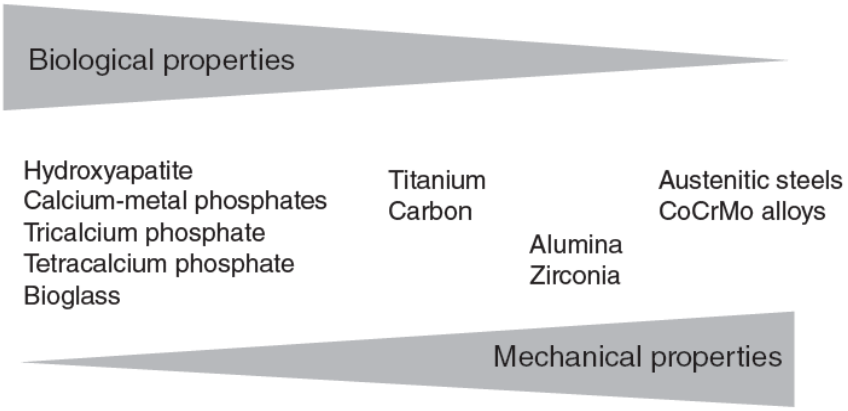

Figure 1.4 The dichotomy between the biological properties versus mechanical properties [4].

Let us consider a metallic implant, coated with Hap, which is applied in the human body. The Hap will soon start a biodegradation process, which generally occurs by two different mechanisms: biodegradation mediated by cellular activity, by both the osteoclasts and osteoblasts, as discussed in section 1.1.3, and biodegradation by dissolution in the physiological media [21]. The dissolution mechanism depends on parameters such as the acidity or basicity of the environment, the solubility of the material and the surface area to volume ratio [22]. Both different biodegradation mechanisms, occurring at the same time, cause the release to the surrounding physiological fluid of the chemical elements required for the precipitation of new Hap, namely calcium and orthophosphate ions, leading to the supersaturation of the physiological fluid and the precipitation of nanosized biologic Hap crystals [22]. Osteoblasts also contribute to the deposition of Hap. The precipitation of Hap is a consequence of the fact that it is the most stable calcium phosphate-based phase in the physiological conditions, therefore it is the thermodynamically favoured phase. However, the deposited Hap layer is more rigorously carbonated hydroxyapatite (CHap).

Another important concept needs now to be introduced: Hap is characterized by having a structure that allows a considerable number of ionic substitutions. Some frequent substitutions include the incorporation of carbonate ions, silicon, magnesium, fluoride, chlorine, among other elements. Actually, structural studies performed in biologic Hap and synthetic carbonated Hap, using combined analytical methods such as X-ray diffraction (XRD), Fourier-transform infrared spectroscopy (FTIR) and other chemical analysis techniques, demonstrated that the most recurrent substitution in biologic Hap is the incorporation of carbonate ions [13]. In fig. 1.5, a simple scheme shows some of the possible ionic substitutions in Hap. The occurrence of these substitutions can modify, in a higher or lower degree, some of the Hap properties: for example, the incorporation of fluorine leads to an increase in crystallite size and a higher stability in aqueous solution due to a solubility decrease (this is the reason why many mouthwashes and toothpastes contain fluorine), while the incorporation of carbonate ions causes a decrease in the crystallite size and an increase in solubility [13]. The substitutions have also influence on the cellular adhesion and may change the adhesion and orientation of the proteins which bind to calcium [23, 24]

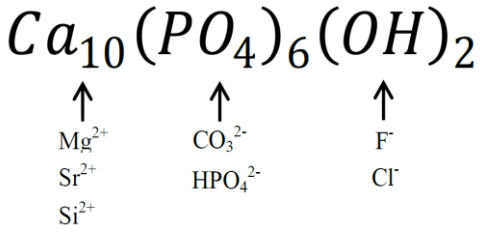

Figure 1.5 Some of the possible ionic substitutions that occur in Hap [13].

Returning to our discussion, it is agreed that the newly forming biologic bone bonds directly to the Hap coating through the carbonated CHap layer [22]. Fig. 1.6 shows a simplified scheme of the discussed bioactivity process, highlighting the biodegradation mechanisms and the precipitation and development of new biologic bone. The solubility and stability of the calcium phosphate compounds in the physiological conditions depend strongly on the calcium to phosphorous ratio (Ca/P ratio – see table 1.3). For lower ratios, the solubility increases, or in other words, the biodegradation kinetics increases. It is very important that the biomaterial is stable enough inside the organism to allow the formation

of the CHap layer. If the material dissolves very quickly, it will not allow the bonding with the newly forming bone. This is the reason why compounds with a Ca/P ratio lower than 1.5 (table 1.3) are very rarely applied. Even pure α-TCP and β-TCP are rarely applied since their degradation kinetics is faster than the rate of new biologic bone formation. Instead, they are usually applied in biphasic formulations (BCP – biphasic calcium orthophosphates) of Hap/β-TCP or Hap/α-TCP, in order to achieve biomaterials with different degradation rates: the higher β-TCP or α-TCP content, the higher the degradation rate. On fig 1.6, it is also important to mention again that the precipitation and formation of new bone are both a consequence of the supersaturation condition and also of the osteoblastic activity [22].

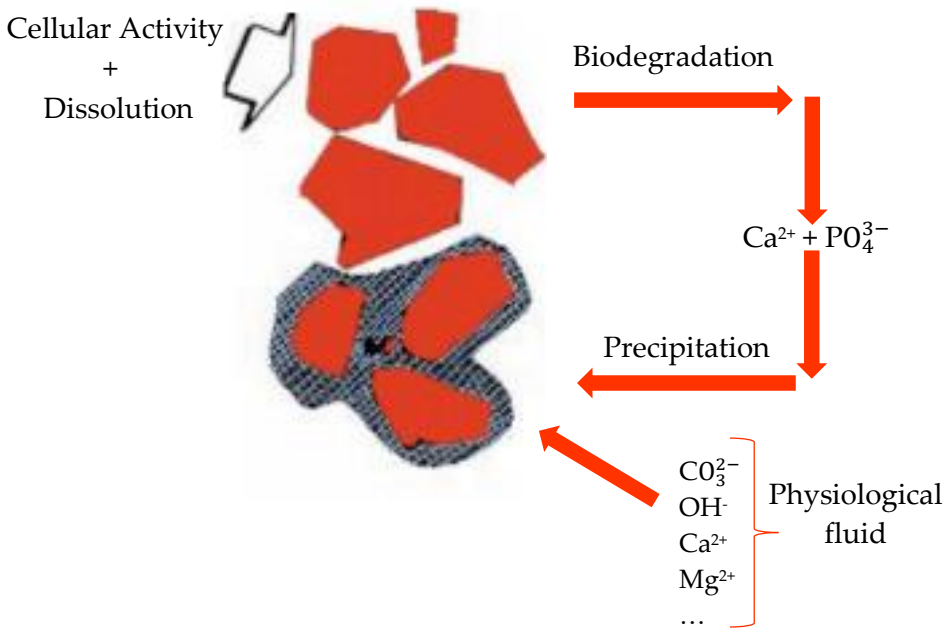

Figure 1.6 Simplified scheme showing the bioactivity process of Hap, highlighting the biodegradation mechanisms, through the combined action of the cellular and dissolution processes, and the precipitation and development of new biologic bone along the Hap surface.

Last but not least, the experimental evidence. Fig. 1.7 shows the results of an *in vivo* study: (a) Ti6Al4V cube (5x5x5 mm), without a Hap coating, implanted on an adult dog's femur; (b) Same setup, but in this case, the Ti6Al4V implant has a Hap bioactive coating. In (a) it clearly visible that between the implant and the bone there is the formation of the

fibrous capsule (connective tissue) that was mentioned before because Ti and Ti alloys are bioinert. This fibrous capsule ensures that the material has minimal interaction with the surrounding tissues, and therefore it does not provide a favourable environment for cellular adhesion and proliferation. Oppositely, in (b) it is visible a smooth and well-defined interface and bonding between the implant and bone, through the Hap bioactive coating. Consequently, the implant fixation is much weaker in (a) compared to (b), and thus the former has improved the mechanical stability and longevity.

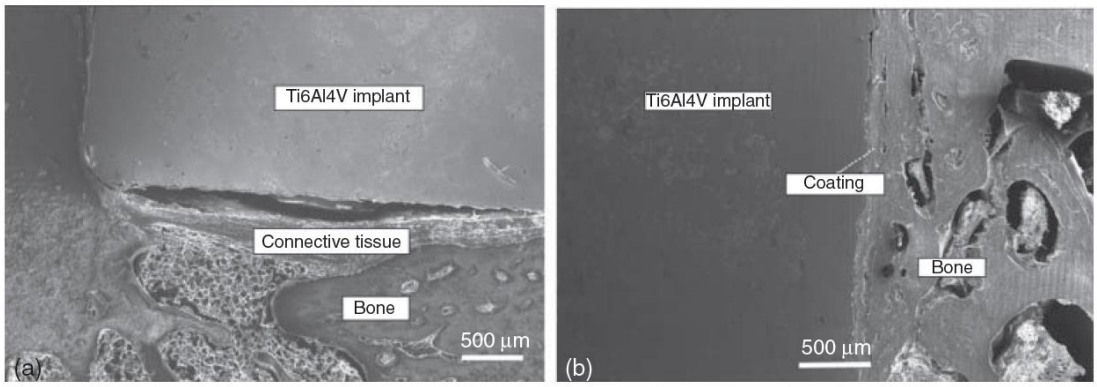

Figure 1.7 *In vivo* biological tests: (a) Ti6Al4V cube (5x5x5 mm) without a Hap coating, implanted on an adult dog's femur; (b) Same setup, but in this case the Ti6Al4V metallic implant has a Hap bioactive coating [4].

1.1.6 Structural and thermal properties of Hap

The most frequent crystalline structure of Hap is hexagonal, belonging to the $P6_3/m$ space group, with lattice parameters a = b = 9.432 Å, c = 6.881 Å and $\gamma = 120^{o}$. Fig. 1.8 shows the hexagonal structure, made of hydroxide ion (OH^-) columns along the c-axis surrounded by the PO_4 tetrahedra, with the Ca^{2+} ions interspaced between the tetrahedra. The Ca^{2+} ions can occupy two different sites in the network, as fig. 1.8 depicts: in the position Ca1 they are arranged in columns parallel to the c-axis and in the position Ca2 they are surrounded by six O^{2-} ions belonging to the PO_4 and OH structural groups, while in Ca1 they are surrounded by six O^{2-} ions from the PO_4 units. The Ca^{2+} ions and PO_4 groups are mainly responsible for the structure and skeleton of Hap, while the OH^- columns are the main responsible for most of its physical properties, as it will be elucidated in subsequent topics.

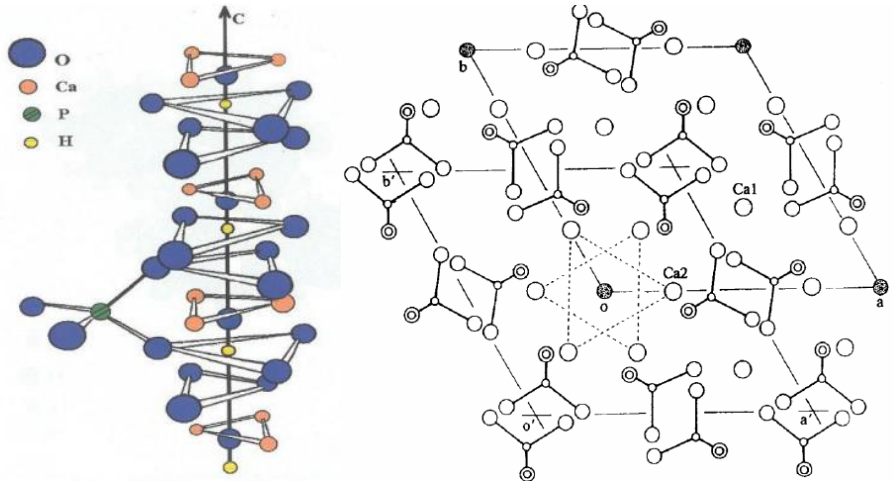

Figure 1.8 In the left: the arrangement of the structural groups around the c-axis. In the right: structural units of the hexagonal Hap. The vertices, represented by the full circles, represent the positions of the OH^- ions [25].

Hap can still exist in another form, the monoclinic crystalline structure [26]. This phase, discovered much later than the hexagonal, belongs to the space group $P2_1/b$ and has lattice parameters a = 9.421 Å, b = 2a, c = 6.881 Å and $\gamma = 120^o$. The structural differences between both phases are very subtle, the main difference being the orientation of the hydroxide ions in the columns: in the monoclinic structure, in a given column, all the hydroxide ions are aligned in the same direction, or in other words, the electric dipole moment vectors point in the same direction (like in fig. 1.8), and the direction is reversed in the next/adjacent column. In the hexagonal structure, in a given column, the hydroxide ions are successively aligned in the opposite direction, in one position the dipole moment points down and in the next it points up [26, 27]. Despite the structural differences between both phases being very small, they are reported to exert a strong impact on the Hap chemical and physical properties. However, the occurrence of the hexagonal phase is much more frequent, because the monoclinic phase requires an almost stoichiometric composition and, as discussed in section 1.1.5, Hap easily incorporates other ionic species in its structure. Characterized by a considerable amount of ionic substitutions, most abundantly CO_3^{2-}, biologic Hap is always hexagonal. For this reason, the great majority of the studies focus on hexagonal Hap. In addition, it is very difficult to synthesize monoclinic Hap, because

impurities have to be minimized and the sinterization (or other required thermal treatments) creates vacancies in the Hap structure, causing the hexagonal phase to be the most stable.

Regarding the thermal properties of Hap, fig. 1.9 shows the FTIR and XRD spectra of Hap (commercial powder) at different temperatures, up to 1500 ºC. Hap is stable up to 1350 ºC, i.e., there is no thermal decomposition up to 1350 ºC [28]. However, a dehydroxylation process occurs, according to reaction 1 [29, 30]:

$$Ca_{10}(PO_4)_6(OH)_2 \leftrightarrow Ca_{10}(PO_4)_6(OH)_{2-2x}O_x[\quad]_x + xH_2O \qquad (1)$$

where $[\ ]_x$ represents an OH^- vacancy. As the reaction shows, for two OH^- ions released, one H^+ proton vacancy (which is the same as an O^{2-} anion) and one OH^- vacancy are created. This reaction typically starts to occur between 800 and 900 ºC, and it is also known as the dehydration of Hap, since it releases water vapor. The $Ca_{10}(PO_4)_6(OH)_{2-2x}O_x[\quad]_x$ compound is known as oxyhydroxyapatite (OHap). In fact, probably almost all of the reports in the literature deal with OHap and not with Hap, because, for example, the sinterization treatments induce the formation of defects according to eq. 1. However, for practical reasons, researchers adopt the Hap designation.

In fig. 1.9 it can be seen that, with the increase of the temperature, the absorbance of the OH^- librational and stretching bands, at about 650 and 3572 cm^{-1}, gradually decrease their intensity, while the bands at about 945 and 1025 cm^{-1}, assigned as the characteristic bands of OHap, appear at around 1200 ºC [28]. The librational band completely disappears at 1300 ºC, while the stretching band is detected at temperatures as high as 1350 ºC, near the thermal decomposition, suggesting that Hap does not lose all the hydroxide groups. In the limit, if all the groups would be released, the OHap would be transformed into oxyapatite, with chemical formula $Ca_{10}(PO_4)_6O$. However, only in very strict conditions oxyapatite will be formed, due to its metastable nature and very narrow thermodynamic stability conditions. At 1400 ºC the thermal decomposition has already taken place, with the formation of tetracalcium phosphate (TTCP) and α-TCP, whose chemical formula is included in table 1.3. Fig. 1.9 shows a clear change in the XRD spectra and the broadband between 950 and 1200 cm^{-1} is typical of α-TCP and TTCP [28]. The sequence of chemical

reactions leading to this decomposition process starts with equation 1, the dehydroxylation of Hap, and subsequently the following reactions 2 and 3 take place [28, 30]:

$$Ca_{10}(PO_4)_6(OH)_{2-2x}O_x[\quad]_x \leftrightarrow 3Ca_3(PO_4)_2 + CaO + (1-x)H_2O \tag{2}$$

and the formation of TTCP:

$$Ca_3(PO_4)_2 + CaO \rightarrow Ca_4(PO_4)_2 \tag{3}$$

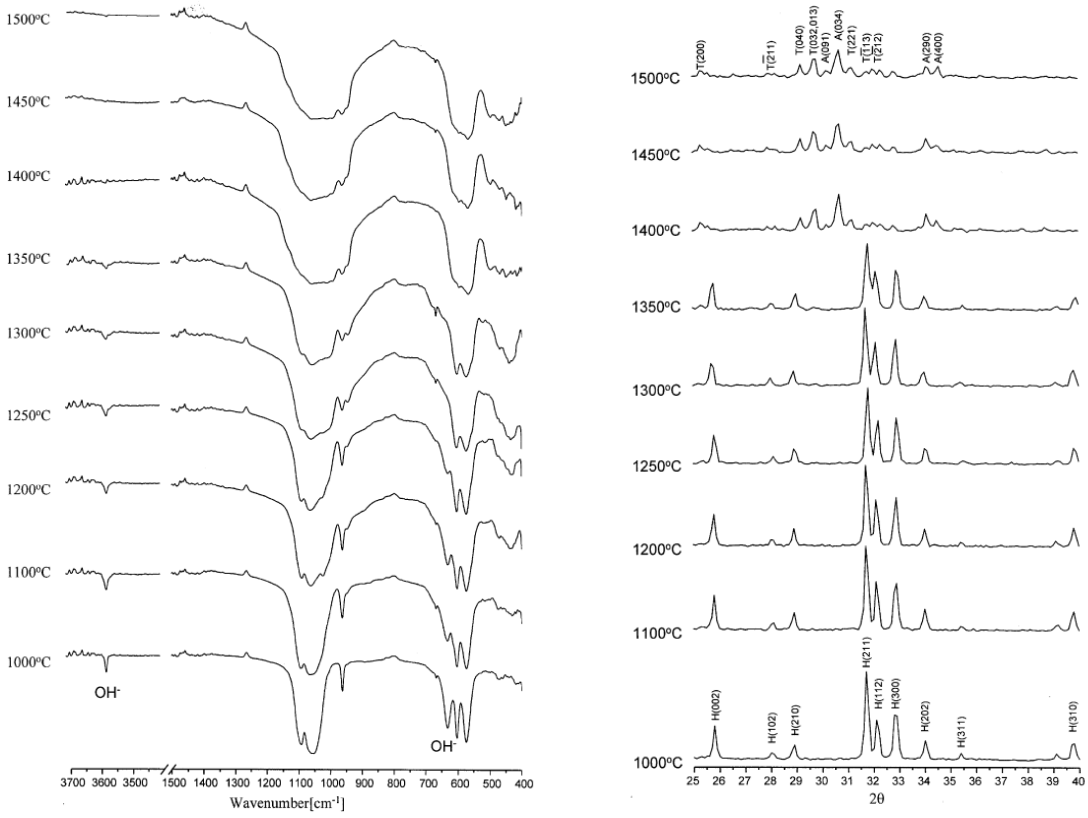

Figure 1.9 In the left**:** FTIR spectra of Hap at different temperatures, up to 1500 ºC. The librational and stretching absorption bands of the OH^- ions are represented in the figure, to allow the visualization of their behaviour in function of the temperature [28]. In the right: XRD spectra of Hap at different temperatures, up to 1500 ºC [H – Hap; T – tetracalcium phosphate (TTCP); A – α-TCP] [28]. The heating rate is 10 ºC/min.

Upon cooling the material, the Hap crystalline phase will be reconstructed, mainly due to rehydration reactions. In the same work, they cooled the Hap with a cooling rate of 10 ºC/min, and the XRD and FTIR spectra show the reconstruction of Hap from TTCP and

α-TCP, although not between 1350 and 1400 ºC, as in the heating situation. However, the reconstitution temperature is reported to be dependent on the cooling rate and atmosphere. Fig. 1.10 shows the thermogravimetric analysis (TGA – thermogravimetric analysis) of Hap heated from 200 up to 1500 ºC and afterward cooled down to 200 ºC. Hap has usually two types of water in its structure: adsorbed and lattice water [28, 31]. The adsorbed water is reversibly removed up to temperatures around 200 ºC, being readsorbed below 200 ºC, without any change in the lattice parameters. On its turn, the lattice water is irreversibly lost between 200 - 400 ºC, with a contraction in the a-axis [31]. The adsorbed water release accounts for the mass loss visible in fig. 1.10 in such temperature ranges. Between 800-900 ºC the dehydroxylation starts, and an inflection is visible in the thermogram. The dehydroxylation is not a narrow process in temperature, occurring across a broad temperature range, as the change of the FTIR absorbance bands in fig. 1.9 corroborate. The significant and abrupt weight loss between 1350 and 1400 ºC marks the thermal decomposition of Hap. On its turn, in the cooling curve, there is initially a small weight loss down to about 1290 ºC, and the weight increases fast in a narrow temperature range, right after 1290 ºC, corresponding to the Hap reconstruction from TTCP and α-TCP. The reconstruction is based on a series of hydration reactions where OH^- ions are reinserted in the structure, and the following reactions 4 and 5 are proposed [28]:

$$3Ca_4P_2O_9 + 3H_2O \rightarrow Ca_{10}(PO_4)_6(OH)_2 + 2Ca(OH)_2 \quad (4)$$

and

$$10Ca_3(PO_4)_2 + 6H_2O \rightarrow 3Ca_{10}(PO_4)_6(OH)_2 + 2H_3PO_4 \quad (5)$$

Subsequently, there is only a very small weight variation between approximately 1000 down to 200 ºC, corresponding to the incorporation of some OH^- ions in the Hap structure. Nonetheless, the structure will retain a considerable number of OH^- and H^+ ion vacancies, which, as it is discussed in the next chapter, is fundamental for the electrical polarization mechanisms of Hap. Such vacancies are usually created during the sinterization thermal treatments, which will be briefly discussed in the ensuing topic.

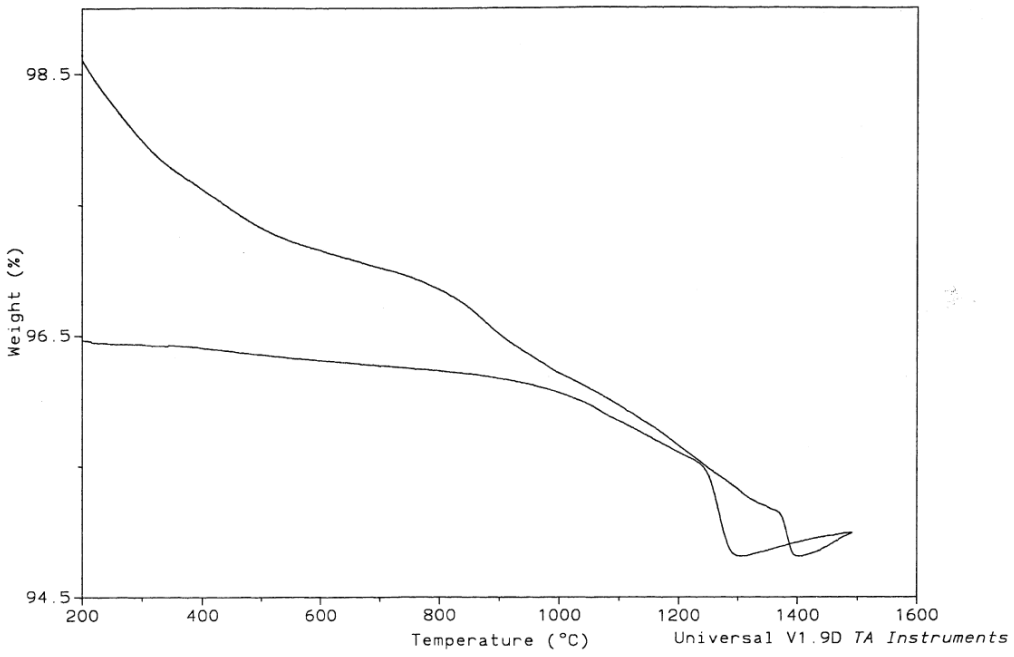

Figure 1.10 TGA thermogram of Hap heated from 200 up to 1500 ºC and afterward cooled down to 200 ºC. The heating/cooling rates are 10 ºC/min [28].

1.1.7 Sinterization of Hap

In the quotidian vocabulary of most of the materials research scientists, sinterization is a paramount high-temperature thermal treatment of a shaped porous powder compact, leading to a compact dense ceramic without pores, depending on the defined temperature and treatment time. In this topic, we compile some of the information contained in the excellent and comprehensive review by E. Champion regarding the sinterization of calcium phosphate bioceramics. This topic is not analysed in detail, the purpose is essentially to provide some useful information regarding the sinterization of Hap bioceramics, primarily the typical temperatures of sinterization.

One of the experimental techniques that can be used to study the sintering ability of a material is the thermomechanical analysis (TMA), where the change in the dimensions of a sample as a function of the temperature is measured. Typically, a plot of the linear shrinkage versus the temperature is presented. The derivative curve gives the sintering rate, in K^{-1} units, versus the temperature. Fig. 1.11 depicts the derivative plots of TMA for some

calcium phosphate bioceramics, under different types of atmospheres [32]. The sintering ability and kinetics may change according to different physical parameters, such as the powder grain size distribution and specific surface area of the initial powder. There are two important stages during sinterization. In the first stage, at lower temperatures (starting at ~ 400 ºC for Hap), there is superficial diffusion that leads to a decrease of the surface area of the Hap powder compacts, due to the welding of the grains through the formation of strong chemical bonds. This first stage occurs with practically no densification up to ~ 700 - 800 ºC, and it depends on the surface area of the initial powder. For this reason, the data presented in fig. 1.11 comprises powder with a similar surface area, 30 m^2/g [32]. So, up to about 750 ºC, the first stage occurs, and thermal expansion of the powder takes place. Afterward, the shrinkage and densification begin by elimination of the pores present in the powder compact. This densification proceeds in accordance with thermodynamic and kinetic conditions, which are summarized in the E. Champion review [32]. Two important parameters can be deduced from the derivative plots of TMA: T_B is defined as the temperature at which the shrinkage begins and T_M is defined as the temperature at which the sintering rate is maximum. In what concerns Hap, these parameters values are reported to be T_B = 750 ºC and T_M = 1050 ºC [32].

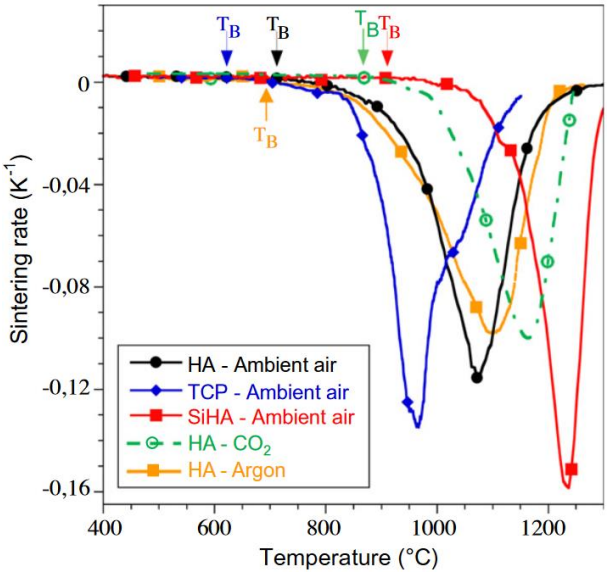

Figure 1.11 The derivative plot of TMA for some calcium phosphate bioceramics, under different types of atmospheres (HA stands for hydroxyapatite, some authors like to use HA, others Hap, others HAp, etc.). The specific surface area of the initial powders is about 30 m^2/g, for all the data [32].

In practice, pressureless sintering (i.e., conventional sintering) of Hap is usually undertaken in the temperature range between 1100-1250 ºC. In this temperature range,

pressureless sintering of Hap is able to attain nearly fully dense ceramics keeping the grain size with dimensions ≤ 1 μm [32]. Higher temperatures will promote grain growth. It is to be noted that sinterization can be seen as a competition between two thermally activated processes driven by solid-state diffusion of matter: densification and grain growth. Hap is stable up to ~ 1350 - 1400 ºC in ambient air, being this temperature dependent on the partial pressure of water vapour. Only partial dehydroxylation (equation 1) will occur, as it discussed in the previous topic.

1.1.8 Electrical properties and polarization mechanisms

This is an important topic, as the title of this thesis suggests. The electrical properties of Hap are in a great extent related to the c-axis and the ionic vacancies that it contains. Furthermore, the electrical properties are dependent on the water in the structure and thermal history of the material. This discussion is centered on polycrystalline Hap, and practically almost all the reports in literature deal with polycrystalline Hap, as well most of the practical applications.

Beginning this topic with the electrical polarization mechanisms, the Hap structure is characterized by hydroxide anion columns along its c-axis, as it is discussed in the former topic 1.1.6. There are two types of defects in these columns: OH^- vacancies and H^+ proton vacancies (an O^{2-} anion in the site of an OH^-), as it is depicted in fig. 1.10 [33]. These defects have opposite effective charges: H^+ vacancies have - 1 effective charge while OH^- vacancies have + 1 effective charge. When one of these defects is created the other is also created, to fulfill the charge neutrality requirements, as equation 1 shows. Those defects are common in Hap due to the sinterization thermal treatments required for the consolidation and mechanical stability of the material, which activates the dehydroxylation reaction. As fig. 1.12 details, when a high-intensity dc electric field is applied at a suitable high temperature, the H^+ protons will be able to migrate along the columns in the direction of the applied field, as shown in fig. 1.12(b). As the protons migrate, both defects will tend to be left in pairs, and they will constitute a defect pair dipole polarization, with the individual electric dipole

vectors pointing from the H^+ vacancy to the OH^- vacancy (fig. 1.12(e)), in the direction of the applied field [33].

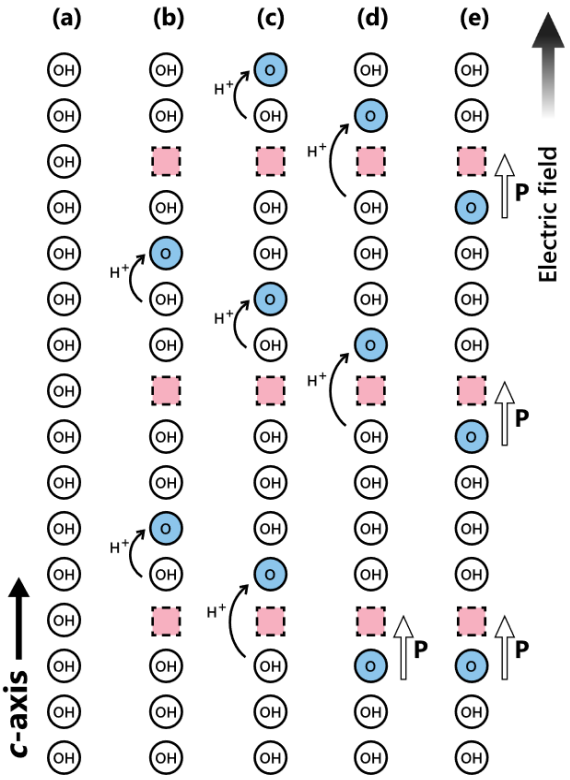

Figure 1.12 The mechanism behind the defect pair dipole polarization of Hap. The H^+ proton vacancies are highlighted in blue (as O^{2-} anions) while the OH- vacancies are highlighted in pink. The H^+ protons are able to migrate along the columns in the direction of the applied electric field, leaving both type of defects in pairs, consequently creating a defect pair dipole polarization [33].

In addition to the defect pair dipole polarization, another mechanism takes place: with the long-range migration of the protons and saturation of the defect pair polarization, the protons will tend to accumulate in the grain boundaries in the direction of the applied electric field, while the protons vacancies (the O^{2-} anions) tend to accumulate in the opposite direction. Hence, a different charge distribution is achieved in the material and a space charge polarization is established within the material, as fig. 1.13 highlights [33].

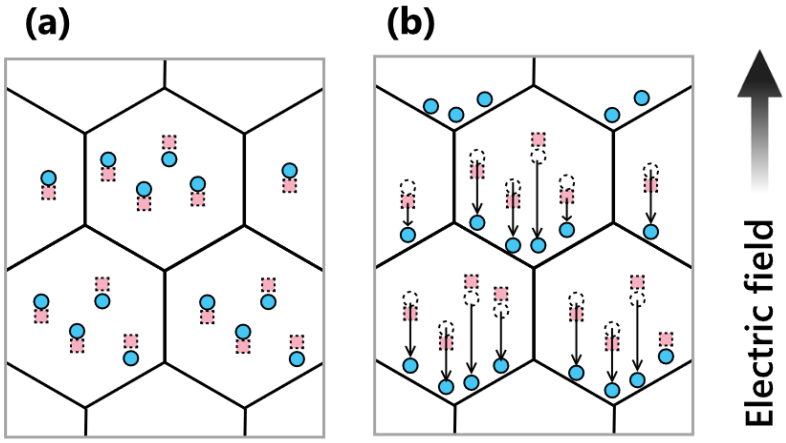

Figure 1.13 The mechanism behind the establishment of the space charge polarization: the H^+ proton vacancies tend to accumulate in the grain boundaries in the opposite direction of the applied electric fields, while the protons tend to accumulate in the direction of the field [33].

The measurement of thermally stimulated depolarization currents (TSDC) is a useful technique that allows to get valuable insight about these polarization processes and, as a matter of fact, most of the knowledge regarding the polarization processes in Hap was achieved through an encompassing analysis of the structural and thermal properties together with TSDC measurements. The theoretical and practical aspects of the TSDC technique are explained in detail in chapter 2, section 2.2. The analysis of the dependency of the polarization with the applied field E_P can provide useful information about the physical process behind a given depolarization process, allowing, for example, the distinction between electric dipolar reorientation and space charge detrapping processes, as it is the Hap case. Such analysis is commonly done by plotting the depolarization peak current density versus the electric field intensity. Fig. 1.14 (the inset) shows this analysis for Hap [33]. In the inset, the blue marks and circles represent the dependence of the lower and higher temperature depolarization processes, respectively, with E_P. The dipolar and space charge processes have distinct dependences on E_P: while the dipolar processes will show a linear dependence, the space charge processes have a hyperbolic relation, as equations 29 and 30 of topic 2.2 shows. Evaluating again the inset of fig. 1.14, it is clear that the lower temperature process displays a linear dependence, while the higher temperature process

displays a nonlinear hyperbolic dependence. This fact, together with knowledge of the type of defects that occur in the c-axis of Hap, led to formulation of the polarization processes introduced at the beginning of this topic: the defect pair dipole polarization and the space charge polarization. The activation energies of the lower temperature depolarization process are reported to be around 0.75-0.80 eV, while for the higher temperature process the energies are higher: Yamashita et. al. reports a value of 1.02 eV, while in our publication we report a significantly higher value of 1.81 eV [33, 34]. The activation energy of the higher temperature process is interpreted as the potential barrier heights for detrapping the charge carriers from the defects in the grain boundaries. The difference between the reported activation energies is due to the fact that, in our work, we applied higher T_P and E_P thermoelectric process parameters, and therefore we were able to activate deeper traps located at the grain boundaries, therefore increasing the activation energy [33, 34].

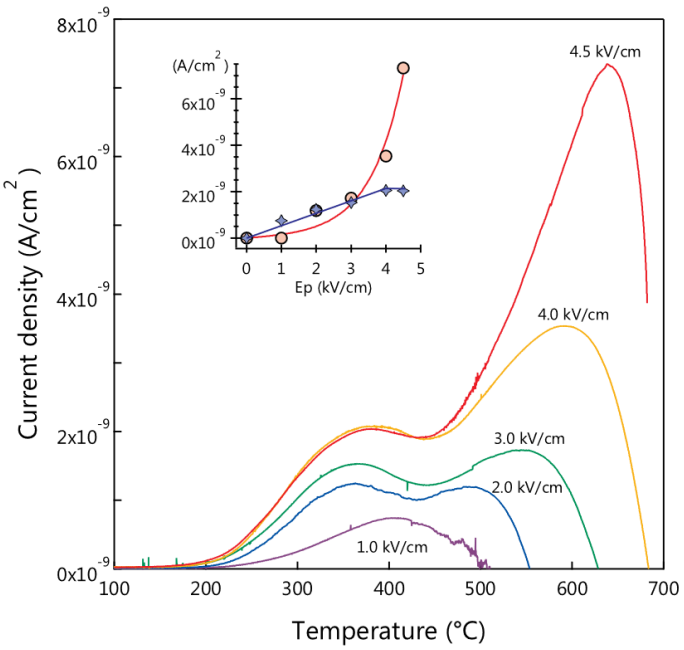

Figure 1.14 TSDC spectra of Hap polarized with electric fields E_P of increasing intensity. The polarization temperature and time are 350 ºC and 60 minutes, respectively. The inset shows the dependence of the peak current density (for both depolarization processes) with E_P [33].

When in a saturation condition. i.e., the polarization process parameters T_P and E_P saturate the polarization, a discernible dependence will not be visible in the current versus E_P plot, instead, the current values will tend to be around the same value. Certainly, it may be important to know the magnitude of the process parameters that saturate the polarization and stored charge density of the material under study. In fig. 1.14, it is obvious that the stored charge is not saturated. In our publication we found that a saturation

condition is achieved for a polarization temperature of 500 ºC and an electric field magnitude of 3 kV/cm, both for pure polycrystalline Hap samples and for biphasic samples with composition 75Hap + 25β-TCP, in wt% [34].

Concerning the dielectric properties, they are essentially determined by the H^+ protonic diffusion along the c-axis. Impedance spectroscopy (IS) measurements show that the dielectric behaviour of polycrystalline Hap can be interpreted as comprising high impedance grain boundaries and proton conductive grains, with reported conductivities of about 10^{-7} S/cm at 300 ºC and 10^{-4} S/cm at 700 ºC [35]. Both reported conductivity values are for polycrystalline samples with relative densities very near the theoretical density (3.16 g/cm^3). The IS spectra show two dielectric relaxation processes, as it can be seen in fig. 1.15 [34]. In our publication, it is concluded that the dielectric relaxations in fig. 1.15 may be related to the TSDC depolarization processes. For the dielectric relaxation at lower temperatures (in the M'' plot), the calculated activation energy through a plot of the Napierian logarithm of the relaxation frequency versus the inverse of temperature [ln(f_{relax}) versus 1/T] yields 0.76 eV, which is in very good agreement with the TSDC results for the defect pair mechanism. Concerning the dielectric relaxation at higher temperatures, the calculated activated energy through the ln(f_{relax}) versus 1/T plot yields 1.56 eV, which agrees satisfactorily with the results of the TSDC measurements for the space charge mechanism. This space charge mechanism is only visible in the M'' plot, as the high-temperature relaxation. The modulus formalism is known to suppress the conductivity effects, highlighting processes that may be overshadowed by the conductivity. In the TSDC spectra of our report, the space charge depolarization mechanism is overlapping with the thermally activated intrinsic ionic conductivity (appears as a shoulder), and for this reason is only clearly visible on the M'' representation [34]. Moreover, we verified that with the applied process parameters (T_P = 500 ºC and E_P = 2, 3, 4 and 5 kV/cm), which, as mentioned, saturate the magnitude of the polarization, the contribution of the space charge mechanism to the total stored charge density is strongly dominant, accounting about 96.4% of the total stored charge, while the defect pair mechanism has only a contribution of about 3.6%. For smaller process parameters values like those of fig. 1.14, the contribution of the space charge will be considerably lower because the saturation state is very far from being reached. For

example, in fig. 1.14, for lower field intensities, the area of both depolarization peaks is similar, implying that they will have an identical contribution to the total stored charge. But for higher fields the contribution of the space charge mechanism clearly starts to become dominant.

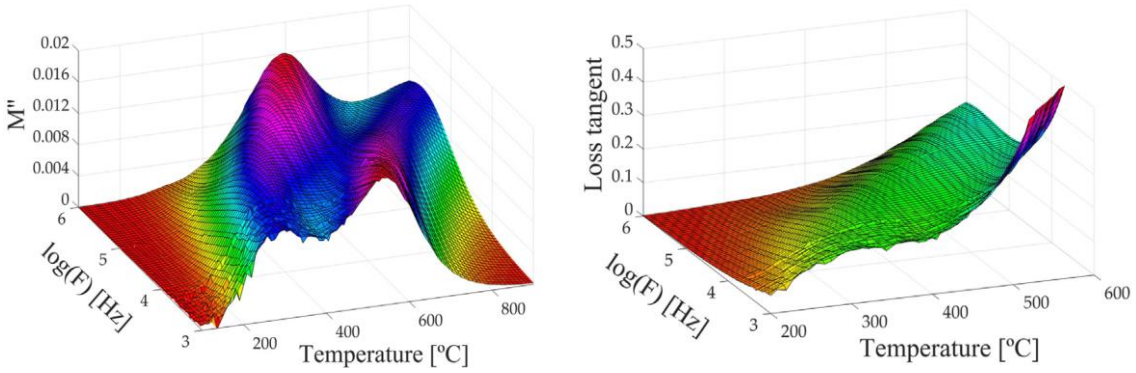

Figure 1.15 In the left: Dependency of the imaginary part of the dielectric modulus with the temperature and frequency for a polycrystalline Hap sample. In the right: Dependency of the loss tangent with the temperature and frequency for a polycrystalline Hap sample [34].

The sinterization atmosphere will also influence the magnitude of the measured depolarization currents, thus of the total stored charge density. The dehydroxylation process (equation 1), responsible for the creation of the defects that will make possible the migration of the H^+ ions along the c-axis, is affected by the atmosphere: a water vapour rich atmosphere will decrease the defect density, because equation 1 involves the release of water vapour, hence a water vapour rich atmosphere will hinder the reaction. On the other hand, a nitrogen (or a noble gas) atmosphere, without water vapour, should maximize the creation of defects. Fig. 1.16 presents the TSDC spectra oh Hap samples sintered under different atmospheres: w-Hap – water vapour reach atmosphere, a-Hap – room air atmosphere and n-Hap – nitrogen rich atmosphere. It is clear that the water vapour atmosphere causes a significant decrease in the magnitude of the measured depolarization currents, implying that the reaction in equation 1 is hindered during the sinterization. For the nitrogen rich atmosphere, the currents are higher, because it is a water vapour free atmosphere.

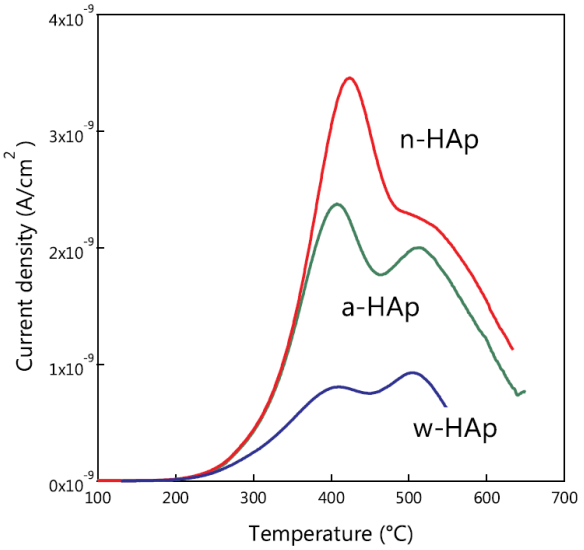

Figure 1.16 TSDC spectra of Hap sintered under different atmospheres: w-Hap – water vapour rich atmosphere, a-Hap – room air atmosphere and n-Hap – nitrogen rich atmosphere. The polarization conditions are: T_P = 400 ºC, E_P = 1 kV/cm and t_P (time of electric field application at T_P) = 60 minutes [33].

Fig. 1.17 depicts the real and imaginary parts of the complex permittivity, for Hap samples sintered under different conditions: (a) and (b) - 1473 K, 2 h; (c) and (d) - 1593 K, 2 h; (e) and (f) – 1653 K, 9 h [35]. The aim of fig. 1.17 is to show the effect of the grain size on the complex permittivity components, especially the real part ε', i.e., the dielectric constant. The average grain sizes are: 0.82 ± 0.24 μm, 2.1 ± 0.7 μm and 13.8 ± 7.0 μm for (a) and (b), (c) and (d) and (e) and (f), respectively. Two dielectric relaxations can be seen, which are labeled as A and B (A for lower frequency and B for the higher frequency). The activation energies are in the range of 0.64-0.71 eV for A and 0.66-0.76 eV for B. Relaxation A is assigned to H^+ proton conduction along the c-axis, i.e., the same mechanism of the defect pair polarization, while relaxation B is assigned to OH^- ions reorientations in the c-axis [35]. The relaxation A is strongly dependent on the grain size, while the relaxation B does not show a great dependency. Analysing the dielectric constant values ε_A and ε_B, the first increases sharply with the increase of the grain size, whereas the former remains around the same value, suggesting that the relaxation strength of the OH- reorientations is not affected by the grain size, but it is strongly influenced by the OH^- concentration, as demonstrated in reference [36]. A Hap sample sintered under a water vapour rich atmosphere will have a higher relaxation strength due to hindering of the reaction in equation 1.

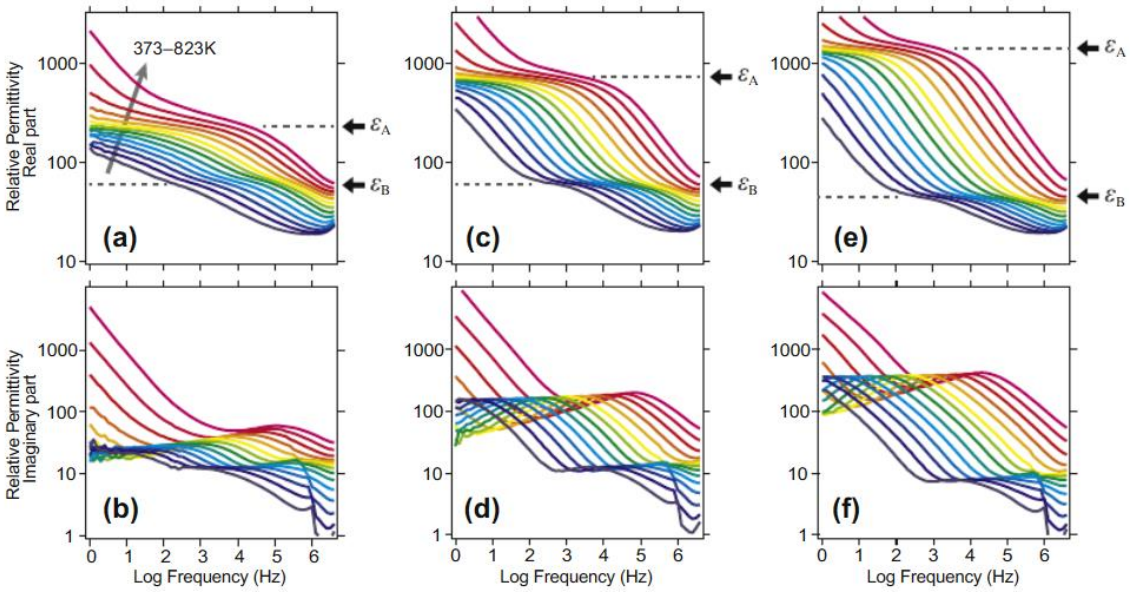

Figure 1.17 Real and imaginary parts of the complex permittivity of Hap sintered under different conditions: (a) and (b) 1473 K, 2 h; (c) and (d) 1593 K, 2 h; (e) and (f) 1653 K, 9h [35].

The electrical properties of Hap are also dependent on the adsorbed and lattice types of water [37]. Gittings et al. reported about IS measurements on dense and porous Hap ceramics sintered in the air or in a water vapour-rich atmosphere. The samples were labeled as dense$_{(air)}$, porous$_{(air)}$, dense$_{(water)}$ and porous$_{(water)}$. Fig. 1.18 shows the ac conductivity logarithm, at 1 kHz, as a function of the temperature, for the samples denser$_{(water)}$, dense$_{(air)}$ and porous$_{(water)}$, for the heating cycle 1 [37]. The samples were thermally cycled in order to investigate the influence of the adsorbed and lattice water on the conductivity and dielectric permittivity. Cycle 1 is the first heating ramp from RT up to 1000 ºC. It is visible in fig. 1.18 that there is an initial decrease in the conductivity, with increasing temperature, up about 200 ºC, which can be possibly assigned to the loss of adsorbed water. Note that the porous material, with a much higher surface area, has the highest conductivity at lower temperatures, presumably due to its greater ability to adsorb higher amounts of surface water. In the temperature region between 400-600 ºC, there is kind of a small conductivity peak for all the samples. The dense samples exhibit higher conductivities at higher temperatures, due to a predominance of the bulk ionic conductivity [37].

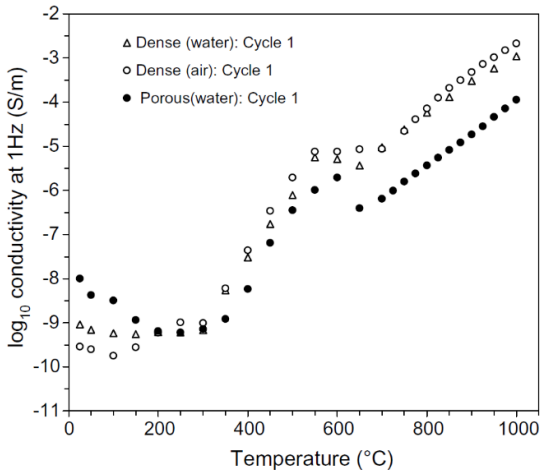

Figure 1.18 The ac conductivity logarithm, at 1 kHz, for the samples dense$_{(water)}$, dense$_{(air)}$ and porous$_{(water)}$, for the heating cycle 1 [37].

In the heating cycle 2 the samples were cooled from 1000 down to 125 ºC and then heated again up to 1000 ºC. The temperature of 125 ºC was chosen to minimize water resorption after cycle 1. Afterward, the samples were cooled down to RT and heated again up to 1000 ºC, consisting in cycle 3. Fig. 1.19 shows the logarithm of the ac conductivity, at 1 kHz, for the sample porous$_{(water)}$, for all the heating cycles. It can be seen that in cycle 2, the initial conductivity decrease in cycle 2 is minimal, and the small conductivity peak is not detected. The reason for the small peak is actually not very clear, but it can be related to strongly-bounded water (it is very improbable to be related to the dehydroxylation process because this process starts at higher temperatures). In cycle 3, the initial conductivity decrease is detected again as well as the small peak, although smaller than cycle 1. For higher temperatures all the samples have very similar conductivity values, and therefore the conductivity is independent of the thermal history [37].

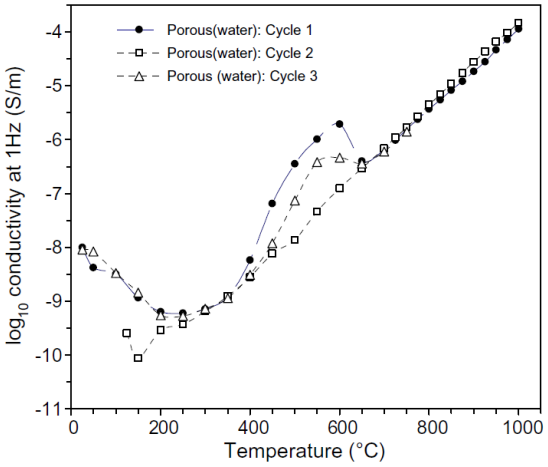

Figure 1.19 Logarithm of the ac conductivity, at 1 kHz, for the sample porous$_{(water)}$, for all the heating cycles [37].

Regarding the OH^- ions orientation, they are responsible for the ferroelectric character of Hap, which possibly can be observed and measured mostly at the nanosize dimension [38]. Fig. 1.20, shows a scheme of the OH^- ions orientations and configuration energy of the nonpolar ($P2_1/b$) and polar symmetries ($P2_1$ and $P6_3$) in Hap [38]. The polar symmetry $P2_1$ is monoclinic and the $P6_3$ is hexagonal, both non-centrosymmetric. Surprisingly, both piezoelectricity and ferroelectricity in synthetic Hap have been demonstrated only a few years ago, despite the fact that a piezoelectric effect in bone was first observed in 1957 [38]. Until very recently, the piezoelectric effect in bone was thought to be due to the organic component of the bone, i.e., collagen, because it was thought that Hap could not display such property. The problem is that almost all of the reported synthetic Hap bioceramics have grain sizes in the range of the few micrometers, and the manifestation of polar effects is very weak due to averaging effects [38]. In fig. 1.20, it can be seen that there is a small energy difference between the non-polar anti-ferroelectric configuration and the polar ferroelectric configurations. It is reported that the smaller nanosized Hap crystals can stabilize the polar configurations due to the higher surface energy of these nanocrystals. Effectively the ferroelectricity of nanocrystalline Hap thin films on silicon substrates was demonstrated by measuring a reversal of spontaneous polarization under an external electric field, using the piezoresponse force microscopy technique, as reported in reference [38]. The piezoelectric effect observed in Hap thin films has a magnitude comparable to other piezoelectric materials such as zinc oxide and polyvinylidene fluoride. As shown in topic 1.1.2, biologic Hap is nanocrystalline, and therefore the piezoelectric and ferroelectric effects may be enhanced. These effects are thought to be important in the biomineralization dynamics, in the bone's density and mechanical stability and ultimately in the hierarchical structure of the bone. However, the mechanisms behind the influence of these effects are still not yet understood, stimulating academic research in different fields of knowledge and applied science.

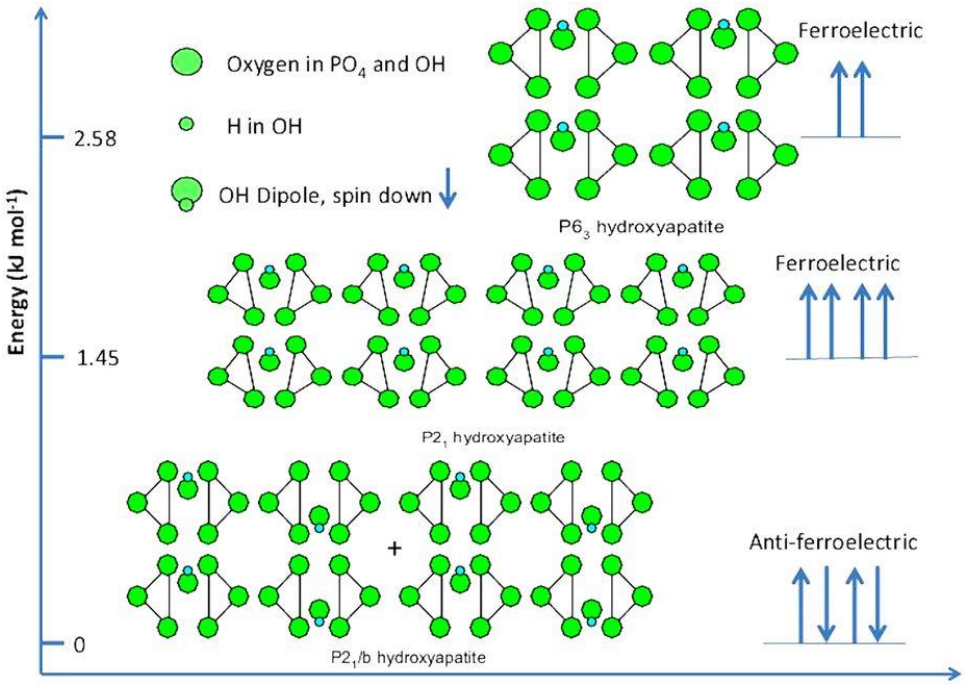

Figure 1.20 Scheme of the OH^- ions orientations and configuration energy of the nonpolar ($P2_1/b$) and polar symmetries ($P2_1$ and $P6_3$) in Hap [38].

1.1.9 Electrical polarization: the bioactivity catalyst

It was in the mid-nineties, with the research developed by Yamashita et al., that it was discovered that the electrical polarization of Hap bioceramics enables the storage of a large charge density magnitude which significantly enhances the bioactivity level. The direct bond and rate of new biologic bone formation (topic 1.1.5) are accelerated due to the stimulation of cellular activity and alteration of the surface properties of the bioceramic [39, 40]. Increased bioactivity has been demonstrated both *in vivo* and *in vitro* in polarized Hap-based materials. Typically, in the literature, the electrical polarization is undertaken at temperatures ranging between 250 and 500 ºC (higher than 400 ºC is uncommon), with applied electric fields in the range of 1-5 kV/cm [37, 41]. Reported stored charge density magnitudes are typically in the 10^{-6}-10^{-5} C/cm^2 range (higher magnitudes are much less frequent), depending, among other factors, on the thermoelectrical polarization process parameters, i.e., temperature and electric field. The enhancement of bioactivity is in part related to the fact that the adsorption of specific proteins and the adsorption and

differentiation of osteoblasts are stimulated by the superficial charge density, although the reason for this proteic and cellular stimulation is not yet quite understood. Another interesting issue concerns the signal of the electric charge which benefits the most the bioactivity level: the majority of the research points out that a negative charge density is preferred, with some (few) contradictory reports being present in the literature, stating that the positive charge is equally favourable [37]. Nonetheless, the almost general consensus falls on the negative charge. Some researchers, observing that the Hap heterogeneous nucleation in a simulated body fluid (SBF) solution (*in vitro* testing) is most favoured by negatively charged surfaces, hypothesize that the electrostatic-driven accumulation of Ca^{2+} ions in the negative surface triggers the initial nucleation and speeds up the precipitation of the CHap layer [42]. Thus, the enhancement of the bioactivity level through the electrical polarization has two components: one is the stimulation of the cellular activity while the other is comprises a bioactivity enhancement in the physiological media related to the interaction of its ionic content with the charged/polarized material. The first component is usually tested and verified through *in vitro* biological tests with osteoblasts, comprising the analysis of their activity through specific protein tagging, and the second component is verified through *in vitro* tests using SBF solutions.

In the proceeding discussion, some concrete and relevant biological studies regarding the electrical polarization effects on the bioactivity are presented. The discussion includes *in vivo* studies, but the majority of the reported studies are performed *in vitro*.

Sagawa et al. studied the *in vivo* response of polarized and non-polarized (test control samples) Hap/β-TCP composites, with composition 70Hap-30β-TCP, in wt% [43]. They implanted Hap/β-TCP cylindrical blocks on the femoral condyle of several rabbits, as depicted in fig. 1.21. As for the polarized implants, both bases of the cylinder are positively charged while the lateral surface is negatively charged, as it is also shown in fig. 1.21. The samples were polarized in air atmosphere at 400 ºC for one hour, with an applied DC field of 2 kV/cm. The TSDC measurements revealed an average stored charge density of 19.5 $\mu C/cm^2$ [43].

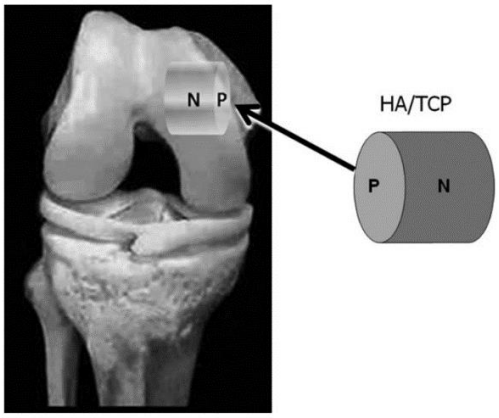

Figure 1.21 Scheme showing the implantation of the Hap/β-TCP cylindrical blocks, in drilled holes with matching size, implanted in the femoral condyle of a rabbit. In the polarized implants, both bases of the cylinder are positively charged (P-surfaces) while the lateral surface is negatively charged (N-surface) [43].

In order to evaluate and quantify the bioactivity performance of the samples, some parameters were measured and estimated. The B.Ar parameter is the newly formed bone area directly contacting the implant, the contact length C.Le parameter is the percentage of newly formed bone directly attaching to the implant and lastly the N.Oc/T.Le parameter provides the ratio between the number of osteoclasts and the total length of the surface [43]. The quantification of osteoclasts and osteoblasts is usually performed using histological staining techniques, in this case, tartrate-resistant acid phosphatase (TRAP) activities were analysed to quantify the number of osteoclasts present. In fig. 1.22, it is possible to compare the biological results six weeks after insertion. The results shown in (B) are for a non-polarized implant (control sample) and in (A) for a negative N-surface. It is clear that the area of newly formed bone, as well as the areas of direct bonding between the implant and the new biologic bone, are much higher for the polarized implant. As a matter of fact, they concluded that after six weeks of insertion, the bioactivity results of the non-polarized implant match, at most, those observed after three weeks in the polarized implant [43].

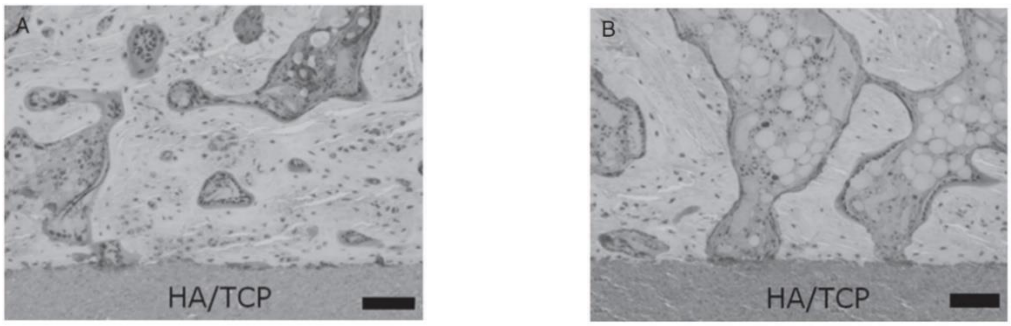

Figure 1.22 Histology staining results of the N-surface (A) and the non-polarized (B) surfaces six weeks after insertion. The scale bar is 100 μm [43].

The quantitative information contained in the histograms of fig. 1.23 supports this assumption. The results are a clear indicator of the bioactivity level enhancement caused by the electrical polarization: the B.Ar. and C.Le. values of 3W-N (three weeks after immersion) are practically the same of 6W-O, and therefore the results show that the time required for a strong bonding between the implant and the surrounding biologic bone may be reduced to half by the electrical polarization. It is to be noted that in the cited work they focused on the negatively charged surface. Moreover, Hap is still able to store a considerable higher charge density than the one reported in this work (19.5 $\mu C/cm^2$) , and therefore it can still have the potential to reduce the bonding time, assuming that we are not in a saturation condition, i.e., further increases in the stored charge density magnitude will not further enhance the bioactivity level. If one thinks in human patients, the implications of such time reduction in the recovery period are very significant for both the patient's comfort and well-being and for the cost-reduction related to the healthcare systems.

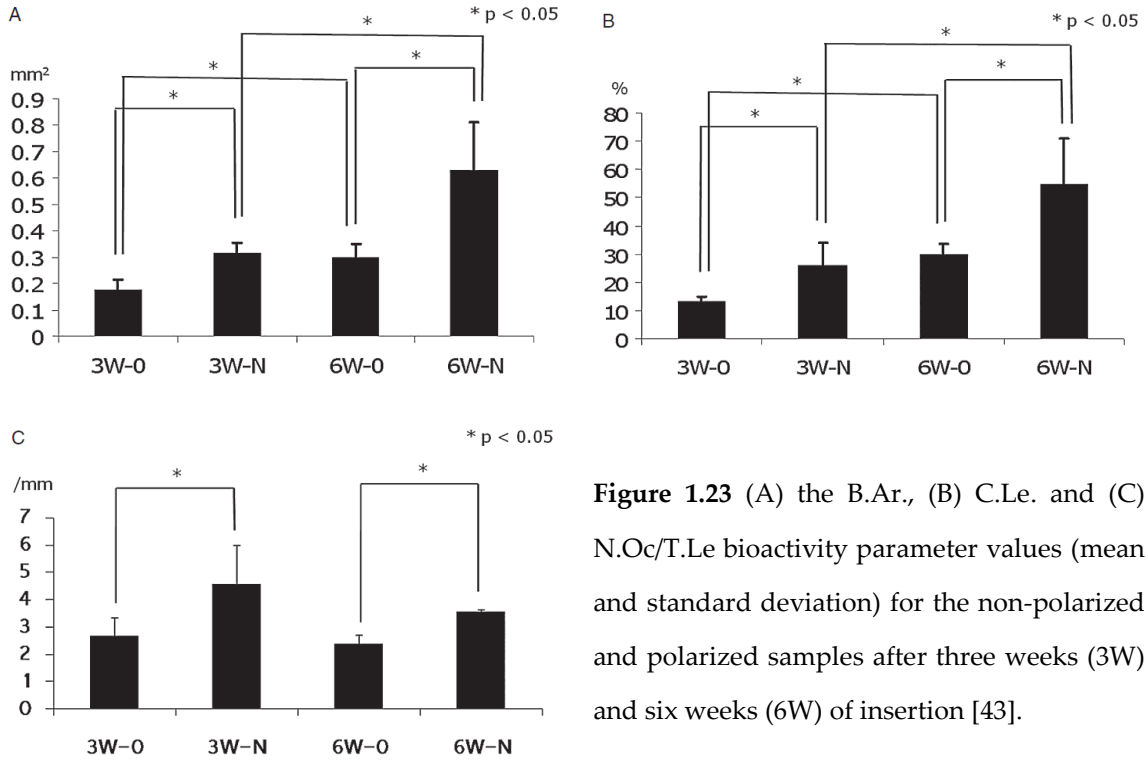

Figure 1.23 (A) the B.Ar., (B) C.Le. and (C) N.Oc/T.Le bioactivity parameter values (mean and standard deviation) for the non-polarized and polarized samples after three weeks (3W) and six weeks (6W) of insertion [43].

In another study, the bonding ability (osteobonding) of polarized and non-polarized Hap implants was analysed by histological staining section experiments for different implantation times [44]. The Hap ceramics, sintered in a water vapour-rich atmosphere at 1250 ºC, were electrically polarized (with a pair of platinum electrodes) at 300 ºC with an applied field of 1 kV/cm, during one hour. The sterilized samples, with an average stored charge density of 3.9 μm/cm^2, were implanted in tibial and femoral diaphyses of ten male New Zeland white rabbits. The samples were collected at one, two and four weeks after implantation. The histological evaluations were performed using the hematoxylin eosin staining method, allowing the visualization of the deposited biologic bone [44]. Fig. 1.24 shows the histology staining results of the collected samples, after different implantation times. It should be noted that the samples were implanted in a way so that a small gap, between 0.2 - 0.7 mm, exists between the implant and the surrounding cortical bone. In fig. 1.24, the gap between the Hap implant and the cortical bone is visible. After one week, a thin 0.02 - 0.05 mm thick compact layer is in direct contact with almost all of the N-surface, while in the regions without bone tissue, fibrin layers with some flattened fibroblastic cells are present together with many clusters of osteoid tissues (a non-mature bone tissue is usually designated as an osteoid, often it only contains the organic component, lacking the mineralization of Hap). The newly formed bone is surrounded by single layers of osteoblasts and osteocytes (see fig. 1.24). At two weeks, the area of newly formed bone increases very significantly and a good gap filling and bonding is already achieved, and at four weeks all the gap is filled and reconstruction/fixation is finished. In the case of the positive P-surface, after one week, a smaller amount, compared to the N-surface, of newly formed bone contacts the Hap surface, whereas most of the surface is still only covered with osteoid tissues. After two weeks the gap starts to be filled, however, there is a clear delay compared to the N-surface. Finally, at four weeks, most of the gap is almost filled, although some relevant inclusions remain near the Hap surface. On the non-polarized 0-surface, after one week the histological analysis shows the abundance of flattened fibroblast-like cells rather than newly formed biologic bone. At two weeks, despite the fact that the gap is occupied with a considerable amount of newly formed bone, according to the authors most of the bone chunks are isolated from each other by layered structures of fibroblast-like cells.

At four weeks, most of the gap is filled with newly formed bone, although they have only partial contact with the 0-surface [44].

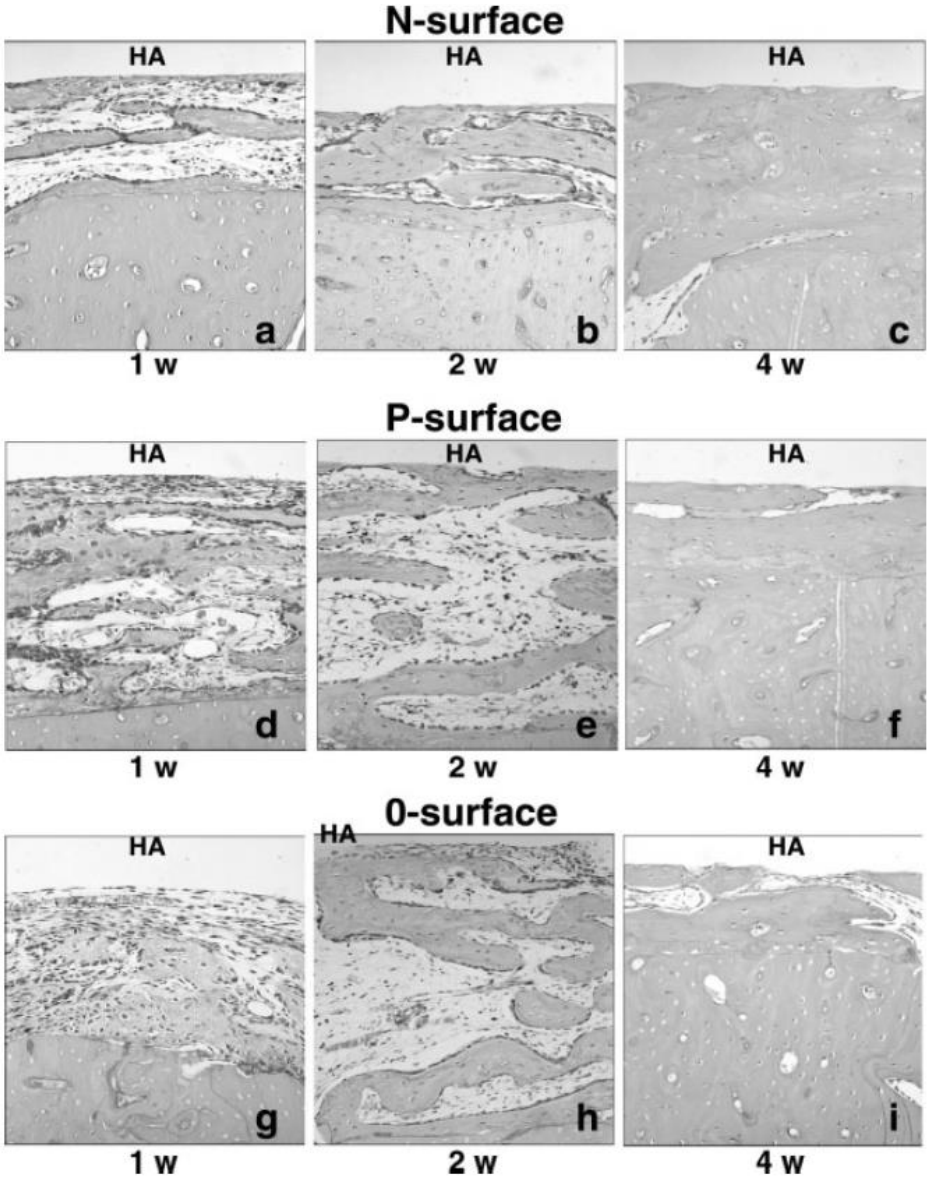

Figure 1.24 Histology staining results of the collected samples, polarized (N- and P- surfaces) and non-polarized (O-surface), after different *in vivo* implantation times. The N-surface, at 1 and 2 weeks, is clearly in a more advanced gap-filling stage compared to the other surfaces [44].

As a small note regarding both the presented *in vivo* studies, although it is not the intent of this thesis to explore such topics, all the procedures were strictly performed according to ethical and experimental guidelines regarding the care and use of animals for

experimental procedures. In the first study, for instance, both guidelines of the National Institutes of Health (NIH) of the USA and of the Tokyo Medical and Dental University were followed.

Finally, the last report being presented is an *in vitro* study. In this work, the influence of surface charge and its polarity on the *in vitro* bone specialized cells adhesion, proliferation and differentiation on electrically polarized Hap coatings on Ti substrates was studied [45]. The sol-gel derived Hap coatings, with an average thickness of 20 ± 1.38 μm, were electrically polarized at 400 ºC with a dc field of 2 kV/cm applied for one hour. The stored charge density was calculated to be around 1.69 μC/cm^2. Non-polarized Hap coatings and uncoated Ti substrates were used as control samples. The *in vitro* mineralization study was performed by immersion on a simulated body fluid (SBF) solution. Remember that the SBF solution, typically used in *in vitro* tests, simulates the ionic composition of the human blood plasma. Typically, during the immersion period, the solution is kept at 37 ºC, in order to mimic the human body conditions. After immersion and being cleaned and dried, the samples were gold-sputtered and their microstructure was observed through SEM microscopy. The weight change was measured to quantitatively characterize the mineralization process. The cytotoxicity, cell morphology and proliferation were also inspected (the particular experimental methodology of each measurement can be consulted in the reference under analysis). Note that the immersion in SBF is a different test than the cell-related tests: the SBF gives information about the mineralization of CHap layers on the surface of the sample, while the cell-related tests give information about their viability and proliferation, differentiation and morphology. The former tests are usually performed with colorimetric MTT (tetrazolium dye) assays and microtiter plates, where the metabolic activity can be studied by means of colorimetry and cell proliferation by performing optical density measurements. Starting with the report results, fig. 1.25 presents SEM micrographs of the samples´ surface after immersion in SBF, at 37 ºC, during five days [45]. On the N-surface, fig. 1.25(a), it is clear that the mineralization is taking place at a fast rate, with the surface being already completely covered with an apatite layer, mostly amorphous in nature. The magnification in (b) shows that there is a preferred needle shape morphology, typical of Hap nanocrystals (probably

some crystallization is already taking place). On the positively charged sample, fig. 1.25(c), the surface presents large amounts of NaCl salt-like deposition. The non-polarized Hap coating, in fig. 1.25(d), shows no signal of apatite layer deposition, i.e., it is visible the top of the Hap coating on the Ti substrate. And lastly, the bioinert surface of the uncoated Ti substrate, fig. 1.25(e), has no indication of mineralization [45]. Additionally, fig. 1.25 includes a graphic of the weight change (mg/cm^2) as a function of the immersion time, for all the samples. After one day of immersion, all the samples do not show any detectable weight change. After five days, it is clear the n-surface shows the highest weight change, comparing to the P-surface and the non-polarized surface. The uncoated Ti bioinert surface does not show any detectable weight change up to seven days of immersion in SBF [45]. Contrarily to an *in vivo* test, where the growth of new bone is also a cellular mediated process, in an *in vitro* test with a SBF solution, where there is no cellular content, only the ionic content of the blood plasma is replicated, it is usually assumed that a selective electrostatic attraction of Ca^{2+} ions in the N-surface, with respect to other solution cations with lower diffusivity and electrostatic attraction (such as Na^+ and K^+), may have an important role in the new bone mineralization acceleration, because the reaction with surrounding anions such as HPO_4^{2-}, HCO_3^- and OH^- would be enhanced, and thus also the heterogeneous nucleation process [45, 46]. In contrast, the P-surface, Cl^- ions are selectively attracted to the Hap surface and react with surrounding cations such as Na^+, Mg^{2+} and $Ca2^+$, etc. Since the ionic concentration (~ 142.0 $mmol/dm^3$) of Na+ ions in a SBF solution is much higher than other cations (e.g., Mg^{2+} - 1.5 $mmol/dm^3$, Ca^{2+} - 2.5 $mmol/dm^3$), the formation of NaCl salts is much more probable on the P-surface,as fig. 1.25 demonstrates [46].

Fig. 1.26 displays optical density measurements translating the osteoblastic cell proliferation on the studied samples, for increasing culture times. For all the analysed culture times, there are significant differences between the N-surface and the other samples: the osteoblastic density on the N-surface is always significantly higher. Moreover, the P-surface inhibited cell proliferation in the early stages, because it presents a lower optical density compared to the non-polarized surface. At eleven days, the differences between the samples are reduced, which is expected, since the cell differentiation and proliferation

stages are achieved faster on the N-surface, therefore stabilizing and saturating the number of osteoblasts for higher culture times in the N-surface.

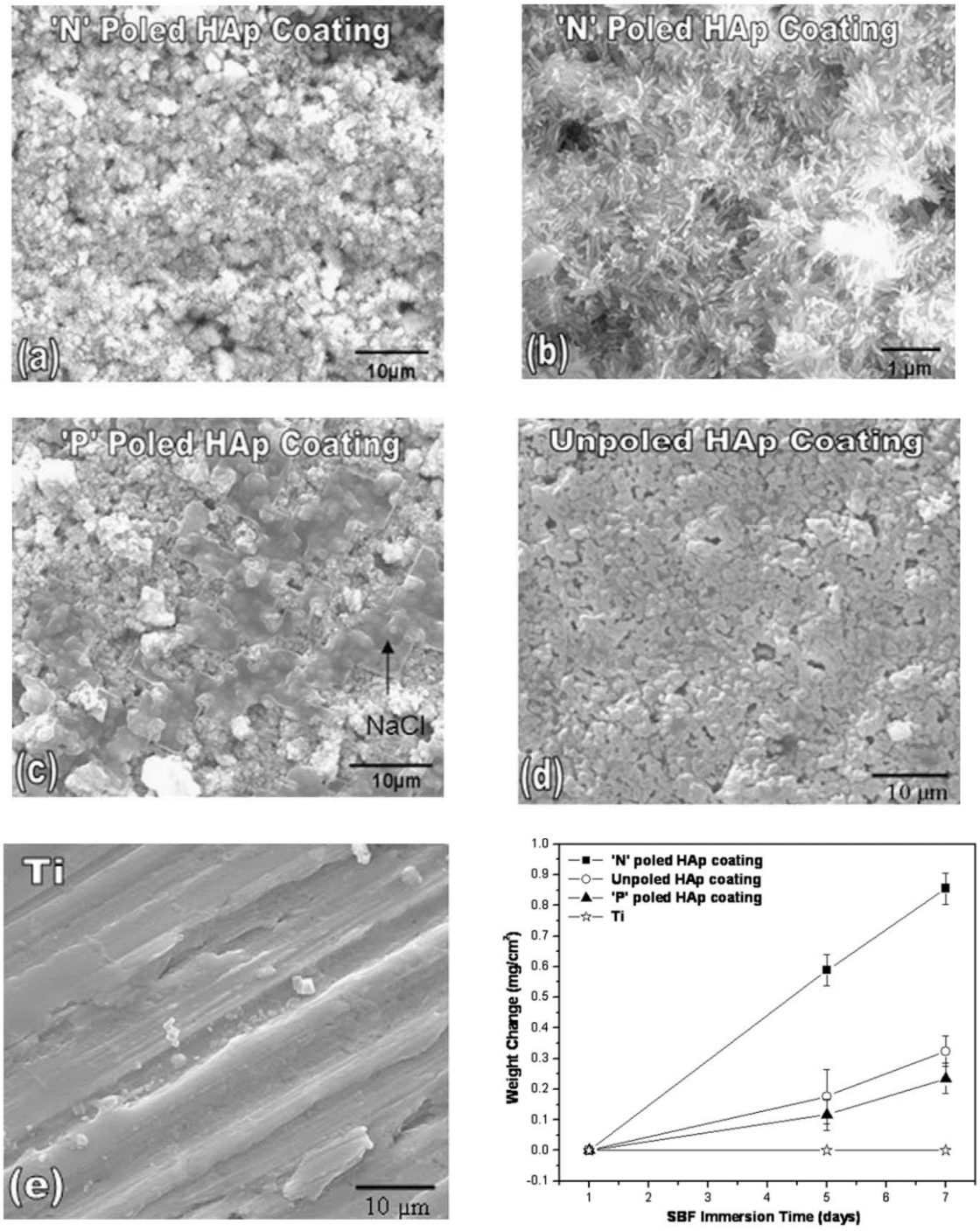

Figure 1.25 SEM micrographs of the samples surface after immersion in SBF, at 37 ºC, for five days. Additionally, the graphic in the lower right corner shows the weight change (mg/cm^2) as a function of the immersion time for all the analysed samples [45].

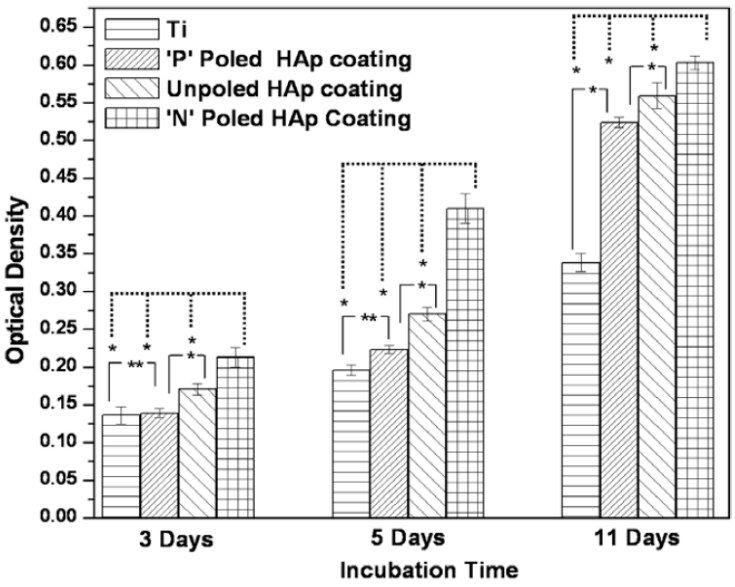

Figure 1.26 Optical density measurements translating the osteoblastic cell proliferation on the studied samples, for increasing culture times (*p < 0.05, n = 5) and (**p > 0.05, n = 5) [45].

With regard to the cellular metabolic activity, fig. 1.27 shows the vinculin protein distribution on the samples surface, after five days of culture, evaluated by immunochemical analysis using confocal imaging [45]. Vinculin is a protein expressed by the osteoblasts which is involved in the creation of focal adhesion sites on the surface where they are going to adhere. Fig. 1.27(a) displays a very strong and well-distributed green fluorescence, indicating the vinculin abundance and therefore a strong bonding between osteoblasts and the surface. On the other hand, the P-surface, fig. 1.27(b), the green fluorescence is very weak, revealing a weak and fragile cellular adhesion to the surface. On fig. 1.27(c), the non-polarized coating surface, the green fluorescence, despite having a stronger signal compared to the P-surface, is still clearly weaker compared to the N-surface. Finally, the Ti uncoated surface, fig. 1.27(d) shows similar results as the P-surface [45].

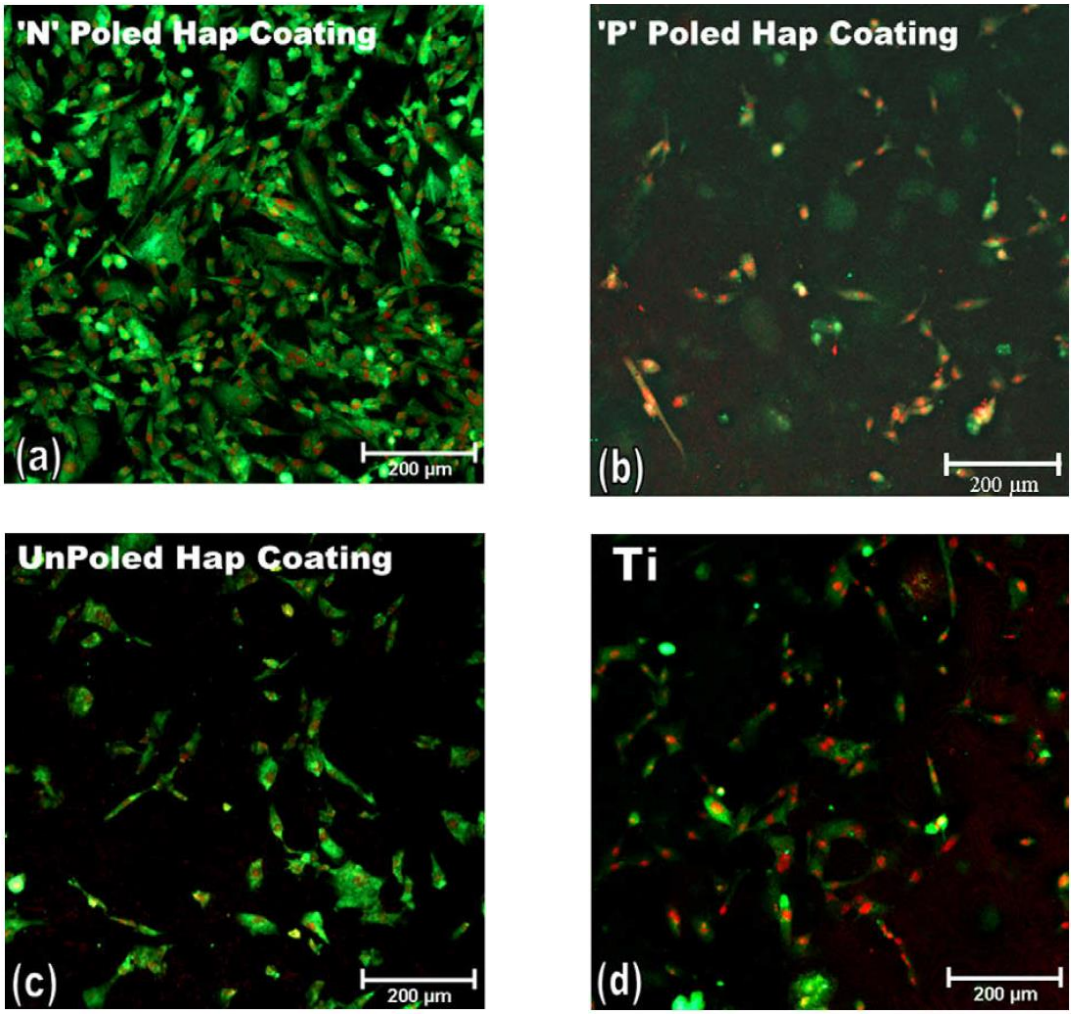

Figure 1.27 Vinculin distribution on the samples surface, after five days of culture, evaluated by immunochemical analysis and using confocal imaging [45]. The green fluorescence signals antibody bound to vinculin, while the red colour signals the osteoblasts nuclei.

To finish the analysis of this biological study, the distribution and abundance of another important protein expressed by the osteoblasts, the alkaline phosphatase (ALP) was investigated. This protein is expressed by differentiated osteoblasts, during the bone remodelling process, and therefore it is used as a differentiation stage marker for osteoblasts. On fig. 1.28(a), a moderate green fluorescence on the N-surface points out that already at day 5 the cells started to differentiate, while in fig. 1.28(b), the results for the P-surface suggest that the cells are still in the growth stage, accounting for the minimal expression of ALP. In the non-polarized coating, the cells are equally in a pre-differentiation

stage, though in a more advanced stage compared to the P-surface, and lastly the uncoated Ti surface seems to be on a similar stage as the non-polarized surface. In this study it is presented also an ALP distribution confocal image for eleven days of culture where it can be seen that for the N-surface the osteoblasts are already in the final stages of their activity differentiation, suggesting an advanced state of osteoid formation and bone matrix mineralization. Disparately, the P-surface showed only restricted osteoblastic differentiation and the non-polarized surface was found to be in an early stage of differentiation. On the uncoated Ti surface, differentiation had not yet occurred [45].

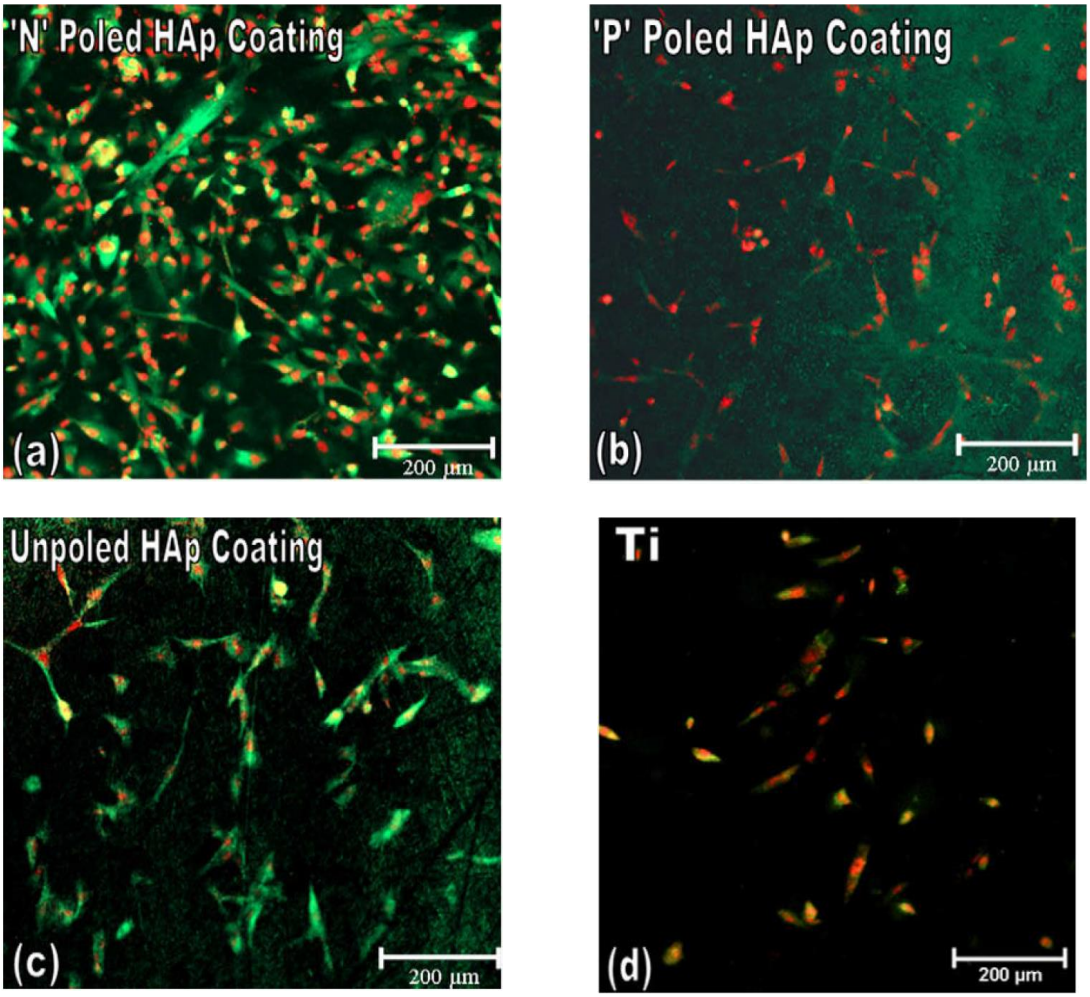

Figure 1.28 Alkaline phosphatase (ALP) distribution on the samples surface, after five days of culture, evaluated by immunochemical analysis and using confocal imaging. The green fluorescence signals antibody bound to ALP, while the red colour signals the osteoblasts nuclei [45].

As a conclusion to this topic, it is experimental evidence that the surface charge density and its polarity have a strong influence on both the *in vitro* mineralization and on the cellular attachment, proliferation and differentiation. Particularly, negatively charged surfaces are those which demonstrate the best *in vitro* and *in vivo* results: early osteoblastic adhesion, proliferation and differentiation are demonstrated on those surfaces, promoting early mechanical stability of the implant and therefore providing it a superior functionality compared to the options available in the market. It is important to mention that there are reports stating that a minimum stored charge density in the magnitude order of 10^{-6} C/cm^2 is required to show significant differences in the biological response both *in vitro* and *in vivo* [45]. Despite the fact that other properties such as wettability and surface energy are thought to have an influence of the bioactivity of Hap-based biomaterials, the electrical polarization is proven to be by far the most efficient bioactivity catalyst, opening new doors towards the next generation of differentiated bioactive coatings intended for orthopaedic applications.

1.2 Coating deposition processes

The purpose of the present section is to explore some of the most popular processes to produce bioceramic coatings on metallic substrates. The spotlight on this section will be given to the plasma spray (PS) process, because it is the dominant and certified industrial process to make bioceramic coatings. By addressing PS with more detail, it will be possible to compare it with the CoBlast process, which is presented separately in section 1.3, because is a relatively recent process.

Despite the vast number of reported coating processes, they can be in a general way divided into thermal and non-thermal processes, although sometimes the distinction may not be completely clear, as it is the case of processes that require a final heat-treatment to crystallize the Hap, like the sol-gel and the electrochemical deposition processes. The non-thermal processes take place at temperatures lower than the Hap melting temperature. As said, most of these processes may require a subsequent heat-treatment to crystallize Hap from amorphous calcium phosphate (ACP) or dehydroxylated precursor phases, such as

octacalcium phosphate. They might also require the calcination of organic components and solvents used during coating deposition [4].

1.2.1 Sol-gel

The first process to be discussed is the sol-gel deposition, framed in the non-thermal category. It is usually performed at RT. As it is known, this wet-chemical process involves reactions of inorganic precursors and/or hydrolysis of organo-metallic alkoxides producing a gel of hydrous oxides that requires a sinterization treatment to produce a dense ceramic material. The process usually starts with very small colloidal particles, typically around the few nanometers (the sol) and as the particle concentration increases, they react and form bonds and chains, yielding a three-dimensional network (the gel) that increasingly fills the liquid phase. Subsequently, with the drying step, the liquid phase is further reduced and the gel hardens, densifies and shrinks. The sinterization further densifies the materials, and eventually all the porosity may be removed. Before the sinterization, the gel can be shaped and dimensioned as one desires, which can be considered as a positive point [4]. Also, one of the main advantages of sol-gel is the high purity of the final material, since the mixing process occurs at the molecular level. However, there are important drawbacks that tend to "repel" industrial interest, particularly the high cost of the organometallic precursors and also the tendency of the dried moulded gel to crack during the thermal treatment, due to the high amount of shrinkage [4]. There are several "recipes" reported for the sol-gel synthesis of Hap, using different precursor chemicals. The calcium and phosphorous sources are usually mixed according to the stoichiometric Hap Ca/P molar ratio, 1.67. Examples of precursors for the synthesis of Hap coatings are triethyl phosphite and calcium nitrate and calcium 2-ethylhexanoate [$Ca(O_2C_8H_{15})_2$] and 2-ethyl-hexyl-phosphate. The pH control is very important: Hap precipitation is favoured for an alkaline pH, typically >10. It was shown that pH values between 6-9 may yield significant amounts of impurity phases such as TCP [47]. Furthermore, it was demonstrated that the choice of the calcium source compound influences the crystallinity and morphology of the Hap particles: the use of calcium nitrate and triethyl phosphate yields particles with spherical morphology, while

calcium acetate yields particles with a fibrous morphology [4]. The sol aging time is also another very important parameter: low aging times, lower than 24 h, do not provide enough time to complete the reactions, and therefore secondary phases such as CaO can be obtained. Several calcination temperatures are reported, but typically, temperatures above 400 ºC are required to promote the Hap crystallization. For example, Liu et. al. deposited Hap films on sand-blasted 316L stainless steel substrates, by means of a water-based sol-gel process [4, 48]. The sand-blasting of the stainless steel surface is required to provide a higher surface area for the coating adhesion to the substrate. It was found that temperatures ≥ 400 ºC are required to promote a good crystallinity, while lower temperatures showed poor crystallinity. The dense coatings reached an average adhesive strength of 44 MPa, as determined in accordance to the standard ASTM C633-13 (2013), which is a very good value, better than the typical adhesion strengths of plasma sprayed coatings (typically in the 20 - 30 MPa range, sometimes lower than 20 MPa). However, the coatings heat-treated at temperatures ≥ 400 ºC revealed some surface cracking, which may be connected to factors such as the non-uniform coating thickness, due to the surface roughness caused by the sand-basting process, and the contraction caused by crystallization of the amorphous or poorly crystalline apatite phase (the authors refer to the contraction caused by sinterization, however as it can be seen in topic 1.1.7, Hap sinterization is not active at such low temperatures because the provided energy is not enough to activate the solid-state diffusion of matter). In another study, Hap coatings were deposited on Ti substrates by sol-gel [49]. Organic and inorganic precursors were used as phosphorous and calcium sources: TEP [$P(C_2H_5O)_3$] and calcium nitrate [$Ca(NO_3)_2.4H_2O$]. The mixture of solutions containing both precursors, mixed according to the Ca/P ratio of Hap and with the desired pH adjustment, was stirred at RT for 72 h and then at 40 ºC for 24 h. The coatings were obtained by dip-coating at a withdrawal speed of 5 mm/min and were dried in an oven at 80 ºC for 12 h and then heat-treated at 500 ºC for 1 h in air. The coatings were free from impurity phases, were dense and uniform and had a thickness of about 5 μm. *In vitro* tests revealed a higher degree of cell proliferation and ALP expression for the coated samples compared to pure Ti samples [49].

Although many more things could be said about the sol-gel technique, the brief overview that was presented serves the intent of section 2.1. Another non-thermal process will be presented in the subsequent topic: the electrochemical deposition (ECD).

1.2.2 Electrochemical deposition (ECD)

This a three-electrode setup that is immersed in an electrolyte solution, as the scheme in fig. 1.29 illustrates. All electrodes are connected to an electrical generator. One of the electrodes consists of a cathode (often designated as the working electrode), which comprises the metallic substrate to be coated, in this case a Ti6Al4V alloy, and finally there are the platinum counter electrode and a reference electrode. The electrolyte solution for Hap deposition typically consists of Ca^{2+} and $H_2PO_4^-$ ions.

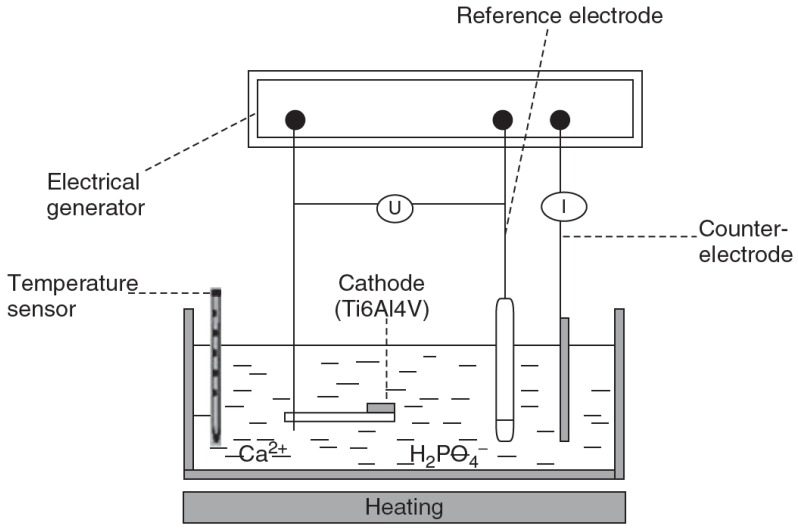

Figure 1.29 Scheme of an electrochemical processing cell for deposition of calcium phosphate-based materials [4].

The following electrochemical reactions take place at the electrode-electrolyte interface [4]:

$$2H_2O \rightarrow O_2(g) + 4H^+ + 4e^- \quad (6)$$

and

$$2H_2O + 2e^- \rightarrow H_2(g) + 2OH^- \quad (7)$$

Reaction 6 consists in the anodic oxidation of water while reaction 7 in the cathodic reduction of water. The water reduction implies an increase of the pH value at the cathode-electrode interface leading to acid-base reactions caused by the pH variation near the cathode. The $H_2PO_4^-$ ions are stable in the pH range between 3 < pH < 6. When the pH increases to the range between 7.2 < pH < 11.8 the HPO_4^{2-}(hydrogenphosphate) ions are predominant and when it increases above 11.8 the PO_4^{3-}phosphate ions will be predominant [4]. The abundance of these ions near the cathode will cause a local supersaturation leading to the precipitation of calcium phosphate phases, according to their solubility and thermodynamic stability in the pH local conditions. Hence, at pH values lower than 6.5, calcium diphosphate dihydrate ($CaHPO_4 2H_2O$) precipitates, between 6.5 and 12, octacalcium phosphate ($Ca_8(HPO_4)_2(PO_4)_4$ precipitates and above 12 Hap precipitates according to the following reaction [4]:

$$10Ca^{2+} + 6PO_4^{3-} + 2OH^- \rightarrow Ca_{10}(PO_4)_6(OH)_2 \quad (8)$$

Eventually, some deviations from stoichiometric can lead to the precipitation of calcium-deficient hydroxyapatite (CDHap), with chemical formula $Ca_{10-x}(HPO_4)_x(PO_4)_{6-x}(OH)_{2-x}$. CDHap is able to comprise Ca/P ratios between 1.33 < CDHap < 1.67. The current density is also an important parameter since it has also influence on the local pH near the cathode [50]. In one study it is reported that Hap precipitation is favoured for current densities above 10 mA/cm^2, while for lower densities other phases such as calcium diphosphate dihydrate can become significant [50]. Still about the former study, fig. 1.30 displays a cross-sectional SEM micrograph of a Hap coating on a Ti substrate, deposited by ECD with a current density of 10 mA/cm^2 and heat-treated at 500 ºC during 1 h. Also, the EDS profiles, along the AB line, of the Ca, P and Ti elements are shown [50]. The coating thickness is about 18.6 μm and the average Ca/P ratio was 1.48, lower than the theoretical value, indicating the deposition of CDHap. More recent methodologies include some additions to the electrolyte, such as hydrogen peroxide (H_2O_2), that after heat-treatment yield stoichiometric Hap. The Ca and P EDS line profiles in fig. 1.30 appear to be relatively uniform over the coating thickness. The mechanical stability was investigated by scratch testing, by plotting a friction-load curve. The coating revealed considerably superior

mechanical properties, for instance in terms of shear stress, compared to the average reported values both for PS and sol-gel coatings [50].

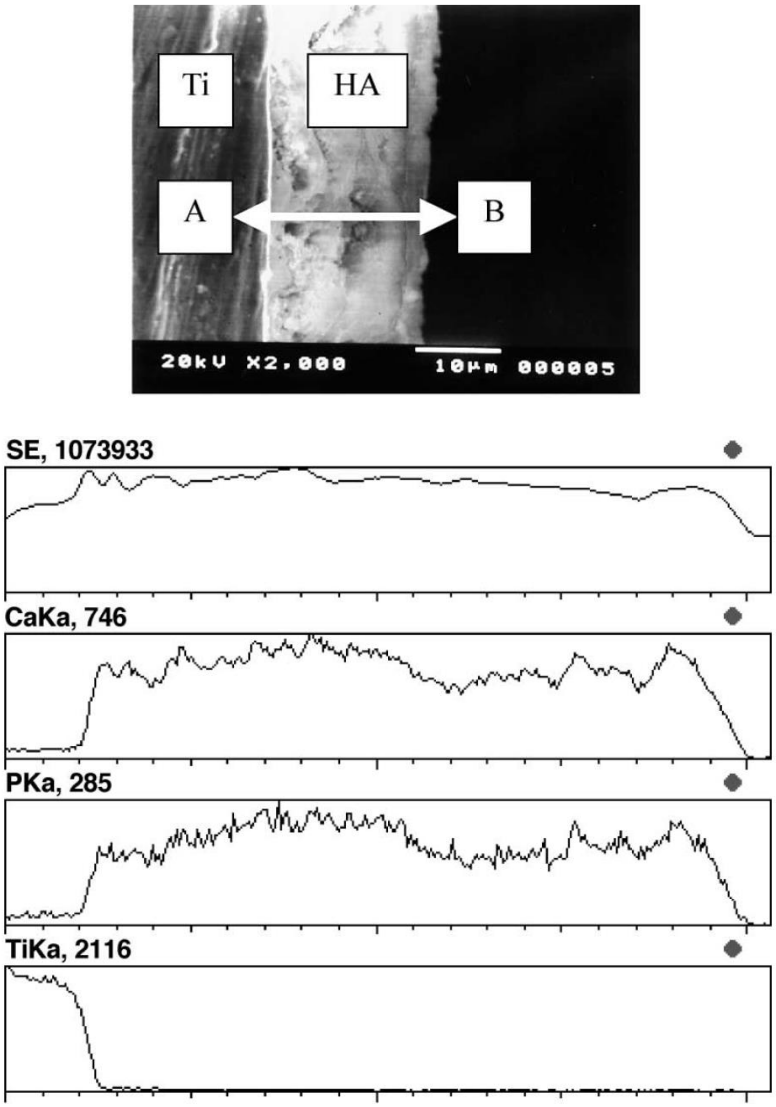

Figure 1.30 Above: cross-sectional SEM micrograph of a Hap coating on a Ti substrate, deposited by ECD. Below: EDS profile, along the AB line, of the Ca, P and Ti elements [50].

1.2.3 Plasma Spray (PS)

Entering in the thermal deposition processes, PS is currently the only certified industrial process to produce Hap coatings on orthopaedic and dental implants. Among the different variations of PS, the classic atmospheric plasma spray (APS) is the most popular. PS processes essentially consist in a rapid solidification process, where the material to be deposited is driven into a plasma jet that melts and projects at high velocity the material against the substrate to be coated. PS can be applied to metallic and ceramic materials with a well-defined melting temperature. As we will see, PS coatings still face some problems regarding the adhesion level to the substrate and the high residual mechanical stresses within the coatings [4]. Fig. 1.31 shows the main components of an APS experimental system [51]. The thermal energy in PS is provided by a high energy plasma which is formed within the plasma gun section. The plasma gun is constituted by a cathode and an anode (nozzle anode) separated by a small gap. A DC current is supplied to the cathode, creating an electric arc discharge in the gap between the cathode and the anode. A plasma ionising gas, such as argon (Ar), helium (He) or an argon/hydrogen mixture, is fed into the electric arc, where it is ionised and forms a high-temperature plasma, which can reach temperatures as high as 14000 ºC. A recirculated cooling system prevents the plasma gun components from overheating during spraying, increasing the components lifetime. In the nozzle (anode), a rapid expansion of the plasma gas takes place, speeding it up to velocities well above the speed of sound, around 800 m/s. During the path within the nozzle, the plasma becomes unstable, due to the rapid expansion, and recombines to form a gas again, releasing a large amount of thermal energy in the form of a plasma jet. The coating powder is usually injected in the point of exit of the plasma jet after the plasma gun perpendicularly to the jet, as depicted in fig. 1.31 [4, 51]. Process parameters in PS include the arc current intensity, spraying distance, powder feeding rate, gun transverse speed, and also other parameters related to the feeding powder particle morphology, size distribution, etc. We will refer to some of them, but the readers interested in more particular information go through the references provided in the present section.

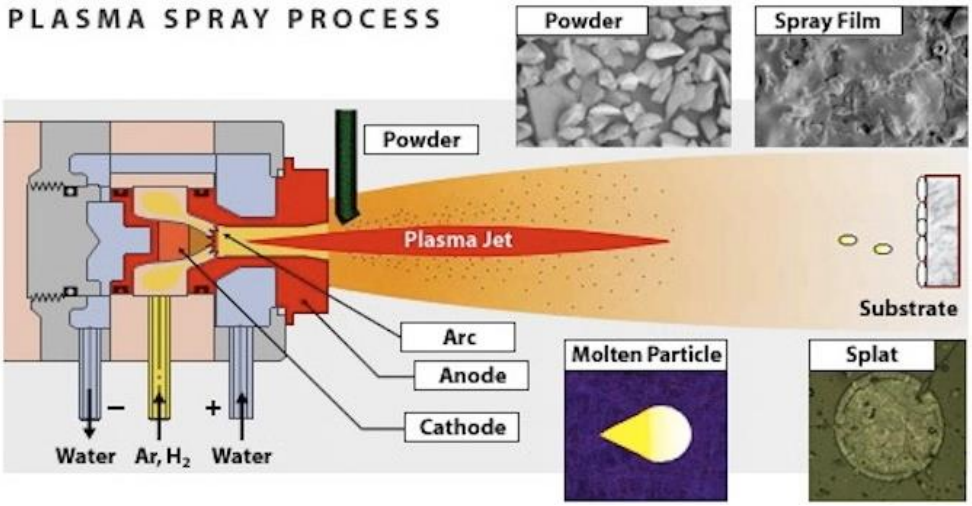

Figure 1.31 Illustration of the main components of an APS experimental system [51].

Momentum is transferred from the plasma jet to the injected powder, and the powder particles acceleration, dV_P/dt, depends on several factors, as equation 9 shows [4]:

$$\frac{dV_p}{dt} = \left[\frac{3C_D.\rho_g}{4d_P.\rho_p}\right](V_g - V_p)|V_g - V_P| \quad (9)$$

where the drag coefficient is given by $C_D = 2[F_D/A_P]/[\rho_g \mu_R^2]$ (F_D is the Stokesian drag force, A_P is the cross-sectional area of the particle, ρ_g is the gas density and $\mu_R = V_g - V_P$); $V_g - V_P$ is the velocity gradient between the gas velocity and the particle velocity, d_P is the particle diameter and ρ_P is the particle density. Eq. 9, known as the Basset-Boussinesq equation of motion, shows the direct and inverse proportionalities of the acceleration imparted to the particles entering in the plasma jet, and that APS is a complex process affected by many parameters [4, 52]. Moreover, the amount of heat that a particle will gain is given by a balance between two forms of energy transfer, the heat acquired by convective energy transfer, given by $Q_C = hA(T_\infty - T_S)$ and the heat lost by radiative energy transfer $Q_R = \sigma\varepsilon A(T_S^4 - T_a^4)$. In the former energy transfer equations, h is the convective energy transfer coefficient, A is the surface area of the particle, T_∞ is the plasma temperature, T_S is the surface temperature of the particle, T_a is the temperature of the surrounding atmosphere, σ is the Stefan-Boltzmann constant and ε is the particle emissivity [4]. The powder particles in APS will always undergo a significant degree of melting. In fact, thermal decomposition

of the Hap during APS occurs, leading to the presence of other calcium phosphate crystalline phases in the coatings, such as α-TCP, β-TCP, TTCP and calcium oxide, although β-TCP is the one which is predominantly detected besides Hap [52]. Additionally, the high cooling rates experienced by the particles will also lead to the presence of ACP in the coatings, producing the habitual amorphous halos observable in the XRD diffractograms. It is important to be aware of the fact that there are international standards that regulate products for biomedical applications. Hap coatings for orthopaedic implants are regulated by a number of ISO (ISO – International Organization for Standardization) and ASTM (it was funded in 1898 as American Society for Testing Materials, but nowadays is known as ASTM International, due to its international scope) standards, that cover different aspects of the coating production, such as the raw materials specifications, the control of the coating process and of the coating properties [52, 53]. ISO 13779-2 specifies that, among other properties not mentioned here, Hap coatings must have a crystallinity percentage higher than 45 %, that the Hap weight percentage must be ≥ 50 %, and that the weight percentage of α-TCP, β-TCP, TTCP and CaO secondary crystalline phases must each be ≤ 5% (if they are detected, of course) [53]. With the development, understanding and refinement of the APS process, nowadays virtually all of the coatings comply with the requirements. McCabe et. al. indicate in their review article the typical values that commercial PS Hap coatings present regarding the properties defined in ISO 13779-2 and also in other standards [53]. For instance, typical values consist of 80% of crystallinity, ~92.7% of Hap mass fraction, 3.2% of α-TCP mass fraction and 4.1% of β-TCP mass fraction [53]. However, as we referred, in many reports only Hap and β-TCP are detected through XRD measurements, together with the habitual amorphous halo assigned to ACP.

When the particles collide with the substrate, they will produce a typical splash pattern. Fig. 1.32 displays the typical surface features of a Hap APS coating [4]. Characteristic overlapping particle splats and some spherical-shaped incompletely melted particles, attached to the surface, can be observed.

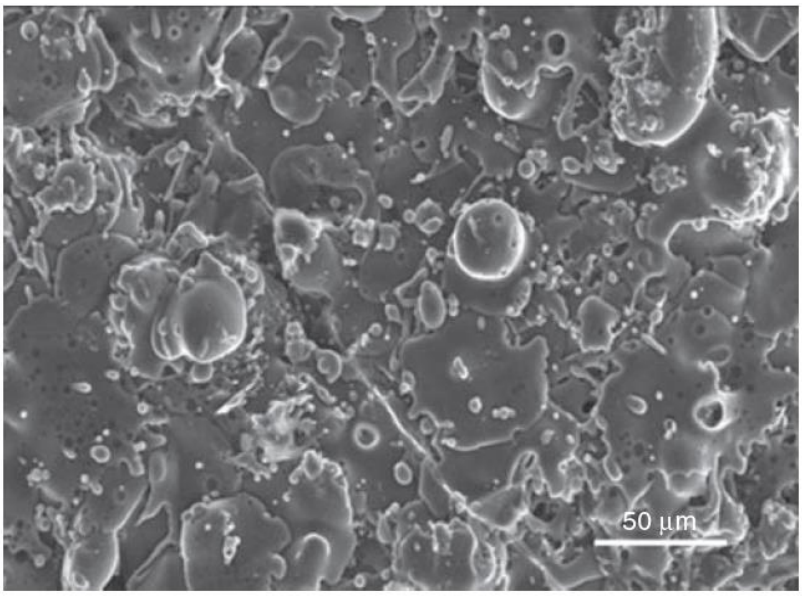

Figure 1.32 Typical surface features of a Hap APS coating [4].

Another important aspect of PS processes, in general, is that the substrate has to be prepared prior to deposition. Substrate texture and roughness are crucial for the adhesion strength of the coatings. The most important step in substrate preparation is the surface roughening, as it greatly improves the coating adhesion strength. In this step, a grit blasting process is used, where the substrate is bombarded with irregular grit particles, typically Al, at high velocity [54]. Surface roughness values in the range of 3-4 μm have been found to be sufficient to produce sufficient adhesion strengths for Hap coatings [54].

Argon is typically used as a plasma gas since it has many advantages: it is relatively cheap, easily ionizable and inert, protecting the powder particles and the electrodes from the environment. The morphology and microstructure of the powders have also an effect on the quality of the coatings: spherical particles have better flow properties compared to irregular ones. Powders with a narrow size distribution are also desirable to produce a more consistent and uniform coating. Further, powder size affects the melting characteristics within the plasma flame. Larger particles are reported to experience a lower degree of melting compared to smaller particles. In consequence, the coating properties tend to deteriorate with increasing particle size: larger sizes lead to coatings with partial unmelted particles, cavities and macroporosity which deteriorate the mechanical properties [55].

Typical particle size used in PS is in the 20-90 μm range, being reported that sizes in the range of 20-45 μm produce much denser, lamellar coatings [55]. Typical distances between the plasma gun and the substance, known as the working distance, are around 10 cm.

A very important subject regarding PS coatings is the residual internal stresses. They can be generally defined as mechanical stresses that exist in material under the absence of external mechanical loads. Residual stresses are inherently induced in the coatings deposited by thermal coating processes because of the differences in the thermal properties of the coating and substrate materials. In the case of Hap, for example, the differences between the thermal expansion coefficients of the different phases within each particle and within the coatings, as well as the temperature gradients experienced by different regions of the coating at different times during the deposition process, contribute additionally to the internal residual stresses [56]. These mechanical stresses can be a problem: delamination between the Hap coating and substrate can prejudice the adhesion level between them. In fact, reoperation cases have been reported due to loosening or dislocation of APS coated implants that were attributed to interfacial fracture of the Hap coating [57].

In the PS processes family, alternatives to APS exist and have been developed, in order to address some of the problems inherent to APS. Nonetheless, APS is still clearly the dominant industrial process. One of the alternatives is the Low-Pressure Plasma Spray (LPPS). In this process, as the name suggests, the plasma chamber is evacuated and after vacuum stabilization, an inert gas, typically argon or helium, is introduced in the chamber, maintaining a low pressure in the range of 50-250 mbar [4]. This process has added the advantage to allow coating reactive materials by preventing oxidation. The lower pressure in the plasma chamber leads to a much longer plasma jet with lower temperatures compared to APS. As mentioned, in APS the plasma temperature can reach ~ 14000 ºC, while reported values for LPPS are around 10000 ºC at 0.25 bar and 5000 ºC at 0.07 bar. Regarding the plasma jet lengths, for APS they are reported to be ≤ 70 mm, whereas for LPPS the lengths are ≤ 150 mm and ≤ 500 mm at 0.25 and 0.07 bar, respectively [4]. The higher particle speeds in LPPS (250 - 600 m/s) are reported to be associated with denser

coatings and considerably higher adhesion strengths compared to APS. Additionally, the combination of the lower plasma jet temperature together with the reduced time in the plasma jet (higher particle velocity) prevents the thermal decomposition of Hap observed in APS. Therefore, LPPS should be adopted to coat oxidation sensitive materials, such as Ti alloys, especially when high adhesion strengths and coating densities are required, as it is generally the case of coatings intended for orthopaedic applications. However, as the prevalent philosophy of a religion known as capitalism, corporations and industries are not interested in providing the best solution to the patients, but the most profitable. LPPS encloses a more complex technology, higher power demands, up to 100 kW, and higher gas consumption rates, and consequently it is not expected to replace APS, despite the advantages.

1.2.4 Cold gas dynamic spraying (CGDS)

The CoBlast™ (trademark of ENBIO Ltd., Irish company; from now one the process will be written as CoBlast, leaving out the trademark symbol) process can be referred as a variation of a process family generally labeled as cold gas dynamic spraying (CGDS). CGDS includes process temperatures up to 700 ºC or even higher, yet, they can be considered as "cold" compared to APS. However, as will be shown, CoBlast takes place near RT. The basic idea behind CGDS is to use a high-pressure gas, such as nitrogen, helium and also air, to accelerate powder particles up to very high speeds (2 up to 4 times the speed of sound) onto the substrate to be coated. Fig. 1.33 illustrates the typical components of a CGDS experimental system [4]. Most of the setups use a Laval-type spray nozzle design to accelerate the powder, and as it will be seen, CoBlast does not require such type of nozzles [58]. Whereas in APS and LPPS the particles experience some degree of melting, in CGDS they remain in the solid-state. Therefore, fast shrinkage during cooling is avoided, reducing considerably the internal stresses within the coatings. Furthermore, due to the nature of the process, the impact of the "cold" solid particles on the substrate and the induced strains tend to stress the coating in compression and not in tension, helping to achieve higher adhesion strengths between the substrate and the coating [4]. In CGDS the powder retains

its original properties, especially in terms of chemistry and phase composition, consisting of an important advantage. Only some mechanical deformation can occur, such as, for example, reduction of grain size during impact (the grains can fragment into smaller grains, this is observed in CoBlast). Still, regarding CGDS methodologies, bonding between the impacting powder particles and the substrate is reported to occur for velocities higher than a critical speed, which, among others, depends on the mechanical properties of the coating particles [58]. The following equation 10 provides an estimate for the critical speed [58]:

$$v_{crit} = \sqrt{\frac{F_1 . 4 . \sigma_{TS} . \left(1 - \frac{T_i - T_R}{T_m - T_R}\right)}{\rho} + F_2 . c_p . (T_m - T_i)} \quad (10)$$

where the tensile strength (σ_{TS}), density (ρ), specific heat (c_p) and melting temperature (T_m) can be taken from standard materials databases [58]. Other parameters are the impact temperature T_i, which reflects the spray conditions, and the reference temperature (T_R) can be set as RT. Finally, F_1 and F_2 are mechanical and thermal calibration factors, calculated by correlating calculated critical velocities based on the properties of the material, with experimentally determined critical velocities [58].

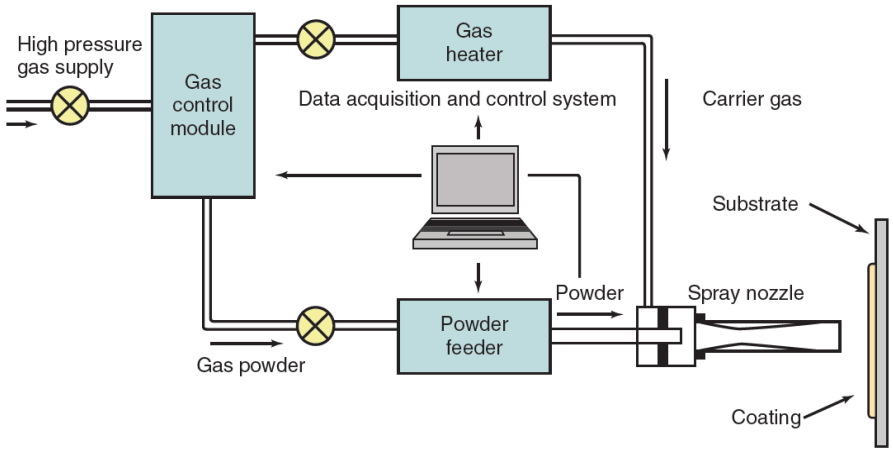

Figure 1.33 The typical components of a CGDS experimental system [4].

Fig. 1.34 shows calculated critical velocity values, using equation 10, for different metals and alloys, with increasing density from left to right, assuming a grain size of 25 μm [58]. Although there is a faint trend for decreased critical velocities with the increase of the

density, fig. 1.34 shows that the other equation parameters (equation 10), translating the material strength and melting temperature, cause substantial deviations from this trend [58].

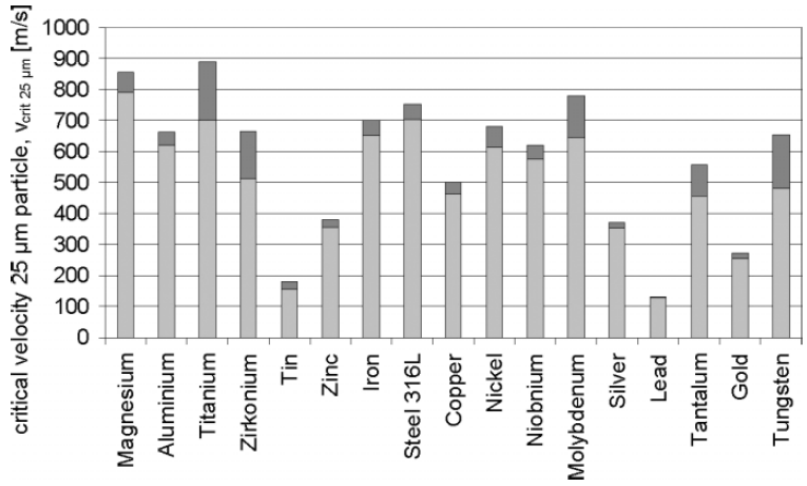

Figure 1.34 Calculated critical velocity values, using equation 10, for different metals and alloys, assuming a grain size of 25 µm [58].

Reports on the CGDS of bioceramic materials, particularly Hap, are still scarce. In part, because one of the drawbacks related to CGDS is that coating materials are restricted to ductile metals such as Ti and Ti alloys, stainless steel, aluminum, etc. These materials are bioinert (remember the discussion of fig. 1.4). Hard and brittle materials, such as bioceramics like Hap, cannot be sprayed in pure form, is most of the time applied as composites within a ductile matrix phase [4]. Substrate materials are also required to be able to stand the abrasive action of the highly accelerated solid particles, which for example excludes most of the polymers. Nonetheless, since the majority of the substrates used in biomedical implants are Ti, Ti alloys and stainless steel (this last one mostly in poorer countries), the substrate requirement is not a big problem, since these metals can withstand the abrasive action. The first problem, the coating materials restriction, makes that the few available reports deal with metal/Hap composites, and usually Hap is the minor component in the composite. For example, composite coatings of sponge-type Ti (a porous form of Ti) and Hap were studied by means of CGDS. The experimental setup is essentially the same

as the one depicted in fig. 1.33. It was concluded that dense coatings could be deposited with Hap contents up to 30 wt%, mainly due to difficulties arising from the widely different physical characteristics of the Ti and Hap powders [59]. Fig. 1.35 depicts, in the left, a cross-sectional micrograph of a sponge-Ti + 20 wt% Hap composite coating, deposited at 600 ºC with an ejection pressure of 35 bar, while the right micrograph displays a magnification of the same coating, accurately polished and etched to reveal the boundaries [59]. The left micrograph shows a dense coating with well-distributed encapsulated Hap particles. These encapsulated Hap particles distributed within the Ti ductile matrix are shown in the magnification. It was also found that despite the initial powder mixture contained 20 wt% of Hap, about 4 wt% of Hap was lost during deposition (probably due to the very high deposition velocities, some particles may rebound). The adhesion strength was averaged to be around 24 MPa, comparable or higher than PS coatings, and higher deposition pressures and temperature will not improve the adhesion strength. Also, the majority of the mechanical failures were cohesive in nature (within the coating), and not at the coating/substrate interface [59]. The characteristic large coating thicknesses, as it can be inferred from fig. 1.35, is a factor which increases considerably the probability of cohesive failures. Further discussion on adhesive and cohesive failures is included in section 2.4, chapter 2.

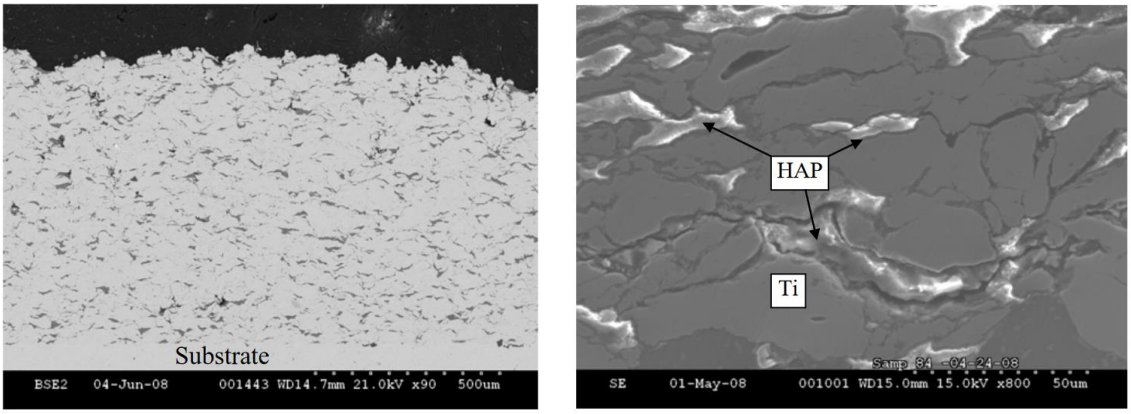

Figure 1.35 In the left: Cross-sectional micrograph of a sponge-Ti + 20 wt% Hap composite coating, deposited at 600 ºC with an ejection pressure of 35 bar. In the right: Magnification of the same coating, accurately polished and etched to reveal the boundaries [59].

Fig. 1.36 shows a cross-sectional micrograph of a sponge-Ti + 50 wt% Hap composite coating, deposited at 700 ºC, with an ejection pressure of 30 bar. In this case, though a considerable amount of Hap powder was encapsulated in the coating, voids are observed within the coating, containing some Hap fragments crushed during the deposition process. In relation to the coating displayed in fig. 1.35, it was observed that decreasing the pressure to around 30 bar and increasing the temperature up to 700 ºC favoured the deposition of composites with larger weight contents of Hap. However, the voids within the coating worsen its mechanical properties, with average adhesion strengths of 18.2 MPa. The failures in the adhesion tests are always cohesive, within the coating. Additionally, the amount of lost Hap powder increased in comparison to the deposition conditions of fig. 1.35, up to 15 wt% [59].

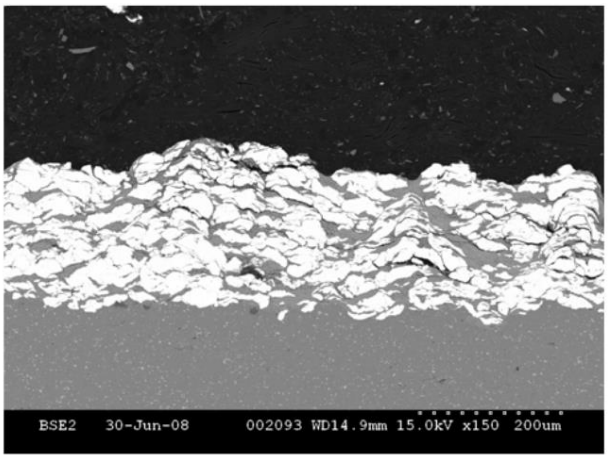

Figure 1.36 Cross-sectional micrograph of a sponge-Ti + 50 wt% Hap composite coating, deposited at 700 ºC with an ejection pressure of 30 bar [59].

1.3 The CoBlast™ deposition process

The Coblast deposition process is a recent low-temperature variant of the CGDS process, developed and patented (patent no. US 8,119,183 B2) in 2007 by ENBIO Ltd. There are still not many reports on the CoBlast process, and not all of them discuss Hap coatings on metallic substrates. CoBlast, being an advanced version of typical micro-blasting systems, uses a co-incident stream of abrasive and dopant particles, both in powder form, projected into the same region of the substrate at the same time. While the inert abrasive

material disrupts the superficial oxide layer (in the case of metallic substrates such as Ti) and the underneath surface, the dopant material gets impregnated in the surface through a combination of mechanical interlocking and chemical bond formation between the bioceramic material and the exposed metal substrate [60-62]. A schematic view of these steps is presented in fig. 1.37 [63]. Despite the fact that fig. 1.37 indicates abrasive particles of approximately 50 μm, most of the reports use particles with higher average sizes, around 100 μm. It is visible in fig. 1.37 that the Hap particles building up in the disrupted surface fragment into smaller particles during the blasting process. At the end of the process, the Hap build-up will produce an adhesive Hap layer [63]. The mechanisms behind the tribochemical bonding will not be discussed here, they do not fit the scope of this thesis, but the interested readers may consult references [64, 65].

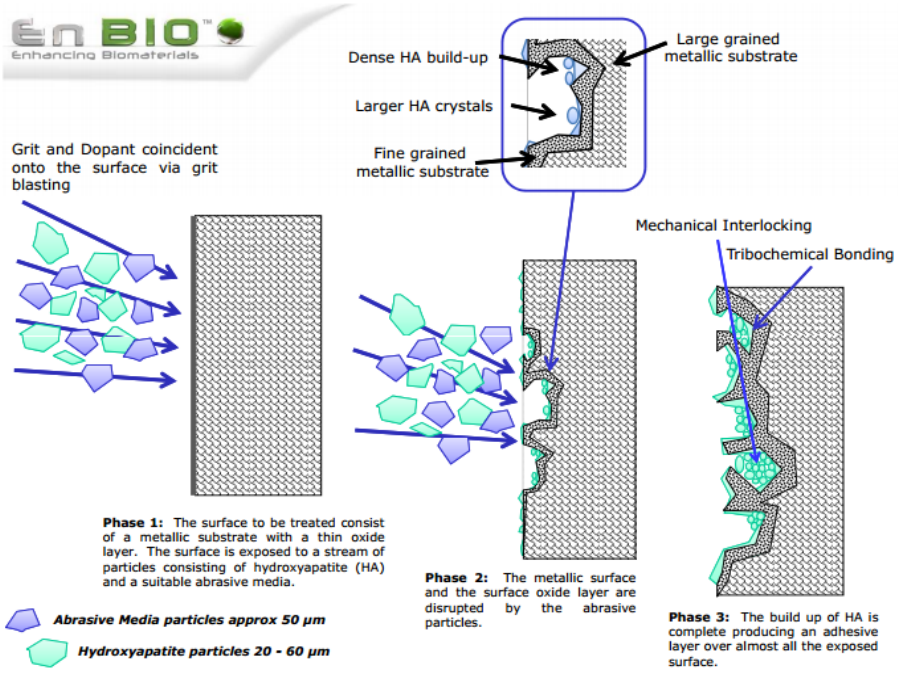

Figure 1.37 The CoBlast deposition steps leading to the buildup and adhesion of a Hap coating in the metallic substrate [63].

Fig. 1.38 depicts an example of an experimental system of the CoBlast deposition process. The processing chamber contains both an abrasive and Hap (of course, in the case

of Hap being the coating material) jet systems, with the respective powder feeders, mounted on a sealed chamber with a proper powder extraction system.

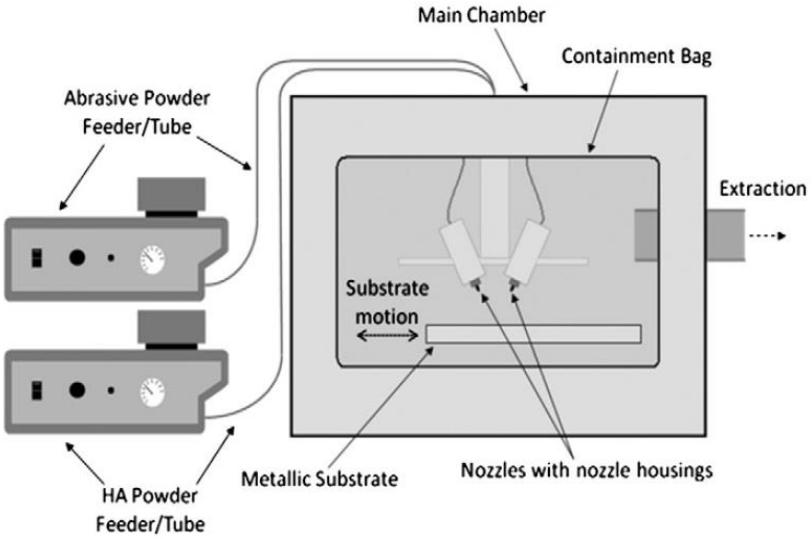

Figure 1.38 Example of a CoBlast experimental system [66].

It is visible in fig. 1.38 that the system contains contain two nozzles, one for the abrasive and another for the dopant. However, the CoBlast developers concluded that a system containing only one nozzle, where both the abrasive and coating materials leave through at the same time, yields the same results as a system with two separated nozzles for each component, reducing the cost (also only one powder feeder is required) and the complexity of the system, including the programming of the nozzles operation and movements [67]. The experimental setup used in this thesis has a one-nozzle configuration, as shown in topic 2.3, fig. 2.24. Typically reported process parameters in CoBlast are ejection distances, i.e., the distance between the nozzle and the substrate, in the range of 10-30 mm (although sometimes higher distances, up to 50 mm, are reported) and ejection pressures in the range of 4-6 bar. Comparing to pressures such as 35 bar, as in the CGDS process (fig. 1.35), it can be seen that CoBlast takes place at much lower pressures. Regarding the choice of abrasive material, Alu is commonly used due to its well-known superior mechanical properties and also because it is bioinert, thus it will not lead to unwanted cytotoxic

reactions within the organism. It is to be noted that, as it will be shown, a small amount of Alu impregnation can occur within the coating.

One of the main advantages of the CoBlast is undoubtedly being a low-temperature deposition process, taking place practically at RT. Fig. 1.39 shows a thermal analysis image of the CoBlast process during deposition on a Ti-6Al-4V metallic substrate [66]. The process parameters are a blast distance of 20 mm, ejection pressure of 5.8 bar for Hap and 4.2 bar for the abrasive (Al), a travel speed of ~ 10 mm/s and a raster offset of 2 mm (offset is defined as the distance between adjacent blast scannings, i.e., imagining a square substrate, the nozzle would make one scan along one dimension, move 2 mm to the side, make another scan, until all the surface is covered). Sometimes different pressures are used for the dopant and abrasive when a two-nozzle configuration is used. However, there are reports where the same pressure is used, and, in a one-nozzle configuration, the same pressure has necessarily to be applied. In fig. 1.39, the blast-zone and the deposition track are visible and distinguishable by the different temperature values. The average maximum temperature, which occurs in the blast zone, was 35 ºC, and sometimes the temperature would increase to a maximum value of 47 ºC [66]. It is clear that the process temperature of CoBlast is much lower in comparison to other processes such as APS or even CGDS.

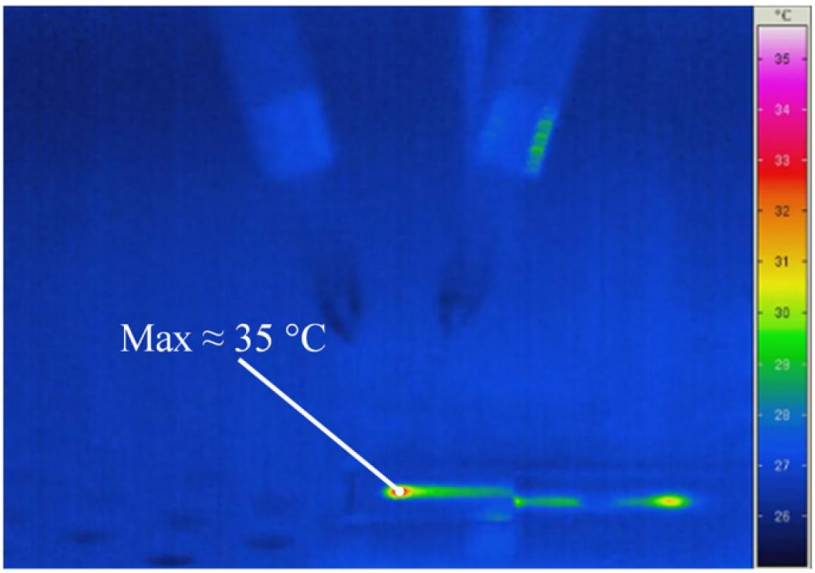

Figure 1.39 Thermal analysis image of the CoBlast deposition process (during deposition) [66].

An importance advantage concerning the low process temperature is the preservation of the substrate properties. As discussed in the historical background, topic 1.1.4., metals like copper, bronze and gold became progressively replaced by Ti and Ti alloys, due to their low success rates. Currently, as defined by ASTM International, six classes of Ti and Ti alloys may be considered as materials for orthopaedic implants: four classes of commercially pure Ti (CpTi) and two Ti alloys. Regarding the CpTi, the physical properties will differ according to the residual oxygen in the metallic matrix and four classes are distinguished: classes 1, 2, 3 and 4. Besides oxygen, the CpTi also contains trace amounts of carbon, hydrogen, iron and nitrogen. The concentration of these elements increases with the increase of the class number, and their particular composition can be consulted in reference [68]. The two Ti alloys most commonly applied in orthopaedic applications are the Ti-6Al-4V and the Ti-6Al-4V (ELI – extra low interstitial alloy) alloys. These alloys can exist in three structural forms, α, β and α-β, and their proportion will depend on the elements in the alloy: aluminium is an α-phase stabilizer, increasing the mechanical resistance and decreasing the density, while vanadium is a β-phase stabilizer, so that it exists as a combination of α and β phases (α-β), providing the alloy mechanical strength [68, 69]. The mechanical properties of all the CpTi and Ti alloys can also be consulted in reference [68]. The selection of which material to use, by the clinicians, will depend on the patient history of parafunctional habits and on the dimensions of the implant: small diameter implants with thin walls will require higher-strength materials [68]. CpTi class 2 and the Ti-6Al-4V alloy are clearly the most commonly applied implant materials in orthopaedics. Proceeding with the CoBlast discussion, its low temperature prevents any change on the Ti and Ti alloys properties. However, in APS, for example, the substrate is subjected to high temperatures (commonly between 400 - 500 ºC) and temperature gradients, which are reported to change the proportion of α and β phases at a superficial level, therefore potentially worsening the mechanical properties at the coating/substrate interface, or, at least, adding some degree of uncertainty in the final product. These problems may be aggravated for low mass implants, like dental implants, where the low mass to volume ratio hinders heat dissipation [66].

Regarding the choice of abrasive material, Alu and sintered Hap (also known as MCD) are reported for CoBlast Hap surfaces. Fig. 1.40 shows SEM micrographs revealing the surface morphology of CoBlast Hap coatings, using MCD and Alu as abrasives, and of a PS deposited Hap coating. Additionally, a topographical line profile for each surface is presented. The CoBlast deposited coatings present similar morphologies regardless of the chosen abrasive material. The line profiles are similar. Contrarily, the APS coating reveals a much rougher surface morphology, including visible cracks as highlighted by the arrows in fig. 1.40. Moreover, higher magnification micrographs of the APS deposited coating revealed a glassy appearance, suggesting that a significant melting of the Hap powder had taken place during deposition [66].

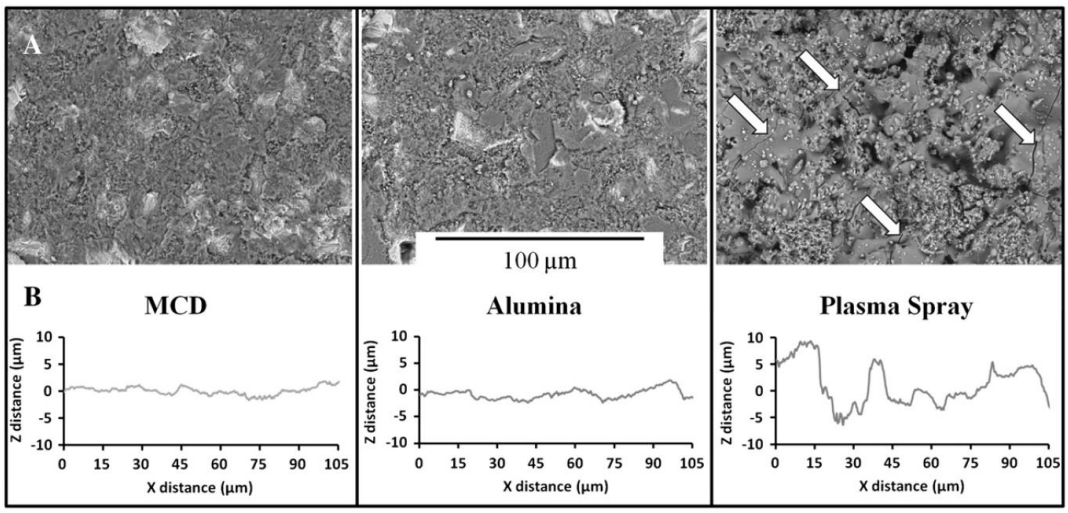

Figure 1.40 (A) - SEM micrographs revealing the surface morphology of CoBlast and PS Hap coatings. The arrows point out cracks in the APS deposited coating (scale bar is 100 µm). (B) - Topographical line profile for each surface [66].

The arithmetic average roughness (R_a) values presented in fig. 1.41 corroborate the topographical line profiles of fig. 1.40. The R_a values are presented for the Hap surface and the metallic substrate surface after the coating removal. It can be seen that the choice of abrasive material in CoBlast has statistical influence in the R_a values: a change in the abrasive type from MCD to Alu yields an increase in R_a from 0.84 to 1.31 µm, which is

attributed to the harder Alu particles. We highlight that the average grain size of both the MCD and Alu powders used in the cited report is very similar, around 100 μm, and differences in the R_a values are explained by differences the mechanical properties of the materials and by kinetic energy considerations, since the mass transported per particle is different due to their different density values and not due to their different size.

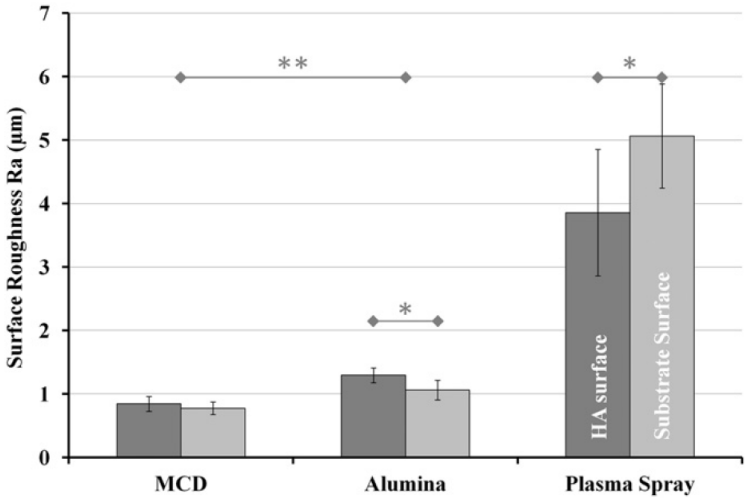

Figure 1.41 Arithmetic average roughness (R_a) of CoBlast and PS Hap coatings. The R_a values are presented for the Hap surface and the metal surface, after the coating removal [66].

Lastly, to finish with the report under analysis, fig. 1.42 presents SEM cross-sectional micrographs of the Hap/Ti alloy interfaces for both the CoBlast and APS processes. The PS coatings have an average thickness of about 26.9 μm, while the CoBlast coatings have an average of 2.5 μm. The cross-sectional micrograph of the APS coating also shows the presence of cracks, which go deep down to the interface, a factor known to cause a deterioration of the coating mechanical properties and potentially unpredictable high dissolution rates, due to an increase in the surface area exposed to the physiological conditions [66]. This problem can be aggravated when other, more soluble calcium phosphate-based secondary phases (β-TCP, TTCP, etc.) are present within the coating, as it can be the case of APS coatings. The same type of morphology and cracks in APS Hap coatings can be found in other reports [70]. The authors also detected the presence of Alu particles beneath the Hap coating [66]. The reason for the presence of Alu particles at the substrate/coating interface is that PS requires *a priori* surface treatment where surface

roughness is created in the metallic substrate in order to promote mechanical interlocking (also known as mechanical anchoring) between the coating and the substrate, therefore increasing the mechanical adhesion. This surface treatment, known as grit blasting, involves blasting the substrate surface with large abrasive particles, typically Al, with sizes between ~ 200 - 400 mm (sometimes the Alu used in grit blasting has a relatively large size distribution) [71]. Grit blasting will always leave grit residues on the surface, which may affect factors such as diffusion between substrate and coating, wetting properties of the powder droplets on the substrate and thermal stresses due to thermal expansion coefficient mismatch between the grit and the metallic matrix [71]. The amount of grit residue on the surface increases with the increase of blasting time [71].

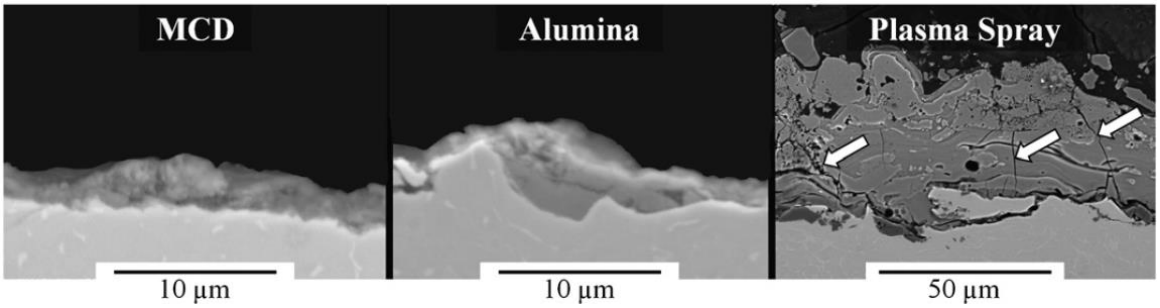

Figure 1.42 SEM cross-sectional micrographs of the Hap/Ti interfaces for both the CoBlast and APS processes. The arrows point out cracks in the APS coating. The scale bars are 10 μm for CoBlast and 50 μm for APS. The micrographs relate to the samples in fig. 1.40 and fig. 1.41 [66].

In another report, the influence of two abrasive materials on the deposition of Hap onto a Ti substrate, using CoBlast, was studied. Additionally, PS coated samples were also studied and considered for comparative purposes [72]. The Hap and abrasive material were projected in the same stream through a single nozzle onto the same region of the substrate, with a jet pressure of 5.5 bar, distance of 50 mm from the substrate, travel speed of 13 mm/min and an offset of 4.5 mm. The PS samples were provided by a specialized company. It is relevant to inspect both XRD diffractograms presented in the report under analysis. Fig. 1.43 depicts, in the left, XRD diffractograms of the as-received Hap powder, the

sHa/HA (sHA - sintered Hap, as labeled by the authors) and Al_2O_3/HA CoBlast surfaces and the PS surface. In the right, XRD diffractograms of the supplied class II CpTi and the modified substrates, after removal of the Hap and PS coatings via acid etch, are presented [72]. It can be seen in fig. 1.43, in the left, that in the PS coating an amorphous halo is present, and peaks assigned to β-TCP are detected, due to the high temperature and temperature gradients characteristic of the process, as explained previously in topic 1.2.3. The CoBlast coatings, on their turn, do not exhibit an amorphous halo and no secondary phases are detected, as expected. Concerning the diffractograms in the right of fig. 1.43, the substrates blasted with Alu both contain peaks assigned to Al_2O_3. The intensity of the Alu peaks is larger for the PS coatings compared to the Al_2O_3/HA CoBlast coatings, indicating a higher amount of Alu impregnation in the PS substrate [72].

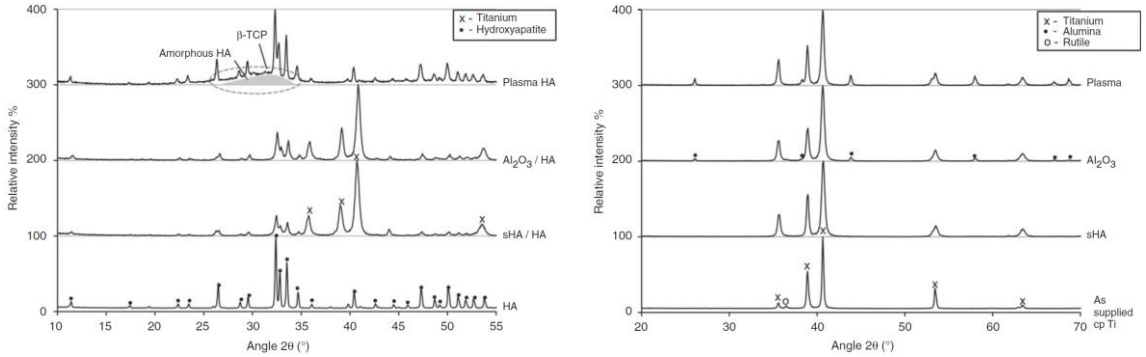

Figure 1.43 In the left: XRD diffractograms of the as received Hap powder, the sHa/HA (sintered Hap as abrasive) and Al_2O_3/HA CoBlast surfaces and the PS surfaces. In the right: XRD diffractograms of the supplied class II CpTi and the modified substrates after removal of the Hap and PS coatings via an acid etch [72].

Fig. 1.44 shows the R_a values of the Hap surface and the metallic substrate surface after coating removal [72]. It is clear that compared to the as supplied CpTi, the R_a values increased after the CoBlast and PS processes. In this case, the R_a values for the CoBlast samples are larger than those in fig 1.41, which is a consequence, in part, of the chosen process parameters. It seems to be lacking in the literature studies providing an overview of the influence of the CoBlast process parameters on some properties of the final

substrate/coating system, not only of intrinsic CoBlast process parameters, such as blast pressure and distance, but also of extrinsic process parameters, such as the mass ratio between the abrasive and the dopant. This thesis addresses some of these problems. Proceeding with the analysis of fig. 1.44, and also considering fig. 1.41, the CoBlast coatings tend to present the same R_a values for the coating surface and the disrupted surface, i.e., the roughness of the disrupted substrate surface is transferred to the surface of the coating. In PS the behaviour is different. Again, as in fig. 1.41, the Al_2O_3/HA samples have larger R_a values compared to sHa/HA.

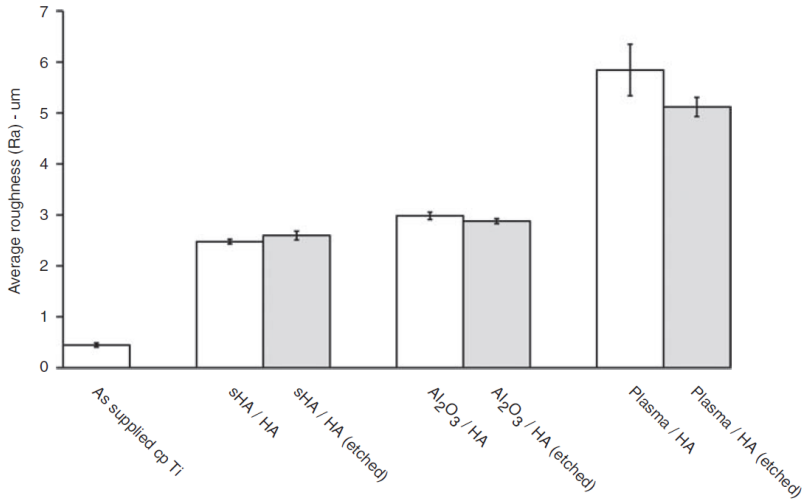

Figure 1.44 Effect of the abrasive material on the coating and substrate surfaces roughness, for both CoBlast and PS processes [72].

The thickness of the CoBlast samples is much lower than the PS samples, as Fig. 1.45 testifies [72]. The CoBlast samples have average thicknesses lower than 10 μm, while the PS commercial coatings have typical thicknesses 50-100 μm range. In CoBlast, the reported thicknesses of the Hap coatings are usually below 5 μm, in the 2-5 μm range, and they are dependent on the chosen process parameters, abrasive/dopant mass ratio, etc. It is however independent of the blasting time, because, since it is a process characterized by a balance between abrasion and deposition, increasing the blasting time and additional passes through the same region will only remove the previously deposited Hap and deposit new Hap, while the thickness will only be modified marginally [66, 72].

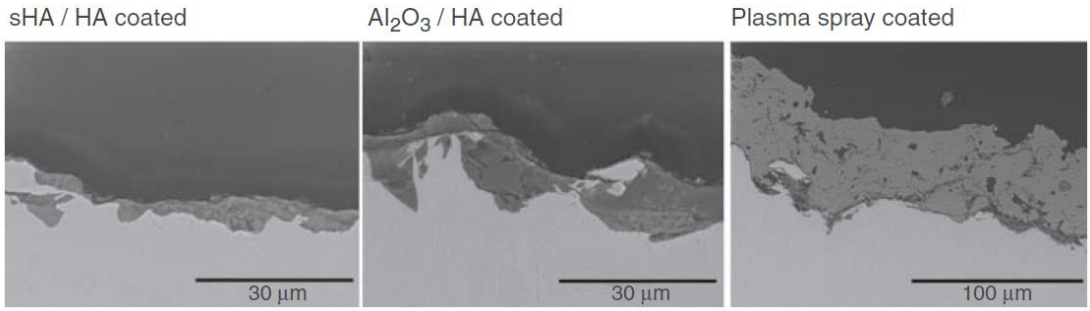

Figure 1.45 SEM cross-sectional micrographs of the sHA/HA, Al_2O_3/HA and PS samples, related to fig. 1.43 and fig. 1.44 [72].

We have discussed before that the PS process produces significant changes in the metallic substrate, in the case of Ti alloys, for example, changing the proportion between the α and β phases at a superficial level. The term "superficial" is not the most accurate since the modifications go to a depth of many dozens of micrometers. Fig. 1.46 displays SEM cross-sectional micrographs showing the effect of the blasting media on the CpTi class II substrates microstructure after coating removal by acid etch [72]. As a small note, the microstructure of CpTi is characterized by equiaxed α grains. The plasma samples revealed the presence of a heat-affected zone (HAZ, as identified in fig. 1.46) which extends to a depth of about 60 µm. The HAZ encloses two regions: a severely deformed surface layer and a region containing coarse back-transformed α grains. Back-transformed means that they form again from β grains, which, in their turn, form because PS is able to heat up the Ti above the β phase transition temperature (882 ºC). After the HAZ, the CpTi class II retains its microstructure. The formation of back-transformed α grains is reported to be associated with the formation of α-case Ti, an oxygen-enriched surface phase, hard and brittle, which may form when the Ti is heat-treated in a normal atmosphere. Due to its poor mechanical properties, if present, the α-case should be removed before putting the metallic part in service, otherwise the risk of delamination is greatly increased. With regard to the CoBlast samples, a region characterized by gross deformation of the grains, which shows the presence of twins, as shown in fig. 1.46, is observed. The formation of twins is stimulated by a high strain shock loading and relatively large grain size. The depth of the microstructure change is dependent on the abrasive material. While the depth of microstructure change for the substrate blasted with sHA is about 25 µm, the depth

increases up to 35 μm for the substrates blasted with Al_2O_3, which is explained by differences in the mechanical properties and kinetic energy of the particles bombarding the substrate, Al_2O_3 has a higher abrasion power than sintered hydroxyapatite.

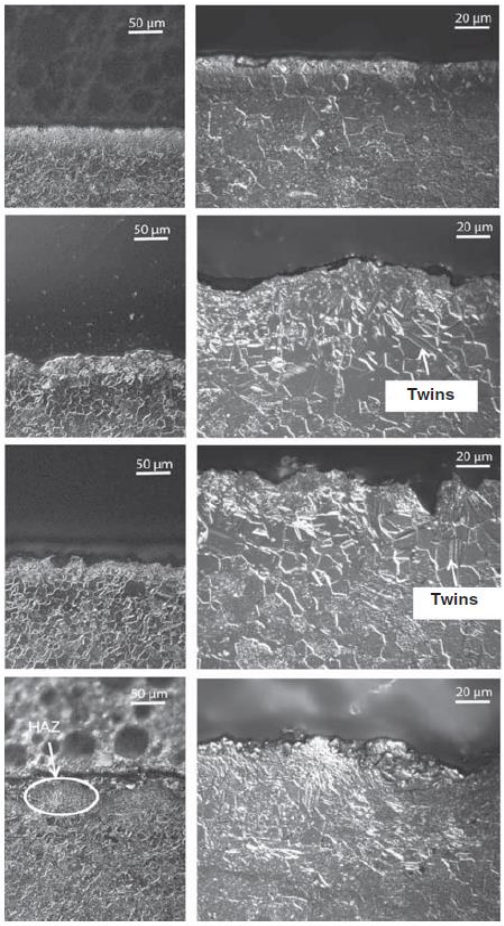

Figure 1.46 SEM cross-sectional micrographs showing the effect of the blasting media on the CpTi class II substrates microstructure, after coating removal by acid etch. The blast media include alumina and sintered Hap (sHA, as labeled by the authors) for the CoBlast process. The micrographs relate to the samples in figs. 1.43, 1.44 and 1.45. The plasma samples revealed the presence of a heat-affected zone (HAZ, as identified in the figure) [72].

We shall focus now on the mechanical properties of the CoBlast Hap coatings, by addressing some tensile bond strength and scratch tests reported in the literature. The methodologies behind these processes and some important concepts regarding mechanical properties are discussed in chapter 2, section 2.4. The adhesion between the coating and the substrate is a fundamental property when considering orthopaedic applications. Its importance justifies the existence of ASTM standards that regulate minimum limits for the adhesion magnitude. Specifically, the ASTM F1147 defines, for Hap coatings on metallic substrates, that a minimum value of 15 MPa is required for the static tensile strength. For the static shear strength, there is no particular requirement, although there are some guidance lines provided by ASTM F1044 and FDA. O'hare et al. performed a comparative

study regarding two different approaches to produce a Hap coating on a metallic alloy: the CoBlast process and direct micro-blasting of Hap onto the metallic surface, i.e., simply bombarding MCD onto the metallic surface [61]. We will just address the mechanical characterization, nonetheless the CoBlast coatings revealed significantly better biological *in vitro* and *in vivo* results [61]. To coat the CpTi grade V substrates, the Hap powder was fed into one nozzle at a pressure of 6.2 bar and at a distance of 20 mm from the substrate, while the Alu abrasive, 100 μm in size, was fed into the second nozzle at a pressure of 6.2 bar and distance of 18 mm, both nozzles moving at a speed of 12 mm/s. The coating adhesion properties were determined by mechanical scratch testing, using a Teer Scratch tester equipped with a Rockwell ´C´ Spherical cone indenter. The scratches were conducted from an initial load of 5 N to a final load of 50 N, increased continuously along the length of the scratch. Fig. 1.47 shows optical images of the scratch tracks created in (a) the Hap micro-blasting coating and (b) the CoBlast coating [61]. Higher magnification images, highlighting a section of the track, are presented for both samples. Fig. 1.47(a) shows the Ti substrate all along the track, indicating that the tip broke near the start of the scratch. Contrarily, in the CoBlast sample, fig. 1.47(b), the Hap coating is observed all along the track.

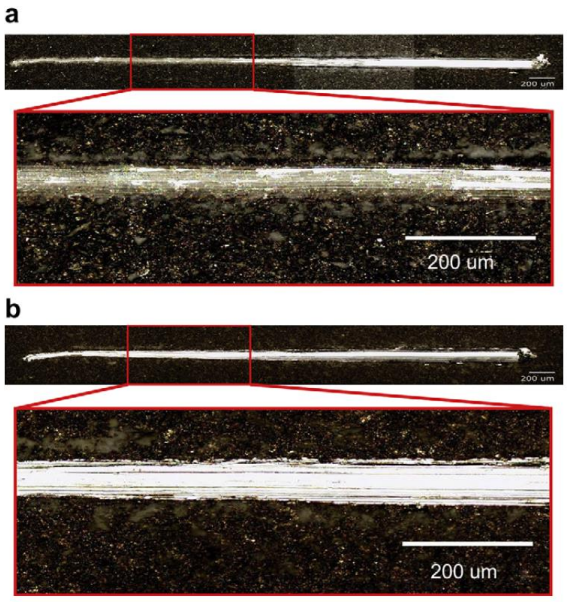

Figure 1.47 Optical images of the scratch tracks created in the (a) Hap micro-blasting coating and (b) CoBlast coating. Higher magnification sections are presented for both samples.

Fig. 1.48 presents EDX results showing the atomic percentage of elements detected at the start, middle and end locations of the scratch tracks displayed in fig. 1.47 [61]. The EDX analysis shows that the CoBlast sample exhibits significant levels of Ca and P in the

totality of the scratch length, while the micro-blasting sample, already in the middle, only shows residual levels of Ca and P. These results confirm that the CoBlast coating is strongly bounded to the Ti substrate, while the micro-blasting coating is poorly bounded to the substrate [61].

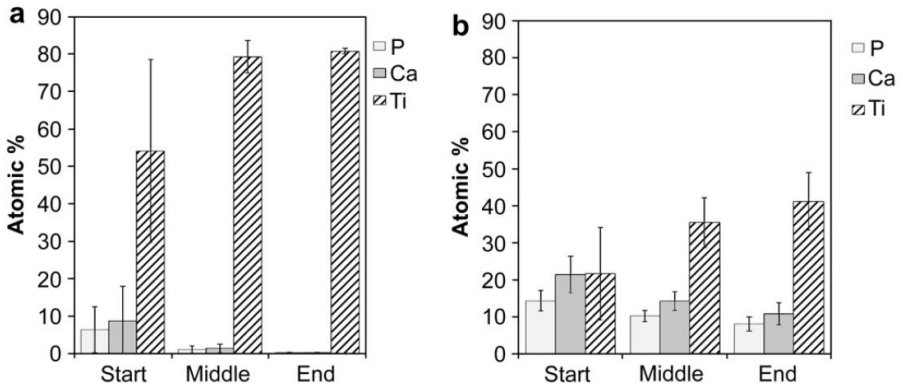

Figure 1.48 EDX results showing the atomic percentage of elements detected at the start, middle and end locations of the scratch tracks displayed in fig. 1.47. (a) Hap micro-blasting coating and (b) Hap CoBlast coating [61].

Generally, tensile adhesion testing according to standards ASTM C633 and ASTM F1147-05 is the most common procedure to determine quantitative adhesion values between the coating and substrate. However, many reports perform such adhesion testing according to variations of the methodologies proposed in the referred standards, because most of the times it is more convenient and cost-effective to perform such testing with other materials and equipment. In addition, such standards are established for materials intended for commercialization, thus companies have indeed to demonstrate that the requirements of such standards are met by their products. At an academic level, other kinds of methodologies to test the adhesion between coating and substrate are perfectly valid as the methodologies defined in the standards. Moreover, fatigue, scratch and pull-out testing, as well as wear resistance, are among the most valuable techniques that provide valuable additional information on the mechanical properties of the coatings. Regarding the report of Barry et al., i.e., the samples analysed in figs. 1.41, 1.42 and 1.43, for the determination of the adhesion of the Hap coatings to the Ti alloy substrates a modified ASTM F1147 tensile test was performed [66]. Epoxy coated 2.7 mm diameter aluminum studs were fixed and

cured to the Hap coatings for 1 h at 150 ºC and then left to cool at RT. The tensile tests were performed after a preload of 1-2 MPa was reached at load of 0.5 mm/min. The tensile bond strength (force/area) was determined by measuring the force required to remove the stud from the surface. The tensile bond strength test results were calculated based on an average of five separate tests. Fig. 1.49 displays, in the left, the test pins on the APS and CoBlast Hap coated samples after the tensile tests and, in the right, the tensile bond strength (MPa) values obtained for the CoBlast samples (MCD and alumina) and the plasma samples [66]. The bond strength is 6% higher for alumina compared to MCD, which is associated to the larger area for mechanical interlocking between the coating and the substrate, because, as we saw, alumina has a larger abrasion power compared to MCD. The plasma samples revealed very poor adhesion strengths, which is very surprising and not easily explainable, considering that the samples were supplied by a commercial provider, therefore, in the worst case, they should reveal values around the minimum required value of 15 MPa, mandatory for commercial products. Usually, the reported values for PS coatings are considerably higher, in the 20-30 MPa range. The cracks observed in the APS coatings, fig. 1.40, maybe a factor that contributes to the lower adhesion strengths. EDX measurements performed on the pull-studs after testing and removal revealed that all failures were adhesive, at the coating/substrate interface [66].

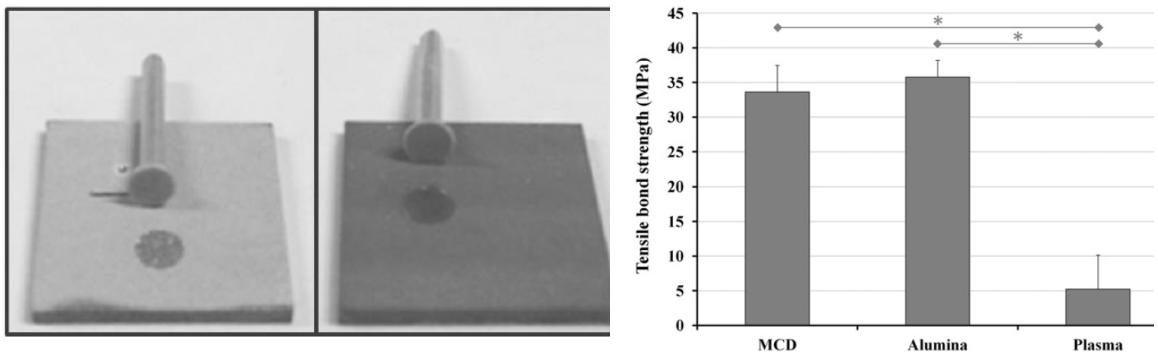

Figure 1.49 On the left: Test pins on the APS (left) and CoBlast (right) Hap coated samples after the tensile tests. In the right: Tensile bond strength (MPa) values obtained for the CoBlast samples (MCD and alumina) and the plasma samples [66].

Even higher tensile bond strength values are reported for CoBlast Hap coatings, in the 50-60 MPa range, whereby the superior adhesion of CoBlast coating is undoubtedly demonstrated [72].

Another advantageous characteristic of CoBlast is the possibility to coat complex structures while retaining its macrostructure. Fig. 1.50 displays an example of a Hap coated Ti grade V foam [73]. The microstructure of the foam was affected in a similar way as depicted in fig. 1.46, although the degree of alteration was lower because grade V Ti has better mechanical properties compared to grade II Ti, particularly, in what concerns the fatigue behaviour [73]. The APS technology is also able to coat complex geometries. Nonetheless, the large thickness of APS coatings, in the 50 - 100 μm range, makes them unsuitable for coating Ti foams without altering or occluding small pore sizes, while the CoBlast typical lower average thicknesses, in the 2 - 5 μm range, preserves the pore size of the material [73].

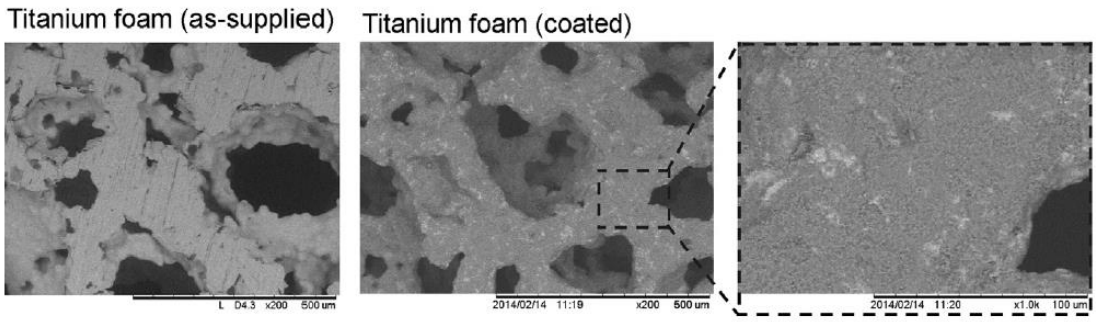

Figure 1.50 SEM micrographs of the surface of an as-supplied Ti foam and the same foam coated with Hap, using the CoBlast process [73].

To conclude this topic, a curiosity regarding CoBlast. Scheduled for launch in 2020, the Solar Orbiter spacecraft, property of the European Space Agency (ESA), will study the Sun at close range, closer than any previous mission. Needless is to say that things will get warm in there. The Solar Orbiter will study the Sun about forty-two million kilometers, closer than Mercury, and it will investigate the heliosphere and its connection to the internal dynamics in the Sun. Such high temperatures and radiation environment required ESA to find next-generation thermal protection systems for the craft's main heat-shield (3.1 x 2.4

m). Furthermore, such thermal protection has to be electrically conductive to avoid the build-up of space charge, which might cause a potentially destructive discharge to the spacecraft. CoBlast comes into play through ENBIO Ltd., which collaborates with ESA since 2011. From that collaboration, two functional coatings have emerged, SolarBlack and SolarWhite, both planned to be used in the Solar Orbiter and, of course, both applied through the CoBlast process. SolarBlack will be the first line of defense of the heat-shield, being described as a "CoBlast skin of black calcium phosphate, which will be applied to the outermost titanium sheet of the Solar Orbiter's multi-layered heatshield" [74]. Black calcium phosphate is actually a carbonaceous calcium phosphate material, known as bone char, produced via calcination of bovine bone under a reduced-oxygen atmosphere. The absence of oxygen during the calcination process avoids the oxidation and combustion of the organic hydrocarbon compounds in the bone matrix, resulting in the formation of carbon-rich ash with a black colour. Bone char was used in quite different and interesting applications, for example as a black pigment in the 30.000-year-old Chauvet Cave paintings in the south of France [75]. SolarBlack possesses high levels of both absorptivity and emissivity while maintaining the electrical conductivity and flexibility of the uncoated metallic substrates, being stable in a temperature range between - 150 up to 550 ºC [75]. SolarWhite is an inorganic coating with minimal absorption and high emissivity, stable in the same temperature range, but intended for applications in the Solar Orbiter which demand lower service temperatures [74].

1.4 Motivation

The penultimate section of chapter 1 is the motivation behind this work. The motivation of particular research work is always grounded on a state of the art and on particular problems that need to be solved, or certain properties that may be improved. Accordingly, we decided to address the motivation at the end of chapter 1. Although this section can be read and fairly appreciated as a "stand-alone" text, without requiring an in-depth knowledge of the state of the art, it will certainly be fully appreciated having in mind the information which was provided and discussed during the course of chapter 1.

We will adopt an analogous approach of that in topic 1.1.1: to present facts and statistics, more particularly, related to THR implants. We could also mention, for example, statistics related to total knee replacements, which follow the same trend of those of THR. Nevertheless, we will focus on THR data, having in mind that similar trends are observable for other orthopaedic implants.

One of the first questions that the patients who will receive a THR will ask their orthopaedic surgeon is the following: "How long will my hip replacement last"? The surgeon, in case of being informed about the statistics, will likely answer: "Expect it to last 15 years without any problem". The fact is that 90 to 95% of the THR's will last about 15 years without requiring any revision or corrective surgery, thus it is true that they are expected to last 15 years without any significant problem [76]. However, by the 20-year mark, 15% of the patients will need a corrective surgery. Recalling the numbers that we provided on topic 1.1.1, 15% is a very considerable number of people. But now the problem gets far worse: up to 35% of the younger patients in their 50's will require corrective surgery and sometimes even a third surgery. Moreover, this problem tends to increase every year. In some regions, the number of younger patients increased more than 200% in just 10 years (see the US case provided in topic 1.1.1). What does this mean? It means higher costs for patients and for the national healthcare systems. For example, in the US, in 2018, the average cost of a THR was about 40.000 US$. Actually, the US is one of the most expensive countries to perform a THR, while, on the other extreme, Poland was one of the cheapest countries in 2018, with an average cost of 5.500 US$ [77]. However, in Poland, it might be cheaper for those who have dollars or euros and are able to perform "medical tourism", but it is certainly not cheap and easily affordable for the average Polish citizen. Considering these data and statistics, a serious problem arises, primarily affecting the patients: while most health insurance plans tend to cover THR procedures, the same is not true for corrective/revision surgeries. Further, corrective surgeries are more complex and longer than the first surgery (known as the primary THR), and they enclose higher risks of complications, such as, for example, higher infection rates. Thus, revision surgeries are as expensive as the primary THR surgeries, potentially comprehending a heavy financial burden for the people.

A possible solution for this problem was discussed during the present chapter: it was found in the middle of the nineties that Hap is able to store a considerable electric charge density (reported values typically in the 10^{-6} – 10^{-5} C/cm^2 range) that significantly increases its bioactivity level, demonstrated both by *in vitro* and *in vivo* biological tests. As referred to in topic 1.1.1, when surgeons place an implant inside the body, in some regions there will be a small gap between the implant surface and the surrounding biologic bone. For a THR, the surgeons carefully open a cavity in the femur where they introduce the implant, thus most of the femoral stem component is surrounded by biologic bone. In the concrete *in vivo* study presented in topic 1.1.9, the negatively charged Hap surface took only two weeks to already achieve good gap filling and bonding, while the positive and non-charged surfaces were clearly much delayed. In summation, we are talking about reducing the probability of early post-operative failures and infections, improvement of short- and long-term stability and reduction of costs, for both the patients and the healthcare systems.

The biggest challenge is now upon us: how can we electrically charge these bioactive coatings? Classic poling contact methods, where electrodes are placed in pressure against the sample, are out of the question, because, as we have shown, these coatings are characterized by considerable surface roughness values, in the micrometric range. The deposition (sputtering for example) of electrodes is also out of the question, for two main reasons. Firstly, these materials will be applied *in vivo* inside the human body, and materials, where metallic electrodes were previously deposited in the coating, will certainly face big hurdles to be certified according to the ISO's and ASTM's standards that regulate this market. Secondly, taking into the account the temperatures at which the conventional polarization of Hap-based materials is usually performed, in the 250–500 ºC range, it is very likely that metallic atoms or ions may diffuse from the electrodes into the coating, so that, for example, a polishing step would not solve the problem. Considering, for example, PS coatings, they possess some cracks which may further promote the diffusion, despite the large thicknesses in the 50-100 μm range. In fact, this is an evidence that we verified during the course of this work: if, for example, a silver conductive paint is applied to a ~ 70 μm thick PS coating, at RT, the electrical resistance of the coating will drop off to the point of practically becoming shorted with the Ti substrate. Moreover, these metallic elements will

evidently interfere with the bioactivity *in vivo* by altering the expected cellular response to the biomaterial.

We believe that the answer to this technical challenge is a technique known as the corona triode charging. The main motivation behind this work is to be able to charge Hap coatings on Ti substrates using the corona triode and to demonstrate their superior bioactivity compared to non-charged Hap coatings. We also highlight all the innovative character of this work, and the challenges resulting therefrom, as a motivation fuelling this work. The concept of producing a stable electric charge density on bioactive coatings intended for orthopaedic applications, through a controllable and non-invasive approach, is indeed a novelty in the literature, and we hope that the first approach undertaken in this work will become a reference in this concept and technical challenge.

1.5 Objectives

The main objectives of this work are the following:

1. To develop "from scratch" a corona triode experimental system. The developed system must be able to allow the reversal of the discharge polarity, i.e., to produce a positive or a negative corona discharge, to allow the determination of the surface potential buildup of the sample, to allow the discharge temperature to be controlled and to maintain a low-humidity reproducible atmosphere.

2. To electrically charge Hap coatings on Ti metallic substrates, through the corona triode charging technique. A negative discharge will be used, taking into account the almost general consensus in the literature regarding the benefits of a negative charge density compared to a positive charge density. Two types of coatings will be tested: coatings produced by APS, provided to us by Ceramed, S.A. (Portuguese company), and coatings produced by us using the CoBlast process.

3. To perform *in vitro* biological tests on charged and non-charged Hap coatings in order to assess the influence of the stored charge density on the bioactivity level of the coatings. Accordingly, the intention is to perform SBF tests, in order to get information about the mineralization of bone-like CHap layers on the surface of the coatings and also cellular tests with osteoblasts. In the SBF tests, the temporal evolution of the Ca^{2+} and P^{5+} ionic concentrations and the pH value for increasing immersion times of the coatings in the SBF solution will be assessed. The cellular tests will include the assessment of the osteoblastic proliferation for increasing culture times in the charged and non-charged coatings. Additionally, the abundance and distribution of two proteins expressed by the osteoblasts in contact with the coatings will be visualized: the vinculin protein provides useful information regarding the adhesion level/"force" of the osteoblasts and the ALP (alkaline phosphatase) protein provides information regarding their differentiation stage.

.

Chapter 2 Experimental procedure and concepts

In the present chapter, it is not intended to describe common experimental techniques such as XRD, SEM-EDX, Raman, etc., since they are extensively reported and well known in the solid-state physics community. Instead, the focus is given to the essential, differentiating techniques used in this work, most notably the corona triode charging technique, the thermally stimulated depolarization currents (TSDC) measurements, the CoBlast deposition process and the tensile pull-off tests. Some theory supporting the discussed techniques is also included, so both theoretical and experimental aspects can be found in the same section, enriching the comprehension of the particular technique.

We also point out that one of the main objectives of this work is the development of a corona triode experimental system. We explain the development of the system in the present chapter, so actually, although this is an "Experimental details" chapter, the section (2.1), where we discuss the development of the corona triode, should be interpreted as belonging to a "Results and discussion" chapter, considering that the development of such system is undoubtedly one of the most important achievements of this work.

We also include in section 2.5 a description of the *in vitro* biological tests experimental protocol. This description is simplified and without some experimental technicalities, thus more adequate for those, like us, who are not experts on this type of biological tests.

2.1 The corona triode

2.1.1 Theoretical concepts

The roots and development of the corona triode charging technique are strongly connected to Brazilian researchers and universities, which in the seventies and the eighties contributed decisively to its development and understanding. Consequently, names such as R.A. Moreno, B. Gross (born in Germany) and later J.A. Giacometti became intimately associated with the corona triode [78-80].

The corona discharge is a stable, self-sustainable, atmospheric electrical discharge that occurs when a sufficiently high potential difference is applied between two asymmetric electrodes, such as a point and plane. DC corona voltages, in the 10 - 15 kV range, under a "normal" or low-humidity atmosphere environment, are frequently applied [81]. The threshold potential difference to start the corona discharge depends upon the availability of free electrons which are able to ionize the surrounding gas molecules, being around 5 kV in a "normal" atmosphere [82]. Two different regions are defined in a corona discharge: the ionization and drift regions. The ionization region is bound to a region close to the point electrode while the drift region extends to the plane electrode. Fig. 2.1 schematizes both regions, including the electric field and ion flow lines [82]. The drift region contains ionic charge carriers of one polarity, and their mobility is relatively low, in the order of a few cm^2/Vs. The current magnitude in the drift region is in the range of a few μA, for potentials in the 10 - 15 kV interval. The corona current always increases with the increase of the corona potential (the potential applied to the point electrode), making the discharge controllable and therefore applicable to generate thermalized ions in order to charge dielectric samples [82].

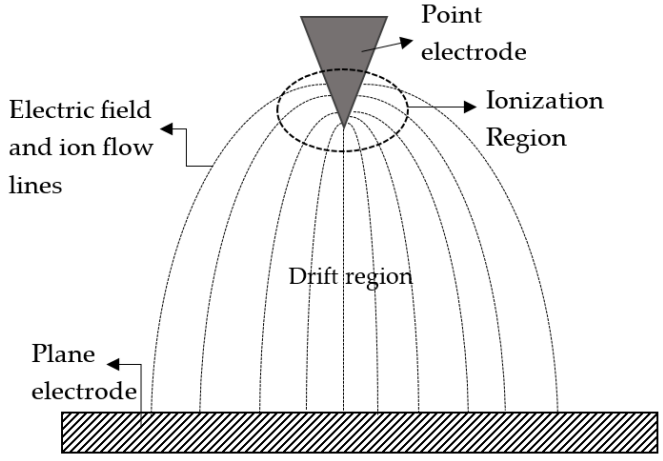

Figure 2.1 The corona discharge on a point and plane electrode system. Two regions are defined: the ionization region, confined close to the point, and the drift region, extending up to the plane electrode. Adapted from [82].

Fig. 2.2 displays a model of positive corona discharge (the sample thickness is exaggerated in this figure) [83]. The corona plasma region, which contains the ionization region, is maintained by processes such as electron and ionic collisions and by photo-ionization. The drift region contains ionic species of the same polarity, which are driven towards the sample covering the grounded electrode. The drift region may also contain

neutral species. In negative corona discharge, in part, electrons are generated by photoemission at the point electrode and captured to form negative ionic species. A very important feature of the corona discharge is that the thermal energy of the ions in the drift region reaching the sample is comparable to that of the environment. For this reason, these ions do not penetrate the sample or damage the surface, they just transfer their excess charge to the surface of the sample [84].

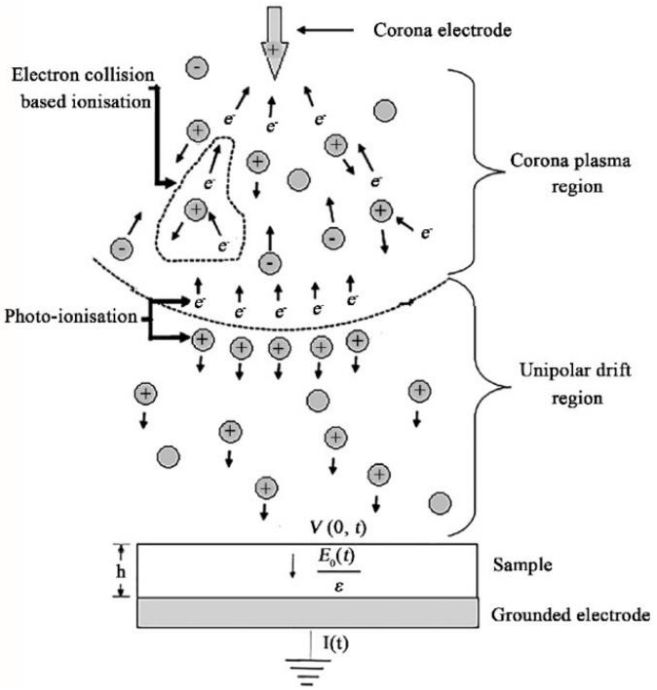

Figure 2.2 Model of a positive corona discharge. The discharge comprises two main regions: the corona plasma and the unipolar drift regions. The plasma region includes the ionization region. The sample thickness is exaggerated in this figure [83].

The ionic species generated in the positive or negative discharges in a normal atmosphere, determined using mass spectroscopy techniques, were found to be dependent on the relative humidity: in positive coronas, the dominant species have the generic chemical formula $(H_2O)_nH^+$, where n is an integer that increases with increasing humidity. For lower relative humidity levels other species will become dominant, such as $(H_2O)_nNO^+$ and $(H_2O)_n(NO_2)^+$. For negative corona discharges the most important ions are CO_3^- and the hydrated form $(H_2O)_nCO_3^-$, where n depends on the relative humidity [82].

The corona discharge has been widely applied in the electrical charging of polymer foils to be used in electret microphones, in the investigation of electret formation and charge stability in dielectric materials, especially in film/foil form, in the study of polarization phenomena in dielectrics and ferroelectrics, in electrophotographic processes, in the

charging of polymer wires to be used in electrostatic air filters and electrical separation of particles from gases (corona-based electrostatic precipitators have found widespread application in the treatment of contaminated gas in heavy industries) [82, 85].

The first corona systems only had two electrodes, the point and plane, and some information would be lost during the charging process, particularly the final surface potential of the sample. Taking into account this limitation and also the necessity of an improved charging current radial uniformity reaching the sample, the corona triode was developed and introduced in 1976 [78]. Three electrodes are used, instead of two, as the name suggests. The introduction of a metallic grid electrode between the point and the plane allows to follow the surface potential buildup of the sample during the charging process and to improve significantly the charging current radial uniformity below the grid [78, 84]. Fig. 2.3 depicts a scheme of a corona triode. One of the voltage sources is connected to the point electrode, and therefore is responsible for producing the corona discharge. The other source is connected to the metallic grid, controlling the grid potential. A picoammeter is connected to the plane electrode (usually also designated as the measurement electrode) to measure the charging current that flows through the sample. The guard copper ring prevents eventual surface currents from reaching the measurement electrode. The sample (the thickness is exaggerated) is placed on the top of the measurement electrode and the guard ring. Typical point/measurement electrode and grid/measurement electrode distances reported in the literature are in the range of 5-10 cm and 2-5 mm, respectively [79, 84].

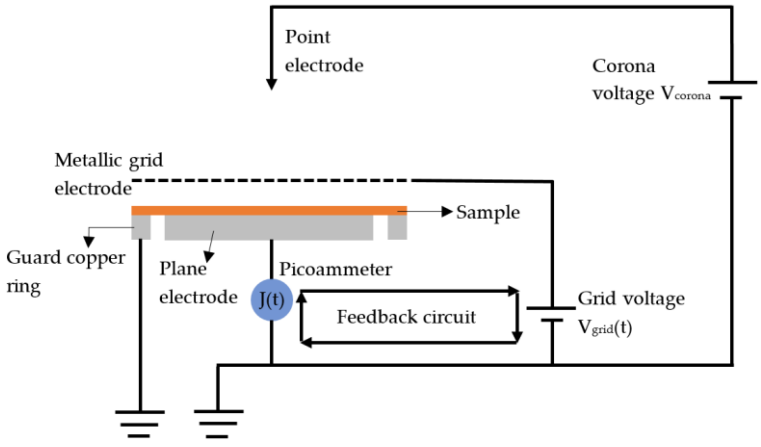

Figure 2.3 Scheme of a corona triode. As the name suggests, three electrodes are used: the point, grid and plane (or measurement) electrodes. Adapted from [84].

The theory behind this technique is now going to be presented, in order to understand the purpose of the "feedback circuit" in fig. 2.3. Consider fig. 2.4, which shows the air gap between the metallic grid and the sample, as well as the relevant physical quantities to be considered for this problem [85]. For simplicity purposes, the physical quantities are assumed to be independent of the lateral position coordinate in the air gap, depending only on the vertical coordinate x perpendicular to the sample and grid surfaces [85]. The air gap conduction current is due to the transport of a unipolar ionic charge density $\rho_{gap}(x,t)$, and the current density J(t) reaching the sample surface (J(t) = I(t)/A, where A is the sample area) is given by equation 11 [85, 86]:

$$J(t) = \left[v + \mu E_{gap}(x,t)\right]\rho_{gap}(x,t) + \frac{\varepsilon_0 \partial E_{gap}(x,t)}{\partial t} \tag{11}$$

where the term $v\rho_{gap}(x,t)$ is the current density due to gas movements produced by the discharge, known as corona wind and $\mu E_{gap}(x,t)\rho_{gap}(x,t)$ is the ionic conduction term, where μ is the mobility. The corona wind term has a small influence on the magnitude of J(t), the ionic conduction term is much more relevant. Equation 11 also shows that J(t) depends on the time derivative of $E_{gap}(x,t)$ multiplied by ε_0. This is actually what is known as a displacement current density: a time-varying electric field in a dielectric medium will produce a displacement current contribution. This was discovered by Maxwell and led to the generalization of the Ampère law, producing the well known as the Maxwell-Ampère equation, which is included in the Maxwell equations. The integration of equation 11 over the air gap thickness, d, yields equation 12 [85]:

$$J(t) = \frac{1}{d}\int_{L}^{L+d}\left[v + \mu E_{gap}(x,t)\right]\rho_{gap}(x,t)dx + \frac{\epsilon_0}{d}\frac{d}{dt}\left[V_{grid}(t) - V_{sample}(t)\right] \tag{12}$$

where $\Delta V_{gap}(t) = V_{grid}(t) - V_{sample}(t)$ is the potential difference between the grid and the surface of the sample [$V_{sample}(t)$]. Thus, $V_{sample}(t)$ is given by equation 13 [84, 85]:

$$V_{sample}(t) = V_{grid}(t) - \Delta V_{gap}(t) \tag{13}$$

Analyzing equations 12 and 13, it is reported that if the current density J(t) flowing through the sample is forced to be constant $J(t) = J_0$, a stationary state for the gap ionic charge density $\rho_{gap}(x,t)$ and for the gap electric field $E_{gap}(x,t)$ is reached, i.e., these quantities become

independent of the time [$\rho_{gap}(x)$ and $E_{gap}(x)$]. In such case, the second term in equation 12 is null and J_0 is equal to the medium value of the first term, the conduction current. Furthermore, $\Delta V_{gap}(t)$ becomes independent of the time. Equation 13 can be rewritten as [85, 87]:

$$V_{sample}(t) = V_{grid}(t) - \Delta V_{gap} \tag{14}$$

Note that in equation 14 ΔV_{gap}, is a constant. Experimentally, ΔV_{gap} is kept constant through the feedback circuit between the current flowing through the sample J(t) and the voltage applied to the grid. During the discharge, as the ionic species transfer their excess charge to the surface of the dielectric sample, its surface potential builds up. The feedback circuit forces J(t) to be at a constant defined value J_0 by increasing the voltage applied to the grid in order to follow the voltage build-up of the surface of the sample, so that ΔV_{gap} is constant. Therefore, during the corona charging, the potential of the surface of the sample can be directly calculated from the potential applied to the metallic grid through equation 14, it is just required to subtract the constant gap potential drop [84, 85].

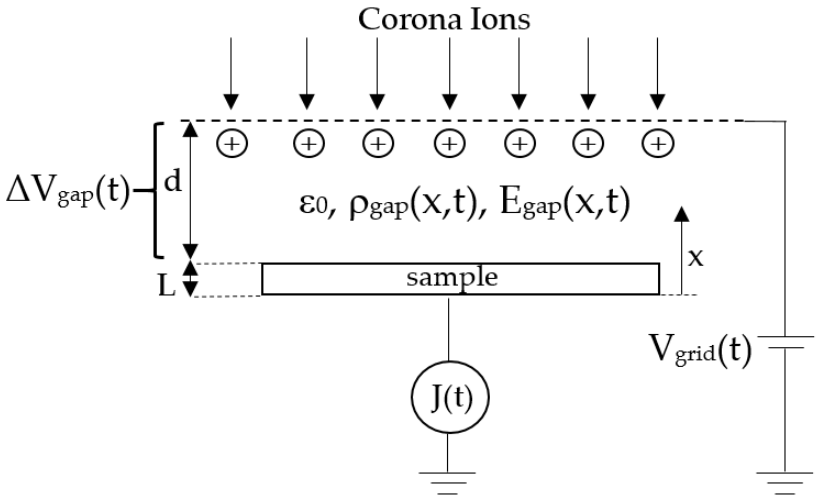

Figure 2.4 Scheme of the air gap between the metallic grid and the sample, with the relevant physical quantities. ε_0 is the vacuum dielectric permittivity, $E_{gap}(x,t)$ is the gap electric field, $\rho_{gap}(x,t)$ is the gap ionic charge density, L and d are the sample and gap thicknesses, $V_{grid}(t)$ is the metallic grid voltage and J(t) is the charging current density flowing through the sample. During the discharge, there is a potential difference between the grid and surface of the sample, $\Delta V_{gap}(t)$. Adapted from [85].

The ΔV_{gap} constant is determined by calibration curves, i.e., the air gap potential drop is determined for the different experimental conditions of the system: for example, the distances between point/measurement electrode and grid/measurement electrode, the polarity of the discharge, the discharge potential applied to the point electrode and the temperature and relative humidity of the system. The calibration curves consist of J_0 vs V_{grid} plots, which are performed without any sample covering the measurement electrode. In this situation, it is easy to see that $V_{grid} = \Delta V_{gap,}$ because there is no sample, the potential applied to the grid is exactly the gap potential drop. Two examples of calibration curves will be presented. Fig. 2.5 shows calibration curves for different grid to measurement electrode distances (note that in the plot, $V_s = \Delta V_{gap}$, they just use a different nomenclature) [85]. As it was stated, these distances are typically in the few millimeters range. It is visible that shorter distances give higher current densities, according to the Child's law, being the current approximately inversely proportional to d^2 [85]. Similar results are obtained for positive polarity.

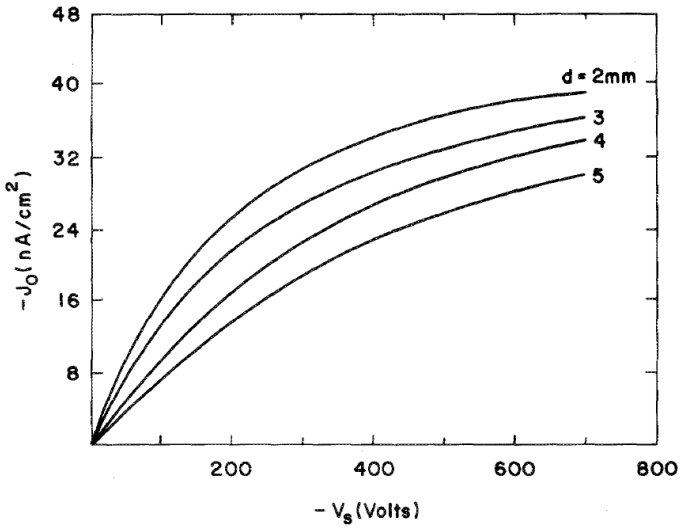

Figure 2.5 Calibration curves obtained for different distances between the grid and the measurement electrode, for a negative discharge polarity. In this plot, $V_s = \Delta V_{gap}$. The point to sample distance is fixed at 6 cm [85].

Fig. 2.6 displays calibration curves for different discharge temperatures [85]. The increase of the air gap temperature tends to decrease the ionic mobility. Similar results are obtained for positive polarity.

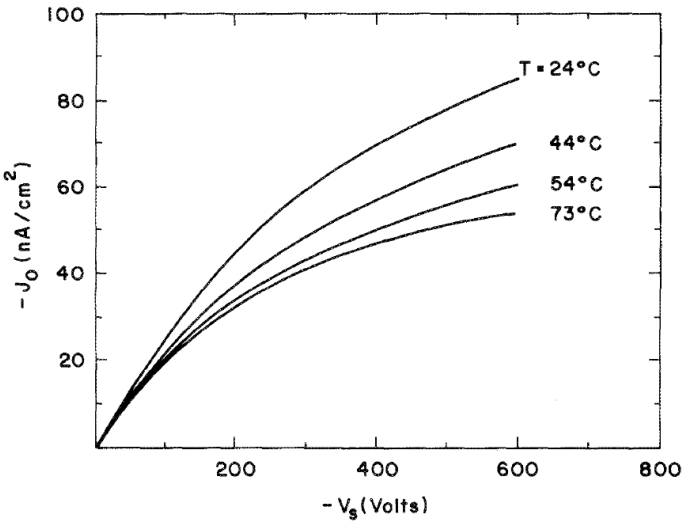

Figure 2.6 Calibration curves obtained for different discharge temperatures for a negative polarity (as in the case of fig. 2.5, $V_s = \Delta V_{gap}$). The corona point to grid and grid to sample distances are fixed at 6 cm and 3 mm, respectively [85].

Another important characteristic of a corona triode is the radial current-density distribution uniformity that reaches the sample, which, as mentioned, is one of the great advantages of the corona triode in relation to the conventional two electrode systems. This uniformity mainly depends on the point to samples distance, as demonstrated in the J.A. Giacometti report regarding this particular subject [79]. In the referred report, the corona system schematized in fig. 2.7 is presented. In the first phase, measurements were performed without the metallic grid, i.e., the configuration in the left scheme of fig. 2.7 was used. This allows to perform a study of the radial J(R) distribution for different D values, without the grid influence. In a second phase, the metallic grid was introduced, so that its influence on the current distribution can be understood. The system includes a moveable circular probe, identified as $J_P(R)$, which allows to perform the radial distribution measurements. As fig. 2.7 shows, the system includes an inner PVC cylinder, which is actually a quite uncommon feature. Most of the reported systems do not include this inner PVC cylinder. Or, in other words, the experimental evidence shows that an inner dielectric cylinder is not required to achieve very good charging current distribution uniformity profiles.

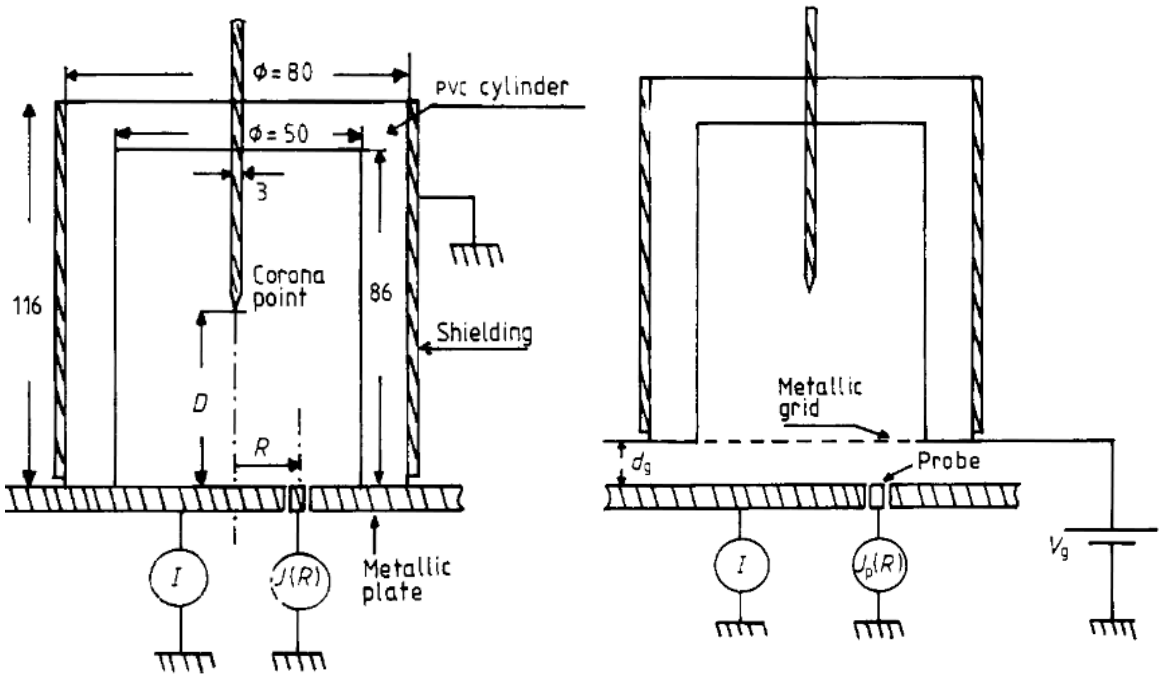

Figure 2.7 A corona triode system scheme. In this particular system, a moveable circular probe, identified as $J_P(R)$, was designed in order to obtain radial current density distributions of the current reaching the sample. The point/sample (D) and grid/sample (d_g) distances can be changed. The distances are in millimeters [79].

Fig. 2.8 shows the results of the J(R) versus D study, without the grid electrode. An important result of this study is that for D values equal or higher than the diameter of the cylinder (50 mm, see fig. 2.7) the current density distribution becomes independent of D, in such a way that, for different corona discharge potentials, it is possible to normalize the experimental curves to one characteristic shape, as fig. 2.9 demonstrates. This result continues to be valid if instead of the PVC cylinder we had a metallic cylinder. Thus, the results demonstrate that distances D equal to or higher than the cylinder diameter are preferred for the corona charging [79]. However, if the sample dimensions are small, distances smaller than the cylinder diameter can be perfectly used without having significant differences in the radial distribution of the current reaching the sample, as fig. 2.8 shows.

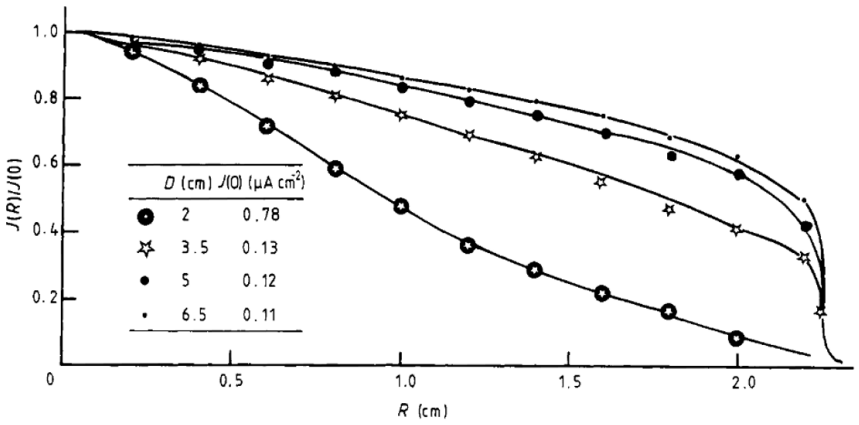

Figure 2.8 The radial distribution of the current density J(R) reaching the sample for different distances D. The experimental values are normalized by J(0), the current density for R = 0, where the current density is maximum [79].

Figure 2.9 Normalization of the experimental curves to a characteristic shape, for different corona currents I_c (which is the same as saying for different discharge potentials) [79].

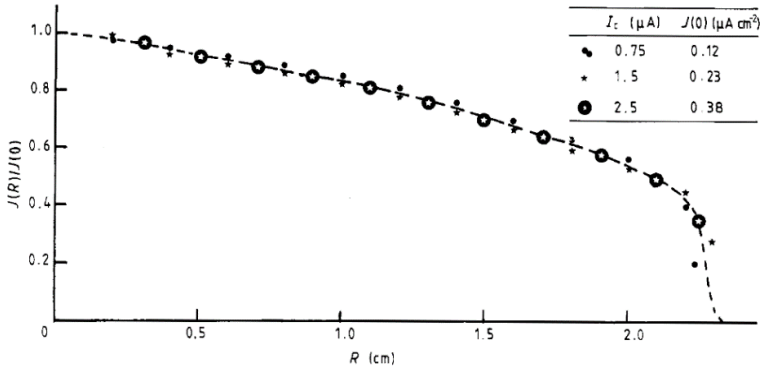

The samples charged with the corona triode present a very good uniformity of the surface potential, due in great part to the presence of the metallic grid electrode. Fig. 2.10 shows an example of a 20 μm thick polymeric sample charged up to a surface potential of 270 V, with a constant current density $J_0 = 1$ nA/cm^2 [79]. It is visible that the surface potential is almost uniform up to a distance of 2 cm, meaning that a 4 cm diameter region can be charged with very good uniformity. Since the cylinder has a diameter of 5 cm, it is normal for the uniformity to decrease near the edges of the cylinder.

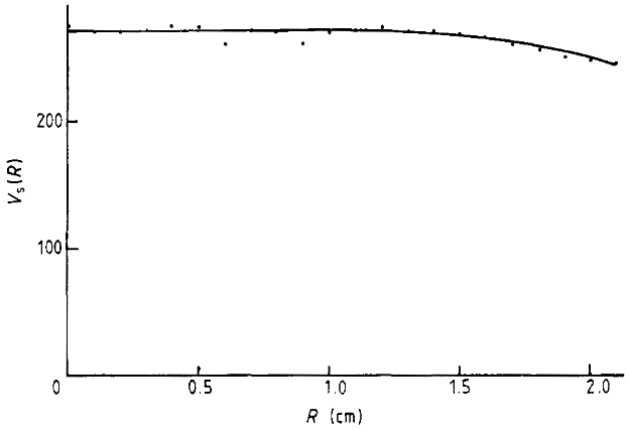

Figure 2.10 The surface potential radial distribution $V_s(R)$ for a sample charged with a constant current density J_0 = 1 nA/cm^2. The sample is a 20 μm thick polymer, polyethylene terephthalate (PET) [79].

Another important factor is the atmosphere relative humidity, which should be a variable to be considered in the determination of calibration curves. Nonetheless, if one finds a way to get a reproducible atmosphere the humidity can be ignored in the calibration curves since it would be similar for all the experiments. As it will be shown, in the system developed in this work, we achieve that by having placed a container with silica gel in an adapted furnace where the corona triode is inserted, yielding a low-humidity reproducible atmosphere.

Summing up, in a corona triode charging experiment the user chooses a constant charging current density J_0 (or current I_0) to charge the sample. Through the calibration curves, the user knows the constant value of ΔV_{gap}, for the defined charging current I_0 and for the particular experimental conditions. Therefore, the user can apply equation 14 to directly calculate and follow the potential buildup of the sample. The feedback circuit to maintain the charging current approximately constant at the defined value I_0 has to be programmed.

What are the advantages of the corona charging regarding conventional contact polarization techniques? Several can be mentioned: it does not require the deposition of an electrode on the sample surface exposed to the corona charges, it allows to polarize/charge samples up to higher surface potentials, even if localized dielectric breakdowns occur (because of the absence of two electrodes), it is a well-suited technique for large scale film charging/poling, it is possible to charge/pole samples with complex, non-planar geometries

(even materials with porosity) and it allows to control the polarity of the discharge and thus the sign of the injected charges in the sample [81, 87]. The avoidance of the deposition of an electrode in the sample surface exposed to the corona charges is a very important advantage regarding the potential application of this technique on the charging of bioactive coatings in orthopaedic implants. The strict regulations required to be complied for the introduction of a new implant in the medical market, as defined by the ISO and ASTM standards that regulate this market, could cause serious complications for the acceptance of electrically polarized materials where metallic electrodes had been previously deposited, even with a posterior electrode removal step, polishing for example. In contact polarization methods, Hap has to be heated up to considerable temperatures, typically in the 250 - 500 ºC range, as described in the state-of-art, chapter 1. Some diffusion of metallic atoms or ions from the electrode to the sample has to be regarded as a very likely possibility, and even if such diffusion does not occur into the bulk of the sample, a polishing step could not be enough to remove the contaminants, which could also interfere with the bioactivity and on the *in vivo* cellular behavior. Such an electrically polarized Hap coated implant would certainly face a high degree of resistance to be approved for marketing, contrarily to the corona charged Hap coated implant. Moreover, to conventionally polarize a Hap coated orthopaedic implant would be a daunting task, due to the simple fact that they are not flat surfaces, they have a considerable surface roughness in the few or dozen of micrometers range. Hence, the corona triode technique contains the requirements that confer it a strong potentiality to be applied in the orthopaedics and dental implantology fields.

2.1.2 Development of a corona triode

A corona triode system was developed "from scratch" in this work. The main requirements which we defined for our experimental system were to be able to polarize materials with a planar geometry (coatings, bulk samples with planar parallel faces - pellets, etc.), to allow the reversal of the corona discharge polarity, to be able to follow the surface potential buildup of the samples and to be able to change the discharge temperature. Furthermore, the system must be contained in a reproducible atmosphere, in terms of humidity, so that the discharges occur approximately in the same conditions Fig. 2.11,

shows 3D concepts of the developed corona triode. The right image displays a top view of the triode. It contains a central teflon lid, represented in blue, where the point electrode is inserted. The red, yellow, green and purple elements of the structure are made with stainless steel, including the three cylindrical support rods. The cylindrical body of the system, in yellow, has outer and inner diameters of 81 mm and 85 mm, respectively, with a 4 mm thick wall, and a height of 140 mm.

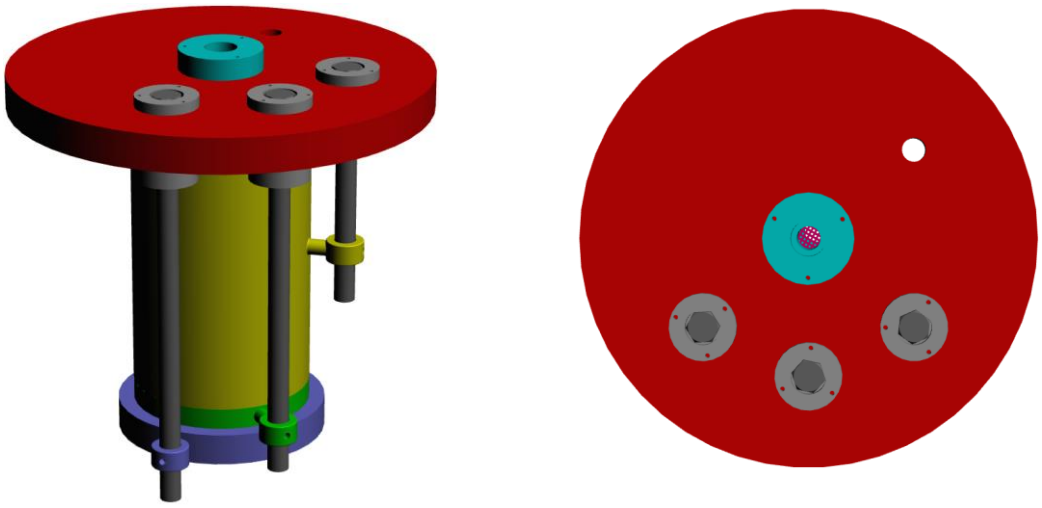

Figure 2.11 3D representations of the developed corona triode. In the right image, a top view of the corona triode. The metallic grid electrode is visible in this view.

The green component in fig. 2.11 is the metallic grid support plate, as highlighted in fig. 2.12. The dimensions are in mm. The metallic grid is placed and stretched in the support plate with the help of a metallic ring, which is not represented in fig. 2.12, but it can be seen in fig. 2.14.

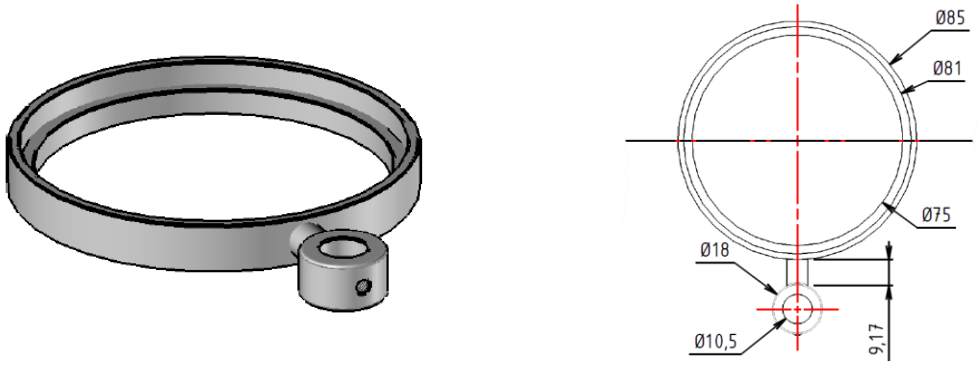

Figure 2.12 The metallic grid support plate, with the dimensions specified in mm.

The purple component in fig. 2.11 contains the teflon support plate for the measurement electrode and the sample (note that the purple structure in fig. 2.11 is metallic, which contains the sample holder in teflon, fig. 2.14 shows both components). Fig. 2.13 depicts this component together with two different perspectives, with the dimensions in mm. This teflon sample holder contains a central opening, 10 mm diameter, where the measurement copper electrode is introduced. The concentric hollow ring-shaped slit, with inner and outer diameters of 22 and 26 mm, is where the copper guard ring is placed, to prevent eventual surface currents from reaching the measurement electrode. In fig. 2.14 the teflon support plate can be seen, containing both the copper measurement electrode and the concentric guard ring. The sample is placed on the top of the measurement electrode in contact with the guard ring. Although not represented in fig. 2.13, there is a small hole that allows the connection of the guard ring to the ground. This hole is actually observable in fig. 2.14, in the metallic support plate (the purple component in fig. 2.11) where the teflon support plate is placed.

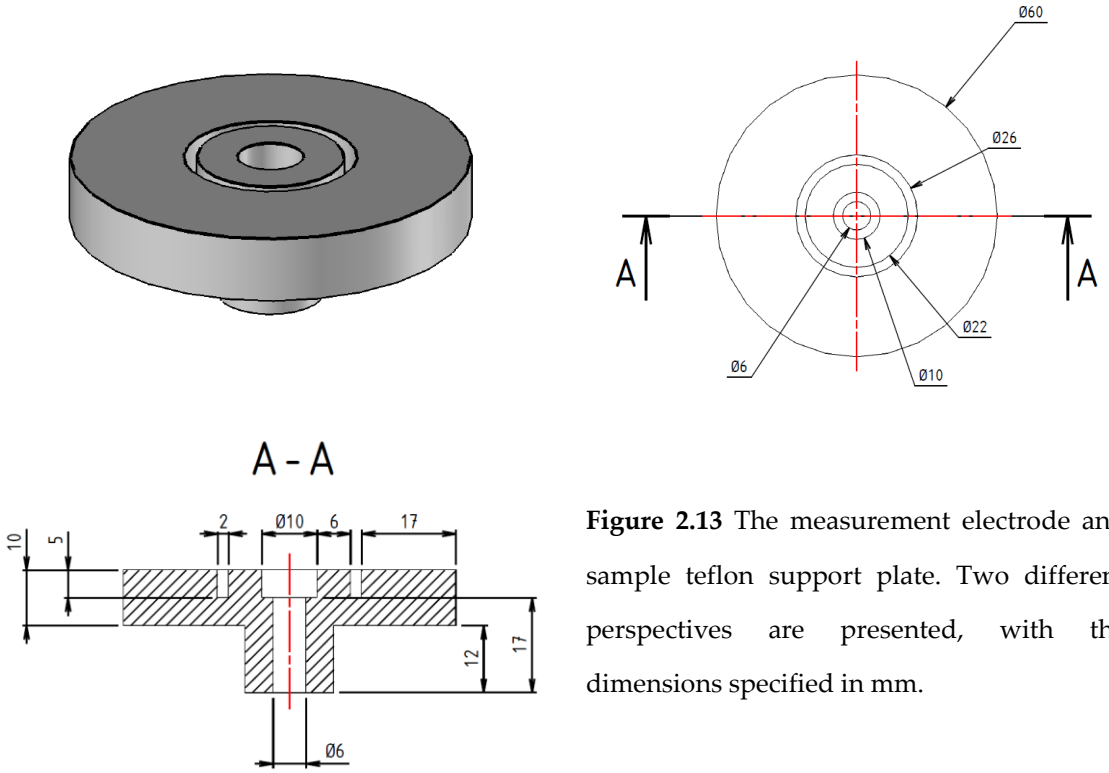

Figure 2.13 The measurement electrode and sample teflon support plate. Two different perspectives are presented, with the dimensions specified in mm.

Fig. 2.14 provides an overview of the corona triode individual components and of the assembled system. The metallic ring stretches the grid so that it is parallel relative to the measurement electrode surface. The grid is made of stainless steel and it has 40 mesh per inch (as defined by the supplier), with a wire diameter of 0.2 mm. One of the requisites of the grid is to have a considerable higher surface area than the sample, which is achieved by the mesh structure and the thin-diameter wire. The distance between the grid and the measurement electrode, without sample, is 5 mm. Since our Ti substrates have a thickness of 1 mm, the grid/sample distance is 4 mm (the coating thicknesses are in the micrometric range, therefore negligible compared to the Ti substrates thickness).

Figure 2.14 Photographs of the developed corona triode. In the left, the disassembled components can be observed. In the right, the assembled system.

The central teflon lid (the blue component in fig. 2.11), is actually a two-piece structure, allowing to introduce the discharge point electrode and close the lid, as fig. 2.15 depicts. The point electrode is a ceriated tungsten electrode (containing 2 wt% of cerium), 15 cm in length and 3.2 mm diameter (except on the tip, obviously). Ceriated tungsten electrodes are generally recommended for DC applications and offer higher chemical

stability and longevity compared to pure tungsten electrodes. Thoriated tungsten electrodes are also very popular, however, thorium is a radioactive element, and some precautions have to be taken by the user. Therefore, we opted for ceriated tungsten. The distance between the point and sample can be easily changed, by just controlling how deep the electrode is inserted in the teflon lid as the right photograph of fig. 2.15 shows. When the total electrode length is inserted in the lid, the distance between the point and the measurement electrode is 7 cm. Thus, the distance between point/sample is approximately 7 cm, disregarding the sample 1 mm thickness.

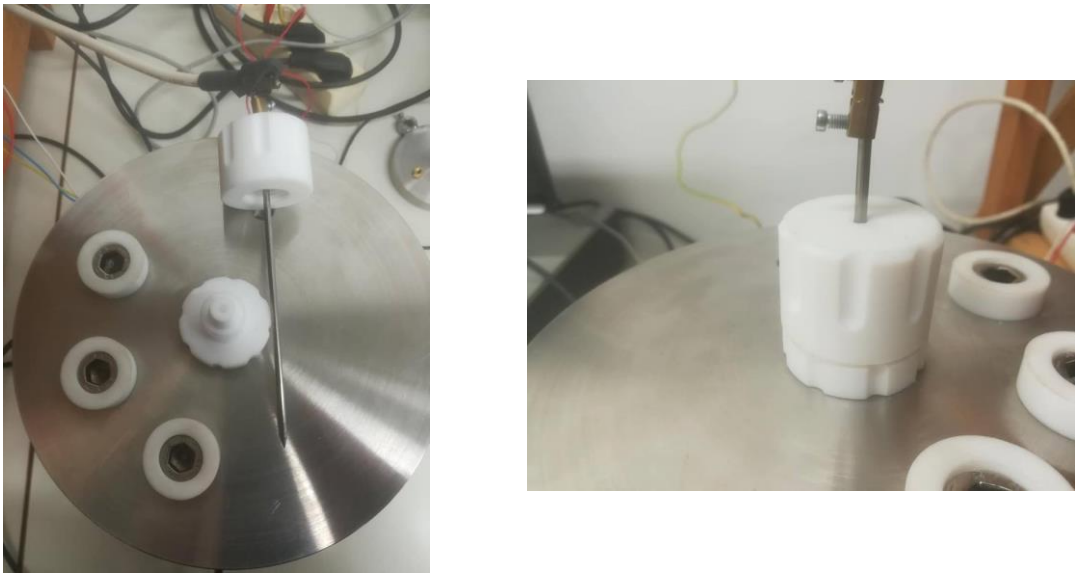

Figure 2.15 The central teflon lid is a two-piece structure that allows to introduce the point electrode and to close the lid.

On fig. 2.16 the metallic support plate (the purple component in fig. 2.11) for the teflon sample support plate, containing both the measurement electrode and the guard ring can be seen, in top and down views. The wire that is used to connect the guard ring to the ground is visible. In the down view, the screw-shaped base of the measurement electrode allows to make electrical connections, in this case, to the picoammeter, responsible for the measurement of the charging current, and to the grid voltage source.

Figure 2.16 Photographs showing top and down perspectives of the metallic support plate containing the teflon support plate for the measurement electrode and the sample.

The electrical equipment used in the corona triode system is shown in fig. 2.17. In (A), the Keithley 6485 picoammeter can be seen, responsible, as it was aforementioned, for the measurement of the charging current flowing through the sample. It is able to measure currents ranging from 20 fA to 20 mA. In (B), the Stanford Research Systems, model PS325 voltage supply is presented. It can apply DC voltages up to 2.5 kV, with a 10.5 mA current capacity and it is able to reverse the output polarity, allowing to control positive and negative corona discharges. This power supply is connected to the metallic grid, therefore being responsible for the grid voltage control. It is fundamental that both the picoammeter and the grid voltage source are able to be programmable, and in both cases, they can be connected to a computer through the GPIB protocol, for the feedback circuit software development. In (C), a Brandenburg 828-20 model, from the gamma series, high voltage supply is shown. This high voltage supply is able to apply positive DC voltages up to 30 kV, with a 3 mA current capacity. Finally, in (D), a Brandenburg model 807R, from the Alpha series, is shown. The 807R model is able to apply both a positive or negative voltage, up to 30 kV, with a 1 mA current capacity. The Brandenburg high voltage sources are used since the seventies, particularly in the corona triode literature that is cited in the present topic.

Figure 2.17 The equipment used with the corona triode system. (A) Keithley 6485 picoammeter; (B) Stanford Research Systems, model PS325; (C) Brandenburg model 828-20, from the Gamma series and (D) Brandenburg model 807R, from the Alpha series.

Fig. 2.18 presents an overview of the entire experimental system. We have adapted a furnace so that we can introduce inside the corona triode through the top. The maximum temperature that the furnace reaches is 300 ºC, but with our system, the maximum temperature we can reach is 200 ºC, because of the teflon components we have in our corona triode. Inside the furnace we use thermal resistant silicone electrical cables. Additionally, we have introduced a silica-gel container inside the furnace. We did some tests and we concluded that the silica-gel container allows to obtain a low-humidity, reproducible atmosphere so that we do not have to consider it for the calibration curves since all the discharges are performed in essentially the same relative humidity conditions. Measurements performed with a Fluke 971 Temperature and Humidity Meter show that

the relative humidity values of the system at 200 ºC (the defined temperature to charge our samples) are below 10%.

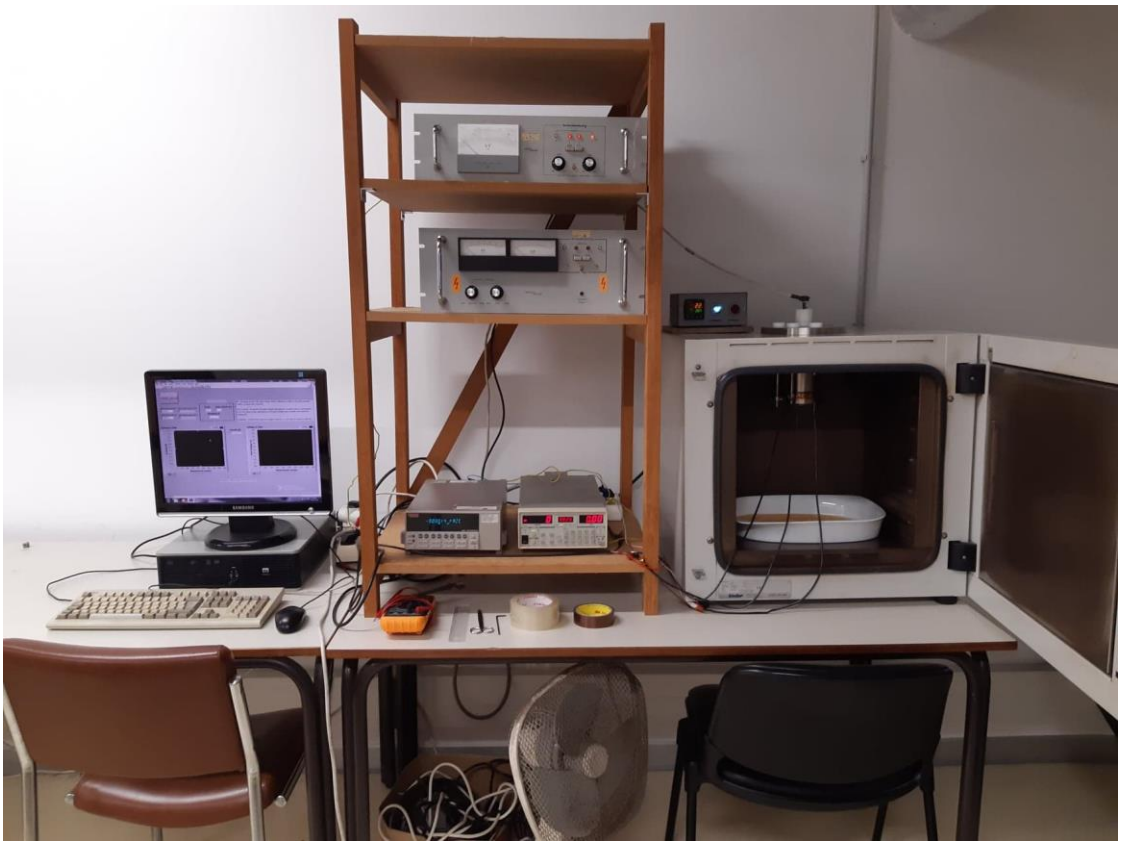

Figure 2.18 An overview of the experimental system. A furnace was adapted so that the corona triode can be introduced inside. Thermal resistant silicone cables are used inside the furnace. A silica-gel container is also placed inside the furnace, in order to obtain a low-humidity, reproducible atmosphere.

The picoammeter and the 2.5 kV voltage supply are controlled by a feedback circuit software developed for this purpose. As mentioned, both equipments are connected to a computer (visible on fig. 2.18) through the GPIB protocol. This feedback circuit tries to maintain the charging current flowing through the sample at a constant user-defined value by continuously updating the grid voltage. Logically, the user has to select a reasonable charging current value, it is important to have in mind the magnitude of currents which we are dealing with. When we discussed fig. 2.1, it was mentioned that typical current

magnitudes in the drift region are in the few μA range, for discharge potentials in the 10 - 15 kV range. When the metallic grid is introduced between the point and the plane, typical current magnitudes in the grid/sample air gap will be in the few nA up to dozens of nA, for the same discharge potential range, depending, obviously, on the grid potential. This gap current can also be increased or decreased according to the grid characteristics, most importantly the wire diameter and mesh spacing, which define the grid ionic transparency. The grid characteristics that we have selected for our corona triode are based on the literature. One very recent trend in the potential applications of the corona triode is related to thin dielectric films [88]. Classically, the corona triode has been applied in micrometric films, polymers primarily. Thin films normally have considerably higher capacitances compared to micrometric films, which means that higher current magnitudes in the grid/sample gap are required, otherwise the charging process may take a non-practical long time, larger currents are required compared to micrometric films. For such purpose, metallic grids with higher ionic transparencies are being researched, together with other approaches such as creating an electrostatic lens (by applying a potential to the cylindrical metallic structure, for example) to further concentrate the ionic charge density and increase the current magnitude [88]. Returning to the discussion about the feedback circuit, the user must, therefore, define a reasonable constant charging current value, commonly in the range of a few nA. Fig. 2.19 shows a screenshot of the user interface panel of the developed feedback circuit program. The control parameters, which must be defined by the user, are highlighted in the panel, including a brief explanation of these parameters in the text box. "I0" is the charging current, as above mentioned. "Vcte Control" is a parameter that controls the grid voltage adjustments. A small value (1 or 2) is recommended to allow a fine adjustment of the grid voltage and a smaller error interval around "I0". Finally, the "Sampling" parameter controls how fast the system responds, in other words, the time interval at which it reads the actual charging current value and adjusts the grid voltage. Usually, we define 1 or 1.5 seconds for this parameter. Two charts, "Current vs Time" and "Voltage vs Time" provide real-time information about the charging current value and the voltage applied to the grid. Note that, according to what we have discussed, the grid voltage is approximately equal to the sample surface potential minus a constant gap

potential drop, therefore the “Voltage vs Time” chart allows to follow the surface potential buildup in real-time, during the charging experiment. The user interface panel also includes a display “Current” which shows the charging current value and is continuously updated according to the defined “Sampling” value. In the end of the experiment, when the sample reaches the saturation surface potential, the user presses the “Save Data” button and a text file appears, containing three columns with the experimental data: the first column contains the time in seconds (the charging time, corresponding to the “Sampling” parameter), the second contains the correspondent charging current values and the third contains the correspondent grid voltage values. The user may subsequently save the text file wherever he wants. Additionally, when the “Save Data” button is pressed, the grid voltage is kept fixed at the surface saturation potential value, so that when the sample is cooled down to RT, both the corona discharge and the grid voltages are fixed. This ensures that the stored charged is “frozen” during the cooling step, which should be as fast as possible, as discussed in section 2.2. To increase the cooling rate, we use a large fan: we open the furnace door, as it is visible in fig. 2.18, and we place the fan in front of the furnace, directed to the corona triode. In about 25 minutes, the temperature in the sample region will drop from 200 ºC down to about RT. Most of the time to reach RT is spent in the low-temperature range, the cooling rate is much faster in the high-temperature range, as expected. Similarly, the temperature versus time profile of a furnace that is cooling based only on its thermal inertia will be an exponential decay where the cooling rate is faster in the high-temperature range and much lower in the low-temperature range. If we did not use the fan, the time required to reach RT would be around 4 hours.

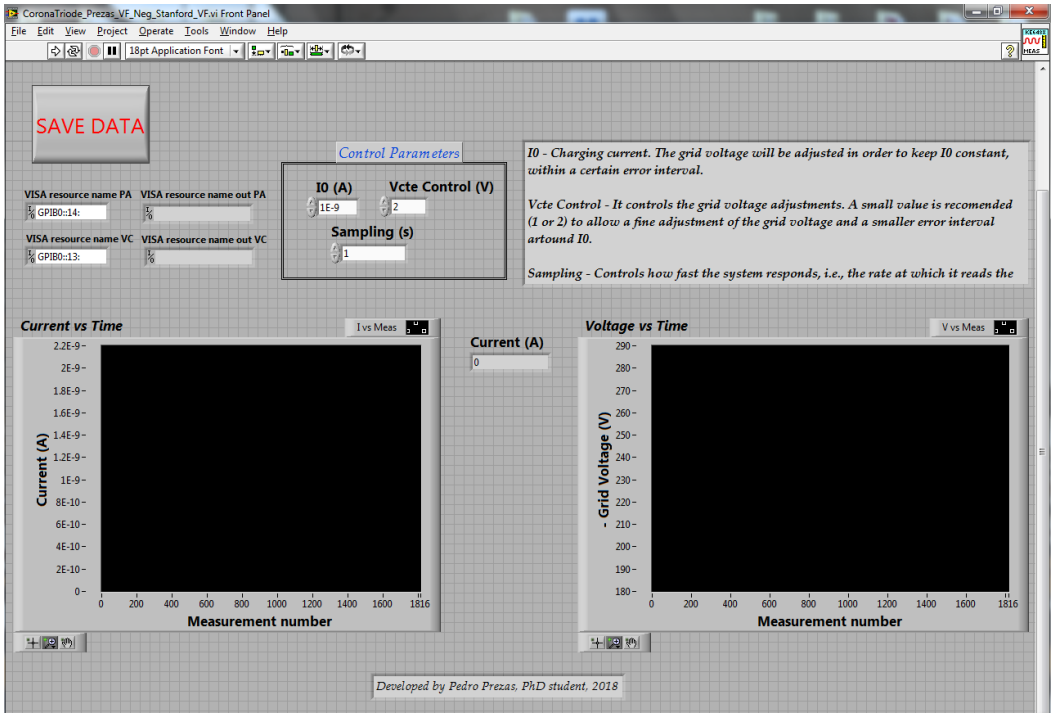

Figure 2.19 A screenshot showing the user interface panel of the developed feedback circuit software. The control parameters "I0"," Vcte Control" and "Sampling" must be defined by the user. Two charts, "Current vs Time" and "Voltage vs Time", provide real-time information about the charging current and the voltage applied to the grid electrode. The former essentially allows following the sample surface potential buildup in real-time.

Besides the user interface panel, there is the block diagram where all the code is built and written. Due to intellectual property reasons and to the considerable effort that its development took, we will not show the code in this thesis. But, in a general way, it can be said that, among other features, the code contains three main cycles which correspond to three different conditions: if the charging current is lower than the defined constant value, if it is higher or if it is equal (this one is very unlikely to occur). Each cycle has a particular control equation so that, for example, if the charging current is lower than the defined constant value, the corresponding particular cycle is "activated" and the voltage applied to grid is increased according to the equation, which takes into account the "I0" and "Vcte Control" parameters. Another advantageous feature is undoubtedly the possibility to easily export and save the relevant experimental data.

2.1.3 Calibration curves of the system

In addition to the feedback circuit, another software was developed in order to perform the "Current vs Grid Voltage" calibration curves, as and explained before. The user interface panel of such software is displayed in fig. 2.20. The control parameters are also highlighted, just as in the feedback program. "Voltage Step" is, as the name indicates, the voltage step applied to the grid during the calibration, "Sampling" in the waiting time for the current measurement (the voltage is applied to the grid and after the "Sampling" time the current is measured) and "Vmax Grid" is the maximum voltage to be applied in the grid. When the maximum voltage is reached and the final current value is measured, the voltage automatically drops to the minimum value that the source is able to apply and a text file containing two columns with the relevant experiment data, time, grid voltage and current, appears and may be saved by the user. The user interface panel also includes a "Current vs Grid Voltage" chart that shows the real-time evolution of the calibration plot.

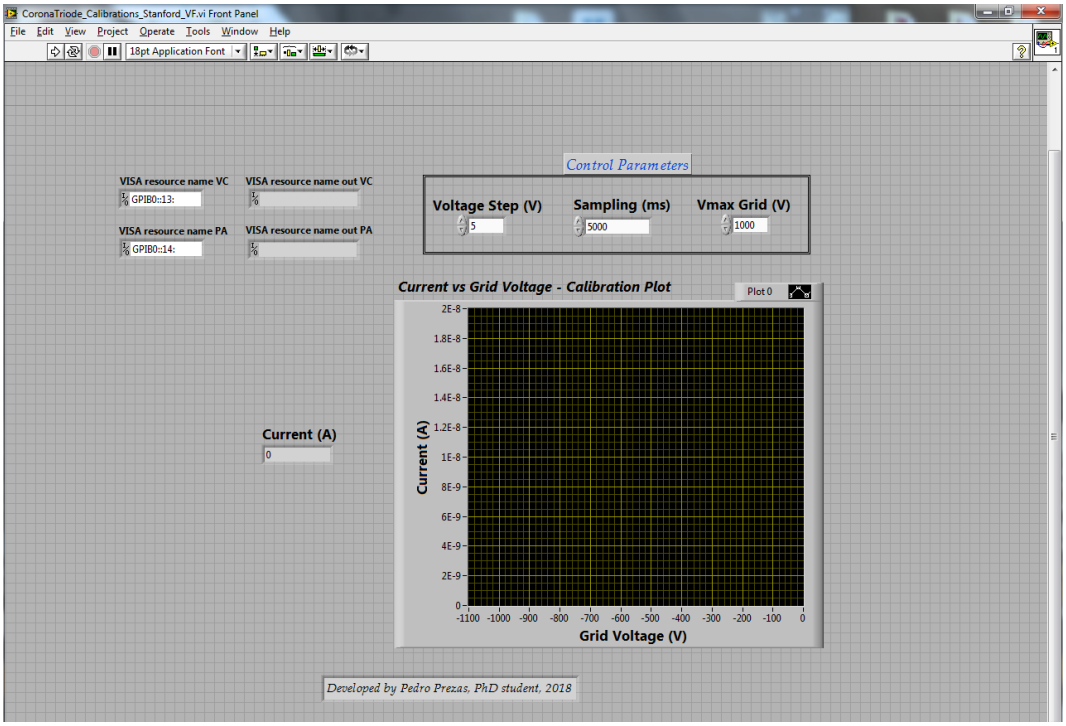

Figure 2.20 A screenshot showing the user interface panel of the developed calibration software. The control parameters "Voltage Step", "Sampling" and "Vmax Grid" must be defined by the user.

It was decided to perform the corona charging of the samples at 200 ºC, the maximum service temperature of our experimental system. Moreover, the samples were subjected to a discharge of negative polarity, taking into account the almost general consensus in the literature and particularly the information presented in topic 1.1.9. The calibration curves of the system, obtained at 200 ºC and for a negative discharge, are shown in fig. 2.21. Four individual calibrations were performed, as the plots in the top show. Each curve is a polynomial fit of the data points. The calibration average curve is shown in the middle plot. The plot in the bottom is just the middle plot multiplied by the area of the electrode, and the reason for the inclusion of this plot will be explained later in chapter 3. The defined control parameters, according to fig. 2.20, are a voltage step of 5 V, a sampling time of 5 s and a maximum grid voltage of - 1000 V. The corona discharge potential was set at - 15 kV, and the point/measurement electrode and the grid/measurement electrode distances are 7 cm and 5 mm, respectively. These values, discharge potential and electrode distances, are well within the common range of values reported in the literature, as discussed before. It is interesting to note that the information which is required from the calibration curve in fig. 2.21 is essentially just a single point. To charge our samples we have to choose a constant charging current value: through the calibration curve, we know the approximately constant gap potential drop for that particular current. Hence, when we charge a sample with that particular current value, we are able to follow the surface potential buildup of the sample directly through the grid voltage: the sample surface potential is the grid voltage minus the constant gap potential drop. Moreover, as fig. 2.21 shows, low charging current values imply lower gap potential drops. If the particular sample being charged with a low current value reaches a high surface potential saturation value, some authors even disregard the gap potential drop and directly assume the grid voltage to be approximately the surface potential of the sample. Either way, the sample surface potential buildup can be followed through the grid potential.

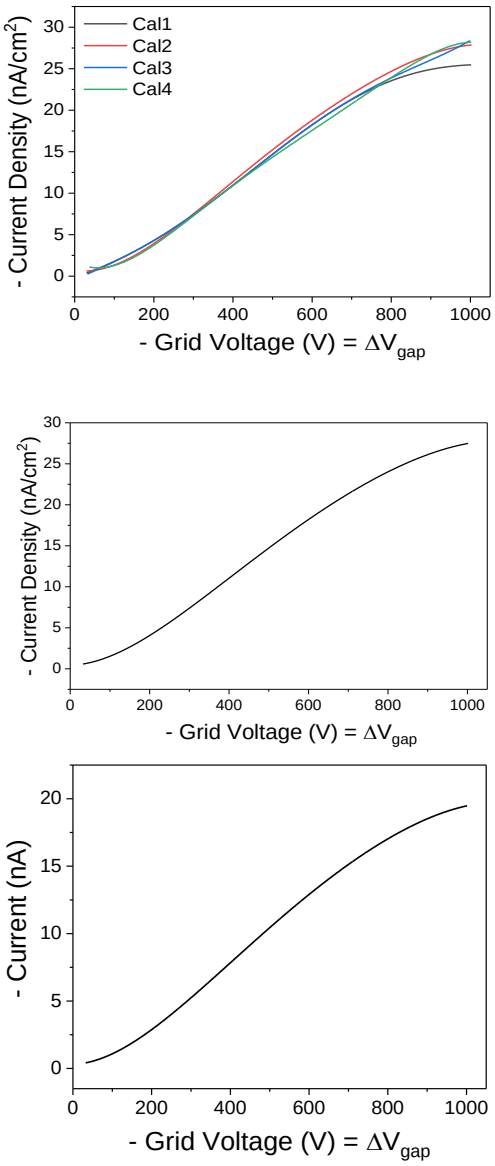

Figure 2.21 Calibration curves obtained for a negative discharge at 200 ºC. Above: four calibrations were performed, labeled as Cal1, (…), Cal4. In the middle: the calibration average curve obtained from the four individual calibrations. Below: the current density plot multiplied by the surface area of the measurement electrode. The control parameters values (see fig. 2.20) are a voltage step of 5 V, a sampling time of 5 s and the maximum grid voltage is - 1000 V. The corona discharge potential was set at - 15 kV. The point/measurement electrode and grid/measurement electrode distances are fixed at 7 cm and 5 mm, respectively.

2.2 Thermally stimulated depolarization currents (TSDC)

Temperature is a key physical variable that influences the physical properties of a given system. The electric and dielectric properties of a given material are a function of it. For this reason, when studying such properties, researchers usually perform measurements by varying the system temperature and the frequency of the applied field. In a thermally stimulated process, a certain physical property is being measured while the sample under analysis is subjected to a controlled heating scheme. Depending on the property being

measured, different thermally stimulated experimental techniques can be identifiable: thermoluminescence, thermally stimulated electron emission, thermal desorption, differential thermal analysis, thermogravimetry, thermally stimulated depolarization and polarization currents, etc. [89].

The measurement of TSDC allows to access useful information regarding the electric and dielectric properties of solid samples as a function of the temperature, notably processes related to dipolar polarization/depolarization and spatial charge detrapping. The technique was introduced by Bucci and collaborators, in 1964, as an effective tool for studying ionic electrical conductivity and other ionic mobility related processes [90]. Curiously, the technique was introduced under the designation "Ionic Thermoconductivity", because at the dawn of its creation it was applied mainly on the analysis of ionic related processes. Later, due to its broader scope, the TSDC designation was adopted, including materials where both ionic and electronic charges contribute to the depolarization currents [91].

TSDC measurements are usually performed on electrically polarized samples. To electrically polarize the sample, it is usually taken to a temperature high enough so that the relaxation time of the material polarizable components is small enough. Under such conditions, when a suitable dc electric field is applied, the polarization should reach its saturation condition in a short time period. Consider fig. 2.22, which outlines the experimental procedure for a TSDC experiment [34, 92, 93]. The main steps, illustrated in fig. 2.22, are the following:

1. The sample is heated up to a temperature T_P, the polarization temperature. Then a suitable dc electric field E_P, the polarization field, is applied between the electrodes in contact with the sample for a given time t_P, the polarization time. At such temperature T_P, the saturation polarization should be reached in a relatively short time period.
2. The sample is cooled down to a temperature T_0, preferably under a fast cooling rate, keeping the field E_P applied. At such temperature, T_0, the polarization (or part of the polarization) becomes "frozen", since the thermal energy is not high enough to

promote the return of the charge carriers to the equilibrium positions, even if E_P is removed. In fig. 2.22, T_0 is represented as RT, but of course, it could a much lower temperature. For instance, many polymers and materials that depolarize fast at RT, the temperature T_0 has to be considerably lower.

3. E_P is removed and the sample is short-circuited (the SC step in fig. 2.22) during a few minutes, in order to remove possible weakly bounded charges.
4. After the SC step, the sample is connected to a sensitive electrometer or picoammeter.
5. The sample is heated under a constant heating rate (common rates are between 1-10 ºC/min) and the short circuit depolarization current is continuously measured as a function of the temperature (or time, one quantity can be easily converted in the other, because the heating rate is constant).

Fig. 2.22 also depicts the behavior of the charge current I_c and of the discharge (or depolarization) current I_d. The charge current increases while E_P is being applied until it saturates. The depolarization processes can be detected as current peaks in an I_d (or I_d density) versus temperature/time plot: each depolarization process becomes detectable when its relaxation time is low enough, generating a depolarization current which increases with temperature, reaches a maximum, and finally falls to zero when the equilibrium distribution is attained.

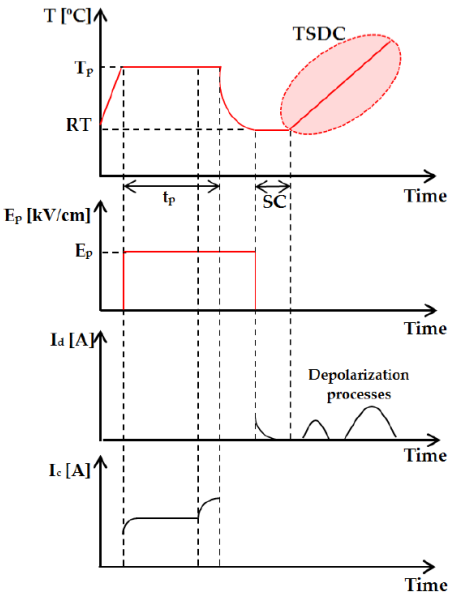

Figure 2.22 Scheme of a typical TSDC experiment, outlining the sample temperature, the applied electric field, the charge current I_c and the depolarization current I_d [34, 92, 93].

However, the situation presented in fig. 2.22, where the depolarization processes yield temperature resolved, well-defined peaks, may not always happen. Sometimes, many depolarization processes will appear as shoulders and may overlap with other depolarization processes or thermally activated intrinsic conductivity of the material. The thermal cleaning technique can be used to separate the depolarization peaks. Assume that two processes have peak temperatures T_1 and T_2, where $T_1 < T_2$. The low-temperature peak can be cleaned by raising the temperature to an intermediate temperature between T_1 and T_2, and subsequently cooling the sample. This procedure should erase (or at least almost totally) the low-temperature peak. To clean the T_2 peak, the sample should be polarized at a temperature T_p, $T_1 < T_p < T_2$, for a time period which fulfills the condition $t \approx \tau_1(T_p) << \tau_2(T_p)$, i.e., at T_p, the polarization during a time t saturates the low-temperature process while the high-temperature process should appear very weak (if it appears) [91]. However, despite the existence of the thermal cleaning technique, which is commonly done to analyze TSDC spectra is to perform deconvolutions, which allows separating and analyzing each individual peak separately. Peaks appearing as shoulders can also be detected when the depolarization is overlapping with background thermally activated conductivity, which in the case of ionic conductivity, presents an exponential dependency with the temperature. In our publication, for example, such overlapping with background thermally activated ionic conductivity is visible [34].

Different physical mechanisms may contribute to the measured depolarization current, of which we can highlight [91]:

1. Orientation and alignment of permanent electric dipoles within the material – dipolar polarization. This applies to polar materials, which contain permanent electric dipoles within their structure.
2. Displacement of the electronic cloud within atoms or ions (induced electronic polarization) and small displacement of ions within the molecules (induced dipolar polarization).
3. Ionic space charge polarization. Ions or ionic vacancies can accumulate in heterogeneities, such as grain boundaries in polycrystalline materials, the interface

between the sample and the electrodes and amorphous/crystalline interfaces in glass-ceramic materials and semi-crystalline polymers.

4. Injection of electrons and/or holes from the electrodes into the sample.
5. Migration of ionic charge carriers can leave defects in the structure that form electric dipoles.

Each particular mechanism has distinct characteristic response timescales: while process 2 is the fastest and responds almost instantaneously to the applied field, due to the low inertia of the electrons, the other ionic mechanisms will require more time to reach the saturation condition. Such time is given by the characteristic relaxation time τ(T), which is a function of the temperature. Recalling topic 1.1.8, the polarization mechanisms of Hap are a practical example of the mechanisms 3 and 5, with a dominance of the space charge trapping mechanism in Hap.

The physical-mathematical formalisms behind TSDC will now be discussed. The following model can be also applied to space charge detrapping mechanisms, although usually the derivation of the model is traditionally shown assuming a dipolar process. Consider the depolarization of dipoles with a single relaxation time, i.e., a dielectric material with one type of non-interacting dipoles in a reasonable diluted concentration [91]. This is an approximation of real physical systems, although this model is probably the most popular when analyzing and treating TSDC spectra. In these conditions, the depolarization kinetics is of the first order, i.e., it can be described by the following rate equation [91, 94]:

$$-\frac{dP(t)}{dt} = \frac{P(t)}{\tau(T)} \tag{15}$$

where $\tau(T)$ is the characteristic relaxation time, a function of the temperature. Integration of equation 15 yields equation 16:

$$P(t) = P_0 exp\left[-\int_{t_0}^{t} \frac{dt}{\tau(T)}\right] \tag{16}$$

where t_0 is the beginning time of the TSDC measurement and P_0 is the saturation polarization (or equilibrium polarization, more rigorously, because the total possible polarization of the sample may not be saturated when beginning the measurement,

depending on the polarization process parameters, T_P and E_P), i.e., the polarization before the start of the measurement. P_0 is expressed as:

$$P_0 = Np\sqrt{cos\theta} \tag{17}$$

where N is the dipole density, p is the individual dipole moment and θ is the angle between the dipoles and the electric field. Considering the approximation of non-interacting rotating dipoles, their spatial orientation can be expressed by:

$$\sqrt{cos\theta} = \frac{pE_p}{3k_BT_p} \tag{18}$$

where k_B is the is the Boltzmann constant, E_P the polarization field (applied field) and T_P the polarization temperature. The combination of equations 17 and 18 yields the Langevin-Debye equation [33, 91, 94]:

$$P_0 = \frac{Np^2E_p}{3k_BT_p} \tag{19}$$

According to equation 19, the dipolar polarization is proportional to the field E_P.

The depolarization current [or current density J(T)] being measured in a TSDC experiment "follows" the return of the aligned dipoles or trapped space charge to the equilibrium states, being expressed as a time variation of the polarization [33, 91, 94, 95]:

$$J(T) = -\frac{dP(t)}{dt} = \frac{P(t)}{\tau(T)} \tag{20}$$

The combination of equations 16 and 20 yields equation 21:

$$J(T) = -\frac{P_0}{\tau(T)} exp\left[-\int_{t_0}^{t} \frac{dt}{\tau(T)}\right] \tag{21}$$

One of the advantages of using a linear heating rate is that it is possible to easily convert time in temperature. The relationship between both physical quantities is:

$$\beta = \frac{dT}{dt} \tag{22}$$

where β is the heating rate. The integration limits in equation 20 can be expressed in function of the temperature:

$$J(T) = -\frac{P_0}{\tau(T)} exp\left[-\frac{1}{\beta}\int_{T_0}^{T}\frac{dT}{\tau(T)}\right] \quad (23)$$

In many physical systems, particularly in ionic solids, the temperature dependence of the relaxation time is described by an Arrhenius dependence [91, 94, 95]:

$$\tau(T) = \tau_0 exp\left(\frac{E_a}{k_B T}\right) \quad (24)$$

where τ_0 is a pre-exponential factor, which can be interpreted as the relaxation time when the temperature tends to infinite, and E_a is the activation energy for the depolarization mechanism. Deviations from the Arrhenius law are reported mostly for organic materials, such as organic polymers. In those cases, the temperature dependence of the relaxation time may follow other laws, such as Eyring type equations or the WLF equation. We will focus on Arrhenius dependency. According to equation 24, equation 23 can be rewritten as [91, 94, 95]:

$$J(T) = \frac{P_0}{\tau_0} exp\left[-\frac{E_a}{k_B T}\right] exp\left[-\frac{1}{\beta\tau_0}\int_{T_0}^{T} exp\left(-\frac{E_a}{k_B T'}\right) dT'\right] \quad (25)$$

Equation 25 is often used as a theoretical model for fitting TSDC spectra, and it describes the temperature dependence of the depolarization current. If necessary, and sometimes it is, the fitting includes an exponential term to fit the background thermally activated intrinsic (of the material) ionic conductivity, and therefore subtract it from the rest of the fitting, as reported by Horiuchi et al., for instance [33]. In equation 25, the first exponential term dominates the behavior for lower temperatures, describing the rise of the depolarization current as the charge starts to return to the equilibrium positions. The second exponential dominates for higher temperatures, gradually slowing down the current rise, especially for high activation energies [94].

Substituting the Langevin-Debye equation (equation 19) into equation 25 we get [91, 94, 95]:

$$J(T) = \frac{Np^2 E_p}{3k_B T_p \tau_0} exp\left[-\frac{E_a}{k_B T}\right] exp\left[-\frac{1}{\beta\tau_0}\int_{T_0}^{T} \exp\left(-\frac{E_a}{k_B T'}\right) dT'\right] \quad (26)$$

Equation 26 is known as the Bucci-Fieschi theory.

The depolarization current reaches its maximum at the peak temperature T_{peak}, and it can be obtained by differentiating equation 26 in order to find the maximum [91, 94]:

$$T_{peak} = \sqrt{\left[\frac{\beta E_a \tau_0}{k_B} exp\left(\frac{E_a}{k_B T_{peak}}\right)\right]} \tag{27}$$

According to equation 27, it can be seen that T_{peak} is independent of both E_p and T_p, being a function of the heating rate β, τ_0 and E_a. When β is increased, the stored charge has to be released in a shorter time, and the dielectric material responds slowly. Therefore, the peak shifts to higher temperatures and increases its amplitude (β also influences the peak amplitude). Fig. 2.23 displays the effect of the variation of β on the TSDC spectra measured in AgCl: 700 ppm Ni crystalline samples [94]. As can be seen in fig. 2.23, a significant effect on the peak displacement and intensity will only be observed for extensive variations of β [94].

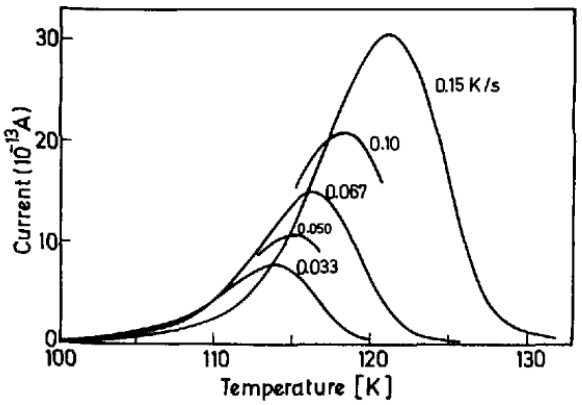

Figure 2.23 The effect of the variation of the heating rate β on the TSDC spectra measured in AgCl: 700 ppm Ni [94].

The area of a TSDC spectrum, current density versus temperature, yields the total stored charge density of the sample, according to equation 28:

$$Q_p = \frac{1}{\beta}\int_{T_0}^{\infty} J(T)dT = P_0 \tag{28}$$

For a peak due to ionic dipolar depolarization, the area of the peak can be used to estimate the dipole density *N* [91]:

$$\int_{T_0}^{\infty} J(T)dT = \frac{Np^2 E_p}{3k_B T_p} \tag{29}$$

For a peak due to space charge detrapping, another equation can be applied, assuming that all the trapped charges have approximately the same mobility. In this approximation, the equation becomes:

$$\int_{T_0}^{\infty} \mathrm{J(T)dT} = 2qLvNt_p exp\left(-\frac{E_a}{k_B T}\right) sinh\left(\frac{qLE_p}{2k_B T_p}\right) = P_{SC} sinh\left(\frac{qLE_p}{2k_B T_p}\right) \quad (30)$$

where q is the ionic charge, L is the ionic jump length, v is the jump frequency, N is the density of the trapped charge, t_P is the polarization time (the time during which E_P is applied, at the polarization temperature T_P) and E_a is the activation energy for detrapping the charge carriers (the energy required to activate a jump). Considering equations 29 and 30, it is visible that the dipolar and space charge depolarizations have distinct dependencies on the field E_P. While in equation 29 it is linear, in equation 30 the relation is hyperbolic. This fact is often used to distinguish or determine the physical mechanism behind a given depolarization peak, by analyzing the dependence between the polarization and the applied field E_P.

The application of equation 25 to adjust the experimental data can be a difficult task, the primary problem is that the integration leads to a convergent infinite series, and so approximations have to be considered [96]. According to R. Chen, for the case $T = T_0 + \beta$, where β is the linear heating rate, the integral can be written as [89]:

$$\int_{T_0}^{T} exp\left(-\frac{E_a}{k_B T'}\right) dT' = F(T, E_a) - F(T_0, E_a) \quad (31)$$

where $F(T, E_a) = \int_0^T exp\left(-\frac{E_a}{k_B T'}\right) dT'$. Since $F(T, E_a)$ is a function that rises sharply with the increase of the temperature, $F(T_0, E_a)$ can be disregarded. One possible way to calculate $F(T, E_a)$ is through an asymptotic expansion of the integral. $F(T, E_a)$ can be written as:

$$F(T, E_a) = T exp\left(-\frac{E_a}{k_B T}\right) \sum_{n=1}^{N} \left(\frac{k_B T}{E_a}\right)^n (-1)^{n-1}(n!) \quad (32)$$

For the case when N = 1, the following approximation of equation 32 can be written:

$$J(T) \cong \frac{P_0}{\tau_0} exp\left(-\frac{E_a}{k_B T}\right) exp\left[-\frac{1}{\beta \tau_0} \frac{k_B T^2}{E_a} exp\left(-\frac{E_a}{k_B T}\right)\right] \quad (33)$$

Similar expressions are found when the relaxation time $\tau(T)$ follows other laws: for example, if $\tau(T)$ obeys the Eyring theory, T^2 must be replaced by T^3 [94]. Some authors prefer to present equation 33 in the following form:

$$J(T) = Aexp\left(-\frac{E_a}{k_B T}\right) exp\left[-B\frac{k_B T^2}{E_a} exp\left(-\frac{E_a}{k_B T}\right)\right] \quad (34)$$

where A, B and E_a are adjusting parameters (E_a is the activation energy). E_a and A can be determined by the initial rise method, first introduced by Garlick and Gibson [97]. This method is based on the fact that for temperatures lower than the peak temperature ($T < T_{peak}$), the integral in equation 25 is negligible, and the equation is simplified as:

$$J(T) = Aexp\left(-\frac{E_a}{k_B T}\right) \quad (35)$$

Thus, E_a and A can be estimated through a linearization related to equation 35:

$$ln\big(J(T)\big) = \ln(A) - \frac{E_a}{k_B T} \quad (36)$$

The B parameter can be calculated based on the peak temperature T_{peak} and in E_a, according to equation 37 [94]:

$$T_{peak} = \sqrt{\left[\frac{E_a}{k_B B} exp\left(\frac{E_a}{k_B T_{peak}}\right)\right]} \quad (37)$$

By knowing B, one can determine τ_0 and then τ, the relaxation time associated with a particular depolarization peak.

As a small note, in the initial rise method, only temperatures in the initial part of the depolarization peak can be used. Furthermore, the current values used in this method for the E_a calculation should be less than 10% of the peak current value [98].

2.3 CoBlast

The CoBlast system used to produce the samples studied in this thesis is at the facilities of the Portuguese company Ceramed, S.A., which develops its activity in the biomaterials area, particularly, it is specialized in coatings for medical devices. Its services

include PS Hap and Ti coatings and PVD (physical vapor deposition) coatings. Ceramed had some collaborations with ENBIO, and through those collaborations, ENBIO provided a CoBlast equipment to the Portuguese company. Following the "chain of collaborations", some elements of our research group at the University of Aveiro, "Physics of Advanced Materials and Devices" (PAMD – belongs to the associate laboratory i3N) have collaborations with Ceramed, which made it possible to use the CoBlast process in this thesis.

Fig. 2.24 shows the CoBlast equipment in the Ceramed facilities and the inside view of the processing chamber, with a single nozzle configuration. The system supports up to four axes of movement: the usual x, y and z axes and a rotation axis w. The equipment is connected to a proper powder extraction system, to prevent the release of powder to the environment. It is also connected to a compressed air supply necessary for various operations, such as several purge operations, electronics chamber purge, etc. Since the equipment requires clean and dry air, it contains an air drier membrane that provides supplementary moisture and oil removal (the compressed air supply system in Ceramed has already a drying system, therefore the membrane in the equipment indeed provides a supplementary action).

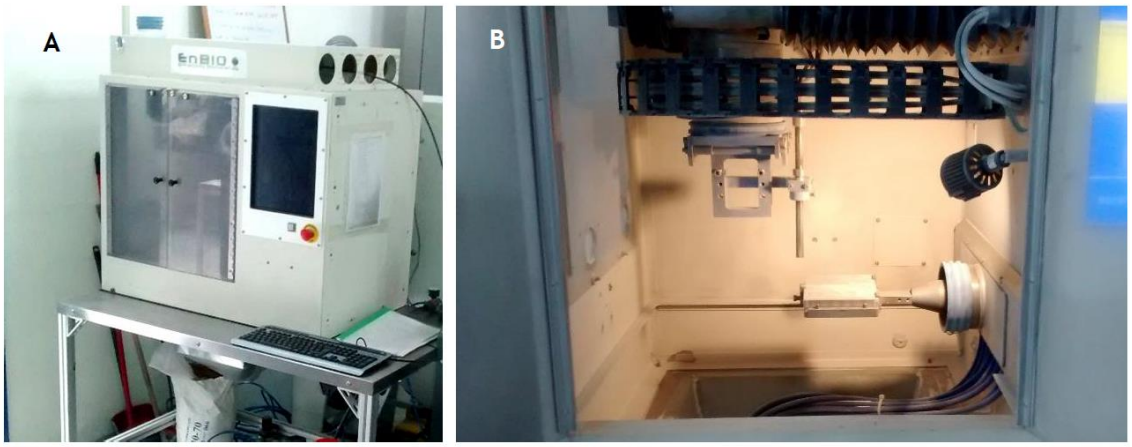

Figure 2.24 (A) The CoBlast equipment in Ceramed. (B) Inside view of the deposition chamber, with a single nozzle configuration.

This system provides different part tooling which allows coating pieces with different geometries. Fig. 2.25 displays such part tooling. A platform and two mandril tooling are available. The mandril tooling allows coating cylindrical shaped pieces, like dental implants, while the platform is suitable for flat pieces.

Figure 2.25 Different part tooling available to coat pieces with different geometries. A platform (which is also visible in fig. 2.24) and two mandril tooling are available.

The processing chamber contains a base spindle with an O-ring where the part tooling connects and becomes attached through vacuum pulling. All the tooling have similar bases that connect to the chamber base spindle, having also seven setscrews that allow the software to recognize the part tooling being connected. In fig. 2.24 it is possible to see the platform attached to the base spindle.

The equipment contains also a user interface, as depicted in fig. 2.26, which allows the user to select the coating program, to activate the vacuum in order to attach the part tooling, etc. In case of any coding error or if the part tooling is not detected, for example, a yellow warning is displayed by the interface listing the detected problems. It also shows the time required to complete the selected program.

Figure 2.26 The CoBlast system user interface. This interface allows the user to select the coating program, to load the part tooling, to display error messages, etc.

The coating programs are developed in industry standard G- and M-codes. These codes are widely used computer numerical control language and allow controlling the movement of machine tools over a coordinate system. G-codes control those movements and M-codes control other several items, such as blasting control, calling subroutines, etc. A quick programming reference for G- and M-codes are included in table 2.1.

Table 2.1 A quick programming reference for G- and M-codes.

G00	Fast move	R	Arc radius (use with G02 or G03)
G01	Vector move	S	Set rotational speed
G02	Clockwise arc, circle or helix	F	Set feedrate
G03	Counter clockwise arc, circle or helix	X	X-axis value
G04	Hold position	Y	Y-axis value
G10	Define position	Z	Z-axis value
G28	Home axes	W	w-axis value
G90	Use absolute coordinates	P	Parameter value (used with G02, G03, G04 and M98)
G91	Use relative coordinates	I	Circle center axis 1 (used with G02 or G03)
M03	Start rotational axis clockwise	J	Circle center axis 2 (used with G02 or G03)
M04	Start rotational axis counter clockwise	T	Time parameter (used with M08)
M05	Stop rotational axis	N	Line number
M30	End program	()	Comment
M98	Call subroutine	^	Scaling (used with G00, G01, G02 and G03)

The metallic substrates coated in this work are Ti grade II squares, with 25 mm of side length and 1 mm of thickness. Thus, the platform part tooling was used. An example of a G-code developed to coat the Ti substrates is provided below, with some comments

about the function of the particular code line. The structure and rules concerning the development of the codes can be consulted in the manual of the CoBlast equipment.

```
[Filename]
name=Fase2_PrezasVF

[Requirements]
PartTooling=COUPON_TRAY (this is the platform part tooling)

[Parameters]
units=mm

[ProgramData]
N10 G91 (use relative coordinates – relative to the default position of the nozzle, visible in fig. 2.25)
N20 G00 y60
N30 G01 x100 z26 F33 (lines N20 and N30 move the nozzle to desired starting position before starting the deposition)
N40 G04 P10 (wait 10 seconds)

N50 G01 x-100 F13
N60 G01 y-2.5 F13
N70 G01 x100 F13
N80 G01 y-2.5 F13
N90 G01 x-100 F13
N100 G01 y-2.5 F13
N110 G01 x100 F13
N120 G01 y-2.5 F13
N130 G01 x-100 F13
N140 G01 y-2.5 F13
N150 G01 x100 F13
N160 G01 y-2.5 F13
N170 G01 x-100 F13
N180 G01 y-2.5 F13
N190 G01 x100 F13
N200 G01 y-2.5 F13
N210 G01 x-100 F13
N220 G01 y-2.5 F13
N230 G01 x100 F13

N240 G04 P1 (wait 1 second)
N250 G28 (move the nozzle to the default position)
N260 M30 (end program)
```

This particular code was made to coat 4 Ti substrates, fixed in the platform one after the other so that a compact row is obtained. In line N40, it is defined a 10 s pause before starting the deposition. In this pause, we start the powder (fig. 2.27) and we set the blast pressure to the desired value. The code section comprising lines N50 up to N230 correspond to the deposition/blasting period: the nozzle performs 10 sweeps along the length of the substrate, with a federate of 13 mm/s, each sweep being separated 2.5 mm from each other (this is what we will call later the “offset” variable). In line N30, when we define “z26”, it means that for this particular case the deposition vertical distance between the nozzle and

the substrates is 20 mm (this is one the process variables that we studied, as it will be discussed).

Another important factor to be considered is the powder feeding system. Since a mixture of abrasive and dopant powders are used, it is important to mix the powder properly, so that, when using different abrasive/dopant weight ratios, such ratio remains approximately homogeneous through all the powder mixture. Fig. 2.27 shows the powder feeder Single-10C system, from Sulzer Metco, with 1100 cm^3 of capacity. In (B) a detailed scheme of the powder feeder is shown, indicating the different components. The powder feeder contains a rotating disk with a powder groove, a spreader and a suction unit. In each complete rotation of the disk, all the powder contained in the groove is ejected to the processing chamber through the suction unit. The powder groove volume is 5.78 cm^3, therefore, this volume of powder will be ejected per rotation. Thus, knowing the density of the bulk powder, the mass flow rate can be calculated using equation 38:

$$\dot{m} = V_{groove} \times \rho_{bulk} \times rpm \tag{38}$$

Since the time of each coating program is known, it is possible to have fairly good control of the mass of powder spent by each program.

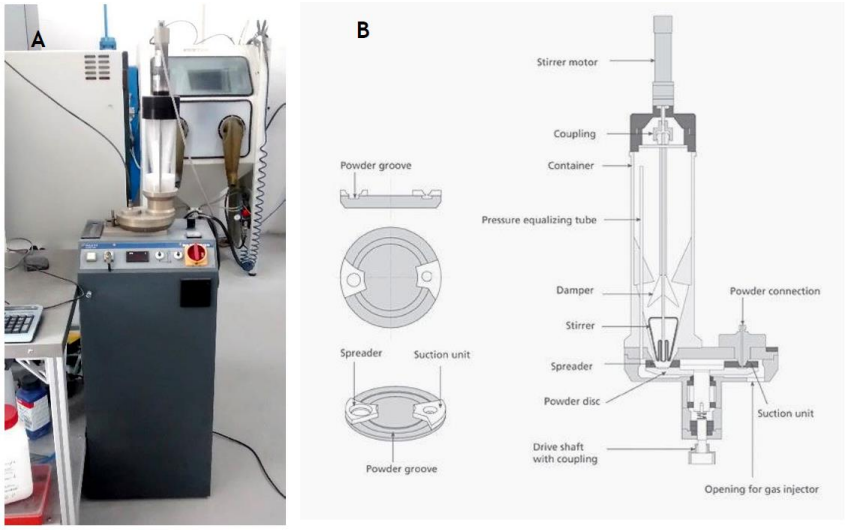

Figure 2.27 (A) The Single-10C powder feeder system from Sulzer Metco, with 1100 cm^3 of capacity. (B) Detailed scheme of the powder feeder, identifying the different components.

Before placing the powder in the powder feeder, the dopant and abrasive have to be already properly mixed. For such purpose, a V-blender is used. There are three popular shapes/geometries of tumble blenders: the double cone, the slant cone and the V-blender, also known as the twin shell blender. These types of blenders rely on gravity to cause the powder to cascade within the rotating container, and they are known by their high efficiency and short blending times [99]. The V-blender is made of two hollow cylindrical shells joined at an angle between 75 and 90º. As the blender tumbles, the powder mixture is continuously splitting and recombining. This is a case of blending promoted by diffusion, characterized by small scale random motion of the solid particles. The blender movements enhance the mobility of the individual solid particles, promoting the diffusive blending. V-blender is among the most popular choices when precise blending formulations are required and when some of the mixture elements have low weight percentages of the total mixture. Typical blending times are in the range of 5-15 minutes. The blending efficiency depends also on the volume of material inserted in the blender: the ideal fill-up volume is in the range of 50 to 60 % of the blender volume. For higher percentages, the time required for proper blending may be doubled. The rotation speed is another important factor in determining the blending efficiency. Low speeds yield low shear forces, while higher speeds may cause significant dusting, through the segregation of fine powders: for higher speeds the fines become airborne and then when the rotation stops they settle on the top of the power bed. There is a critical speed when this process starts to happen, and V-blenders are usually operated at 50 to 80% of the critical speed. Rotation rates in the 8-24 rpm range are reported to exert little influence on the mixing mechanism, i.e., the diffusion mechanism applies, and in this range, the mixing time is inversely proportional to the rotation rate [99]. Hence, rotation rates near 24 rpm lead to faster blending times. The blender used in this work is a prototype made of polytetrafluoroethylene (PTFE) machined according to the dimensions described in Brone et al., as shown in fig. 2.28 [99]. The blender, with an inner volume of 1 liter, is connected to a three-phase motor which creates a rotational rate of 20 rpm.

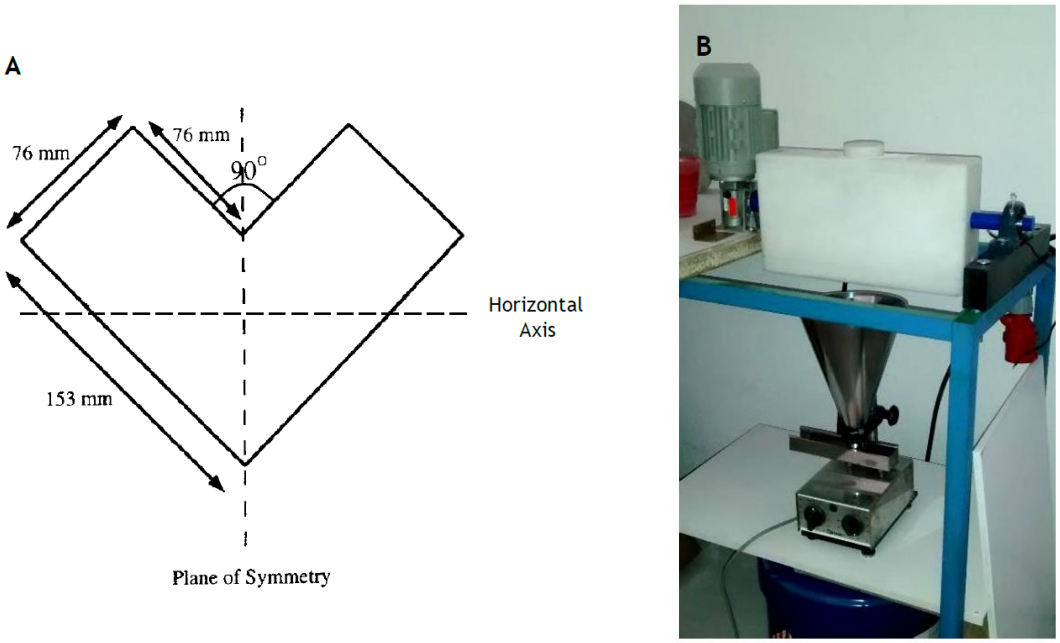

Figure 2.28 (A) A planning scheme of the V-blender according to Brone et al. Photograph of the V-blender in the Ceramed facilities.

Concerning the CoBlast samples, they were produced at the Ceramed facilities, and different sets of samples were obtained. The rationale behind the first set of samples was to explore a broad set of CoBlast process parameters. The studied process parameters were the blast pressure, the blast distance and the weight ratio between dopant and abrasive. Table 2.2 shows the process parameters set for the first set of samples. Three samples were produced for each set of process parameters, so, 81 samples result from table 2.2. The samples were labeled in such a way that the process parameters are easily identifiable, for example Z20_P5_50/50 or Z30_P4_65/35

Table 2.2 The CoBlast process parameters defined for the first set of samples.

Composition (wt%)	*Blast distance: Z = 10 mm*			*Blast distance: Z = 20 mm*			*Blast distance: Z = 30 mm*		
50/50 Hap/Alumina	4 bar	5 bar	6 bar	4 bar	5 bar	6 bar	4 bar	5 bar	6 bar
65/35 Hap/Alumina	4 bar	5 bar	6 bar	4 bar	5 bar	6 bar	4 bar	5 bar	6 bar
35/65 Hap/Alumina	4 bar	5 bar	6 bar	4 bar	5 bar	6 bar	4 bar	5 bar	6 bar

Additionally, the blasting offset was also studied as a process parameter. The samples in table 2.2 were produced with a defined offset of 2.5 mm. In addition, offset values of 1.5, 3 and 3.5 mm were considered, as displayed in table 2.3. Thus, 9 more samples are included in table 2.3, making a total of 90 samples produced for the first set of samples.

Table 2.3 The blasting offset, a process parameter also considered in the first set of samples.

Composition (wt%)	***Blast distance: Z = 20 mm***		
50/50 Hap/Alumina	Off: 1.5 mm	Off: 3 mm	Off: 3.5 mm

In the second set of samples, the process parameters were reduced/filtered according to the interpretation of the results of the structural and morphological analysis of the first set of samples. Thus, to discuss the second set of samples it is necessary to discuss the results of the analysis of the first set of samples. Since this is the "Experimental details" chapter, it is logical to discuss them in the subsequent chapter, the "Results and Discussion".

2.4 Tensile pull-off tests

The mechanical performance of a bioceramic coating depends on the adhesion of the coating to the metallic substrate and on the intra-coating properties. The adhesion is thought to be determined to a higher extent by the mechanical interlocking between the coating and the substrate. Chemisorption and epitaxial/topotaxial processes are also considered to be important contributors to the coating adhesion. This "importance degree" of such processes is still under discussion in the literature, because they are not easily quantifiable. However, they are thought to be more important in high-temperature processes, for example, plasma-based processes where, thermally activated bonding mechanisms may be activated. The adhesion of the coatings is governed by three main mechanisms [4]:

1. Mechanical interlocking: As discussed, the metallic substrate surface roughness has a very important role. In PS, the metallic substrate surface is grit blasted prior to Hap deposition, in order to purposely create a large surface roughness to promote a higher degree of mechanical interlocking. In some cases, the adhesion strength was found to be directly proportional to the roughness magnitude. In the case of high-temperature deposition processes, the totally or partially molten droplets impacting the surface must have sufficient plasticity, low viscosity and good wettability in order to adhere and cover the surface roughness. Otherwise, the substrate surface will only be partially covered and voids will occur at the surface/coating interface, hindering the mechanical adhesion.
2. Physical adhesion: This mechanism is governed by diffusive bonding, where the diffusivity increases with increasing contact temperature according to Fick's law. In principle, this kind of adhesion could be enhanced by substrate preheating treatments. Nonetheless, due to the small diffusion depth (caused by the fast solidification rate), this mechanism is generally assumed to play only a minor role as an adhesion mechanism.
3. Chemical adhesion: as mentioned, they may play a relevant role, particularly for high-temperature processes. This adhesion mechanism may involve the formation of a metallurgical-like bond at the substrate-coating interface. However, despite the fact that the bond may be strong, normally it is not referred as a metallurgical or chemical bond. For example, a metallurgical bonding would require some alloying of the materials at the interface, which typically is not observed in PS coatings. The truth is that this kind of adhesion mechanism is still not well explained and clear in the literature.

These mechanisms have influence over different length scales: they are classified as micro-bonding or macro-bonding according to their influence area. Micro-bonding is assigned to bonding that occurs along very small surface areas, the size of an individual particle of sprayed powder. Macro-bonding occurs along much larger areas, one or two orders of magnitude larger. Therefore, macro-bonding mechanisms relate to mechanical interlocking processes while micro-bonding relates to chemical adhesion mechanisms.

Tensile pull tests are usually recommended for qualification and test control of Hap coatings intended for commercialization. ASTM F1147 standard requires a static tensile strength higher than 15 MPa for PS Hap coatings. It should be noted that most of the standards are defined having in mind the PS coatings, however, these standards are also the basis to test different coating processes. To determine the static tensile strength of the coating the standard provides a methodology that is essentially a tensile pull-off test. In a tensile pull test, the bonding strength (or cohesive strength, depends on the failure mode) of the coating is determined by the maximum tensile load required to separate the two test fixtures with a cross-sectional area A: the strength is given by the force divided by the area. There are different failure modes on a tensile pull-off test, illustrated in fig. 2.29. If the failure occurs at the coating/substrate interface the failure is adhesive and the reported value provides the adhesive strength of the coating. The failure can also occur within the coating, and in this case, the reported value provides the cohesive strength of the coating. The failure can also occur within the adhesive, which marks a poor test unless the failure strength is higher than the value required for the qualification of the Hap coating. In such case, the test is valid, because in that case it is known for sure that the cohesive or adhesive strength of the coating is higher than the value required in the standard.

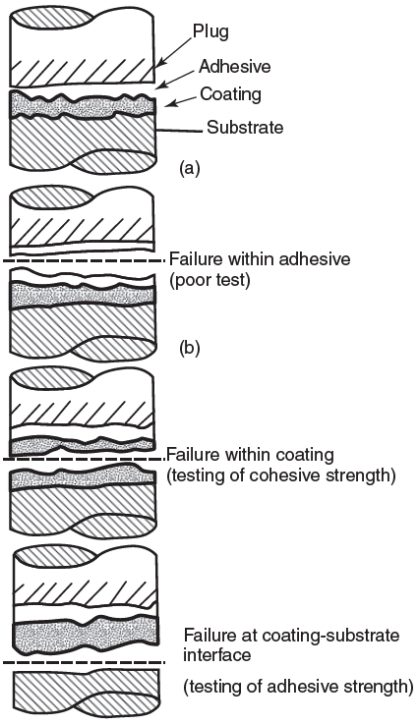

Figure 2.29 The possible failure modes in a tensile pull-off test. A failure within the adhesive is considered a poor test unless the failure strength is higher than the value (15 MPa) required by the standard ASTM F1147.

The standards usually specify some requirements for the testing equipment. The ASTM F1147 deals with Hap coatings. The ASTM C633-13 standards deal particularly with the adhesion of thermal sprayed coatings. Fig. 2.30 depicts the ASTM C633-13 adhesion testing principle. A pull force is exerted on steel test cylinders with a diameter of 25 mm. The coating to be tested is sprayed on the surface of one the cylinders and glued to the other cylinder. The adhesive must have a cohesive strength higher than 15 MPa. In general, in an academic context, researchers are not particularly worried about the conditions established in the standard, for example, the diameter of the cylinders, etc. They will just use the equipment they have available to perform mechanical tests. However, when commercialization is intended, the standards have to be followed. For such purpose, specialized companies are usually the solution in order to certify the coatings according to the methodologies defined in the standards.

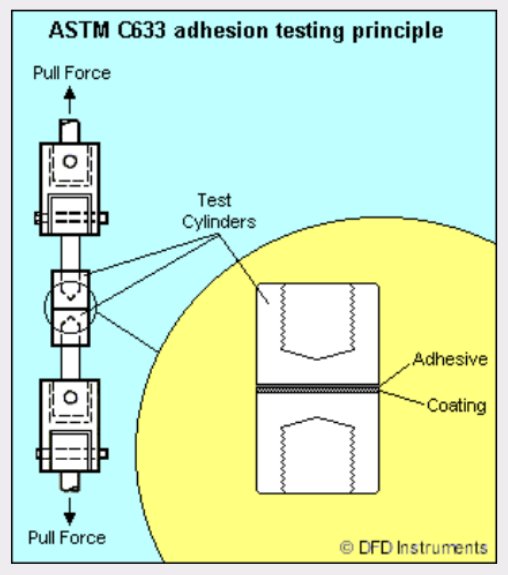

Figure 2.30 The ASTM C633-13 adhesion testing principle. A pull force is exerted on steel test cylinders with a diameter of 25 mm. The coating to be tested is sprayed in the surface of one of the cylinders and glued to the other cylinder [100].

2.5 *In vitro* biological tests

The *in vitro* biological tests on the coatings charged through our corona triode experimental system were carried out at the lab facilities of the CENIMAT (Center of Materials Research) research center, belonging to the i3N (Institute for Nanostructures, Nanomodelling and Nanofabrication) associate laboratory. In particular, they were

performed in collaboration with researchers of the Soft and Biofunctional Materials Group (SBMG).

The *in vitro* biological tests comprised two components: immersion of the charged coatings in an SBF solution for different times and osteoblastic proliferation and metabolic activity tests. Thus, as discussed in topic 1.1.9, both components of the bioactivity level enhancement induced by the stored charge in the coatings are tested: the bioactivity enhancement in the physiological media related to the interaction of its ionic content with the charged coating, tested through the SBF solution, and the stimulation of the cellular activity, tested through the osteoblastic proliferation and metabolic activity tests.

The main goal of the SBF tests was to study the variation, in function of the immersion time, of the concentration of the Ca^{2+} and P^{5+} ions, as well as the pH value. For the SBF solution preparation, 750 ml of high purity deionized water were introduced in a 1 L capacity glass beaker. A magnetic stirrer was also introduced in the beaker and the system was placed in a hot plate/magnetic stirrer, at 37 ºC under a constant stir rate. Subsequently, the following reagents were added in the following order: 7.996 g of NaCl, 0.350 g of $NaHCO_3$, 0.224 g of KCl, 0.228 g of $K_2HPO_4.3H_2O$, 40 ml of 1 M HCl, 0.0278 g of $CaCl_2$, 0.071 g of Na_2SO_4, 6.057 g of $(CH_2OH)_3CNH_2$ and 0.305 g of $MgCl_2.6H_2O$. Afterward, the pH was measured and taken to 7.4, using 1 M HCl. Lastly, the volume of the solution was taken to 1 L and the pH was verified again, in order maintain the 7.4 value. Each sample was immersed in glass containers with SBF solution for a maximum period of 3 days. The ratio between the sample surface area and volume of SBF solution was defined to be 0.0075 cm^{-1}. The glass containers remained inside an incubator at 37 ºC. The concentration of the Ca^{2+} and P^{5+} ions, and the pH value was obtained for different immersion times: 0, 1, 3, 6, 12, 24, 48 and 72 hours. For each immersion time, 0.5 ml of solution was removed and ICP-AES (inductively coupled plasma atomic emission spectroscopy) measurements were performed.

Concerning the osteoblastic proliferation and metabolic biological tests, to analyse the cell-surface interaction, human osteoblasts (SAOS-2 cell line, ATCC, American Type Collection, ref. HTB-85) were seeded on the charged and non-charged surfaces. Cell culture

medium was McCoy's 5A (Sigma-Aldrich #M4892) supplemented with 2.2 g/L sodium bicarbonate (Sigma-Aldrich, #S5761), penicillin (100 μg/ml) and streptomycin (100 μg/mL) (Invitrogen, #15140122) and 10% FBS (Fetal Bovine Serum, Invitrogen, #10270106). Cultures were maintained in a CO_2 incubator (Sanyo MCO10AICUV).

Samples were sterilized with ethanol 70% for 10 min and left to dry. Samples were then placed in a 12-well tissue culture plate (Sarstedt, Germany) and pre-wetted with culture medium. Cells were seeded at a density of $3x10^4$ cells per cm^2. Cell controls were set by seeding cells at the same density directly over the surface of the tissue culture plate (TCP) wells.

Cell adhesion ratio was determined by evaluating cell population 24h after seeding and proliferation rates by evaluating cell population every other day. Cell viability was assayed using a resazurin (Alfa Aesar) solution (0.04 mg/mL in PBS) as cell viability indicator. Viable cells reduce resazurin (with an absorption peak at 600 nm) to resorufin (with an adsorption peak at 570 nm). For the assay, all media were replaced by a 1:1 mix of complete medium with the resazurin solution. This medium was also dispensed in wells without cells to be used as a reference. After 2h20m of incubation in the CO_2 incubator, medium absorbance was measured at 570 nm with a reference wavelength of 600 nm (Biotex ELX 800UV microplate reader). The corrected absorbance (obtained by subtracting the absorbance measured at 600 nm from the one measured at 570 nm and subtracting the medium control) is proportional to cell viability. The combined standard uncertainty was calculated by propagation of uncertainties.

In order to observe cell morphology, cells were stained after 5 days in culture. Cells were fixed with 3.7% paraformaldehyde, permeabilized with Triton X-100 (0.5% in PBS) and blocked (to avoid non-specific staining by the secondary antibody) with a 1% bovine serum albumin solution containing 0.2% Triton X-100. Cells were then immunostained with the primary antibody against vinculin, a focal adhesion protein (Anti-Vinculin antibody, Mouse monoclonal, clone hVIN-1, purified from hybridoma cell culture, Product Number V9264, Sigma-Aldrich) followed by the secondary antibody (Goat anti-Mouse IgG (H+L) Cross-Adsorbed Secondary Antibody, Alexa Fluor 488, Catalog #:A-11001, Molecular

Probes, Thermo Fisher Scientific). To observe the F-actin cytoskeleton, cells were stained with Acti-stain 555 Phalloidin (100 nM in PBS) (Cat. # PHDH1, Cytoskeleton, Inc.) and to observe nuclei with DAPI (4',6-Diamidino-2-Phenylindole, Dilactate, Cat # D3571, Invitrogen: 300 nM in PBS). All samples were mounted on glass coverslips with fresh PBS and imaged with an epi-fluorescence microscope Nikon Ti-S.

Chapter 3 Results and discussion

3.1 CoBlast coatings

3.1.1 Structural and morphological analysis

The first set of samples, as described in tables 2.2 and 2.3, were subjected to structural and morphological analysis, with the aim of reducing and filter the process parameters for the second set of samples. In other words, the goal was to find out if some of the process parameters could be disregarded by considering the results of the structural and morphological analysis. In fact, some good arguments were found in favor of disregarding some of the CoBlast process parameters. XRD measurements were performed and the intensity ratio between the highest Hap peak and the highest Ti peak was considered. This ratio is a qualitative indicator of the amount of deposited Hap because the peak intensity is proportional to the weight fraction of the component [101]. Moreover, powder XRD is a bulk analysis technique, so the ratio is representative of the bulk and not just a particular point. The XRD diffractograms were obtained using a PANalytical Empyrean Powder X-ray Diffractometer.

Fig. 3.1 shows, in the left, the XRD diffractograms of the coatings produced with different pressures P = 4, 5 and 6 bar, for a fixed distance of 20 mm and a 50/50 wt% mixture. The diffractograms show the presence of crystalline Hap, Ti and also Alu. The detection of the Ti substrate is related to the low thickness of the coatings together with the fact, as aforementioned, that powder XRD is a bulk analysis technique. In agreement with the literature, a small peak assigned to Alu impregnation within the coatings is detected. Proceeding with the analysis of fig. 3.1, the XRD Hap/Ti intensity ratios for the samples whose process parameters are identified in the plots in the right are shown. Considering both plots in the right, the 50/50 Hap/Alu weight ratio mixture clearly yields a higher quantity of deposited Hap, compared to the other weight ratios. The 65/35 mixture, in spite of containing more Hap, yields coatings with a lower quantity of Hap, because the lower Alu weight content diminishes the abrasive power of the mixture, implying a lower surface area available for mechanical interlocking (see fig. 1.37). We already have a solid reason to

disregard the 65/35 mixture: Hap is simply being wasted. Considering an industrial production process, it certainly would make no sense to use a 65/35 Hap/Alu mixture knowing that a 50/50 mixture produces coatings with higher Hap contents: money and Hap are being wasted on the 65/35 mixture, also taking into account that Hap is more expensive than Alu. The 35/65 mixture, despite the fact of having higher abrasive power, does not lead to higher Hap contents on the coatings.

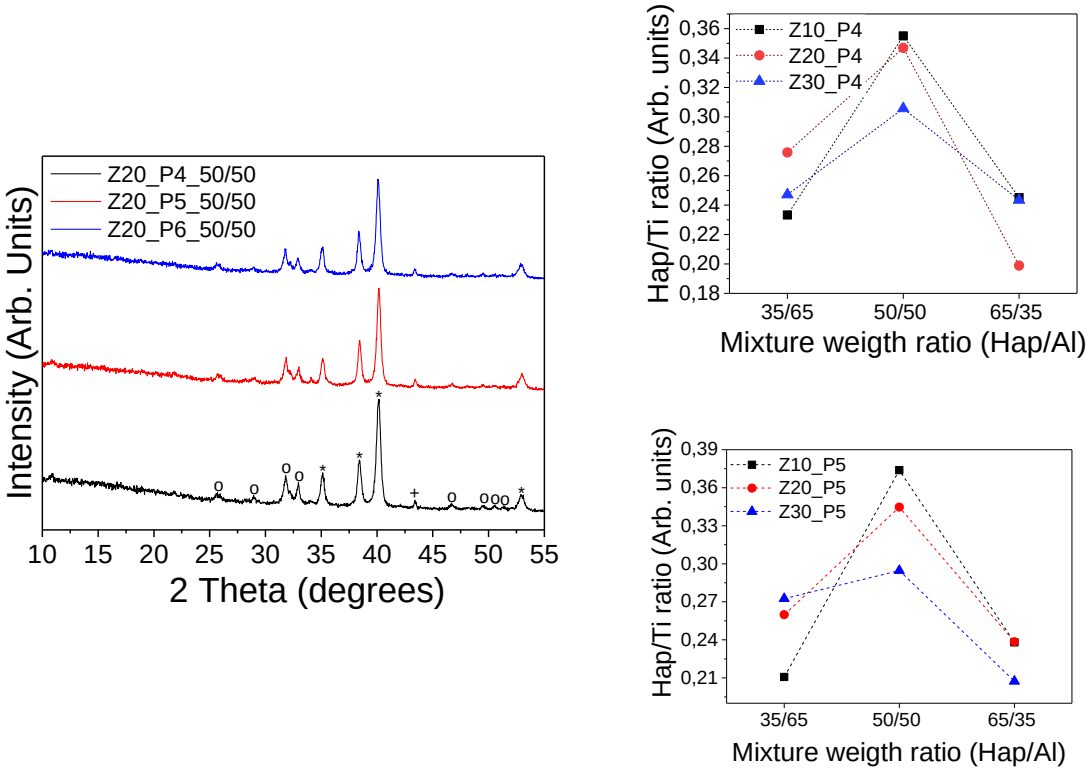

Figure 3.1 In the left: XRD diffractograms of the coatings produced with different pressures P = 4, 5 and 6 bar, for a fixed distance of 20 mm and a 50/50 wt% mixture (O - Hap, * - Ti, + - Al). In the top right corner: the XRD Hap/Ti intensity ratio versus the mixture weight ratio, for the coatings produced with different distances Z (mm) and for a pressure P = 4 bar. In the bottom right corner: same representation for a pressure P = 5 bar. For P = 6 bar the results are similar.

Fig. 3.2 shows more XRD diffractograms: in the left plot, it is clear that the higher distance Z = 30 mm causes a significant decrease in the quantity of deposited Hap. The same information can be withdrawn from the plot in the right. From the information presented

until now, we can find solid arguments to disregard the 65/35 mixture and the Z = 30 blast distance. The 35/65 mixture could be disregarded by considering fig. 3.1 results. Nonetheless, we will present more results supporting this conclusion.

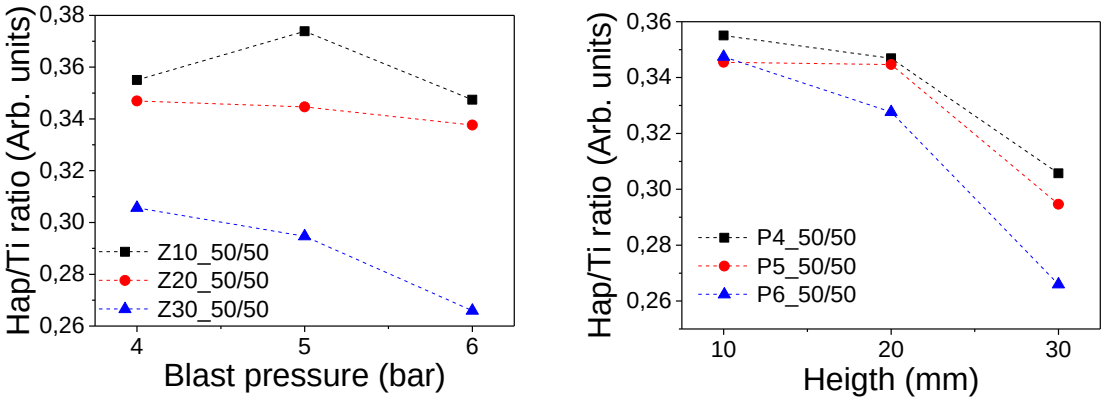

Figure 3.2 In the left: the XRD Hap/Ti intensity ratio versus the blast pressure, for the samples produced with different distances Z and for a 50/50 weight ratio. In the right: the XRD Hap/Ti intensity ratio versus the distance Z, for the samples produced with different pressures P = 4, 5 and 6 bar and for a 50/50 weight ratio.

SEM micrographs and EDX mappings of the coatings were obtained, using a Vega 3 TESCAN microscope. In the EDX mappings that will be presented, the analyzed areas are squares with about 230 μm of side length. Fig. 3.3 displays EDX maps of the Z20P5 samples for different Hap/Alu ratios. The relevant chemical elements are identified in fig. 3.3. The 50/50 sample clearly demonstrates a superior Hap coverage compared to the other samples, which lies in agreement with the XRD results presented in fig. 3.1. Like XRD, EDX is a bulk analysis technique, thus it is no surprise that it is able to detect the metallic Ti substrate since the CoBlast films have thicknesses in the range of few micrometers, as discussed in section 1.3.

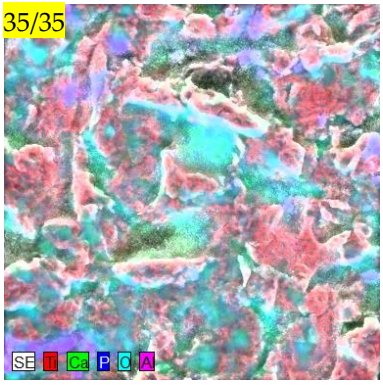

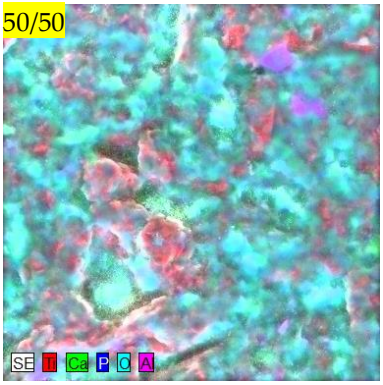

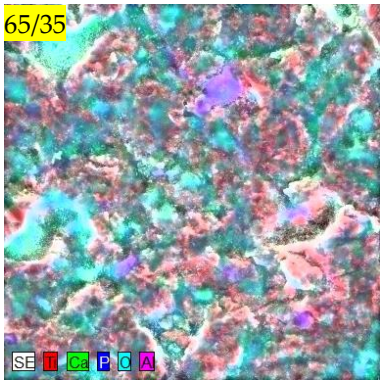

Figure 3.3 EDX maps of the Z20P5 samples, for different Hap/Alu weight ratios, identified in each particular micrograph.

The Ti distribution is shown in fig. 3.4. Again, it is clear that there is a better Hap coverage in the 50/50 mixture because the Ti signal is stronger in the 35/65 and 65/35 samples, indicating a higher average film thickness in the 50/50 samples.

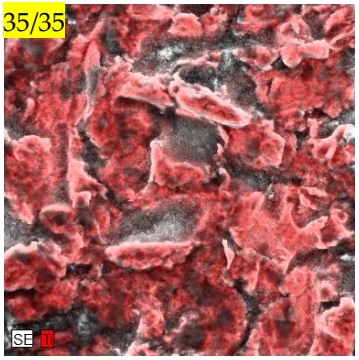

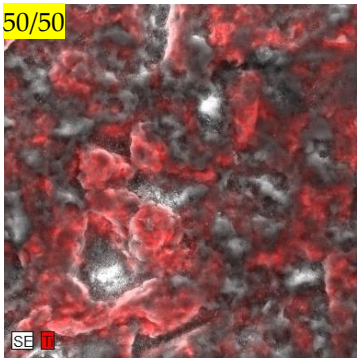

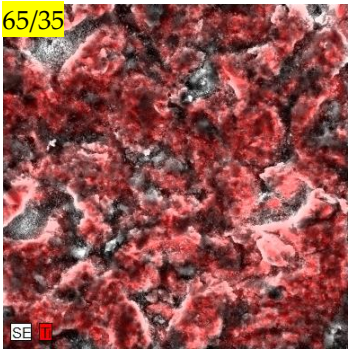

Figure 3.4 EDX maps showing the Ti distribution in the Z20P5 samples, for different Hap/Alu weight ratios, identified in each particular micrograph.

Fig. 3.5 provides a "qualitative picture" regarding the Alu impregnation within the coatings. As expected, Alu impregnation is greater on the 35/65 mixture, contrarily to the other mixtures. Alumina, as it was discussed, is a bioinert material commonly used as a blast medium in the pre-treatment of medical implants prior to the coating deposition. In APS, for instance, some Alu particles have been shown to be embedded in Ti surface even after ultrasonic cleaning, acid passivation and sterilization. Although it is bioinert, it has been reported that the release of Alu particles into the surrounding physiological tissue can potentially interfere with the integration and fixation of the implant, by promoting third-body wear, unwanted tissue reactions and loosening in metal-on-metal total hip replacements [102]. Therefore, the 35/65 mixture compared to the 50/50, yields lower amounts of deposited Hap and a higher amount of impregnated Alu.

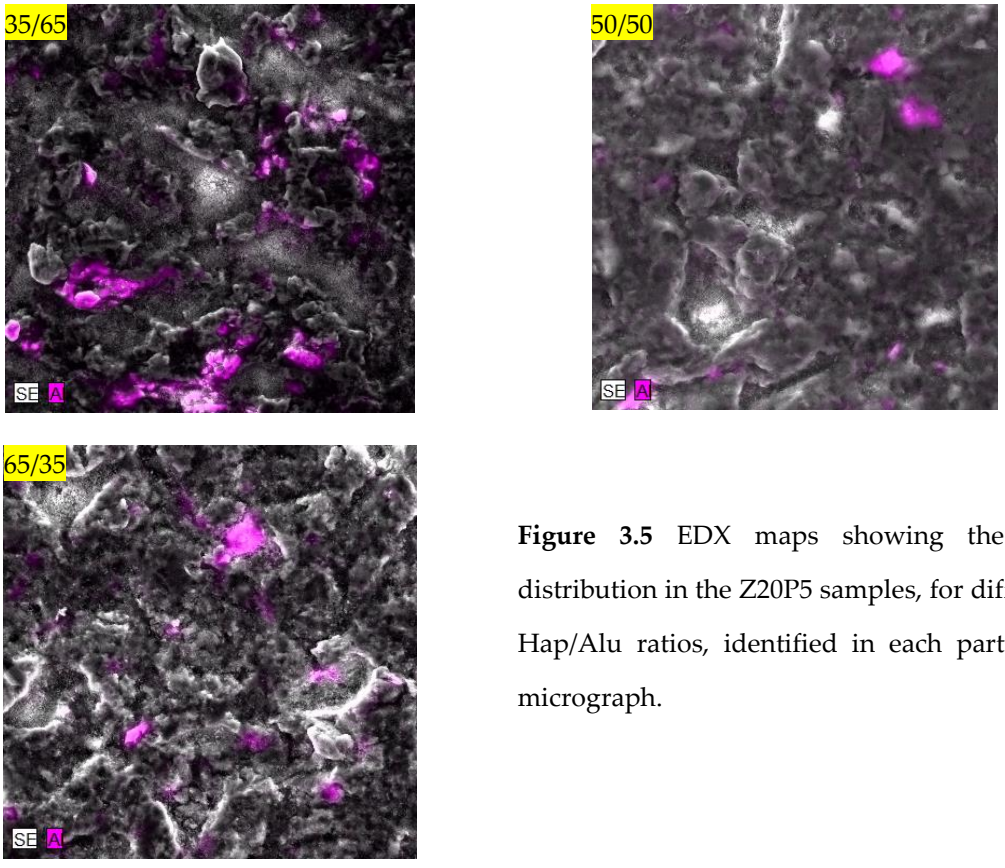

Figure 3.5 EDX maps showing the Alu distribution in the Z20P5 samples, for different Hap/Alu ratios, identified in each particular micrograph.

For the reasons mentioned above, we have disregarded the 35/65 and 65/35 mixtures for the production of the second set of samples. However, before starting with the discussion of the second set of samples, optical profilometry measurements were

performed on the first set samples, in order to determine the arithmetic average surface roughness (S_a) of the samples. While the arithmetic average roughness (R_a) provides the roughness over a given evaluation length, S_a provides the same information over a given surface area, therefore rending a more representative analysis of the coating. These measurements were performed using a Sensorfar S Neox 3D optical profiler.

It is generally assumed in the literature that the surface roughness affects the osteoclastic and osteoblastic attachment, proliferation and differentiation. However, on the other hand, there are contradictory reports stating that the cellular attachment, proliferation and differentiation processes are not dependent on the roughness on a relatively large range of values, going from submicron up to micron surface roughness. On one side, there are reports showing that a variety of bone marrow cells are able to orient themselves in the grooves or edges of the biomaterial surface and that osteoclastic and osteoblastic attachment, proliferation and differentiation are significantly enhanced by rough surfaces with irregular morphology [103, 104]. Although it is not clearly defined, rough surfaces can be defined as those with roughness values in the range of a few micrometers, while submicron and close to the unit values can be considered as smoother surfaces, although some probably would label a one-micrometer rough surface as a "moderately rough" surface. On the other side, there are reports stating that the cellular processes are statistically independent of the surface roughness on a relatively large range of values. On a particular report, it is concluded that the cellular processes are independent of the surface roughness of a Hap coating, within values ranging from 0.13 up to 3.36 μm [105]. On another report, it was concluded that three different roughness values (0.73, 2.86 and 4.68 μm) had no significant differences in the cell morphology and on the osteoblastic ALP expression [106]. However, early stronger fixation rates and long term mechanical stabilization will be enhanced on rough surfaces, because, as the case of CoBlast, where the abrasive powder is responsible for providing surface area for mechanical interlocking between the Hap and the Ti substrate, the roughness of the Hap coating also provides surface area for mechanical interlocking between the Hap coating and the growing biologic bone. For this reason, surface roughness values in the 2-5 μm range are preferred over lower roughness values [107].

Fig. 3.6 displays the arithmetic surface roughness (S_a) values of samples with different Hap/Alu weight ratios as a function of the blast pressure. One particular aspect of the CoBlast, as it is reported elsewhere, is that the surface roughness of the underlying Ti substrate is approximately the same as the Hap coating surface: the induced roughness on the Ti substrate is "transferred" to the coating [72]. Observing fig. 3.6, one immediate conclusion that can be drawn is that, as expected, the 65/35 samples have lower S_a values, because they have lower abrasive power. The 35/65 samples tend to have higher S_a values for the 5 and 6 bar ejection pressures (except in the Z10_P5_50/50 sample). For the blast pressure 4 bar this trend is not discernible between the 35/65 and 50/50 samples. Excluding the Z20_P6_35/65 and Z30_P6_35/65 samples, the S_a values for all the samples are below 3 μm. However, considering fig. 3.6, it is clear that S_a values for samples with the 65/35 weight ratio are lower compared to the 35/65 and 50/50 samples. Each data point is the average of at least three surface roughness values obtained at different locations within the same sample. The error associated with each point is always below 10% and in most cases is around 5%.

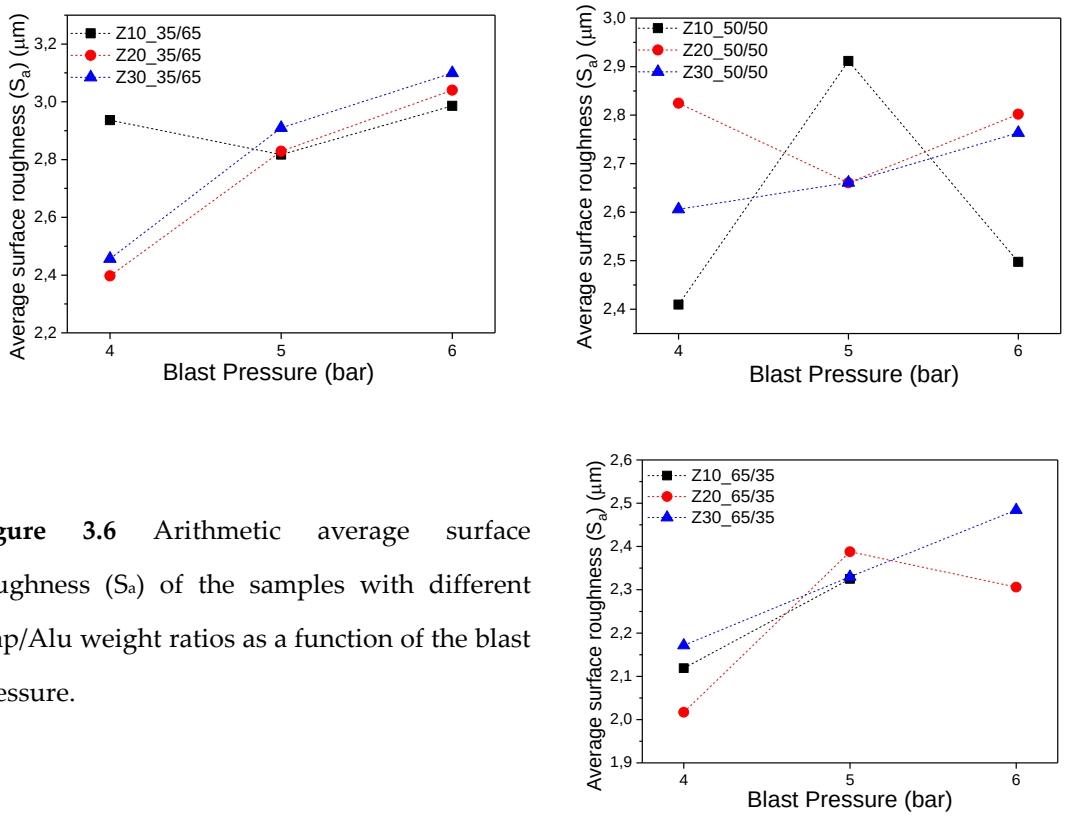

Figure 3.6 Arithmetic average surface roughness (S_a) of the samples with different Hap/Alu weight ratios as a function of the blast pressure.

Fig. 3.7 shows one example of a topographical map that can be obtained through the optical profilometry measurements, in this particular case for a Z20_P5_50/50 sample. The S Neox SensoSCAN software was used to obtain such 3D topographical maps. The S_a value obtained in each measurement is calculated over a large surface area as indicated in fig. 3.7 (~ 351 x 264 µm), therefore providing a representative value of all the coating.

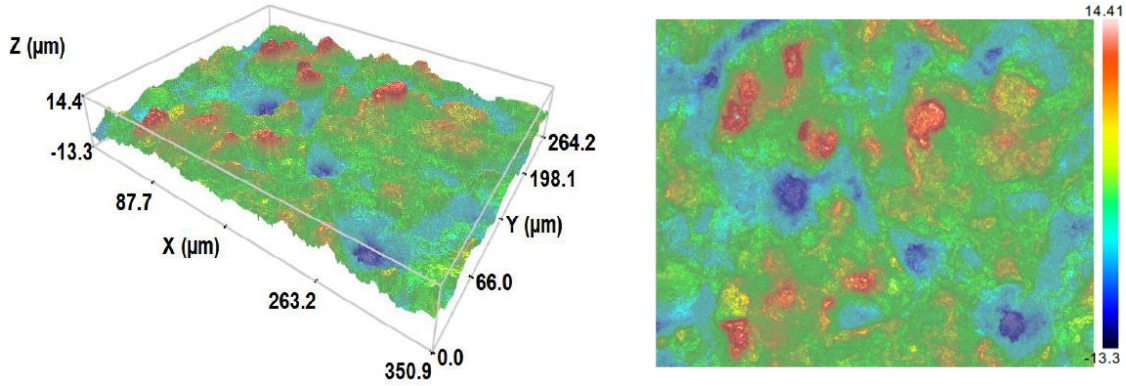

Figure 3.7 A 3D surface topographical map of a Z20_P5_50/50 sample.

After the first set of samples, the process parameters were reduced/filtered to Z10_50/50 (4, 5 and 6 bar) and Z20_50/50 (4, 5 and 6 bar). Thus, the second set of samples with these process parameters were produced for the realization of pull-off adhesion tests and also to start with the corona discharge experiments.

3.1.2 Mechanical pull-off tests

In this topic, the mechanical pull-off adhesion experiments are introduced, which were characterized by some technical difficulties. These tests, which allow to determine the static tensile strength of the coatings, were performed resorting to the functionalities of a Shimadzu mechanical testing machine. Fig. 3.8 shows part of the methodology behind the pull-off adhesion tests. Test pins made of aluminum, with a diameter of 14 mm, are attached to the Hap coating. Before the test, the surface of the pin that is going to be attached to the coating is subjected to a roughening treatment (using a polishing machine and sandpapers) in order to create a superficial roughness and therefore to increase the surface area available

for the bonding between the pin and the coating, as shown fig. 3.8 A). Then the pin is attached to the surface of the coating through an adhesive, fig. 3.8 B), complying with the adhesive full cure time as indicated by the suppliers. Finally, fig. 3.8 C) shows how the pull-off test is carried out: a special "claw" applies a tensile force, increasing at a constant rate, until the pin is detached from the coating, and the maximum applied tensile force is recorded.

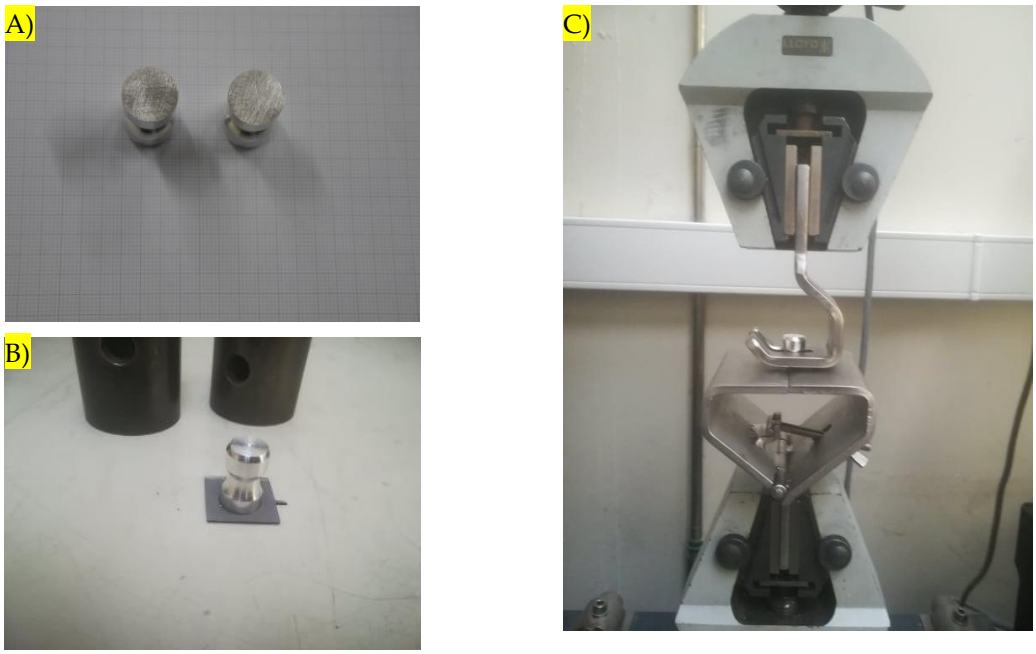

Figure 3.8 A) The aluminum test pins, with a diameter of 14 mm. A roughening treatment was applied in the pin surfaces, in order to increase the surface available for bonding with the coating. B) A test pin attached to a sample, after complying with the adhesive full cure time as indicated by the supplier. C) During the pull-off test, a special "claw" applies a tension, increasing at a constant rate, until the pin is detached from the coating.

We considered the ASTM F1147 standard, which defines that for Hap coatings on metallic substrates, a minimum value of 15 MPa is required for the static tensile strength. Accordingly, all the adhesives which were tested for attaching the pin to the coating had a cohesive tensile strength considerably higher than 15 MPa, as informed in the technical sheet of the products. Specific items to handle the adhesives were also purchased, including static mixing nozzles (all the used adhesives had two components) and dispensing guns.

The first tests were performed using the IRS 2111 All-purpose Epoxy Adhesive, which "typically" has a cohesive tensile strength of 44 MPa, as stated in the technical sheet. When we performed the pull-off tests, all the failures occurred within the adhesive and in the 2 - 3 MPa range. These tests are negative, they would only be valid if the failure tension was higher than 15 MPa, as required by the ASTM F1147 standard. In fig. 3.9 we present the results of one of the tests performed on a Z20_P5_50/50 sample. The tension versus strain plots shows the failure occurred at about 2.6 MPa, therefore comprising a negative test.

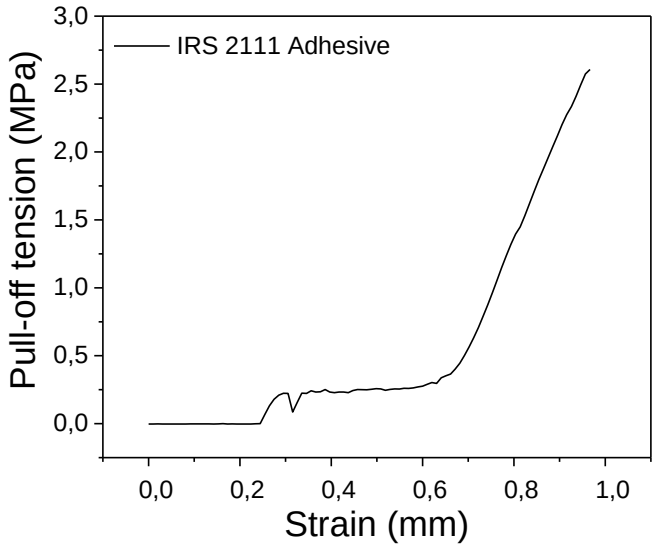

Figure 3.9 Pull-off test performed on a Z20_P5_50/50 sample, using the IRS All-purpose Epoxy Adhesive. The failure occurred within the adhesive, at about 2.6 MPa.

We thought that for some reason this IRS 2111 adhesive could not be effective for Hap coatings (some kind of reaction could be occurring at the interface, for instance), so, we purchased two new adhesives: the PX628HP, supplied by ROBNORADHESIVES, and the LOCITE® EA 9497™. As indicated in the technical sheets, the first has "typically" a cohesive tensile strength of 60 MPa and the second 52.6 MPa. However, during the pull-off tests, all the failures were again within the adhesive and all were below 10 MPa, thus invalid tests. We contacted the corresponding authors of the references [66], [72] and [108] because they report positive adhesion tests for Hap coatings. The contact reason was to access what kind of adhesive they used in their reports. We got a single reply from the authors of reference [72], stating that their tests were performed by a company certified and specialized in this type of adhesion tests, QUAD GROUP Inc. We also learned that Ceramed certifies the adhesion of their coatings through the services of the CRITT Mechanical Engineering & Composite Materials, a specialized institute in France. The fact is that one of

the main difficulties related to the use of this kind of adhesives is that the cohesive tensile strength values specified by the suppliers are "ideal" and almost impossibly replicable in a laboratory academic context. This is why companies and even academic researchers tend to resort to outside specialized companies and institutes to evaluate the adhesion of their coatings and to certify them according to the ASTM F1147 standard, if commercialization is intended. With regard to this work, we did not proceed with the pull-off tests, which would imply to buy further adhesives. CoBlast is already established in the literature regarding the superior adhesion strength of the coatings and therefore it was decided to not spend more resources on these mechanical tests.

3.1.3 Corona charging experiments

In these experiments, there were some issues that were not initially foreseen. The reason is straightforward: it is not possible to control the charging current on the CoBlast coatings. The cause for this can be understood by observing fig. 1.37, for example. Due to the nature of the CoBlast process, there are significant regions of the Ti substrate which are not covered with Hap. Consequently, if we have regions of Ti substrate directly exposed to the corona discharge, then, there is no possibility of controlling the charging current, since the sample is conductive. We tried some approaches to find out if we could obtain a sample where the Ti surface would be completely covered, however, we did not manage to achieve that goal. One of the approaches, to make additional depositions on an already coated sample, is unfruitful. As referred before, due to the abrasive nature of the CoBlast process, to make additional depositions is essentially to remove the Hap coating which was already deposited and to produce a new one, thus the problem is not solved. We also tried different Hap/Alu weight ratios, without success, the same problem would persist. However, in chapter 4 section 4.2, the future work suggestions, we suggest an approach that could be tested for the CoBlast coatings.

3.2 PS coatings

3.2.1 Structural/morphological analysis

The PS coatings were provided by Ceramed, which is specialized in producing Hap coatings on orthopaedic implants, such as total knee replacements or THR. The coatings were produced in the same kind of metallic substrates used to produce the CoBlast coatings: Ti grade II square substrates, with 25 mm of side length and 1 mm of thickness. The average thickness of the PS coatings is around 70 μm (this is information was provided to us by Ceramed). We remember that PS Hap commercial coatings have typically thicknesses in the 50-100 μm range. Fig. 3.10 contains a photograph showing the aspect of the PS coatings

Figure 3.10 Photograph showing the aspect of the PS coatings provided to us by Ceramed. The coatings have an average thickness of 70 μm.

XRD measurements were performed in order to identify the phases present within the coatings. Fig. 3.11 displays the XRD diffractogram of a PS coating. The results are in agreement with the literature of PS Hap coatings, which was also presented and discussed in chapter 1. Hap and β-TCP crystalline phases are detected, including the typical amorphous halo, ascribed to ACP (see table 1.3 to recall the existing calcium orthophosphates). Sometimes it can be found in the literature the designation "amorphous hydroxyapatite" associated with the amorphous halo (fig. 1.43, for instance), but the correct designation is amorphous calcium phosphate, ACP. The high temperatures experienced by the powder particles during the PS deposition can promote their partial melting and the

subsequent high cooling rates cause the presence of a glassy phase within the coatings. It is also worth mentioning that the Hap coatings produced by Ceramed are in compliance with the international standards regulating such coatings (intended for commercialization), particularly with ISO 13779-2. This particular ISO, as we also referred in topic 1.2.3, stipulates some properties of the coatings, such as the Hap crystallinity ratio must be at least 45 %, the weight percentage of Hap must be at least 50 %, the weight percentage of secondary crystalline phases cannot be higher than 5 % (for each phase), it stipulates the limit (in ppm) or heavy metals, etc. We recall, for those more interested in these matters, that McCabe et al. indicate in their review article typical values that commercial PS Hap coatings present regarding the properties defined in ISO 13779-2 and also in other standards (such as ASTM F1147).

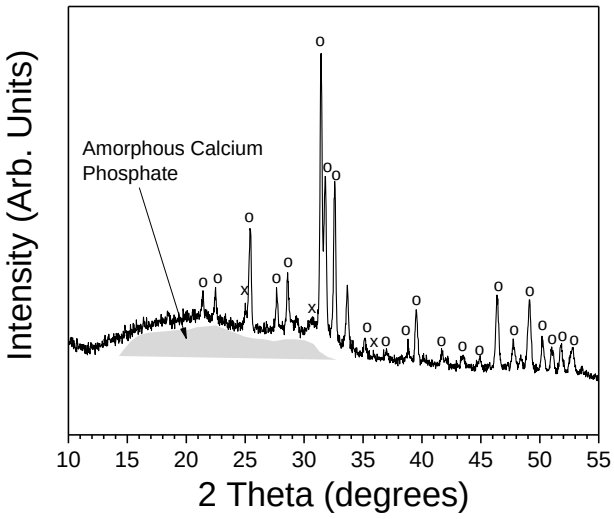

Figure 3.11 XRD diffractogram of a PS coating. Hap and β-TCP crystalline phases are detected, including the habitual amorphous halo observed in PS coatings; (O - Hap, X - β-TCP).

We also performed optical profilometry measurements on the PS samples, in order to determine the S_a of the samples. A 3D surface topographical map of a PS Hap coating is displayed in fig. 3.12. As expected, the S_a values of the PS coatings are considerably higher than the CoBlast coatings. Some coatings were analyzed and the S_a values are around 11 μm.

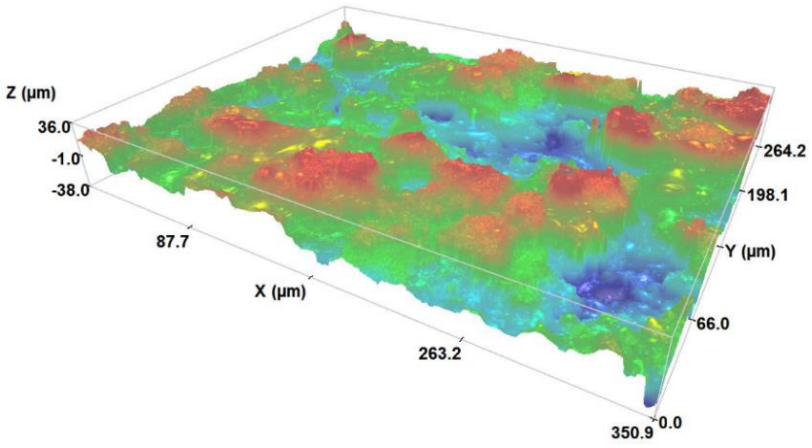

Figure 3.12 A 3D surface topographical map of a PS Hap coating.

3.2.2 Corona charging experiments

In contrast with the CoBlast coatings, the PS coatings can be successfully charged through the corona triode technique. The fact that the entire Ti metallic substrate is covered with a thick Hap coating is the reason why it is possible to charge them, there are no significant Ti regions directly exposed to the discharge, as it is the case of the CoBlast coatings.

Two charging methods were used in the PS samples: the constant current method and a simpler method which we designate as the "classic" method. In the "classic" method, the grid and the point potentials are fixed during the experiment, without charging current control. According to the theory presented in section 2.1, the potential of the grid limits the maximum potential that the surface of the coating can reach. We performed experiments with fixed grid potentials of - 0.4, - 2 and - 2.5 kV, which means that, in theory, the maximum surface potential that the samples could reach would be -0.4 - 2 and - 2.5 kV, respectively. Despite the fact of being a simpler method, it may be as effective as the constant current method, precisely because it is simpler and could be easier to implement at an industrial level. During the course of this topic, the differences between both methods and what each one can offer will be discussed.

We recall that TSDC is the experimental technique that was used to measure stored charge density in the samples. Further, this technique is also able to provide an estimate of the stored charge stability, for example, the time required for total discharge at RT. These

are the physical quantities that are relevant to ascertain in the context of this work and the medical application of the samples: stored charge density and its temporal stability. If we would charge a PS Hap coating, but the discharge time would be a few hours or less, then it would not be practical to charge them since the stored charge would not produce its effect *in vivo*. Similarly, if the stored charge density magnitude would be too low, in the 10^{-7} C/cm^2 magnitude or below, then it probably would not produce any significant enhancement of the bioactivity level. We recall that since most of the reported stored charge densities are in the 10^{-6} C/cm^2 range, it is generally assumed that stored charge densities in that magnitude are required to produce a significant bioactivity enhancement [45].

When we started the first charging experiments on the PS coatings, an issue was detected when we were going to perform the TSDC measurements. In these measurements, we need to apply an electrode in the surface of the coating, so that we can measure the depolarization current in function of the temperature. Accordingly, we painted the surface of the charged samples with a special high-temperature silver conductive paste (PELCO® High-performance Silver Paste), with a maximum service temperature of 927 ºC. After letting the silver paste cure at RT, the electrical resistance of all the samples, measured with a conventional multimeter, dropped sharply from resistances in the order of 10 MΩ down to the point of the coating practically being in short-circuit with the Ti substrate. The conclusion is that already at RT, there is significant diffusion of silver into the coating, and it is our opinion that such diffusion should occur along the cracks that these coatings may contain. In figs. 1.41, 1.43 and 1.46, such cracks can be observed. The PS coatings are commonly relatively dense (for example, Hap coatings with relative densities near 90% of the theoretical are reported [109]), however, these cracks may act as regions through which the silver diffusion can take place. Anyhow, as we will show, these coatings can be charged up to high surface potentials, meaning that the possible existence of the cracks does not cause any hindrance to a successful charging of these coatings through the corona triode.

One of the main advantages of a constant current method is allowing to be sure that we are effectively charging our coatings despite the fact that we are not able to perform the TSDC measurements on them. It does not provide information about the temporal stability

of the stored charge, but it allows to affirm without doubt that the coatings can be charged. Fig. 3.13 shows surface potential buildup curves for two PS Hap coatings charged with a constant current of approximately - 1 nA, at 200 ºC and for a fixed discharge potential of - 15 kV. As we mentioned before when discussing the calibration curves, we decided to set the potential discharge as - 15 kV for all the samples. In addition, the point/sample and grid/sample distances are fixed at 7 cm and 4 mm, respectively, for all the samples. The dimensions of the samples are 10x10x1 mm (we cut the original 25x25x1 mm samples into smaller pieces). We show the data exactly as we get it through the feedback software, it is not smoothed or manipulated. All the samples display surface potential buildup curves with the same characteristic shape shown in fig. 3.13. They start with approximately linear behaviour and subsequently a sublinear behaviour is observed, where the surface potential increases at a slower rate up to the saturation value. Note in fig. 3.13 how the surface potentials start with a high value in the initial time of the experiment. If we started the charging experiments with very low grid potentials, the charging currents would be extremely low (far below - 1 nA) and experiments would take a lot of time. Thus, what we do is to start with a high grid potential value so that the charging through the sample is near the desired value of - 1 nA. Then we start the feedback program which controls the grid potential in order to try to maintain the charging current around - 1 nA. The rationale behind the feedback circuit is to perform a "fine-tuning" of the grid potential at a rate defined by the "Sampling" parameter, not to sharply increase the grid potential until the desired charging current of - 1 nA is reached and then to perform the "fine-tuning". In future work, the control software will be expanded in order to include a new initial first stage, prior to the "fine-tuning" stage, responsible for rapidly increase the grid potential up to the value which leads to desired charging current. Currently, this initial stage is performed manually.

Another question that needs to be clarified is charging current value (- 1 nA in the case of fig. 3.13). Some authors usually present a charging current density value, where density refers to the area of the sample exposed to the discharge. Others present a current value (not a current density), as we do, and that current value refers to the total current in the measurement electrode area. In this way, the determination of the gap potential drop

through the calibrations curves is direct, since the calibrations are performed only with the measurement electrode. Thus, for a charging current of - 1 nA, the calibration curve displayed in the bottom plot of fig. 2.22 gives us the correspondent gap potential drop, which is around - 93 V. But we can also indicate easily what is the current density in the samples correspondent to - 1 nA in the measurement electrode, which in our system has an area of approximately 0.71 cm^2. Accordingly, the charging current density in the samples is - 1.4 nA/cm^2, which is around the same values that classically have been used to charge polymer foils. It should be noted that, actually, the charging current density is independent of the sample size and is equal to the charge density in the measurement electrode, as long as the sample area is larger than the area of the electrode. Indeed, when using the constant current method, the samples have to cover all the electrode, i.e., we cannot have the electrode directly exposed to the discharge, otherwise the current flowing through the sample cannot be controlled.

One fact that we observed in the many samples that were charged is the following: in some aspects, they present different behaviors. While the surface potential buildup curve shape is similar, different samples may reach different saturation surface potentials and may take distinct times to reach such potentials. The saturation potential is related to the amount of electric charge that the particular sample can store since electrons are being trapped. Given the "violent" nature of the PS process, although macroscopic properties of the coatings may be fairly reproducible (thickness, average surface roughness, adhesion strength, ISO requirements are fulfilled, etc.), more specific properties such as surface area and density of traps maybe not reproducible, explaining why the samples present different behaviors. Nonetheless, the saturation potential in almost all of the samples which we charged (most of them for the *in vitro* biological tests) falls within the - 1400-1800 V range. Considering the average thickness of samples (70 μm), the electric field across the samples is in the ~ 200 - 257 kV/cm range, surprisingly high values, especially considering that conventional contact polarization of Hap employs electric fields magnitudes in the 1 - 5 kV/cm range, however, at higher temperatures (250 - 500 ºC). As we referred, one of the advantages of the corona triode charging is precisely allowing to charge dielectric materials up to higher surface potentials, because the absence of two electrodes guarantees that even

localized dielectric breakdown events do not disturb the charging experiment, while a two-electrode measurement configuration would become short-circuited.

During the charging, the total current density across the dielectric sample can have two contributions, the conduction and the displacement currents, according to equation 39 [84, 85]:

$$J_0 = J_c(x,t) + \frac{\partial D(x,t)}{\partial t} \tag{39}$$

where the first term is the conduction current density and the second term is the displacement current density. Recall that, as referred in section 2.1, for simplicity purposes, the physical quantities are assumed to be independent of the lateral position coordinate, depending only on the vertical coordinate x perpendicular to the sample. This is a general approach in the literature concerning the corona discharge. The electric displacement is given by equation 40:

$$D(x,t) = \varepsilon_0 E(x,t) + P(x,t) \tag{40}$$

In the Hap case, as we will explain later, the dipolar polarization component can be disregarded compared to the contribution of the trapped spatial charge. For materials where the polarization term P(x,t) is not much significant, equation 40 is generally rewritten as including the polarization term in the first term, according to equation 41 [84, 85]:

$$D(x,t) = \varepsilon_0 \varepsilon_r E(x,t) \quad [assuming\ that\ in\ a\ linear\ medium\ P(x,t) \cong \chi \varepsilon_o E(x,t)] \tag{41}$$

where ε_r is the dielectric constant of the sample and χ is the dielectric susceptibility.

Upgrading equation 39 according to equation 41 yields:

$$J_0 = J_c(x,t) + \varepsilon_o \varepsilon_r \frac{\partial E(x,t)}{\partial t} \tag{42}$$

For an insulating material the conduction current component can be disregarded, thus equation 42 can be written as:

$$J_0 = \varepsilon_0 \varepsilon_r \frac{\partial E(x,t)}{\partial t} \xLeftrightarrow[Integration\ over\ sample\ thickness]{} \frac{I_0}{C} = \frac{dV(t)}{dt}; where\ C = \varepsilon_0 \varepsilon_r \frac{A}{L} \tag{43}$$

where C is the sample capacitance, A is the area and L the thickness of the sample. As will be discussed, the conduction current term in equation 42 can in fact be disregarded in the initial time of a corona triode charging experiment. Analyzing equation 43, if the potential buildup of the sample is linear, it is a strong indication that current through the sample is dominated by the capacitive component and that the charge being deposited on the sample is essentially at a surface level, otherwise the potential would not increase linearly with the time [85]. In a material like Teflon, for example, a high insulator nonpolar polymer, the surface potential buildup is linear practically all the charging time. According to equation 43, it is possible to calculate the sample capacitance through the slope of the potential buildup curve. Moreover, samples with lower thicknesses will have lower slopes because they have a higher capacitance, thus they require more time to be charged. For instance, Giacometti and Campos calculated the capacitance of Teflon foils with different thicknesses through the constant charging current method, and the obtained values agreed within 3% with the values obtained using a capacitance bridge [85]. Observing the typical potential buildup profiles of our samples in fig. 3.13, they tend to show an initial linear behavior that can be associated with a capacitive dominance on the charging current, suggesting that the charge is being stored at a more superficial level. The sublinear behavior indicates that the conduction term (charge leakage) starts to be relevant, although the surface potential continues to increase more slowly. This sublinear behavior is also associated to charge injection and trapping at a bulk level in the sample, which is also desirable when considering *in vivo* applications. As discussed before, when inside the body, part of the bioactive coating is replaced by new biologic bone, and this replacement takes place not only at a superficial level, thus the existence of stored charges at a bulk level is a very positive factor. Taking into account that we are working with polycrystalline Hap coatings subjected to a "violent" thermal deposition process, high levels of bulk charge trapping are to be expected. When the saturation potential is reached, the current through the sample is only determined by the charge leakage through the sample, i.e., it is purely a conduction current. Regarding the polarization term, the second term of equation 40, it can be relevant in samples with a strong polar character, for example, the well-known β-PVDF ferroelectric and piezoelectric polymer. Giacometti and Campos have shown in their brilliant work that

the potential buildup of these polymers display an initial linear stage, then a plateau where the potential increases very slowly, and then, after the plateau, the potentials increases quickly to the saturation value. The plateau corresponds to the development of the ferroelectric dipolar polarization in the sample: the development of the dipolar polarization compensates the charge that is being transferred by the corona ions and thus the potential buildup shows a plateau. When the ferroelectric polarization reaches its saturation, the potential increases up to the saturation point. It is even possible to estimate the remanent (or permanent) ferroelectric polarization: the constant charging current density multiplied by the time duration of the plateau provides an estimate of the remanent polarization [85, 87]. This estimation is valid assuming that the conduction current through the sample is negligible during the plateau stage, which is true in low humidity atmospheres [85, 87]. This demonstrates the importance of low humidity atmospheres when performing these experiments, a factor which was considered in the development of our experimental system.

In Hap, we know that polar effects are usually weak, especially in polycrystalline materials with grains in the micrometric range. As it was discussed in topic 1.1.8, two depolarization mechanisms are described in the literature regarding TSDC measurements of Hap: the defect pair and the space charge mechanisms. Further, if the polarization is performed with high enough process thermoelectric parameters (temperature and electric field) the defect pair dipolar mechanism is negligible compared to the space charge process. We recall that in previous work we found that, for process parameters that tend to saturate the stored charge density, the defect pair dipolar mechanism had a contribution of only about 3.6% to the total stored charge, while the space charge accounted for 96.4%, approximately. Thus, it is no surprise that no detection of any plateau related to the development of a dipolar charge in our samples, since its contribution to the stored charge density is very small. The idea of using the corona triode to charge Hap coatings was in part fueled from our previous work, where we learned that Hap is able to store a significantly large space charge density.

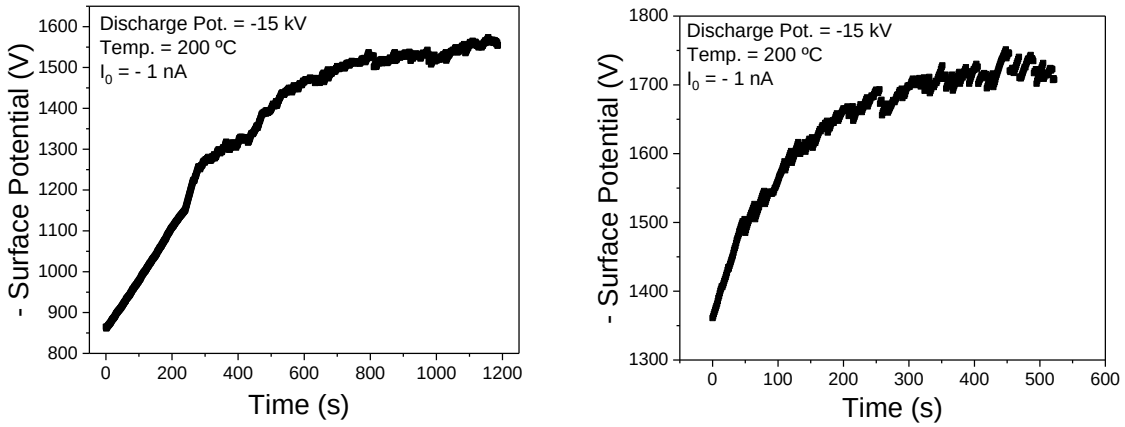

Figure 3.13 The surface potential buildup curves for two PS Hap coatings charged with a constant current of - 1 nA.

The charging current versus time data correspondent to the sample in the left plot of fig. 3.13 is presented in fig. 3.14. The right plot shows a magnification of the 200-300 s time interval. The majority of the experimental points, i.e., charging current values, are concentrated around the defined value of - 1 nA. The magnification plot makes this picture clear, showing a strong concentration of current values around - 1 nA, most of them fluctuating between - 0.9 and - 1.1 nA, constituting excellent current controllability. Fig. 3.14 also makes clear that there are events where the current increases more pronouncedly, notably those few where the current reaches the 10^{-8} A order of magnitude. These rarer events where the current increases significantly can be assigned to localized electric discharges through the sample. Additionally, they tend to occur for higher times, suggesting the charge accumulation may promote localized discharge events. These regions where the discharges occur may be charged again while the sample is exposed to the discharge. Nonetheless, by any means, they compromise the experiment and the potential buildup, as fig. 3.13 demonstrates, their influence is only manifested as some oscillations on the potential buildup curve. Considering our samples and the application they are intended for, the occurrence of these events and surface potential oscillations are not a problem, as long as the surface potential saturates and a large and stable stored charge

density is produced. Nonetheless, an approach to reduce or even eliminate the occurrence of the discharge events is to charge these coatings with lower current values, keeping in mind that the samples would take more time to reach the surface saturation potential.

The charging current versus time data distribution in fig. 3.14 is presented as providing an example of the data distribution for a PS Hap coating charged in our corona triode. Some samples may present similar data distribution while others may present more or less dispersion, i.e., more events where the current increases significantly.

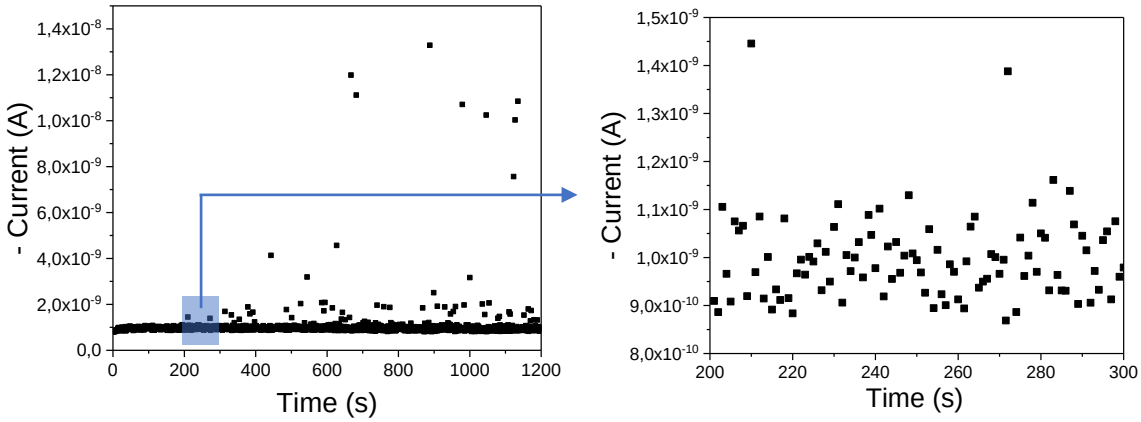

Figure 3.14 The charging current versus time data correspondent to the sample in the left plot in fig. 3.13. The right plot shows a magnification of the 200-300 s interval.

Another factor responsible for some of the fluctuations in the potential buildup curves, like those observable in the right plot of fig. 3.13, notably when the saturation potential is being reached, is our picoammeter. In the - 2-3 nA range of currents, the picoammeter changes its range. This change of range, which obviously occurs in events where the charging current increases, causes some "noise" or oscillations in the potential buildup. For instance, in the right plot of fig. 3.13, near the end, some small discontinuities in the curve are visible, caused by the change of range in the picoammeter. Some of these discontinuities can also occur for lower charging times, depending on the data dispersion presented by each individual sample. However, in a "macro" analysis, the potential buildup curves are still relatively smooth and clean, clearly allowing the visualization of a

characteristic shape for all the samples. For the referred reasons, we avoided charging currents in the - 1.5-3 nA range. It is not a significant loss, however, since that for materials where space charge is being injected, it is important to use low charging current values in order to promote charge trapping at a surface level [85, 110]. Higher charging currents may give primacy to bulk injection and/or increase of the conduction current contribution and therefore increase the charge leakage through the sample. Furthermore, they can also cause much more oscillations in the potential buildup and instability in the charging current. Fig. 3.15 makes clear these issues, strikingly regarding the charging current instability. Notice how the potential buildup is much more unstable and "noisy" compared to the samples charged with - 1 nA, and how this instability is observed in most of the experiment time. The charging current values are also much more dispersed, and the events where the current is significantly higher tend to occur along all the experiment time, in contrast to fig. 3.14. The fluctuation of values around - 3.5 nA, where most of points are, is much higher compared to fig. 3.14. Despite the charging current being approximately 3.5 times higher than the one of the samples in fig. 3.13, the time required for the potential to reach the saturation region is comparable to the sample of the left plot in fig. 3.13. This can mean two things: the first is that that the conduction current contribution through the sample is much higher in the - 3.5 nA case, otherwise, the sample should reach the saturation potential much faster, even considering that the samples present different behaviors, as we mentioned. The second is a favoring of charge trapping at a bulk level instead of a surface level, which can be allied to an increased conduction current through the sample. Moreover, of all the charged coatings, it was clearly the one which achieved the lowest surface saturation potential, another indicator of an increased conduction current through the sample and/or the possibility of the enhancement of charge trapping at a bulk level. Taking into account these reasons, we decided to adopt the - 1 nA charging current for all the samples, especially for those prepared for the *in vitro* biologic tests.

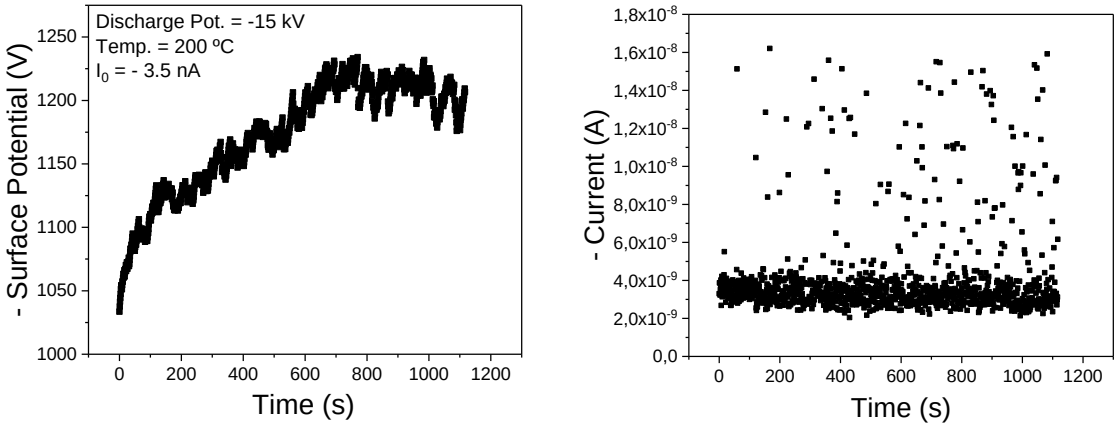

Figure 3.15 In the left: the surface potential buildup curve for a PS Hap coating charged with a constant current of approximately - 3.5 nA. In the right: the correspondent charging current versus time data.

As referred, we are not able to perform TSDC measurements on the coatings. However, we adopted a complementary strategy: Hap pellets were prepared from the same commercial powder used in the PS process, were charged with the corona triode and then we performed the TSDC measurements. The objective is to find out if somehow if we can infer some information regarding the coatings through the pellets results. The pellets, with 20 mm of diameter, were prepared using a hydraulic press. The mass of powder used was always 700 mg, leading to a thickness of about 1 mm when applying a tension of 9 tons for 5 minutes. The pellets were subsequently sintered at 1150 ºC for 2 hours. One of the prepared pellets is shown in fig. 3.16.

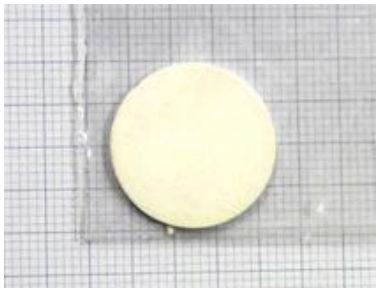

Figure 3.16 Photograph of one of the Hap pellets prepared from the same Hap commercial powder used in the PS process.

As explained at the beginning of present topic, two charging methods were employed in the pellets: the constant charging current method, the same employed in the

coatings, and the "classic" method". We will start by addressing the "classic" method results. In this simpler method, we do not need the feedback software, the discharge and grid potentials are fixed for a given time (including during the cooling of the sample), where the grid potential corresponds, theoretically, to the maximum value that the sample surface potential can reach. Contrarily to the constant charging current method, we do not know, at the end of the experiment, the surface potential that the sample reached. In fig. 3.17, the TSDC spectra of two pellets charged through the "classic" method are presented. The TSDC measurements were performed with a heating rate of 5 ºC/min and the depolarization current was measured using a Keithley 617 electrometer. The temperature was controlled by a Eurotherm 3508 controller.

In the left spectrum of fig. 3.17, the grid potential was fixed at - 2 kV, while in the right spectrum it was fixed at - 2.5 kV, which is the maximum value that the voltage supply can provide. A clear depolarization process is observable on both spectra, right before the intrinsic ionic conductivity of Hap starts to increase exponentially, around the 700-750 ºC temperature range. Compared to our previous work, where we polarized Hap and Hap-based bioceramics through conventional contact polarization [34], one difference is that in this case the depolarization process, which we broadly identify as the detrapping of the injected space charge, is located before the intrinsic ionic conductivity of Hap starts to increase exponentially. In that work, the process assigned to space charge detrapping (accounting for about 96.4% of the total stored charge) was located at higher temperatures, overlapping with the intrinsic conductivity and detected as a "shoulder" in the spectra [34]. However, the situations are different and comparisons are not straightforward: the space charge caused by the conventional polarization is due to the migration of H^+ protons along the c-axis which accumulate in the grain boundaries, while H^+ vacancies accumulate in the opposite side (this is discussion is included in topic 1.1.8). While the mechanisms are understood for the conventional polarization, in this work we are doing something new and different, we are injecting electrons in the sample, which are trapped at surface and bulk levels. The explanation at a more fundamental level of the TSDC spectra of our samples taking into account the negative charge transferred by the corona ions to the sample and the mechanisms behind the conventional polarization is a future work subject.

Our intent in this work is to demonstrate for the first time that we can charge Hap bioceramics using the corona triode and to perform TSDC measurements in order to calculate the stored charge density and estimate its temporal stability, which are the most important parameters considering the medical and biological applications of our samples. Nonetheless, we broadly identify the depolarization peaks detected in our samples as resulting from a thermally activated space charge detrapping.

The red straight lines in fig. 3.17 represent the fitting of the depolarization peaks, performed using the Origin software. For the fitting procedure, we implement a baseline correction, because a small contribution of the intrinsic exponential ionic conductivity has to be subtracted to the depolarization peaks, explaining why the cumulative fitting curve does not match exactly with the experimental data. Moreover, the criteria for all the fittings, including those in fig. 3.18, was to achieve an R^2 value ≥ 0.99. In fig. 3.20 we include a more detailed example showing the fitting process. These fittings allow to perform more accurate calculations of the stored charge density and its stability. These parameters will be shown later in a global table including all the different samples.

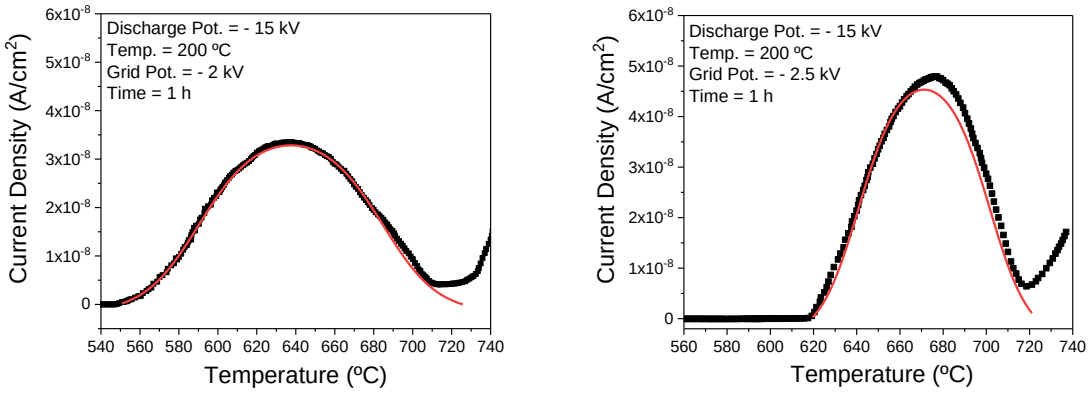

Figure 3.17 TSDC spectra of two pellets charged through the "classic" method. In the left: the grid potential was fixed at - 2 kV. In the right: the grid potential was fixed at - 2.5 kV. The red straight lines represent the fitting of the depolarization peak.

With respect to the constant charging current method, fig. 3.18 displays the TSDC spectra of samples charged with different current values: - 1, - 3 and - 3.5 nA, as indicated in each individual spectrum. The surface potential values saturated at approximately - 326, - 342 and - 294 V, respectively, as indicated in each particular spectrum. Moreover, the potential buildup curves have the same characteristic shape visible in fig. 3.13, which was already discussed. While the sample charged with - 1 nA presents a spectrum with one clear depolarization process, like the samples charged through the "classic" method, the samples charged with larger currents present two depolarization peaks. The peak centered at lower temperatures seems to be especially favoured for larger charging current values, comparing the - 3 and - 3.5 nA samples. In the pellets it becomes very hard to control charging currents above - 3.5 nA, probably due to their large thickness (1 mm) and electrical resistance. We recall that the corona triode has been traditionally used to charge/polarize polymers in film/foil form with thicknesses below 100 μm [84, 87]. Nonetheless, the current in the pellets can be fairly controlled for lower current values, although the control is much better in the coatings, as it will be shown.

It is interesting to note that the sample charged with the highest current presents the lowest saturation surface potential. Consider table 3.1, which presents the stored charge density and the discharge time at RT for the pellets charged through the "classic" and constant current methods. The sample charged with - 3.5 nA has the larger stored charged density although it reaches the lowest surface potential, meaning that the increase of the charging current promotes charge trapping at a bulk level and not at a surface level. This is in agreement with what we discussed for the PS Hap coatings charged with - 1 and - 3.5 nA: likewise, the coatings charged with the highest current values tend to reach the lowest saturation potentials. For the pellet charged with - 3 nA this behaviour is not observed, suggesting that the charge trapping at a bulk might not be yet dominating for this particular charging current value. The explanation for the appearance of a second depolarization process at higher currents, which seems to increase with the charging current, is suggested as future work. In chapter 4, section 4.2, we provide some insights regarding the procedure to adopt in order to obtain more detailed information about the depolarization processes.

Observing table 3.1, the stored charge density values, calculated through equation 28 (section 2.2) for all the samples, are very encouraging even for the samples charged through the "classic" method, which present lower values than the constant current samples. The literature demonstrates that the significant increase of the bioactivity level of Hap is observed both *in vitro* and *in vivo* for stored charge densities in the 10^{-6} C/cm^2 magnitude. Our samples are well above, in the 10^{-5} and 10^{-4} C/cm^2 magnitudes. The constant current method yields higher stored charge densities compared to the "classic" method. A possible explanation is that since the fixed grid the potential is very high in both cases (- 2 and - 2.5 kV), the current in the air gap reaching the sample is very high and the charge leakage (conduction current component) through the sample is much larger, therefore yielding a lower stored charge density. The calibration curves in section 2.1 (and also included in fig. 3.22) show how the current is already near - 20 nA for a grid potential of - 1 kV. In order to test this theory, we applied the "classic" method to a pellet, but with a smaller fixed grid voltage of - 400 V. Fig. 3.19 shows the results, which support our theory. The stored charged density increased compared to the samples where the grid potential was fixed at - 2 kV and - 2.5 kV, although it is still lower than the samples charged through the constant current method. However, with more extensive experiments, it is our opinion that one could find process parameters (grid potential and time) which could lead to stored charge densities similar to those presented by the constant current method. The idea of performing a two-step experiment could also be considered, i.e., to apply two different fixed grid potential values for a given time.

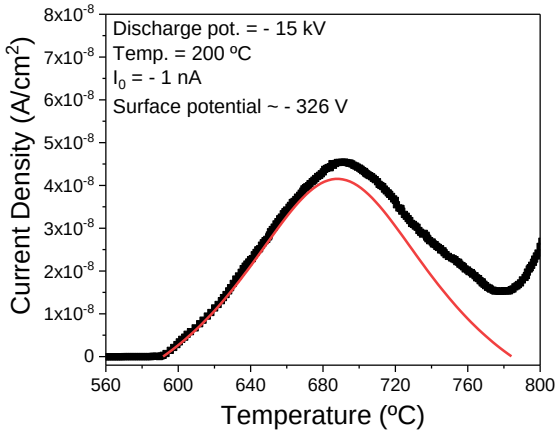

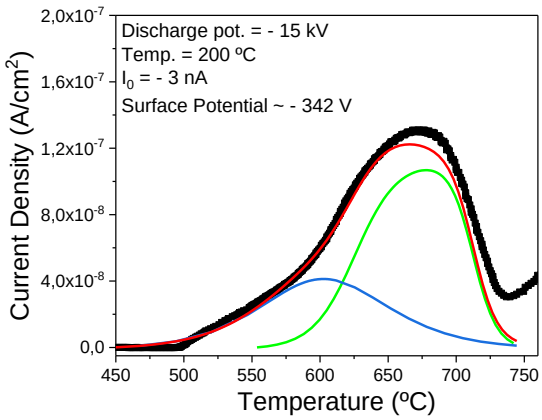

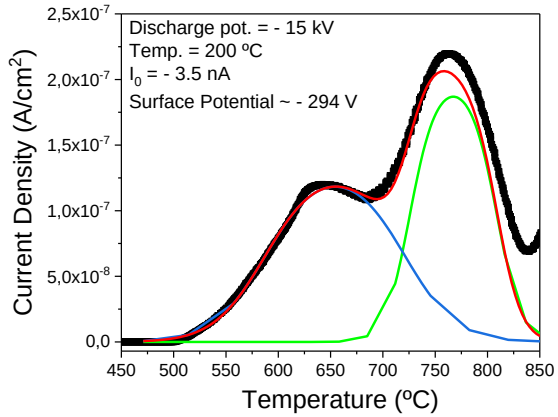

Figure 3.18 TSDC spectra of pellets charged with different charging currents: - 1, - 3 and - 3.5 nA, as indicated in each individual spectrum. The surface potential values saturated at approximately - 326, - 342 and -294 V, respectively.

Table 3.1 The stored charge density and discharge time at RT for the pellets charged through the "classic" and constant current methods.

	"Classic" method		Constant current		
	- 2 kV	- 2.5 kV	- 1 nA	- 3 nA	- 3.5 nA
Stored charge density (x 10^{-4} C/cm^2)	0.40	0.37	1.00	1.81	4.05
Discharge time at RT (months)	~ 7	~ 6	~ 15	~ 22	~ 13

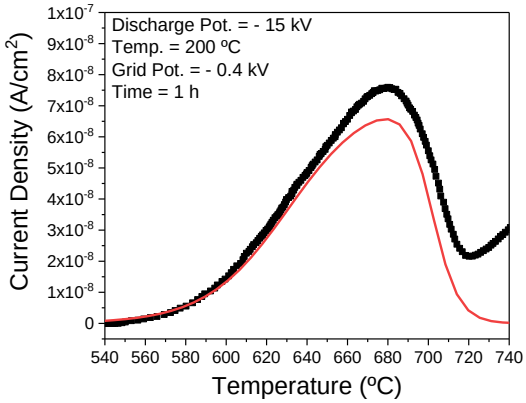

	"Classic" method
	- 0.4 kV
Stored charge density (x 10^{-4} C/cm^2)	0.64
Discharge time at RT (months)	~ 11

Figure 3.19 TSDC spectrum of a sample charged through the "classic" method, with a fixed grid potential of - 400 V. The stored charge density and an estimate of the discharge time at RT are presented in the table.

The stored charge temporal stability values, presented in table 3.1, are also highly encouraging. The discharge time at a given temperature (τ(T)) can be estimated according to equation 44:

$$\tau(T) = \frac{1}{\beta J(T)} \int_T^\infty J(T) dT \qquad (44)$$

where β is the heating rate. Equation 44 translates that an estimation of the discharge time at particular temperature T is given by the ratio between the charge stored by the sample and the short-circuit current measured at that temperature T. Table 3.1 shows an estimate for the discharge time at RT. The "classic" method yields lower discharge times because the stored charge density is lower compared to the constant current. Still, all the values are extremely interesting providing more than enough time for the stored charge to take its effect *in vivo*.

Fig. 3.20 includes a more detailed example showing some steps of the fitting procedure using the Origin software. This example corresponds to a sample charged with – 3 nA, in fig. 3.18. The intrinsic ionic conductivity is fitted with an exponential function ($y = y_0 + A\exp(R_0 x)$), as it is visible in the left spectrum of fig. 3.20. The R^2 value of this particular fitting is 0.9996(…). This exponential is the baseline which we have to subtract to

the spectrum, yielding the subtracted spectrum shown in the right plot. At this point, we only have the contribution of the depolarization processes to the depolarization current, thus we can proceed with the fitting. The subtracted spectrum is fitted using the Asym2Sig (asymmetric double sigmoidal function: $(y = y_0 + A\frac{1}{1+e^{-\frac{x-x_c+w_1/2}{w_2}}}\left(1-\frac{1}{1+e^{-\frac{x-x_c-w_1/2}{w_3}}}\right))$ function, which allows to fit peaks that may be characterized by a certain degree of asymmetry. The condition for the fittings was to achieve an R^2 value ≥ 0.99, which is fulfilled for all the samples. In the particular case of fig. 3.20, two depolarization peaks have to be considered, otherwise the fitting will not converge. In this particular fitting, the R^2 value is 0.998(…). The stored charge density and its stability are then calculated

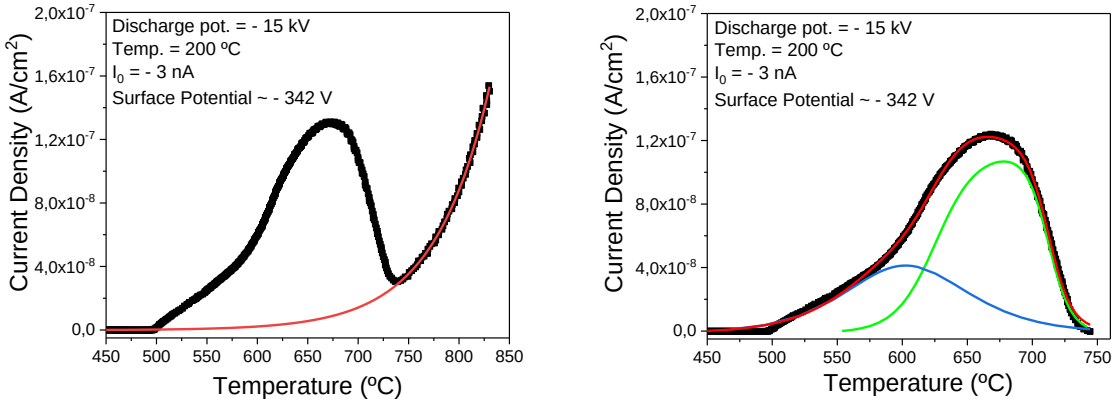

Figure 3.20 A more detailed example of the fitting procedure, adopted to all the samples, using the Origin software. This particular example corresponds to the sample charged with - 3 nA, in fig. 3.18. In the left, the TSDC spectrum is fitted with an exponential function, in order to get the baseline. In the right, the subtracted spectrum is fitted using Asym2Sig functions.

As was aforementioned, the current control is much better in the coatings. Fig. 3.21 corroborates this fact by comparing the current versus time data distribution of the coating charged with - 1 nA (in the right plot in fig. 3.14) with the data for the pellet charged with - 1 nA. The data in fig. 3.21 shows how the current values are more concentrated around -1 nA in the coating, fluctuating between - 0.9 and - 1.1 nA, while the pellet shows a larger dispersion amplitude around - 1 nA. The much larger thickness of the pellets (1 mm versus an average of 70 μm for the coatings) implies that the probability of larger fluctuations in

the charging current is much higher in the pellets. Nonetheless, the current controllability is still reasonable in the pellet. However, for higher charging currents, as it was observed in the coatings, the current controllability also decreases for the pellets, as the current versus time data dispersion for the pellet charged with - 3.5 nA, also presented in fig. 3.21, suggests. Still concerning the data presented in fig. 3.21, the mean and standard deviation values of the data, in the particular time interval between 200-300 s, are presented in table 3.2. For the coating, we did not include the two current points which clearly are out of the baseline (fig. 3.21), where most of the points are oscillating around - 0.9 and - 1.1 nA. The results in table 3.2 support our analysis of fig. 3.21. The charging current mean values for the coating and the pellet charged with - 1 nA are very close to the defined value, but the standard deviation of the data is higher for the pellet. The pellet charged with - 3.5 nA presents a mean value, in this time interval, above the defined value, and the largest standard deviation.

One could argue that comparing the pellets results in table 3.1, that the ratio between the mean current and the standard deviation, also known as the coefficient of variation, is actually slightly lower for the - 3.5 nA pellet compared to the - 1 nA (0.19 vs 0.23). Thus, one could affirm that current controllability is slightly better for - 3.5 nA, because in terms of magnitude, the deviations relative to the medium value are slightly lower in the - 3.5 nA pellet. That would not be a correct analysis (or a practical one). When we discuss current controllability, actually, we cannot think only on the current values, it is also important to take into account in the context of the experimental technique that depends on the current oscillations. Consequently, it is relevant to acknowledge that variations of the charging current are associated with variations of the grid potential, of the sample surface potential and of the gap potential drop. Consider in fig. 3.22 the current versus gap potential drop calibration curve of the system, replicated from fig. 2.21, in order to allow better visualization. As the calibration curve shows, current oscillations around - 1 nA produce lower gap potential drop variations compared to oscillations around - 3.5 nA, because the former is in a region of the curve with a higher slope, compared to the - 1 nA region, which is a plateau-like region. Therefore, and observing fig. 3.21, current oscillations in the - 3-4.5 nA range produce higher gap potential drop and sample surface potential

oscillations compared to current oscillations in the - 0.75-1.25 nA range. Thus, the current controllability is better in the pellet charged with -1 nA. What matters is the magnitude of the variations of the charging current flowing through the sample and the way they affect the gap potential drop, which can be seen in the calibrations curves.

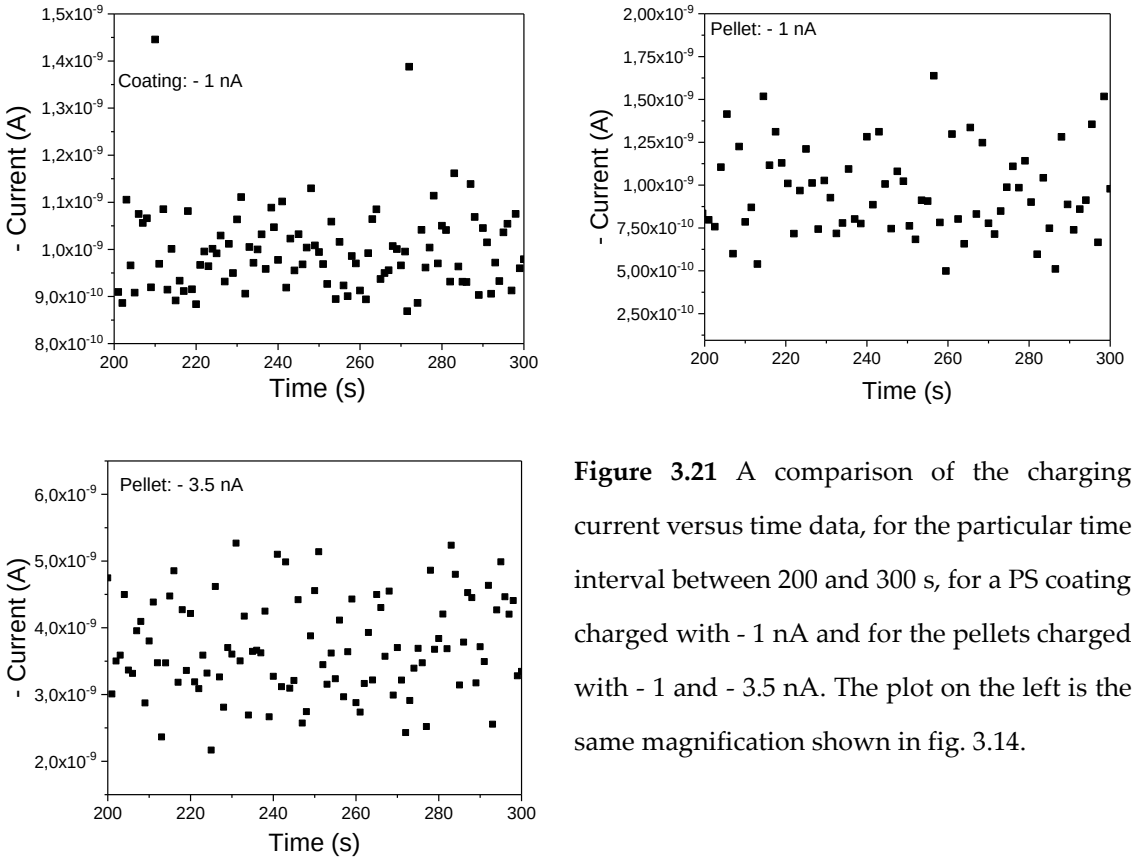

Figure 3.21 A comparison of the charging current versus time data, for the particular time interval between 200 and 300 s, for a PS coating charged with - 1 nA and for the pellets charged with - 1 and - 3.5 nA. The plot on the left is the same magnification shown in fig. 3.14.

The previous discussion, although not very important for our samples and their intended application, is important to be included in this work, especially for those who eventually might be interested in learning about the experimental particularities of the corona triode technique. Suppose that this technique would be applied in materials where surface potential oscillations should be minimized, for some particular reason. Based on our results and discussion, we can affirm that those materials would have to be charged with small charging current values, as small as possible, taking also into account the time required for the surface potential to saturate increases for lower charging currents.

However, despite the longer time, very smooth potential buildup curves would be obtainable.

Table 3.2 The mean and standard deviation values of the data presented in fig. 3.21, in the particular time interval between 200-300 s. The values for the coating do not include the two current points clearly are out of the baseline of points (see fig. 3.21).

	Coating: -1 nA	**Pellet: -1 nA**	**Pellet: -3.5 nA**
Mean Current (x 10^{-9} A)	- 0.99	- 1.03	- 3.70
Standard deviation (x 10^{-9} A)	± 0.07	± 0.24	± 0.72

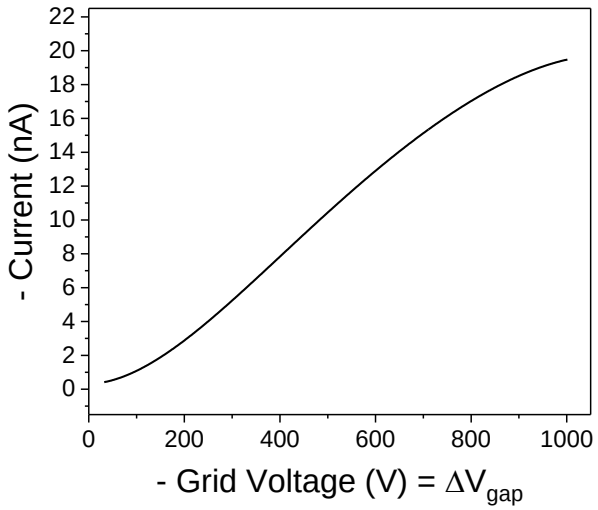

Figure 3.22 The current versus gap potential drop calibration curve of the experimental system, replicated from fig. 2.21. Current oscillations in the - 1 nA region produce less significant gap potential drop and, consequently, sample surface potential oscillations, compared to oscillations around - 3.5 nA.

As a small note, it is important to recall that, despite the fact that the coatings and the pellets have different areas exposed to the discharge (coatings - 10x10 mm squares; pellets - 20 mm diameter), the charge density in the samples is the same. Both the coatings and the pellets have larger areas than the measurement electrode, implying that the charge current density is determined by the electrode. Thus, when we compare in fig. 3.21 the

current versus time data for a coating and a pellet charged with - 1 nA, we are comparing samples charged with the same current density of - 1.4 nA/cm^2, making it a "fair" comparison.

Another difference between the pellets and the coatings concerns the occurrence of the localized discharge events through the sample. It was shown in figs. 3.14 and 3.15 that the coatings present these discharges, causing punctual significant increases in the measured charging current, especially for the coating charged with - 3.5 nA. These events are not detected in the pellets, as fig. 3.23 demonstrates. The current versus time data for the pellets charged with - 1 and - 3.5 nA, displayed in fig. 3.23, reveal the absence of significant discharge events. This does not mean that they do not happen, simply, the large thickness of the samples, combined with increased electrical resistance, may avoid that the increased current caused by these discharge events reach the measurement electrode.

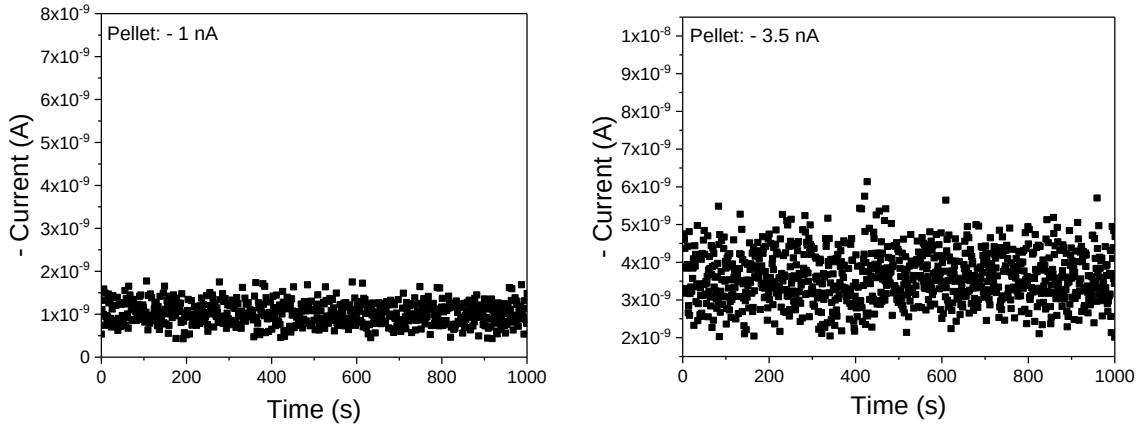

Figure 3.23 The current versus time data for the pellets charged with - 1 and - 3.5 nA, The plots reveal the absence of localized discharge events in the samples, in contrast with the coatings, notably the coating charged with - 3.5 nA (fig. 3.15).

Remember that the charging experiments on the pellets were comprised as a complementary strategy to find out if we can infer some information regarding the coatings, because we cannot perform TSDC measurements on them. We can, in fact, infer one important fact regarding the coatings. While the surface saturation potential of the

pellets, as indicated in fig. 3.18, reached values below - 350 V, the coatings reached much higher potentials, as fig. 3.13 attests.

3.2.3 Charge storage in the samples

Consider fig. 3.24, depicting an illustration of a Hap sample and the stored charge, at surface and bulk levels, after a charging experiment. The back electrode, in the case of the coatings, is obviously the Ti substrate, while for the pellets it can be interpreted as the measurement electrode. Fig. 3.24 displays essentially what is known as a real charge electret, containing trapped charges both at surface and bulk levels. An electret can also contain dipolar charges, defined as a dipolar charge electret. For instance, β-PVDF, a well-known ferroelectric polymer, is a dipolar charge electric, sometimes referred more specifically as a ferroelectret. Oliver Heavyside was the first to introduce the term electret, in 1885, defining it as dielectric material that has a quasi-permanent electric charge or dipole polarization. For the reasons explained before, we can disregard the contribution of dipolar charge to the total stored charge in Hap, therefore we do not include dipoles in the illustration depicted in fig. 3.24. The trapped charges create an intense internal electric field in the sample and also create external electric fields. As a small aside, the contemporary research activity on electrets is relatively low. The number of publications raised from about 100, in the seventies, up to around 300 in the last years (information from 2016 - [111]). It is also clearly a research field with more experimental practical knowledge than theoretical (we are not saying that the theoretical knowledge may not be practical!), explaining why many phenomena are not fully understood. For instance, how the crystallinity in a semi-crystalline polymer affects the charge trapping and stability or better models to describe how the temperature and humidity affect the discharge time. Frequently used electret materials are mainly polymers, such as Teflon and PVDF, P(VDF-TrFE) copolymer and FEP (fluorinated ethylene propylene) and also inorganic materials, such as SiO_2, Si_3N_4 and some SiO_2-based glasses [111].

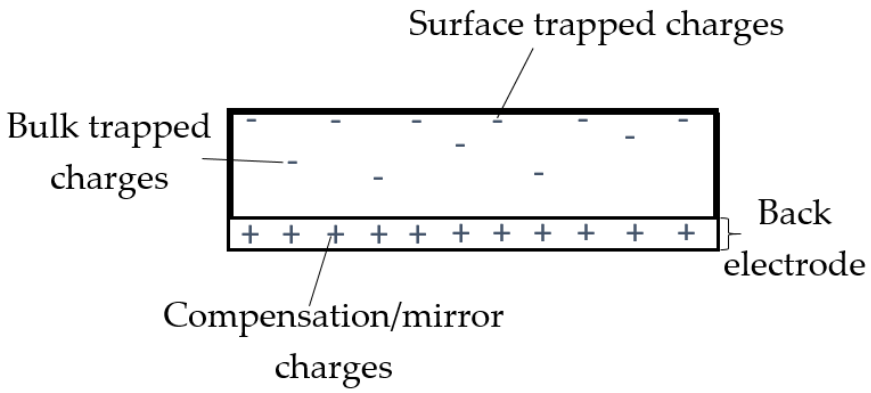

Figure 3.24 Illustration of the Hap sample and the stored charge, at surface and bulk levels, after a charging experiment. The back electrode, in the case of the coatings, is the Ti substrate while for the pellets it can be interpreted as the measurement electrode.

Actually, the charge storage in the samples is not fully explained by fig. 3.24. While analysing the data, we have made some developments in the understanding of charge storage in the samples. Recalling table 3.1, we saw that the magnitude of the stored charge in the pellets is in the 10^{-4} C/cm^2 range. Consider now fig. 3.25, which shows the surface potential buildup for a Hap pellet negatively charge with a current of - 3 nA (the same characteristic curve shape is observed for the other pellets charged with - 1 and - 3.5 nA. At the charging time of 2000 s (actually it is about 2150 s, because of an initial part we cannot follow due to the sample resistance) it is possible to see that the surface potential is in the saturation region, thus, according to the literature, it can be an indicator that charge storage in the sample is residual, as it has been described for polymers that present similar potential buildup curves, like Teflon [112]. However, it may not be the case in our samples.

Figure 3.25 Surface potential buildup for a Hap pellet negatively charged with a constant current of - 3 nA. The same characteristic curve shape is observable for the other samples charged with - 1 and - 3.5 nA.

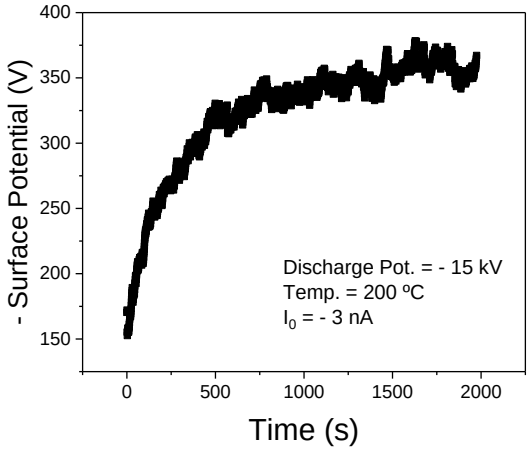

The following question arises: in 2150 s, what was the charge density deposited by the corona charge in the sample? This charge density is given by equation 45:

$$Q_{corona} \cong J_0 t_{charging} \quad (45)$$

where J_0 = - 4.2 nA/cm^2 (the charge density in the sample corresponding to I_0 = - 3 nA/cm^2, which is determined by the plane/measurement electrode). Applying equation 45 we get $Q_{corona} \approx 9 \times 10^{-6}$ C/cm^2. Observing Table 3.1 it is possible to see that this value, Q_{corona}, is significantly lower than the total stored charge measured in the TSDC. Thus, only the storage of the electrons transferred by the corona discharge cannot explain the total stored charge. However, there is a possible explanation for this result: we believe that in the potential saturation region the electrons transferred by the discharge are still being trapped in the bulk, not only those but also all the electrons that the sample continued to receive during the 30 min cooling step down to RT. Similarly to the conventional thermoelectrical polarization, in the corona charging, during the cooling step, the discharge and grid potential remain applied, to prevent any eventual discharge in the sample. Thus, the following question arises: why are the electrons still being trapped in the bulk, even during the cooling step? They are activating the space charge polarization mechanism in the Hap, which was explained topic 1.1.8 (see the discussion of figs. 1.12 and 1.13).

The reason why we are measuring in higher stored charge densities in the TSDC is because the field set up by the electrons in the bulk is able to activate up to a certain degree the Hap space polarization mechanism. In a previous work, where we have undertaken conventional thermoelectrical contact polarization on Hap pellets, we have measured stored charge densities in the 10^{-4} C/cm^2 magnitude for a temperature of 500 ºC and an applied field of 5 kV/cm [34]. Further, higher stored charge densities have been reported [refs]. The scheme in fig. 3.26 depicts the charge storage processes in our samples, updating fig. 3.24. As the scheme in the left shows, the electrons coming from the corona discharge are trapped at the surface and then in the bulk of the sample. In parallel, the electric field produced by the electrons trapped in the bulk will be able to activate the space charge polarization mechanism of Hap. This polarization will not develop in all the sample thickness, but starting from a given depth within the sample where the electric field is high

enough to activate it. As mentioned, the contribution to activate the Hap space charge polarization comes not only from the electrons transferred during the charging time correspondent to fig. 3.25, but also from the electrons that the sample kept receiving during the 30 minute cooling step. Additionally, it is known the corona current in the air gap current between the grid and the sample increases for lower temperatures [ref]. Thus, we are able to justify the total stored charge densities calculated through the TSDC measurements.

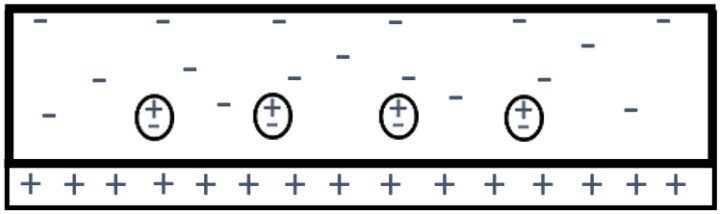

Figure 3.26 The contribution of the Hap space charge polarization in the samples. The electric field created by the electrons trapped in the bulk is able to activate the space charge polarization mechanism of Hap.

3.2.4 Stored charge at a surface level

Resorting to the electrostatic laws, the integral form of the Gauss's law generalized for a dielectric material can be written according to equation 46:

$$\oint \vec{D}.d\,\vec{A} = Q_t \tag{46}$$

where the left term is the displacement field flux and the right term can be interpreted as the total trapped space charge (Q_t), at surface and bulk levels, by the dielectric material (or, more rigorously, the space charge enclosed by the Gaussian surface associated to the surface integral). The displacement field, also given in equation 41, can be rewritten in a more general vectorial form as:

$$\vec{D} = \varepsilon_o \varepsilon_r \vec{E} \tag{47}$$

where ε_r is the dielectric constant of the dielectric material. Again, when considering Hap, we disregard the polarization component contribution to the total stored charge density by

the material, when compared to the contribution of the trapped space charge, at surface and bulk levels. Thus, we can rewrite equation 46 as:

$$\oint \vec{E}.d\vec{A} = \frac{Q_t}{\varepsilon_0 \varepsilon_r} \tag{48}$$

Equation 48 is considered to be a general form of Gauss's law. Consider a Gaussian surface that encompasses the superficial trapped charges along the surface of the sample, with a superficial area A. We can write the electric field magnitude as:

$$E = \frac{Q_S}{\varepsilon_0 \varepsilon_r A} = \frac{\sigma_S}{\varepsilon_0 \varepsilon_r} \tag{49}$$

where σ_S is the superficial charge density. One may be in doubt about equation 49, for instance, considering that in the coatings, with considerable average surface roughness, the infinitesimal surface area elements are not in the same direction of the electrical field. However, note that Gauss's law is valid for any closed Gaussian surface, with any irregular shape, so that one can choose any particular closed surface where all the infinitesimal surface area elements and electric field are in the same direction so that equation 49 is valid.

Considering the relationship $E = V_S/d$, where V_S is the surface potential and d is the thickness of the sample, we can rewrite equation 49 as:

$$\sigma_S = \frac{\varepsilon_0 \varepsilon_r}{d} V_S \tag{50}$$

According to equation 50, the surface charge density is proportional to the surface saturation potential and dielectric constant of the sample, being inversely proportional to the thickness. Thus, based on this information, we can infer the following fact: the superficial stored charge density in the coatings is much larger compared to the pellets (after we will make some estimations based on equation 50). The fact that the coatings are able to store such a larger superficial charge density can be explained, besides the thickness factor, in terms of superficial area and of the "violent" nature of the PS process.

The superficial area explanation can be understood by observing the illustration of fig. 3.27. Comparing the pellets and the coatings, for the same surface section dimensions, the increased surface area of the coatings allows them to store much larger amounts of

surface charge. The thermally "violent" nature of the PS deposition process (discussed on topic 1.2.3 and also section 1.3) is also another factor that can explain the increased surface charge density. The presence of a secondary phase (β-TCP), although below 5 wt%, and also of ACP constitutes heterogeneities that may potentiate charge trapping. The extremely high temperatures that the Hap powder particles experience during deposition, with partial or total melting taking place and the fast cooling rates, may also be a factor potentiating the creation of defects within the material's structure, and therefore trapping sites.

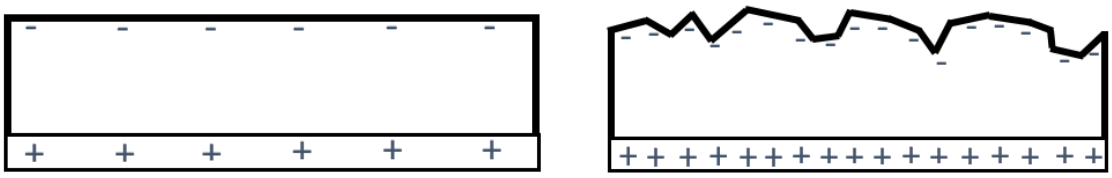

Figure 3.27 Assuming that the surfaces in the illustrations have the same dimensions, the increased surface area of the coatings, represented in the right, compared to the flatter surface of the pellets, in the left, is one of the reasons explaining why the coatings are able to store such a large surface charge density.

Based on equation 50, we can make some estimations for our samples. According to Gittings et al. we estimate the dielectric constant of our samples to be around ~ 25, at 200 ºC (remember that we charged the samples at 200 ºC) [37]. The pellets reached surface potential values between - 294 and - 342 V, while the coatings are in the - 1400-1800 V range. Let us assume a V_S (equation 50) value of 320 V for the pellets and 1600 V for the coatings. The thickness of the pellets is 1 mm while the average thickness of the coatings is 70 μm. Applying equation 50, the following values for the surface charge density are obtained: ~ - 7×10^{-9} C/cm^2 for the pellets and ~ - 5×10^{-7} C/cm^2 for the coatings. These estimates show us how the surface stored charge density is much larger in the coatings. Also, observing table 3.1, the stored charge in the pellets at a surface level is only a very small fraction of the total stored charge, showing, as expected, very high levels of bulk trapping. Concerning the coatings, although we cannot perform TSDC measurements to calculate the total stored charge density, we expect a similar behaviour. However, due to the much smaller average

thickness of the coatings, allied to the factors which were discussed (surface area and PS process), the surface charge density is much higher in the coatings. Regarding the stored charge temporal stability in the coatings, we can suggest that a larger stored charge density can be associated with longer discharge times compared to the pellets, as equation 44 shows. According to equation 44, even if the short-circuit current measured at a temperature T is higher in the coatings due to their smaller thickness (the electrical resistance diminishes for lower thicknesses), a much higher stored charge density can easily promote the increase the time of discharge.

Table 3.3 shows the electronic work function required to remove an electron from the surface, determined through photoelectron emission spectroscopy, of different samples: sample 1 is a pellet charged through the "classic" method (grid: - 2.5 kV, 1 h at 200 ºC); sample 2 is a pellet charged with constant current (- 1 nA, 200 ºC); sample 3 is a coating charged with constant current (- 3.5 nA, 200 ºC); sample 4 is a coating charged with constant current (-1 nA, 200 ºC). These experiments were made in collaboration with Prof. Dr. Yuri Dekhtyar, director of the Biomedical Engineering and Nanotechnologies Institute of the Riga Technical Institute, in Latvia. We sent some charged samples and a very brief explanation of the technique goes as follows: the samples are irradiated with UV light, scanning several wavelengths, in a high vacuum chamber (10^{-5} Pa) and the UV light causes the ejection of electrons from the surface of the sample. Through the ejected electrons, with proper detection equipment and data analysis, they are able to determine the work function required to remove an electron from the surface. Note that this is a superficial analysis, because the UV light is only able to penetrate a few nanometers into the sample. The rationale behind these measurements is the following: comparing two surfaces, the one with the highest surface potential must have a higher work function, because more energy is required to remove an electron from such surface. As it can be seen, the results on table 3.3 are in agreement with our corona triode charging experiments. We saw that the coatings reach much higher saturation surface potentials compared to the pellets and, as table 3.3 shows, the pellets present significantly lower work functions. Additionally, we saw that the coatings charged with higher charging currents (- 3.5 nA) tend to reach lower surface potentials compared to coatings charged with lower currents (- 1 nA). Accordingly, sample

3 presents a lower work function compared to sample 4. Thus, the photoelectron emission spectroscopy results corroborate and strengthen our charging experiments.

Table 3.3 The work function required to remove an electron from the surface of the samples. Sample 1 - pellet charged through the "classic" method (grid: - 2.5 kV, 1 h at 200 ºC); Sample 2 - pellet charged with constant current (- 1nA, 200 ºC); Sample 3 - coating charged with constant current (- 3.5 nA, 200 ºC); Sample 4 - coating charged with constant current (- 1 nA, 200 ºC).

	Sample 1	**Sample 2**	**Sample 3**	**Sample 4**
Work function (eV)	4.47	4.58	4.76	4.83
Standard deviation (eV)	0.04	0.03	0.04	0.04

As a small aside, it was referred at the end of topic 1.1.9, and also mentioned in the present topic, that some reports state that stored charge density magnitudes at least in the 10^{-6} C/cm^2 magnitude are required to produce significant differences in the biological response both *in vitro* and *in vivo*. It is obvious that the 10^{-6} C/cm^2 value is not a surface charge density. For instance, some reports where conventional polarization of bulk Hap samples is undertaken may lead to the wrong idea that the stored charge density calculated through TSDC measurements is at a surface level in the material [113], while in most of the charge is in the bulk of the material (grain boundaries, defects, etc.).

To finish the discussion contained in the present topic, we would like to make some comments regarding a hypothetic industrial application of the corona triode to charge Hap coatings in orthopaedic implants. Firstly, although we have demonstrated (directly on the pellets) that the charge is very stable, the rationale behind the preparation of an implant to be introduced in a patient should be to charge the coating in the implant shortly before its application *in vivo*. Therefore, the best possible service is being provided to the patient, even though the charged implants could have some "shelf life", in an appropriate environment with controlled temperature and humidity. Secondly, it seems to us that the most appealing corona triode method to be introduced in the production cycle of an implant with a charged

coating would be the "classic" method because it is easier to implement. It does not require a picoammeter, a feedback circuit controlling the grid potential and the charging current, all the connections to this equipment, etc. Additionally, as we have shown, it allows to obtain high stored densities, in the case of our pellets, already in the 10^{-5} C/cm^2 order of magnitude. An industrial section dedicated to the corona triode charging of the implants, through the "classic" method, could be imagined as containing several point electrodes evenly separated from each other, a large metallic grid below all the point electrodes and below the grid some implant holding structures where the implants could be placed. Ideally, these implant holders should rotate the implants while they are being subjected to the discharge. Depending on the demand, several implants could be charged at the same time, if necessary. Regarding the evenly spaced point electrodes, multiple needle cylindrical electrode structures could do the job, as fig. 3.28 shows [114]. Several of these structures could be installed side by side, covering areas as large as necessary.

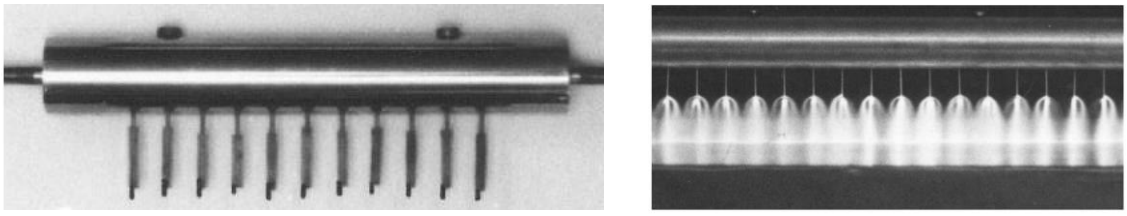

Figure 3.28 In the left: a multiple needle electrode structure. In the right: a positive corona discharge produced on such structure connected to a positive DC high voltage supply [114].

As a finishing note, in this manuscript, particularly in the present topic, we refer to the charging experiments in our samples as "corona triode charging of the samples". In the literature one can find the same expression "corona triode charging of the samples" or "corona triode polarization of the samples", some authors make the distinction. We use the term charging to because we are promoting extrinsic charge storage at surface and bulk levels in the samples. For instance, if instead of Hap our samples were to be ferroelectric polymer foils, probably we would use the "corona triode polarization" expression, due to the activation of the dipolar ferroelectric properties. In the same way, a real charge electret

is distinguished from a dipolar charge electret. Concerning the conventional polarization of Hap and its mechanisms, discussed in topic 1.1.8, we always write "conventional polarization of…" or "polarization mechanisms of Hap" or even "defect pair dipole and space charge polarization mechanisms". In the case of conventional contact polarization, the use of the word "polarization" is widespread. The use of "charging" in the corona triode may also useful to distinguish it from the conventional method: in the corona triode, we are injecting ("charging") charges in the sample, while the same is usually not happening in the conventional method. Therefore, it sounds right to say "corona triode charging ", while "conventional contact charging" would not sound right.

3.2.5 *In vitro* biological tests

As mentioned, the *in vitro* biological tests were carried out at the lab facilities of the CENIMAT (Center of Materials Research) research center, in the New University of Lisbon, through a collaboration with researchers belonging to the Soft and Biofunctional Materials Group (SBMG).

We sent 26 samples for tests, 13 control (not charged) and 13 charged. The corona triode charging experimental procedure was the same for all the coatings: they were charged at 200 ºC with a negative constant charging current of - 1 nA. Of the 13 charged samples, 7 were used in the SBF tests and 6 for the osteoblastic metabolic activity tests. All the samples have a square geometry with approximate dimensions of 10x10x1 mm.

As a small aside, fig. 3.29 shows how a sample is placed on the top of the measurement electrode, in the teflon support plate, for the charging experiment. Kapton insulating tape is used to fix the sample in the measurement electrode because it is able to withstand a temperature of 200 ºC. It can be also noticed in fig. 3.29 that we are not using the copper guard ring and that, even if the guard ring was placed in the ring-shaped slit, the sample would not cover or even touch it. The reason for this is actually very simple, something that we have learned as our knowledge on the corona triode developed. The guard ring can only be used in samples in which the face that is not exposed to the corona discharge, i.e., in contact with the measurement electrode and with the guard ring, is not

metalized. For metalized surfaces, like our coatings on the Ti substrates, the charging current flowing through the sample will flow through the guard ring connected to the ground and not through the picoammeter, because the picoammeter has always a certain internal resistance. Even considering that this internal resistance is small, the current will always flow through the guard ring because the "ground resistance" is always lower. Therefore, if our samples were in contact with the guard ring, we would not be able to measure the current and use the constant charging current method. The guard ring is used for example when charging polymer foils to avoid that eventual superficial current interferes with the measurement. However, for experimental systems with low atmospheric relative humidity levels (like ours), these superficial currents are negligible.

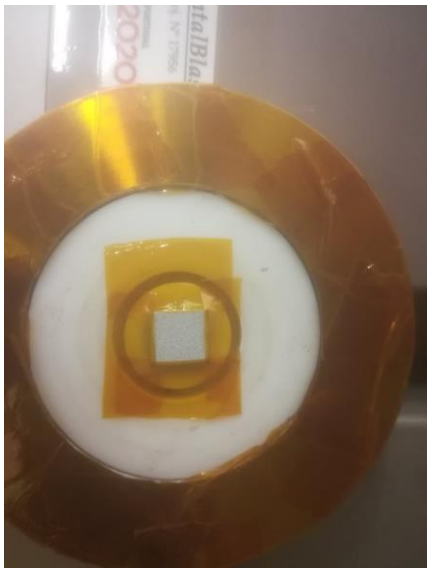

Figure 3.29 Photograph showing how a sample is placed on the top of the measurement electrode in the Teflon support plate. The sample is fixed on the measurement electrode using kapton insulating tape, able to withstand temperatures of 200 ºC.

Before discussing the biological results, it is important to have in mind the following fact: the time gap between the charging of the coatings and the performance of the biological tests is about one month. According to our results analyzed in the previous topic, we do not expect one month to be significant in terms of the discharge of the stored charge in the samples. Nonetheless, it constitutes a good opportunity to test our samples and results.

The first results, contained in fig. 3.30, show the osteoblastic cell proliferation in the charged and non-charged coatings, for increasing culture times. As discussed in topic 1.1.9, cellular proliferation is usually assessed by performing optical density measurements. The

results in fig. 3.30 corresponds to a ratio between the optical density of the charged and non-charged samples and the optical density of a cellular control population, as explained in section 2.5. The control population shows an expected behavior: a fast initial growth and later a slower growth rate, with the stabilization of the number of cells. It is also normal for the control population to increase faster than the samples in the first days. The control cells are seeded directly in the culture plate well, and the stabilization of their number, after an initial high growth rate, occurs because the surface area of the plate well becomes completely occupied with cells, therefore stabilizing its number. The samples results indicate that, for all the analyzed culture times, the osteoblastic proliferation is increased in the charged coatings, compared to the non-charged samples, becoming more evident for higher culture times (as it is the case of fig. 1.26). One month after charging, the stored charge is able to clearly promote the osteoblastic proliferation in the charged samples.

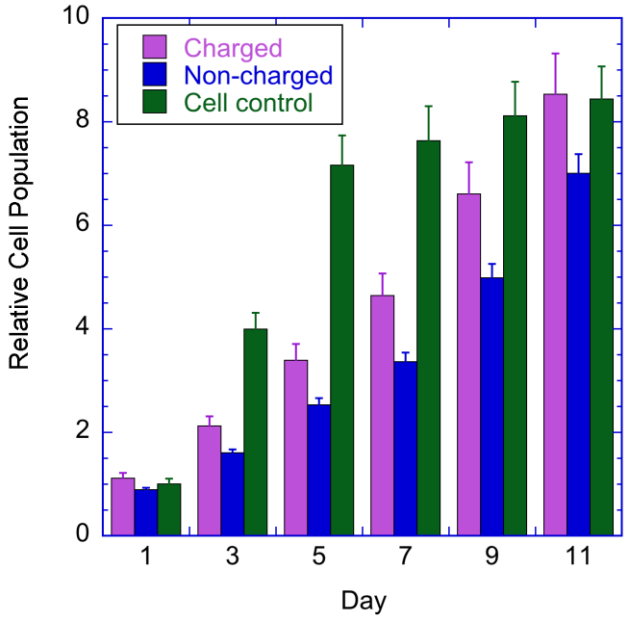

Figure 3.30 Osteoblastic cell proliferation in the charged and non-charged coatings, for increasing culture times. These results were obtained through optical density measurements.

Fig. 3.31 contains fluorescence images obtained after fixing and staining the osteoblasts after 5 days of culture in the coatings. The red fluorescence indicates the cytoskeleton of the osteoblasts, the blue fluorescence the osteoblasts nuclei and the green fluorescence the vinculin protein. Images (a), (b) and (c) - charged coating; (d), (e) and (f) - non-charged coating. The images correspond to an area of about 330 μm x 424 μm. The

fluorescence images in fig. 3.31 complement the resazurin proliferation information contained in fig. 3.30, by showing a clear and abundant osteoblastic proliferation in the charged and non-charged surfaces after 5 days of culture. The elongated morphology of the nuclei, the blue fluorescence in fig. 3.31, shows that the osteoblasts adhere and interact well with the coating surface. In surfaces where the osteoblasts do not adhere well, they would assume a round morphology, not elongated. The well-developed, projected and elongated cytoskeleton displayed in the red fluorescence images corroborate the strong osteoblastic adhesion and positive interaction with the surface. If the adhesion and interaction of the osteoblasts with the surface were poor, then, a well-developed, projected cytoskeleton would not be observable after 5 days of culture. Finally, the well-distributed green fluorescence translating the vinculin protein shows a strong bonding and adhesion between the osteoblasts and the surface of the coatings. The fluorescence microscope used in this work is not confocal, explaining why some out-of-focus spots are visible in fig. 3.31, taking into account the large surface roughness of the PS Hap coatings.

It should be noted that a qualitative analysis of the results in fig. 3.31 should be avoided, i.e., for instance, to compare images a) and d) and conclude that the osteoblastic adhesion and surface interaction is better in a) compared to d). Or to compare images c) and f) and conclude that the vinculin distribution along the surface is better in the charged coating compared to the non-charged coating. In fact, the conditions to be able to perform a qualitative analysis like the one contained in topic 1.1.9 for fig. 1.27 are very hard to obtain, only in very strict conditions such analysis can be correctly and confidently performed. For example, to perform such a similar analysis in our samples, we would have to be sure that the regions in fig. 3.31 contain exactly the same cell density, which is very hard considering the micrometric surface roughness of our coatings and also the fact that we are not using a confocal fluorescence microscope. Thus, the information contained in fig. 3.31 is interpreted as a complementary information concerning the proliferation results in fig. 3.30. While fig. 3.30 shows an enhanced osteoblastic proliferation in the charged coatings, fig 3.31 provides, after 5 days of culture a visual confirmation, of the osteoblastic proliferation and additionally that the osteoblasts have a positive interaction and strong adhesion with the surface of the coatings.

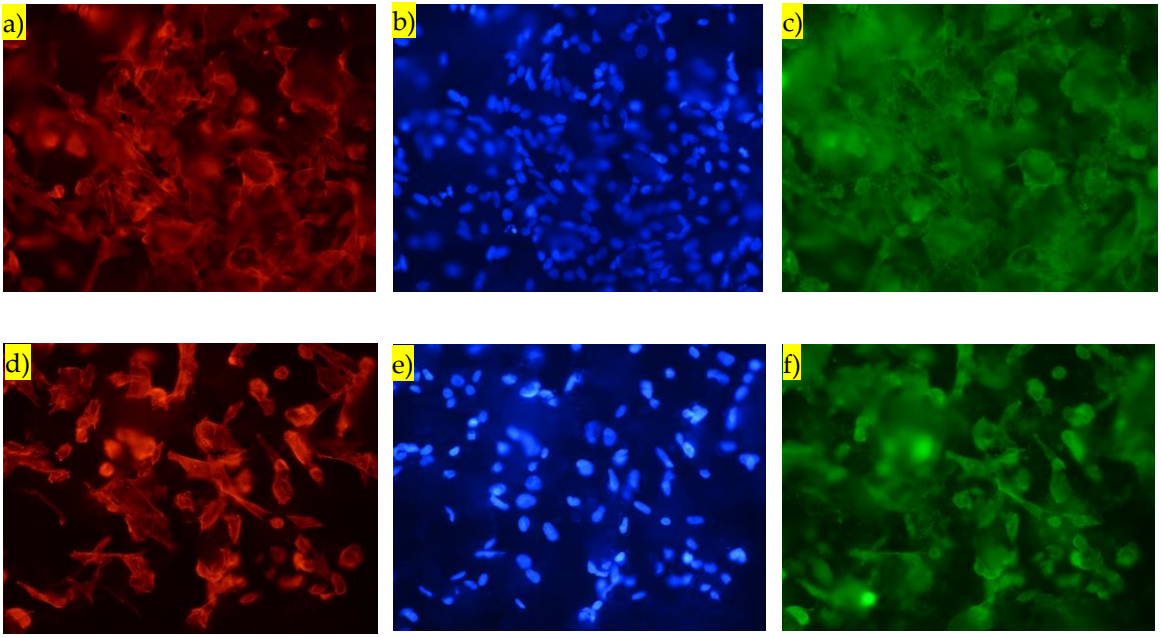

Figure 3.31 Fluorescence images obtained five days after culture. The red fluorescence indicates the cytoskeleton of the osteoblasts, the blue fluorescence the osteoblasts nuclei and the green fluorescence the vinculin protein. Images (a), (b) and (c) - charged PS Hap coating; (d), (e) and (f) - non-charged PS Hap coating. The images were obtained with the 40x objective, and correspond to an area of about 330 μm x 424 μm.

Moving on to the SBF results, fig. 3.32 shows the variation of the Ca^{2+} and P^{5+} ionic concentrations for increasing immersion times (0, 1, 3, 6, 12, 24, 48 and 72 h) in the SBF solution, for the charged and non-charged samples. The results follow the same trend reported in the literature for PS Hap coatings [115], i.e., an initial strong rise of the Ca^{2+} and P^{5+} ionic concentration and subsequently, their concentration starts to decrease.

The initial strong increase is caused by the partial dissolution of Ca^{2+} and P^{5+} ions from the Hap coating. As discussed in the state of the art, the PS process leads to a reduction of the Hap crystallinity within the coatings, as well as to the presence of secondary phases such as β-TCP and ACP. β-TCP, having a lower Ca/P ratio compared to Hap, has lower stability in the physiological conditions, i.e., dissolves faster (table 1.3). ACP can have a wide range of Ca/P ratios, comprehended between 1.2 - 2.2, therefore it also possesses a higher dissolution rate (the crystallinity is another factor, as it will be discussed later in this topic). This is the reason why calcium orthophosphate compounds with Ca/P ratios lower

than 1.5 are not applied in orthopaedics: they are too unstable and dissolve too quickly inside the body, i.e., their degradation kinetics is faster than the rate of new biologic bone formation. Even β-TCP, with a Ca/P ratio of 1.5, is very rarely applied alone, being instead applied in biphasic BCP Hap/β-TCP formulations. The rationale of these BCP compounds is to achieve materials with different degradations rates: the higher the β-TCP content, the higher the degradation rate. The bioactivity of a material with a higher dissolution rate is considered to be higher than a material with lower dissolution rate, as long as the higher dissolution rate does not compromise the biomaterial/new biologic bone interface stability. In summation, the SBF *in vitro* tests provide information regarding the two bioactivity factors: the dissolution rate and the interaction of the biomaterial with the ionic content of the human blood plasma. Considering again fig 3.32, there is a dominant factor, besides the Ca/P ratio, explaining the initial strong increase in the Ca^{2+} and P^{5+} ionic concentrations: the low crystallinity of the PS coatings. It is well-known in the calcium orthophosphates literature that the dissolution rate in the physiological conditions increases with the decrease of crystallinity of the material [116, 117]. The PS process produces coatings in which Hap has a considerable lower crystallinity compared to the initial Hap powder [53, 118]. Interestingly, recalling the information about the PS Hap coatings included in the state of the art of this thesis, while PS coatings have worst mechanical properties, both within the coating (residual stress levels) and at the coating/metallic substrate interface, they actually have the positive factor of possessing higher bioactivity levels compared to coatings where Hap retains a high crystallinity level, since they have higher dissolution rates, without compromising the coating/new biologic bone interface. Moreover, another advantage of the PS coatings which was alluded in the previous topic is that the high amount of defects and heterogeneities produced by the PS process enhance the charge storage capacity of these coatings. The results in fig. 3.32 for a Hap coating in which the Hap retains a high crystallinity level or for a bulk Hap sample would be different. An initial strong increase in the Ca^{2+} and P^{5+} concentration would not be observable, due to the low dissolution rate of the referred materials, only the decrease in the Ca^{2+} and P^{5+} concentrations would be observable [119, 120].

The results in fig. 3.32 show that right after the initial strong increase of the Ca^{2+} and P^{5+} ions, just one hour after immersion, the concentration tends to stabilize. For higher immersion times, 48 and 72 h, there is a significant decrease in the Ca^{2+} and P^{5+} ionic concentration, suggesting that the development of a bone-like Hap layer is taking place at a significant rate, i.e., ions from the solution are being incorporated in the developing apatite layer. It should be note that the steps leading to the development of the bone-like apatite layer most likely already occurring for shorter immersion times, already a few hours after immersion [121]. However, a decrease in the Ca^{2+} and P^{5+} ionic concentration is not visible because it is "masked" by the initial strong ionic concentration increase. The stabilization trend of the Ca^{2+} and P^{5+} ionic concentration a few hours after immersion is most likely related to the fact that the coating surface is starting to be completely covered with a developing bone-like Hap layer, blocking the coating dissolution effect.

Fig. 3.33 depicts a schematic illustration of the steps leading to the formation of a bone-like apatite layer on the Hap surface immersed in an SBF solution, as well as the importance of the electrostatic interactions [121]. It should be noted that the electrostatic interactions are assumed in the literature to be important even for non-charged Hap bioceramics. As fig. 3.33 depicts, when immersed in SBF, it is thought that Hap reveals a negative surface charge by exposing the hydroxyl and phosphate structural units, as depicted in the first illustration on the left [121]. This negative surface charge is able to selectively attract positive ions in the fluid, particularly Ca^{2+} ions since the electrostatic attraction is stronger compared to other ions such Na^{+} and K^{+}. Consequently, a Ca-rich ACP layer is continuously being formed, already a few hours after immersion. On its turn, the development of this Ca-rich ACP layer develops a positive surface charge which attracts negative phosphate and $HC0_3^-$ ions in the solution, leading to the formation of Ca-poor ACP. Remember that the most common ionic substitution in the biologic Hap is the incorporation of carbonate ions, thus in SBF, which replicates the human blood plasma ionic content, the same behaviour is observed. Subsequently, and also accounting the fact that Hap is the thermodynamically favoured phase in the *in vivo* and SBF conditions, the Ca-poor ACP layer will tend spontaneously to evolve to bone-like Hap, by incorporating calcium and phosphate ions mainly, together with other ions, notably carbonates [121]. This

last step of bone-like Hap development is reported to start as soon as between 9 - 12 hours after immersion in SBF [121]. Fig. 3.33 does not include dissolution of Ca^{2+} and P^{5+} ions from the coating into the SBF solution, which is true for highly crystalline near-stoichiometric Hap. However, as aforementioned, PS coatings are characterized by a partial ionic dissolution process, therefore the Ca^{2+} concentration decrease due the formation of Ca-rich ACP (fig. 3.31) and then the P^{5+} concentration decrease due to the formation of Ca-poor ACP are "masked" by dissolution of ions from the coating into the SBF solution. Moreover, while the processes in fig. 3.33 are taking place, some dissolution can still be occurring in some regions of the coating. Finally, in fig. 3.32, for the 48 and 72 h immersion times, the decrease in the Ca^{2+} and P^{5+} concentrations is observed, assigned to the development of the bone-like Hap layer.

If the electrostatic interactions of non-charged Hap bioceramics are assumed to be important, then the influence of an additional large negative stored charge density becomes clear: such negative charge must further accelerate the processes depicted in fig. 3.33. Particularly, observing the results in fig. 3.32, for the highest immersion times, the decrease in the concentration of the Ca^{2+} and P^{5+} ions is more pronounced in the charged samples compared to the non-charged samples, strikingly concerning the P^{5+} concentration, indicating a more advanced stage of bone-like Hap development on the charged surfaces.

The variation of the pH value shows an initial increase trend followed by a stabilization behaviour. This behaviour is typically observed in the literature for bioactive materials such Hap coatings (also in other forms, such as biocomposites) and bioactive glasses and glass-ceramics characterized by some degree of dissolution (frequently also designated as biodegradation) in the physiological conditions, consequently, also some degree of dissolution in SBF conditions [117, 122-124]. Such behaviour is commonly explained by the release of the alkaline earth ions Ca^{2+} and also of OH^- ions from the Hap which increase the pH value. Also, some ionic exchange between ions released by the Hap with ions present in the SBF solution can contribute to the pH increase [117, 123, 124].

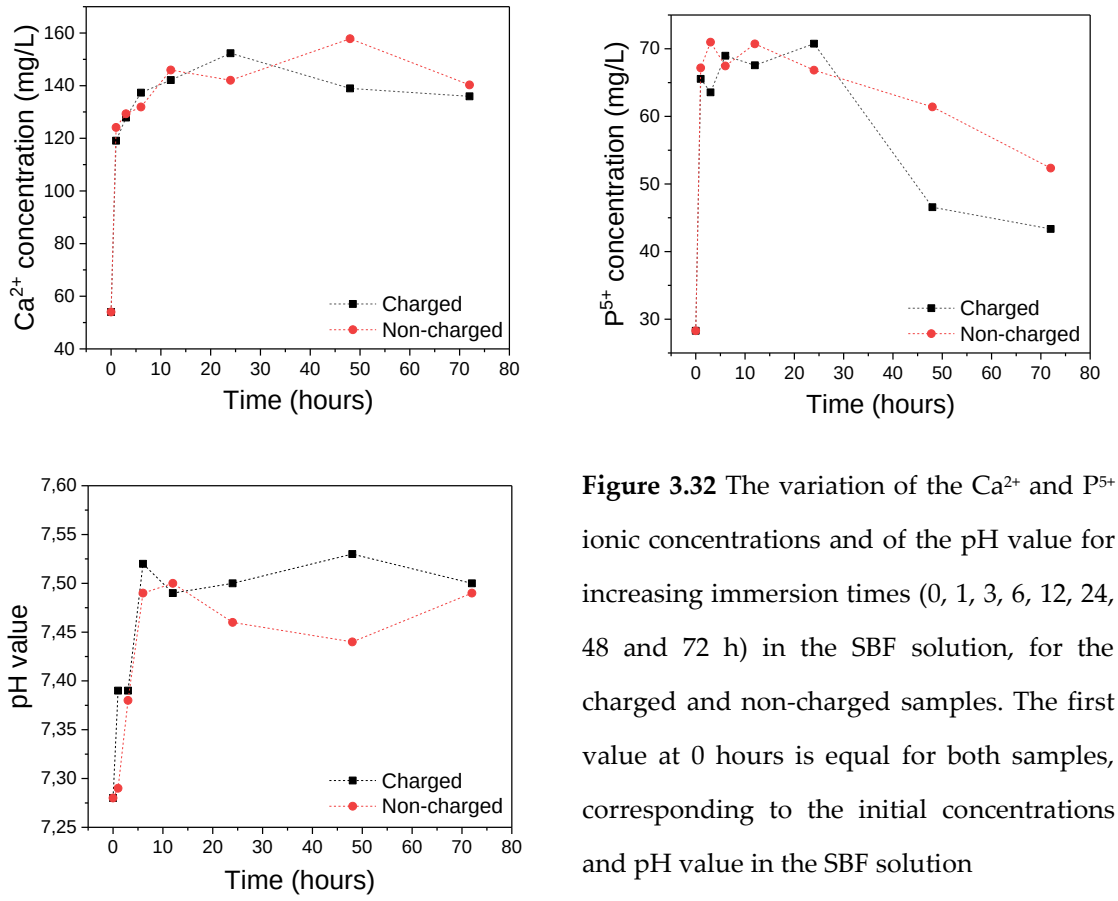

Figure 3.32 The variation of the Ca^{2+} and P^{5+} ionic concentrations and of the pH value for increasing immersion times (0, 1, 3, 6, 12, 24, 48 and 72 h) in the SBF solution, for the charged and non-charged samples. The first value at 0 hours is equal for both samples, corresponding to the initial concentrations and pH value in the SBF solution

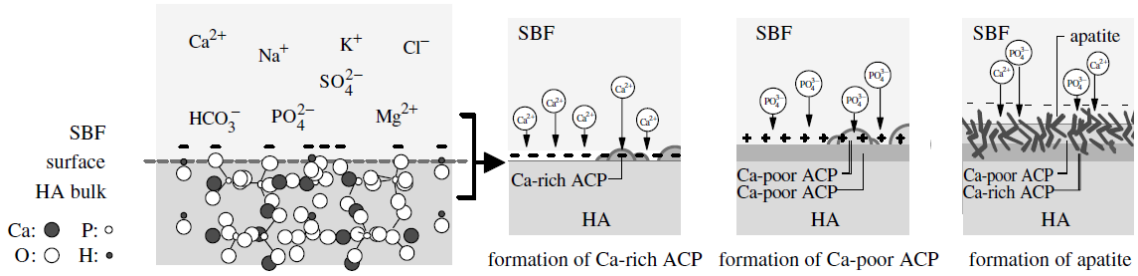

Figure 3.33 Schematic illustration of the steps leading to the formation of a bone-like apatite layer on the Hap surface immersed in a SBF solution. This illustration also shows the influence of the electrostatic interactions [121].

The SEM micrographs displayed in fig. 3.34 show the surface morphology of the charged coatings for different SBF immersion times: 1, 6, 48 and 72 h. After 1 h, it is visible that there are already structures precipitating on the surface of the coating. At 6 h, the typical cauliflower-like structures assigned to the precipitation and development of new biological Hap are clearly visible. These structures do not cover uniformly all the coating

surface, being more developed in some regions and less pronounced on other regions. This behaviour is typically observed in the literature. At 48 and 72 h, a radical modification of the initial surface morphology is evident, with the surface being completely covered with the newly forming apatite. These results show that the formation of the new Hap is taking place at a fast rate, attesting the high bioactivity level of the coatings. We can also make a correlation between these results with the SBF results on fig. 3.32. As it was discussed in the fig. 3.32 discussion, we said that the Ca^{2+} and P^{5+} concentrations decrease for the lower immersion times could be "masked" by the partial dissolution occurring in the coatings, while for the higher times of 48 and 72 h, the concentrations decrease could signify that all the coating surface would be already covered with the newly forming bone-like Hap. The micrographs in fig. 3.34 corroborate this line of thought, showing an incomplete surface coverage for lower times and complete surface coverage for 48 and 72 h.

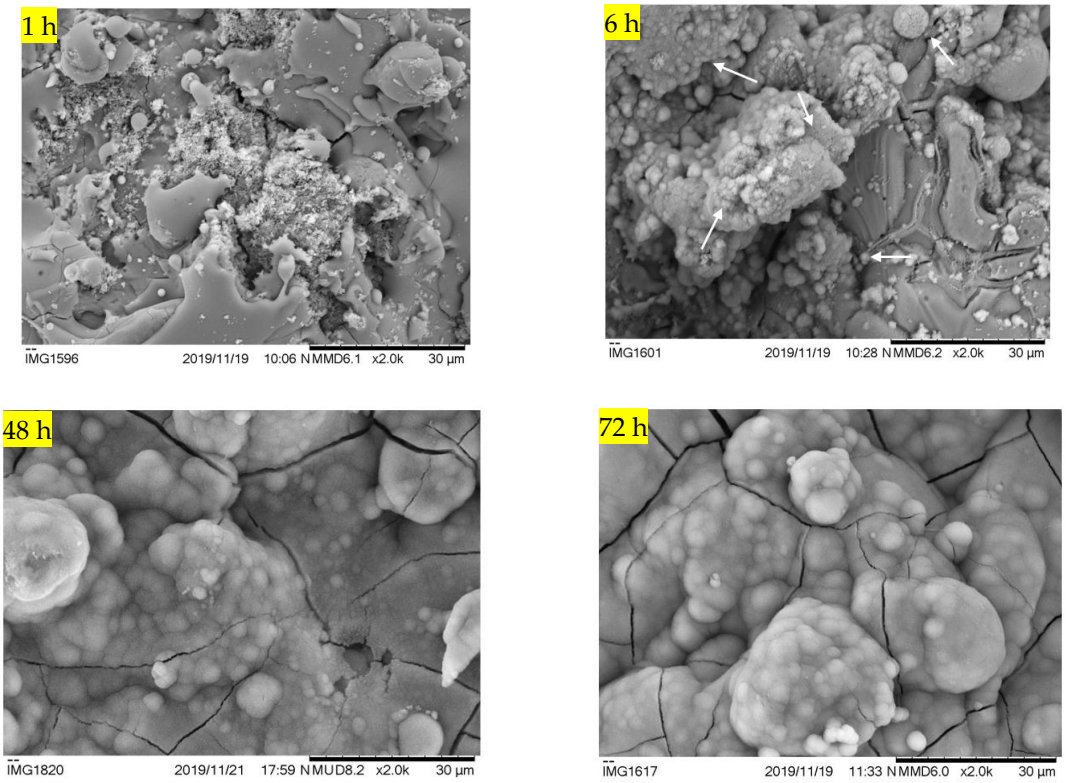

Figure 3.34 SEM micrographs revealing the surface morphology of the charged coatings for different immersion times: 1, 6, 48 and 72 h.

Chapter 4 Conclusion and future work

4.1 Conclusion

In this section, we shall make a reflection regarding the three main objectives of this work, contained in section 1.5.

With respect to the first objective, we successfully managed to develop "from scratch" a functional corona triode experimental system. The developed system is able to produce a positive or negative discharge, thus, it allows the user to define the charge polarity to be injected in the sample, an important feature and advantage of our system. Besides the possibility of applying the simpler "classic" method, our system offers the possibility of applying the more complex constant charging current method, where the charging current through the sample can be controlled and the sample surface potential buildup can be followed in real-time during a charging experiment. Moreover, the temperature of the experimental system can be controlled up to 200 ºC and a low humidity, reproducible atmosphere is maintained in all the charging experiments, an important feature to be considered in the development of a corona triode system.

The following process parameters of the CoBlast process were investigated: the weight ratio between abrasive and dopant, the blast distance and the blast pressure. It was shown that 50/50 weight ratios and distances lower than 30 mm are advantageous.

Concerning the second objective, the PS Hap coatings can be successfully charged through the corona triode technique. The coatings produced by the CoBlast process are characterized by having regions where the Ti substrate is not covered with a Hap layer, making the sample conductive. Due to the abrasive nature of the CoBlast process, additional depositions on an already coated Ti substrate will not produce a coating completely covering the metallic surface, i.e., to make additional depositions is essentially to remove the Hap coating which was already there and to produce a new one. Therefore, the charging current cannot be controlled in the CoBlast coatings.

Concerning the PS coatings, the constant charging current method revealed to be of particular importance, i.e., despite the fact that we are not able to perform TSDC measurements on the coatings, in order to calculate the stored charge density and estimate the trapped charge temporal stability, this method allows us to conclude that the PS coatings can be charged up to very high surface potentials. This is the advantage of being able to follow in real-time the surface potential buildup through the metallic grid potential.

The surface potential buildup curves for all the charged PS coatings present the same characteristic shape. A first linear stage suggests charge trapping is occurring essentially at a surface level. Subsequently, the sublinear behaviour, where surface potential buildup rate decreases, can indicate two things: that conduction current contribution started to be dominant compared to the linear stage capacitive current, or that charge trapping is occurring at a bulk level. Our results for the pellets show a high level of charge trapping at a bulk level. Finally, in a third stage, the surface potential tends to reach the saturation value. At this point, the current through the sample is essentially conductive. The charging current versus time data shows that the current controllability in the coatings is much better for lower charging current values. A coating charged with a current of - 1 nA (current density of - 1.4 nA/cm^2) displays the majority of the charging current values between - 0.9 and - 1.1 nA. A few events where the current increases significantly are detected, assigned to localized discharges in the sample. However, these events, which tend to occur for higher charging times (for lower charging currents) do not compromise by any means the experiment and the surface potential buildup, their influence is only manifested as some oscillations on the potential buildup curve. On the other hand, for higher charging currents, these events tend occur during all the charging time, being translated in higher surface potential fluctuations. Moreover, coatings charged with higher currents reach lower saturation surface potentials, suggesting that charging trapping at a bulk level is being favoured instead of trapping at a surface level, as it is reported in the literature [85].

The pellets prepared in this work were produced using the same Hap powder used in the PS deposition process, in order to perform TSDC measurements on the pellets. The rationale was to adopt a complementary strategy in order to find out if we can infer some

information regarding the coatings through the pellets results, notably regarding the stored charge density and its temporal stability, the most important parameters taking into account the biological applications of the PS Hap coatings.

The pellets presented a similar behaviour in terms of current controllability: lower charging currents yield better controllability, although such controllability is better on the coatings because the much larger thickness of the pellets increases the probability of current fluctuations.

With respect to the total stored charge density in the pellets, it is in the order of magnitude of - 10^{-5} and - 10^{-4} C/cm^2, for the "classic" and constant current methods, respectively. These are extremely interesting values, considering that they are well above the 10^{-6} magnitude, reported as the necessary magnitude to produce significant *in vitro* and *in vivo* bioactivity enhancements in Hap biomaterials [45]. It is our opinion that, by choosing appropriate process parameters values (grid potential and time), it would be possible to further increase the stored charge density values produced by the "classic" method, even the application of more than one grid potential could be considered. The stored charge temporal stability (time for complete discharge at RT) estimates are also very encouraging, with values ≥ 6 months for the "classic" method and ≥ 13 months for the constant charging current method, providing much time for the stored charge to take its effect *in vivo*.

A striking difference between the pellets and the coatings concerns the surface saturation potential, being much higher in the coatings. Making the bridge between the pellets results and the coatings, we demonstrated how the increased surface potential in the coatings, together with their lower thickness, means that the surface stored charge density in the coatings is much higher than the pellets. Accordingly, we estimated surface charge density values in the - 10^{-9} and - 10^{-7} C/cm^2 magnitudes for the pellets and the coatings, respectively. A very high level of bulk charge injection also occurs in both types of samples. Due to the large stored charge densities in the coatings, a high temporal stability is to be expected.

We have shown in this work that with the corona triode charging method we can achieve very high stored charge densities, in the 10^{-4} C/cm^2 order of magnitude, which is

hardly achieved through conventional polarization, and rarely reported in the literature. Furthermore, while we achieved such charge densities at 200 ºC, though conventional polarization much higher temperatures are required. As suggested in the following section 4.2, a very interesting future work will be to investigate if similar results can be obtained at lower temperatures. This advantage of the corona triode technique is also attested, for instance, for polymeric materials such as β-PVDF: while it was originally thought that temperatures up to 150 ºC were required for a successful polarization of β-PVDF, the first applications of the corona triode in this polymer demonstrated that a large and stable polarization can be achieved at RT [81].

Concerning the *in vitro* biological test results, the osteoblastic proliferation is enhanced in the charged coatings compared to the non-charged coatings. Since these tests were carried out about one month after the coatings were charged and demonstrate the bioactivity enhancement caused by the stored charge, they also clearly attest the stability of such stored charge, both for the cellular and SBF tests. The fluorescence images complement the proliferation results and show a well-developed, projected osteoblastic cytoskeleton and a well-distributed vinculin, clear indicators of a positive interaction and strong adhesion between the osteoblasts and the coatings.

The behaviour of the coatings in the SBF solution shows a strong initial release of Ca^{2+} and P^{5+} ions, caused by partial dissolution of the Hap coating, which is expected taking into account the properties of the Hap coatings produced by the PS process. The process of development of a bone-like Hap apatite layer on the surface of the coatings, reported to start a few hours after immersion in SBF, is accompanied by a decrease of the Ca^{2+} and P^{5+} ionic concentration in the SBF solution. However, such ionic decrease is "masked" during the first immersion day due to the coating dissolution. For the immersion times of 48 and 72 h, the Ca^{2+} and P^{5+} concentrations decrease, meaning that the coating dissolution stopped to be significant, most likely due to the fact that all or almost all of the coating surface is already covered with an apatite layer developing into bone-like Hap, blocking the coating dissolution. The decrease of the Ca^{2+} and P^{5+} ionic concentrations occurs most strikingly in the charged coatings, indicating a more advanced stage of bone-like Hap development on

the charged surfaces. The SEM micrographs revealing the surface morphology of the coatings for different SBF immersion times can be correlated with the variation of the Ca^{2+} and P^{5+} concentrations. Particularly, for the higher immersion times of 48 and 72 h, it is evident all the initial surface is already fully covered with a newly forming biologic Hap layer, being in agreement with the Ca^{2+} and P^{5+} concentration decrease observed for 48 and 72 h.

One month after being charged through the developed corona triode experimental system, the *in vitro* biological tests show how the stable stored negative charge density is able to enhance the bioactivity of the charged Hap PS coatings compared to the non-charged coatings. Thus, for the first time, a stable and large charge density was achieved on PS Hap coatings intended for orthopaedic applications through a non-invasive electrode-free charging technique. These charged coatings, with enhanced bioactive properties, would not face any problem concerning the international standards regulating the market and would comprise a differentiated, advantageous orthopaedic solution proving a better service and care to a continuously increasing number of patients.

4.2 Future work suggestions

We propose several future work topics, which are listed below:

1. Expand the corona feedback software in order to include the first stage, prior to the "fine-tuning" stage, responsible to, as fast as possible, increase the grid potential up to the value which leads to the constant charging current defined by the user (this is related to the resistance of the sample, for example, if it is significantly lower than the air gap resistance, then it would be very fast to reach the desired current) .
2. Explain at a more fundamental level the mechanisms behind the TSDC spectra of the samples, taking into account the differences between the corona triode charging and the conventional polarization technique. In other words, considering the depolarization peaks observed in the samples, explain the mechanisms behind them taking into account the negative charge trapped by the samples, at bulk and surface

levels, and the mechanisms reported in the literature behind the conventional polarization. In order to explain the appearance of a second depolarization peak for higher charging currents, one possible procedure to adopt is to perform a considerable number of charging experiments with high charging current values, estimate the electric field across the sample through the surface saturation potential, and then try to find the dependency of the peak current of each depolarization peak with the electric field. As discussed in topic 1.1.8, according to the dependency, a particular depolarization peak can be assigned to space charge detrapping or, for instance, to a dipolar reorientation mechanism.

3. Perform the corona triode charging experiments at different temperatures and compare the results with those obtained in this work for 200 ºC. If necessary, biological tests might also be carried out to compare the results. The idea behind this suggestion is to investigate if similar results can be obtained for lower discharge temperatures.
4. Despite the fact that it is not possible to control the charging current on the CoBlast coatings, one possible approach that could be researched would be to perform charging experiments using the "classic" method and subsequently perform biological tests to access if some enhancement of the bioactivity level would be observed. The rationale is that, although there are many regions where the Ti metallic substrate is directly exposed to the discharge, maybe the regions covered with Hap are able to store charge. The magnitude and stability of such stored charge would also be questions to be taken into account.
5. Undertake more biological tests on charged and non-charged coatings in order to further improve the statistics of the results. Moreover, the possibility of performing *in vivo* tests should be considered.

List of references

[1] C. LaWell, Orthopaedic Industry Reaches $49 Billion in 2017 (https://www.orthoworld.com/index.php/publications/orthoknow_content/orthopaedic-industry-reaches-49-billion-in-2017). 2018 (accessed May 13.2018).
[2] I. Global Industry Analysts, MCP-1637: Bone graft substitutes - A global strategic business report (http://www.strategyr.com/pressMCP-1637.asp). 2016 (accessed 26 March.2018).
[3] B. Morseth, N. Emaus, L. Jørgensen, Physical activity and bone: The importance of the various mechanical stimuli for bone mineral density. A review, Norsk Epidemiologi 20(2) (2011) 173-178.
[4] R.B. Heimann, H.D. Lehmann, Bioceramic Coatings for Medical Implants: Trends and Techniques, (2015) 496.
[5] E. Hutkin, Hip replacements are on the rise (http://www.sandiegouniontribune.com/news/health/sdut-hip-replacements-increasing-2015mar10-story.html). 2015 (accessed 26 March.2018).
[6] R. Aido, M. Sousa, A. Pereira, J. Ramos, R. Coelho, R. Lemos, A Influência da Osteoartrose e da Astroplastia da Anca sobre a Atividade Laboral em Doentes de Idade Ativa, Portuguese Journal of Orthopaedica and Traumatology 21(3) (2013) 371-379.
[7] X. Wang, S. Xu, S. Zhou, W. Xu, M. Leary, P. Choong, M. Qian, M. Brandt, Y.M. Xie, Topological design and additive manufacturing of porous metals for bone scaffolds and orthopaedic implants: A review, Biomaterials 83 (2016) 127-141.
[8] M.L. Brandi, Microarchitecture, the key to bone quality, Rheumatology 48 (2009) iv3-8.
[9] U.H. Lerner, Osteoblasts, osteoclasts, and osteocytes: Unveilling their intimate-associated responses to applied orthodontic forces, Seminars in Orthodontics 18(4) (2012) 237-248.
[10] K. Matsuo, Osteocytes communicate with osteoclast lineage cells via RANKL, IBMS BoneKEy 9(39) (2012) 1-3.
[11] N. Choi, Kidney and phosphate metabolism, Electrolytes and Blood Pressure 6(2) (2008) 77-85.
[12] Clinical Applications of Biomaterials, NIH Consens Statement 4(5) (1982) 1-19.
[13] R.Z. LeGeros, Calcium phosphate-based osteoinductive materials, Chem. Rev. 108 (2008) 4742-4753.
[14] E.M. Riviera-Muñoz, Hydroxyapatite-based materials: Synthesis and characterization, in: P.R. Fazel (Ed.), Biomedical engineering - frontiers and challenges2011.
[15] P. Wiles, The classic: the surgery of the osteo-arthritic hip, Clinical Orthopaedics and Related Research 417 (2003) 3-16.
[16] A. Ravaglioli, A. Krajewski, Bioceramics: Materials, properties and applications, Springer Netherlands1992.
[17] J.G. Moore, S.M. Ross, B.A. Williams, Regional anesthesia and ambulatory surgery, Current Opinion in Anaesthesiology Journal 26(6) (2013) 652-660.
[18] S. Dorozhkin, Calcium Orthophosphates: Applications in nature, biology and medicine, 2012.
[19] S.V. Dorozhkin, Bioceramics of calcium orthophosphates, Biomaterials 31 (2010) 1465-1485.
[20] M. Canillas, P. Pena, A.H. Aza, A. Rodríguez, Calcium phosphates for biomedical applications, Boletín de la Sociedad Española de Cerámica y Vidrio 56 (2017) 91-112.
[21] S.V. Dorozhkin, Self-setting calcium orthophosphate formulations: Cements, concretes, pastes and putties, International Journal of Materials and Chemistry 1(1) (2011) 1-48.
[22] S.V. Dorozhkin, Calcium orthophosphate-based bioceramics, Materials 6(9) (2013) 3840-3942.
[23] E.S. Kovaleva, M.P. Shabanov, V.I. Putlayev, Y.Y. Filippov, Y.D. Tretyakov, V.K. Ivanov, Carbonated hydroxyapatite nanopowders for preparation of bioresorbable materials, Materials Science & Engineering Technology 39(11) (2008) 822-829.
[24] N. Patel, S.M. Best, W. Bonfield, I.R. Gibson, K.A. Hing, E. Damien, P.A. Revell, A comparative study in the in vivo behaviour of hydroxyapatite and silicon substitute hydroxyapatite granules, Journal of Materials Science 13(12) (2002) 1199-1206.
[25] J.C. Elliott, Structure and chemistry of the apatites and other calcium orthophosphates, Elsevier.
[26] G. Ma, X.Y. Liu, Hydroxyapatite: Hexagonal or monoclinic?, Crystal Growth & Design 9(7) (2009) 2991-2994.
[27] O. Hochrein, R. Kniep, D. Zahn, Atomistic simulation study of the order/disorder (monoclinic to hexagonal) phase transition of hydroxyapatite, Chemistry of Materials 17 (2005) 1978-1981.
[28] C. Liao, F. Lin, K. Chen, J. Sun, Thermal decomposition and reconstitution of hydroxyapatite in air atmosphere, Biomaterials 20 (1999) 1807-1813.

[29] T. Wang, A. Dorner-Reisel, E. Müller, Thermogravimetric and thermokinetic investigation of the dehydroxylation of a hydroxyapatite powder, Journal of the European Ceramic Society 24(4) (2004) 693-698.
[30] J. Cihlář, A. Buchal, M. Trunec, Kinetics of thermal decomposition of hydroxyapatite bioceramics, Journal of Materials Science 34(24) (1999) 6121-6131.
[31] C. Yoder, J. Pasteris, K. Worcester, D. Schermerhorn, M. Sternlieb, J. Goldenber, Z. Wilte, Dehydration and rehydration of carbonated fluor- and hydroxyapatite, Minerals 2 (2012) 100-117.
[32] E. Champion, Sintering of calcium phosphate bioceramics, Acta Biomater. 9 (2013) 5855-5875.
[33] N. Horiuchi, M. Nakamura, A. Nagai, K. Katayama, K. Yamashita, Proton conduction related electrical dipole and space charge polarization in hydroxyapatite, Journal of Applied Physics 112(7) (2012) 074901.
[34] P.R. Prezas, B.M.G. Melo, L.C. Costa, M.A. Valente, M.C. Lança, J.M.G. Ventura, L.F.V. Pinto, M.P.F. Graça, TSDC and impedance spectroscopy measurements on hydroxyapatite, β-tricalcium phosphate and hydroxyapatite/β-tricalcium phosphate biphasic bioceramics, Applied Surface Science 424(1) (2017) 28-38.
[35] N. Horiuchi, K. Madokoro, K. Nozaki, M. Nakamura, K. Katayma, A. Nagai, K. Yamashita, Electrical conductivity of polycrystalline hydroxyapatite and its application to electret formation, Solid State Ionics 315 (2018) 19-25.
[36] N. Horiuchi, J. Endo, N. Wada, K. Nozaki, M. Nakamura, A. Nagai, K. Katayama, K. Yamashita, Dielectric properties of stoichiometric and defect-induced hydroxyapatite, Journal of Applied Physics 113 (2013) 134905.
[37] J.P. Gittings, C.R. Bowen, A.C.E. Dent, I.G. Turner, F.R. Baxter, J.B. Chaudhuri, Electrical characterization of hydroxyapatite-based bioceramics, Acta Biomaterialia 5(2) (2009) 743-754.
[38] S.B. Lang, S.A.M. Tofail, A.L. Kholkin, M. Wojtas, M. Gregor, A.A. Gandhi, Y. Wang, S. Bauer, M. Krause, A. Plecenik, Ferroelectric polarization in nanocrystalline hydroxyapatite thin films on silicon, Scientific Reports 3 (2013) 1-6.
[39] K. Yamashita, K. Kitagaki, T. Umegaki, Thermal-instability and proton conductivity of ceramic hydroxyapatite at high temperatures, J. Am. Ceram. Soc. 78 (1995) 1191-1197.
[40] K. Yamashita, N. Oikawa, T. Umegaki, Acceleration and deceleration of bone-like crystal growth on ceramic hydroxyapatite by electric poling, Chem. Mater. 8 (1996) 2697-2700.
[41] Y. Tanaka, T. Iwasaki, M. Nakamura, A. Nagai, K. Katayama, K. Yamashita, Polarization and microstructural effects of ceramic hydroxyapatite electrets, Journal of Applied Physics 107(1) (2010) 014107.
[42] S. Itoh, S. Nakamura, M. Nakamura, K. Shinomiya, K. Yamashita, Enhanced bone regeneration by electrical polarization of hydroxyapatite, Artificial Organs 30(11) (2006) 863-869.
[43] H. Sagawa, S. Itoh, W. Wang, K. Yamashita, Enhanced bone bonding of the hydroxyapatite/ β-tricalcium phosphate composite by electrical polarization in rabbit long bone, Artificial Organs 34(6) (2010) 491-497.
[44] S. Nakamura, T. Kobayashi, K. Yamashita, Numerical osteobonding evaluation of electrically polarized hydroxyapatite ceramics, Journal of Biomedical Materials Research Part A 68(1) (2004) 90-94.
[45] S. Bodhak, S. Bose, A. Bandyopadhyay, Electrically polarized HAp-coated Ti: *In vitro* bone cell-material interactions, Acta Biomaterialia 6 (2010) 641-651.
[46] S. Bodhak, S. Bose, A. Bandyopadhyay, Role of surface charge and wettability on early stage mineralization and bone cell-materials interactions of polarized hydroxyapatite, Acta Biomaterialia 5 (2009) 2178-2188.
[47] I. Bogdanoviciene, K. Tõnsuaadu, M. Valdek, I. Grigoraviciute-Puroniene, A. Beganskiene, A. Kareiva, pH impact on the sol-gel preparation of calcium hydroxyapatite, $Ca_{10}(PO_4)_6(OH)_2$, using a novel complexing agent, DCTA, Central European Journal of Chemistry 8(6) (2010) 1323-1330.
[48] D.M. Liu, T. Troczynski, D. Hakimi, Effect of hydrolysis on the phase evolution of water-based sol-gel hydroxyapatite and its application to bioactive coatings, Journals of Materials Science: Materials in Medicine 13(7) (2002) 657-665.
[49] H. Kim, H. Kim, J.C. Knowles, Fluor-hydroxyapatite sol-gel coating on titanium substrate for hard tissue implants, Biomaterials 25(17) (2004) 3351-3358.
[50] M.C. Kuo, S.K. Yen, The process of electrochemical deposited hydroxyapatite coatings on biomedical titanium at room temperature, Materials Science and Engineering C 20 (2002) 153-160.
[51] S.L. Hub, Plasma-spray coating (https://www.sciencelearn.org.nz/resources/245-plasma-spray-coating). 2014 (accessed 27 June 2018).
[52] T.J. Levingstone, M. Ardhaoui, K. Benyounis, L. Looney, J.T. Stokes, Plasma sprayed hydroxyapatite coatings: Understanding process relationships using design of experiment analysis, Surface and Coatings Technology 283 (2015) 29-36.

[53] A. McCabe, M. Pickford, J. Shawcross, The history, technical specifications and efficacy of plasma spray coatings applied to joint replacement prostheses, Reconstructive Review 6(4) (2016).
[54] Z. Mohammadi, A.A. Ziaei-Moayyed, A. Sheikh-Mehdi Mesgar, Grit blasting of Ti-6Al-4V alloy: Optimization and its effect on adhesion strength of plasma-sprayed hydroxyapatite coatings, Journal of Materials Processing Technology 194(1-3) (2007) 15-23.
[55] S.W. Kweh, K.A. Khor, P. Cheang, Plasma-sprayed hydroxyapatite (HA) coatings with flame-spheroidized feedstock: microstructure and mechanical properties, Biomaterials 21(12) (2000) 1223-1234.
[56] Y. Yang, E. Chang, Measurements of residual stresses in plasma-sprayed hydroxyapatite coatings on titanium allow, Surface and Coatings Technology 190(1) (2005) 122-131.
[57] Y. Otsuka, D. Kojima, Y. Mutoh, Prediction of cyclic delamination lives of plasma-spayed hydroxyapatite coating on Ti-6Al-4V substrates with considering wear and dissolutions, Journal of the Mechanical Behavior of Biomedical Materials 64 (2016) 113-124.
[58] F. Gartner, T. Schmidt, T. Stoltenhoff, H. Kreye, Recent developments and potential applications of cold spraying, Advanced Engineering Materials 8(7) (2006) 611-618.
[59] A. Choudhuri, P.S. Mohaunty, J. Karthikeyan, Bio-ceramic composite coatings by cold spray technology, Thermal Spraying (2009) 391-396.
[60] L. O'Neill, C. O'Sullivan, P. O'Hare, L. Sexton, F. Keady, J. O'Donoghue, Deposition of substituted apatites onto titanium surfaces using a novel blasting process, Surface & Coatings Technology 204 (2009) 484-488.
[61] P. O'Hare, B.J. Meenan, G.A. Burke, G. Byrne, D. Dowling, J.A. Hunt, Biological responses to hydroxyapatite surfaces deposited via a co-incident microblasting technique, Biomaterials 31 (2010) 515-522.
[62] C. O'Sullivan, P. O'Hare, G. Byrne, L. O'Neill, K.B. Ryan, A.M. Crean, A modified surface on titanium deposited by a blasting process, Coatings 1(1) (2011) 53-71.
[63] E. Ltd., http://www.enbio.eu/. (accessed 16-11.2018).
[64] M.A. Wimmer, A. Fischer, R. Buscher, R. Pourzal, C. Sprecher, R. Hauert, J.J. Jabobs, Wear mechanisms in metal-on-metal bearings: The importance of tribochemical reaction layers, Journal of Orthopaedic Research 28(4) (2009).
[65] D. Yue, T. Ma, Y. Hu, J. Yeon, A.C.T. van Duin, H. Wang, J. Luo, Tribochemical mechanism of amorphous silica asperities in aqueous environment: A reactive molecular dynamics study, Langmuir 31(4) (2015) 1429-1436.
[66] J.N. Barry, B. Twomey, A. Cowley, L. O'Neill, P.J. McNally, D.P. Dowling, Evaluation and comparison of hydroxyapatite coatings deposited using both thermal and non-thermal techniques, Surface & Coatings Technology 226 (2013) 82-91.
[67] C.F. Dunne, B. Twomey, C. Kelly, J.C. Simpson, K.T. Stanton, Hydroxyapatite and fluorapatite coatings on dental screws: effects of blast coating process and biological response, Journal of Materials Science: Materials in Medicine 26(1) (2015).
[68] M. McCracken, DDS, MSBE, Dental implant materials: commercially pure titanium and titanium alloys, Journal of Prosthodontics 8(1) (1999) 40-43.
[69] J.E.G. González, J.C. Mirza-Rosca, Study of the corrosion behavior of titanium and some of its alloys for biomedical and dental implant applications, Journal of the Electroanalytical Chemistry 471(2) (1999) 109-115.
[70] L. Sun, C.C. Berndt, C.P. Grey, Phase, structural and microstructural investigations of plasma sprayed hydroxyapatite coatings, Materials Science and Engineering: A 360(1-2) (2003) 70-84.
[71] J. Wigren, Technical note: grit blasting as surface preparation before plasma spraying, Surface and Coatings Technology 34 (1988) 101-108.
[72] C.F. Dunne, B. Twomey, L. O'Neill, K.T. Stanton, Co-blasting of titanium surfaces with an abrasive and hydroxyapatite to produce bioactive coatings: substrate and coating characterization, Journal of Biomaterials Applications 28(5) (2014) 767-778.
[73] C.F. Dunne, B. Twomey, K.T. Stanton, Effect of a blast coating process on the macro-and microstructure of grade 5 titanium foam, Materials Letters 147 (2015) 75-78.
[74] ENBIO, Ltd., Solar Orbiter, (http://enbio.eu/solar-orbiter/) (accessed 23-11-2018.).
[75] K.A.J. Doherty, C.F. Dunne, A. Norman, T. McCaul, B. Twomey, K. Stanton, Flat absorber coating for spacecraft thermal control applications, Journal of Spacecraft and Rockets 53(6) (2016) 1035-1042.
[76] R.H.F.E. Shmerling, Harvard Health Publishing), How long will my hip or knee replacement last? (https://www.health.harvard.edu/blog/how-long-will-my-hip-or-knee-replacement-last-2018071914272) (accessed 23-09-2019). 2018).

[77] Statista, Cost of a hip replacement in selected countries as of 2018 (in U.S. dollars), (https://www.statista.com/statistics/450373/cost-of-a-hip-replacement-in-various-countries/) (accessed 23-09-2019). 2019).
[78] R.A. Moreno, B. Gross, Measurement of potential buildup and decay, surface charge density, and charging currents of corona-charged polymer foil electrets, Journal of Applied Physics 47(8) (1976) 3397.
[79] J.A. Giacometti, Radial current-density distributions and sample charge uniformity in a corona triode, Journal of Physics D: Applied Physics 20 (1987) 675-682.
[80] B. Gross, Radiation-induced charge storage and polarization effects, in: G.M. Sessler (Ed.), Electrets, Springer-Verlag Berlin Heidelberg1987.
[81] G.M. Sessler, Poling and properties of polarization of ferroelectric polymers and composites, Key Engineering Materials 92-93 (1994) 249-274.
[82] J.A. Giacometti, N.O. Oliveira Jr., Corona charging of polydmers, IEEE Transactions on Electrical Insulation 27(5) (1992) 924-943.
[83] P. Dhima, F. Vila, Determination of volume conductivity of polyethylene using positive corona, when the current through the sample depends linearly on grid potential, Journal of Materials Science and Chemical Engineering 5 (2017) 40-51.
[84] J.A. Giacometti, S. Fedosov, M.M. Costa, Corona charging of polymers: recent advances on constant current charging, Brazilian Journal of Physics 29(2) (1999) 269-279.
[85] J.A. Giacometti, J.S.C. Campos, Constant current corona triode with grid voltage control.Application to polymer foil charging, Review of Scientific Instruments 61(3) (1990) 1143-1150.
[86] O.N. Oliveira, G.F.L. Ferreira, Grid-to-plate current-voltage characteristics of a corona triode, Review of Scientific Instruments 56(10) (1985) 1957-1961.
[87] J.A. Giacometti, P.A. Ribeiro, M. Raposo, J.N. Marat-Mendes, J.S.C. Campos, A.S. DeReggi, Study of poling behavior of biaxially stretched poly(vinylidene fluoride) films using the constant-current corona triode, Journal of Applied Physics 78(9) (1995) 5597.
[88] J.A. Giacometti, Constant-current corona triode adapted and optimized for the characterization of thin dielectric films, Review of Scientific Instruments 89 (2018) 055109.
[89] R. Chen, Methods for kinetic analysis of thermally stimulated processes, Journal of Materials Science 11(8) (1976) 1521-1541.
[90] C. Bucci, R. Fieschi, Ionic thermoconductivity. Method for the investigation of polarization in insulators, Physical Review Letters 12(1) (1964) 16-19.
[91] R. Chen, Y. Kirsh, The analysis of thermally stimulated processes, Pergamon Press1981.
[92] P.R. Prezas, M.P.F. Graça, Thermally stimulated depolarization and polarization currents, in: M.P.F. Graça (Ed.), Electrical measurements: Introduction, concepts and applications, Nova Science Publishers2018.
[93] C. Hong, D.E. Day, Thermally stimulated polarization and depolarization current (TSPC/TSDC) techniques for studying ion motion in glass, Journal of Materials 14 (1979) 2493-2499.
[94] J. Vanderschueren, J. Gasiot, Field-induced thermally stimulated currents, in: P. Braunlich (Ed.), Thermally stimulated relaxation in solids, Springer Berlin Heidelberg1979, pp. 135-223.
[95] J.V. Turnhout, Thermally stimulated discharge of electrets, in: G. Sessler (Ed.), Electrets, Springer Berlin Heidelberg1987.
[96] S.H. Carr, Thermally stimulated discharge current analysis of polymers, in: D.A. Seanor (Ed.), Electrical properties of polymers, Academic Press1982.
[97] G.F.J. Garlick, A.F. Gibson, The electron trap mechanism of luminescence in sulphide and silicate phosphors, Proceeding of the Physical Society 60(6) (1948) 574-590.
[98] C. Christodoulides, Errors involved in the determination of activation energies in TL and TSDC by the initial rise method, Journal of Physics D: Applied Physics 18 (1985) 1665-1671.
[99] D. Brone, A. Alexander, F.J. Muzzio, Quantitative characterization of mixing of dry powders in V-blenders, Particle Technology and Fluidization 44(2) (1998) 271-278.
[100] D. Instruments, ASTM C633 (http://dfdinstruments.com/astm-c633/) (accessed 09/07/2019).).
[101] H.P. Klug, L.E. Alexander, X-Ray diffraction procedures for polycrystalline and amorphous materials, John Wiley & Sons, New York, 1974.
[102] M. Bohler, F. Kanz, B. Schwarz, I. Steffan, A. Walter, H.J. Plenk, K. Knahr, Adverse tissue reactions to wear particles from Co-alloy articulations, increased by alumina-blasting particle contamination from cementless Ti-based total hip implants. A report of seven revisions with early failure., The Journal of Bone and Joint Surgery. British Volume 84(1) (2002) 128-136.
[103] F. Ahmed, H. Rashid, S. Farookhi, V. Verma, Y. Mulyar, M. Khalifa, Z. Sheikh, Surface modifications of endosseous dental implants by incorporation of roughness and hydroxyapatite coatings, Journal of the Pakistan Dental Association 24(4) (2015) 162-171.

[104] P.G. Korovessis, D.D. Deligianni, Role of surface roughness of titanium versus hydroxyapatite on human bone marrow cells response, Journal of Spinal Disorders & Techniques 15(2) (2002) 175-183.
[105] M.G. Holthaus, L. Treccani, K. Rezwan, Osteoblast viability on hydroxyapatite with well-adjusted submicron and micron surface roughness as monitored by the proliferation reagent WST-I, Journal of Biomaterials Applications 27(7) (2012) 791-800.
[106] D.D. Deligianni, N.D. Katsala, P.G. Koutsoukos, Y.F. Missirlis, Effect of surface roughness of hydroxyapatite on human bone marrow cell adhesion, proliferation, differentiation and detachment strength, Biomaterials 22(1) (2000) 87-96.
[107] A. Wennerberg, T. Albrektsson, C. Johansson, B. Andersson, Experimental study of turned and grit-blasted screw-shaped implants with special emphasis on effects of blasting material and surface topography, Biomaterials 17(1) (1996) 15-22.
[108] M. Roy, A. Bandyopadhyay, S. Bose, Induction plasma sprayed nano hydroxyapatite coatings on titanium for orthopaedic and dental implants, Surface and Coatings Technology 205(8-9) (2011) 2785-2792.
[109] Y.C. Tsui, C. Doyle, T.W. Clyne, Plasma sprayed hydroxyapatite coatings on titanium substrates Part 1: Mechanical properties and residual stress levels, Biomaterials 19(22) (1998) 2015-2029.
[110] G.F. Leal Ferreira, M.T. Figueiredo, Corona charging of electrets: models and results, IEEE Transactions on Electrical Insulation 27(4) (1992) 719-738.
[111] A. Thyssen, Charge distribution and stability in electret materials, Department of Micro- and Nanotechnology, DTU Nanotech, Denmark, 2016.
[112] O.N. Oliveira, G.F. Leal Ferreira, Electron transport in corona charged 12 μm Teflon FEP with saturable deep traps, Applied Physics A 42 (1987) 213-217.
[113] S. Bodhak, S. Bose, A. Bandyopadhyay, Influence of electro-thermal polarization on surface properties of hydroxyapatite, in: R. Narayan, A. Bandyopadhyay, S. Bose (Eds.), Biomaterials science: Processing, properties and applications2011.
[114] A. Samuila, A. Iuga, R. Morar, V. Neamtu, L. Dascalescu, Electrostatic technologies for materials recovery in high-intensity electric fields, Simpozionul Impactul AQ-ului comunitar asupra echipamentelor şi tehnologiilor de mediu, Agigea, Romania, 2006.
[115] Y.W. Gu, K.A. Khor, P. Cheang, In vitro studies of plasma-sprayed hydroxyapatite/Ti-6Al-4V composite coatings in simulated body fluid (SBF), Biomaterials 24 (2003) 1603-1611.
[116] F.J. Gil, A. Padrós, J.M. Manero, C. Aparicio, M. Nilsson, J.A. Planell, Growth of bioactive surfaces on titanium and its alloys for orthopaedic and dental implants, Materials Science and Engineering C 22 (2002) 53-60.
[117] L.L. Hench, Bioceramics: From concept to clinic, Journal of the American Ceramic Society 74(7) (1991) 1487-1510.
[118] R. Kotian, P.P. Rao, P. Madhyastha, X-ray diffraction analysis of hydroxyapatite-coated in different plasma gas atmosphere on Ti and Ti-6Al-4V, European Journal of Dentistry 11 (2017) 438-446.
[119] H. Shibata, T. Yokoi, T. Goto, K. I.Y., M. Kawashita, K. Kikuta, C. Ohtsuki, Behavior of hydroxyapatite crystals in a simulated body fluid: effects of crystal face, Journal of the Ceramic Society of Japan 121(9) (2013) 807-812.
[120] M. Kamitakahara, T. Saito, K. Ioku, Synthesis and *in vitro* evaluation of hydroxyapatite with controlled morphology, 4th International Symposium on Functional Materials (ISFM2011), Journal of Physics: Conference Series, Sendai, Japan, 2012.
[121] H. Kim, T. Himeno, M. Kawashita, T. Kokubo, T. Nakamura, The mechanism of biomineralization of bone-like apatite on synthetic hydroxyapatite: an *in vitro* assessment, Journal of the Royal Society Interface 1 (2004) 17-22.
[122] Z. Xuhui, Y. Lingfang, Z. Yu, X. Jinpinh, Hydroxyapatite coatings on titanium prepared by electrodeposition in a modified simulated body fluid, Chinese Journal of Chemical Engineering 17(4) (2009) 667-671.
[123] Y. Deng, Y. Yang, Y. Ma, K. Fan, W. Yang, G. Yin, Nano-hydroxyapatite reinforced polyphenylene sulfide biocomposite with superior cytocompatibility and *in vivo* osteogenesis as a novel orthopedic implant, The Royal Society of Chemistry 7 (2017) 559-573.
[124] N.S. Sambudi, S. Cho, K. Cho, Porous hollow hydroxyapatite microspheres synthesized synthesized by spray pyrolysis using a microalga template: preparation, drug delivery, and bioactivity, The Royal Society of Chemistry 6 (2016) 43041-43048.